



Polish Maritime Research

Special Issue S3 (99) 2018
Vol. 25

Marine Processes Studies and Marine Engineering

ADDRESS OF PUBLISHER
& EDITOR'S OFFICE:

GDAŃSK UNIVERSITY
OF TECHNOLOGY

Faculty of Ocean Engineering
& Ship Technology
G. Narutowicza 11/12
80-233 Gdańsk, POLAND

EDITORIAL STAFF:

Wiesław Tarełko
| Editor in Chief
Janusz Kozak
| Deputy Editors-in-Chief
Wojciech Litwin
| Deputy Editors-in-Chief

Price:
single issue: 25 PLN

Prices for abroad
single issue:
- in Europe EURO 15
- overseas USD 20

WEB:
pg.edu.pl/pmr

e-mail : pmr@pg.edu.pl

ISSN 1233-2585

CONTENS

- | | |
|----|--|
| 5 | Lili Dong, Gouhui Liu, Xin Ye, Wei Wang
<i>STUDY ON THE DESIGN OF CONTAINER HIGHWAY AND RAILWAY AUTOMATIC TRANSFER VEHICLE IN OCEAN PORT</i> |
| 13 | Jun Du, Ruo Nan Li, Xin Wu, Yan Zhang
<i>STUDY ON OPTIMIZATION SIMULATION OF SCR DENITRATION SYSTEM FOR MARINE DIESEL ENGINE</i> |
| 22 | Caiyun Gu, Peng Zhao, Li Wang, Hongxia Guo
<i>TECHNICAL APPLICATION OF PETROLEUM LOGGING INSTRUMENTS IN MARINE LOGGING</i> |
| 29 | Bianjiang Hu
<i>APPLICATION OF EVALUATION ALGORITHM FOR PORT LOGISTICS PARK BASED ON PCA-SVM MODEL</i> |
| 36 | Yanzhe Hu, Mengjie Xu, Yang Li
<i>SIMULATION MODEL AND STATE ANALYSIS OF SHIP TRANSMISSION LINE</i> |
| 43 | Desen Kong, Meixu Deng, Yi Liu, Xiaoyan Tan
<i>STUDY OF THE FORCE AND DEFORMATION CHARACTERISTICS OF SUBSEA MUDMAT-PILE HYBRID FOUNDATIONS</i> |
| 54 | Qinxi Li, Shuping Jiang, Xiang Chen
<i>EXPERIMENT ON PRESSURE CHARACTERISTICS OF SUBMERGED FLOATING TUNNEL WITH DIFFERENTSECTION TYPES UNDER WAVE CONDITION</i> |
| 61 | Nan Lyu, Jingyuan Zhao, Minghua Lyu
<i>EXPLORATION OF LAND DEVELOPMENT INTENSITY INDEX OF PORT CONTAINER LOGISTICS PARK BASED ON QUANTITATIVE ALGORITHM AND PENT ANALYSIS METHOD</i> |
| 68 | Weizhuang Ma, Yunbo Li, Yong Ding, Kaiye Hu, Linxin Lan
<i>NUMERICAL SIMULATIONS OF LINEARLY STRATIFIED FLOW PAST SUBMERGED BODIES</i> |
| 78 | Lisheng Pan
<i>EXPLORATION AND MINING LEARNING ROBOT OF AUTONOMOUS MARINE RESOURCES BASED ON ADAPTIVE NEURAL NETWORK CONTROLLER</i> |

ADDRESS OF PUBLISHER
& EDITOR'S OFFICE:

GDAŃSK UNIVERSITY
OF TECHNOLOGY

Faculty of Ocean Engineering
& Ship Technology
G. Narutowicza 11/12
80-233 Gdańsk, POLAND

- 84 **Zhiyong Pei, Qingning Yuan, Weiguo Wu**
DEVELOPMENT OF "4E" LEVEL RIVER-SEA-GOING SHIP
- 91 **Zhiyong Pei, Tao Xu, Weiguo Wu**
PROGRESSIVE COLLAPSE TEST OF SHIP STRUCTURES IN WAVES
- 99 **Li Qiang, Yang Bing-Dong, Hong Bi-Guang**
*CALCULATION AND MEASUREMENT OF TIDE HEIGHT FOR THE NAVIGATION
OF SHIP AT HIGH TIDE USING ARTIFICIAL NEURAL NETWORK*
- 111 **Fu Qiang, Chen Ming, Wang Xiuli, Zhu Rongsheng, Zhang Guoyu, Yu
Jianen**
*STABILITY OF AIR NUCLEUS IN LIQUID WATER AND CAVITATION INCEPTION
ON MARINE ENGINEERING*
- 120 **Fan Qinglai, Gao Yufeng**
*EFFECT OF REINFORCEMENT RATIO AND VERTICAL LOAD LEVEL ON
LATERAL CAPACITY OF BRIDGE PILE FOUNDATIONS*
- 127 **Ping Shi**
*MODEL TESTS ON CHARACTERISTIC OF SUCTION CAISSONS IN SATURATED
FINE SAND UNDER INTERMITTENT LOADING*
- 136 **Qihong Sun, Junhai Zhang, Xinhang Xu**
*RESEARCH AND APPLICATION OF RULE UPDATING
MINING ALGORITHM FOR MARINE WATER QUALITY MONITORING DATA*
- 141 **Danje Wu**
*IMPACT OF GREEN TOTAL FACTOR PRODUCTIVITY IN MARINE ECONOMY
BASED ON ENTROPY METHOD*
- 147 **Jiuming Xie, Dengyue Sun, Chengying Xu, Jin Wu**
*THE INFLUENCE OF FINITE ELEMENT MESHING ACCURACY ON A WELDING
MACHINE FOR OFFSHORE PLATFORM'S MODAL ANALYSIS*
- 154 **Bo Zhang, Zhuo Wang, Tao Wang**
*HYDRODYNAMIC LOAD AND PARAMETRIC DESIGN OF GROUTED CLAMP
USED ON OFFSHORE JACKET*

Editorial

POLISH MARITIME RESEARCH is the scientific journal with a worldwide circulation. This journal is published quarterly (four times a year) by Gdansk University of Technology (GUT). On September, 1994, the first issue of POLISH MARITIME RESEARCH was published. The main objective of this journal is to present original research, innovative scientific ideas, and significant findings and application in the field of :

Naval Architecture, Ocean Engineering and Underwater Technology,

The scope of the journal covers selected issues related to all phases of product lifecycle and corresponding technologies for offshore floating and fixed structures and their components.

All researchers are invited to submit their original papers for peer review and publications related to methods of the design; production and manufacturing; maintenance and operational processes of such technical items as:

- all types of vessels and their equipment,
- fixed and floating offshore units and their components,
- autonomous underwater vehicle (AUV) and remotely operated vehicle (ROV).

We welcome submissions from these fields in the following technical topics:

- ship hydrodynamics: buoyancy and stability; ship resistance and propulsion, etc.,
 - structural integrity of ship and offshore unit structures: materials; welding; fatigue and fracture, etc.,
 - marine equipment: ship and offshore unit power plants: overboarding equipment; etc.
-

Scientific Board

Chairman : Prof. JERZY GIRTLEK - Gdańsk University of Technology, Poland

Vice-chairmen : Prof. CARLOS GUEDES SOARES, Universidade de Lisboa, Lisbon, Portugal

Vice-chairmen : Prof. MIROSŁAW L. WYSZYŃSKI - University of Birmingham, United Kingdom

Prof. POUL ANDERSEN Technical University of Denmark Denmark	Prof. STOJCE DIMOV ILCEV Durban University of Technology Durban, South Africa	Prof. JERZY MATUSIAK Helsinki University of Technology Finland
Prof. JIAHN-HORNG CHEN National Taiwan Ocean University Keelung, Taiwan	Prof. YORDAN GARBATOV Universidade de Lisboa Lisbon, Portugal	Prof. JERZY MERKISZ Poznań University of Technology Poland
Prof. VINCENZO CRUPI University of Messina, Italy	Prof. STANISŁAW GUCMA Maritime University of Szczecin Poland	Prof. VALERI NIEKRASOV Admiral Makarov National University of Shipbuilding Mikolaiv, Ukraine
Prof. MAREK DZIDA Gdańsk University of Technology Poland	Prof. ANTONI ISKRA Poznań University of Technology Poland	Prof. JÓZEF SZALA University of Technology and Science in Bydgoszcz Poland
Prof. ODD M. FALTINSEN Norwegian University of Science and Technology Norway	Prof. JAN KICIŃSKI Institute of Fluid-Flow Machinery of PASci Gdańsk, Poland	Prof. TADEUSZ SZELANGIEWICZ Maritime University of Szczecin Poland
Prof. MASSIMO FIGARI University of Genova Genova, Italy	Prof. ZBIGNIEW KORCZEWSKI Gdańsk University of Technology Poland	Prof. DRACOS VASSALOS University of Strathclyde Glasgow, United Kingdom
Prof. HASSAN GHASSEMI Amirkabir University of Technology Tehran, Iran	Prof. JÓZEF LISOWSKI Gdynia Maritime University Gdynia, Poland	

STUDY ON THE DESIGN OF CONTAINER HIGHWAY AND RAILWAY AUTOMATIC TRANSFER VEHICLE IN OCEAN PORT

Lili Dong¹
Gouhui Liu¹
Xin Ye²
Wei Wang¹

¹ College of Architecture and Urban Planning of Chongqing Jiaotong University, Chongqing, China

² College of International of Chongqing Jiaotong University, Chongqing, China

ABSTRACT

To realize “seamless” connection of ocean port container multimodal transport, efficiently carry out “door-to-door” transport of ocean port containers and overcome the shortcomings of existing highway and railway vehicles, this study takes the standard for heavy-duty container vehicles in TB1335-1996 Railway Vehicle Strength Design and Test Identification Code as the design basis and designs a new ocean port container transport vehicle in combination with automatic guidance technology. This study innovatively designs the automatic lifting system of the bogie and the docking part of the vehicle, introduces the automatic guidance technology and the remote-control technology to optimize the car body structure, and uses the SAP software to carry out the finite element analysis of the car body load capacity and Flexsim software to carry out the simulation analysis on the operation of vehicles. The designed transfer vehicle can improve the transfer efficiency of ocean port containers, reduce the transit time of field and station equipment and container transport links, and improve the level of multimodal transport and comprehensive economic benefits.

Keywords: Ocean port, Multimodal transport, highway and railway, unmanned automatic, seamless connection

INTRODUCTION

China is one of the major foreign traders, whose annual throughput of ocean port container has reached the top in the world in 2016. As an important transit point in multimodal transport, ocean ports often face problems such as the large-scale container turnover and rapid conversion of different transportation modes. As the economy and science and technology progress, the transformation and upgrading from traditional manpower to automation will certainly become its future development trend. At present, there are three major factors restricting the multimodal transport efficiency of an ocean port container. Firstly, the residence time is caused by the technical limitations of field and station equipment when changing the transport vehicle; secondly, all the departments fail to establish mature supporting information sharing service platforms and mechanisms in processing container-related business documents, which causes residence time. Thirdly, there is no information sharing platform established between transportation enterprises, leading to scattered transportation

strength, decentralized businesses, and limited transportation efficiency. Therefore, it is of great significance to the development of modern port logistics to study and design a highway and railway ocean port container automatic transfer vehicle with diversified functions, intelligent operations, and complete service platform in accordance with the development trend of the ocean port and future market demand.

STUDY ON AND DESIGN OF VEHICLES

DESIGN IDEAS

This study introduces the automatic guidance technology into the design of the transfer vehicle, upgrades the automatic lifting system to replace the bogie of the existing highway and railway vehicle, and use automatic docking device to complete automatic docking between transfer vehicles, thus to design a new type of automatic transfer vehicle.

After the empty vehicle in the railway mode arrives at the dock, it enters the unloading area, and retracts the railway wheels with the automatic lifting system in the vehicle, which means it has been converted to the highway mode. Then the vehicle automatically breaks into individual transfer vehicles, which enter the ocean port along a given route under the control of the automatic guidance system (Figure 1).



Fig. 1. Operation effect of highway mode

Each automatic transfer vehicle in the ocean port carries containers along the established route, passing through the yard and security gates to the railway freight station. There is a transfer vehicle waiting area near the railway freight station. With the remote operation of the central control system, all the vehicles line up in a row, with each two of them in a pair, the tail of the front one connecting with head of another in an integrated manner and go above the railway track (Figure 2).



Fig. 2. Switching process between highway and railway modes

The automatic lifting system puts down the bogie and lifts the vehicle up, thus the vehicle is converted to the railway mode. The connection device of the automatic docking system of the first vehicle head is automatically connected with the train to complete the transshipment of the ocean port container. In actual operation, the vehicle switching between the highway and railway modes is performed simultaneously in the unloading area and the waiting area (Figure 3).



Fig. 3. Operation effect of railway mode

STUDIES OF TECHNIQUES

This research mainly involves five parts, including vehicle body design, force analysis, finite element analysis, three-dimensional model drawing of vehicle body, and model simulation [1]. The vehicle is designed to carry containers weighing 40ft, thus it belongs to heavy-duty vehicle. Technical parameters are designed according to *TB1335-1996 Railway Vehicle Strength Design and Test Identification Code* (Table 1) [2].

Tab. 1. Main technical parameters of automatic transfer vehicle

Items	Parameters
Vehicle weight (<i>t</i>)	18.2
Types of containers (<i>m</i>)	6.1 and 12.2
Maximum payload (<i>t</i>)	60
Speed on highway (<i>km/h</i>)	10.8~21.6
Outline dimension (<i>m</i>)	15×3×1.5

DESIGN OF VEHICLE BODY FUNCTION UNIT

The vehicle body design includes the wheel design, the design of the automatic lifting system, the design of the automatic docking system, and the composition and functional design of other vehicle systems under both the highway and railway modes [3].

(1) Wheel design

According to the vehicle load, 8 highway wheels and 8 railway wheels are designed. Each highway wheel has a diameter of 1.1m, a width of 0.184m and a mass of 0.2t. Each railway wheel has a diameter of 840mm and mass of 0.9t.

(2) Design of automatic lifting system

The automatic lifting system consists of an automatic lifting device, a hydraulic lifter, a sleeve device and a railway wheel set. Different from conventional highway and railway bogie, the bogie is designed to be operated separately in a block with highway [4]. The discrete operation mode of bogie and highway blocks makes the lifting device with automatic control, easy operation, and the central control system of the vehicle responsible for the operation [5].

- 1) Driving device, whose function is to drive the hydraulic pump to discharge the hydraulic oil out of the hydraulic lift under the control of the central control system when the vehicle is switched from the railway mode to the highway mode;
- 2) Hydraulic cylinder whose function is to store hydraulic oil;
- 3) Hydraulic pump, whose function is to discharge the hydraulic oil from the hydraulic lift when the vehicle is switched from the railway mode to the highway mode;

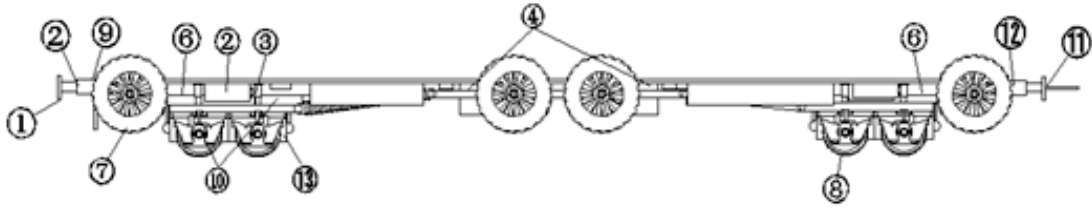


Fig. 4. Elevation of vehicle body under railway model

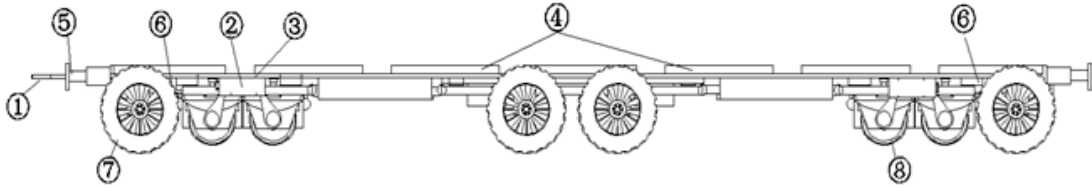


Fig. 5. Elevation of vehicle body under highway model

- 4) Hydraulic lift, whose function is to withdraw bogie with the discharge of hydraulic oil;
- 5) Lifting device and mounting frame connecting part (locking and retaining ring devices)
- 6) Shock absorber, with a sleeve structure and hinged connections with retaining ring and the vehicle body. The shock absorber is inwardly contracted, which is not subject to lateral forces but only serves to connect the vehicle body, lifting device and bogie.

- 1) Locking device
- 2) Retaining ring device
- 3) According to the force analysis, a single hydraulic device should have a pushing weight of 10t, and a lifting height of 30cm. The lifting device in the automatic lifting system is connected with the bogie by a locking device and a retaining ring device, and the locking device can be automatically locked or unlocked. Its operation is controlled by the vehicle's central control system. It can be rapidly transformed into the bogies for railroad tracks of other countries during cross-border railway transportation (Figure 7).

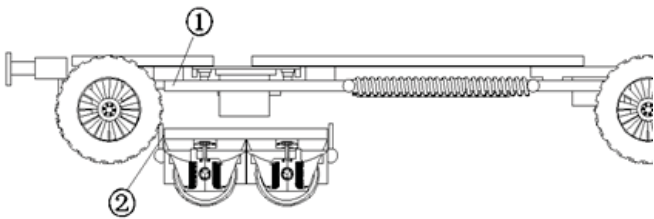


Fig. 6. Locking and retaining ring devices

(3) Design of automatic docking system

It is composed of induction unit, control unit and connection unit, which are distributed in the front and back of the unmanned transfer vehicle. The induction unit consists of a laser positioning device and a magnetic induction device, which is responsible for positioning calibration and docking before the vehicle is

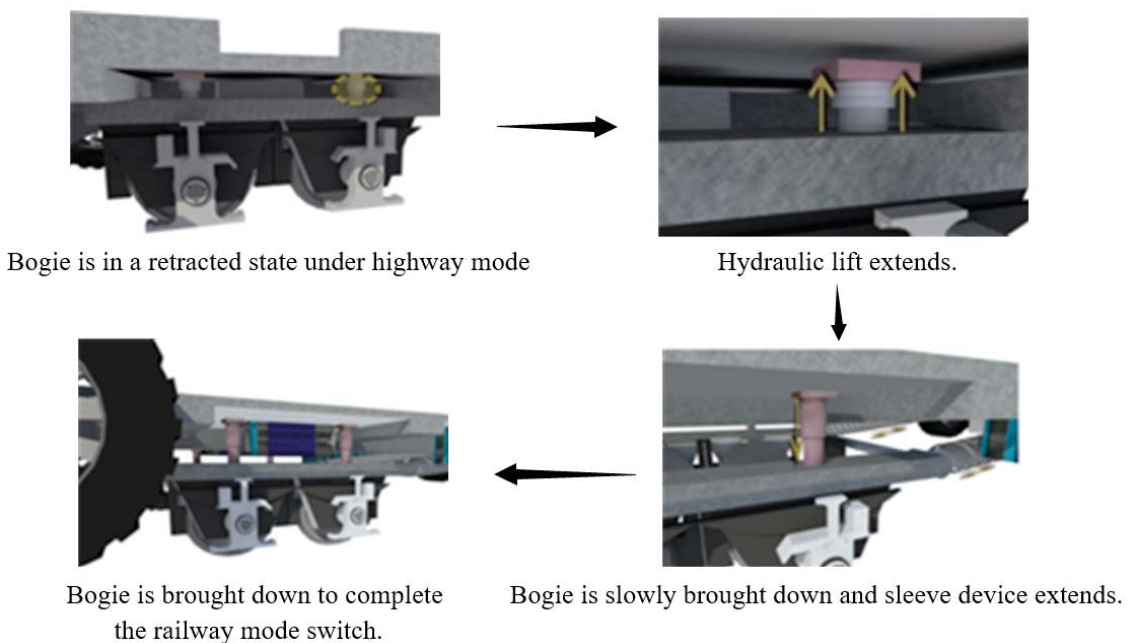


Fig. 7. Working process of lifting system

connected. Mainly composed of an autonomous processing decision system and a control system, the control unit has self-processing and operating functions, which is responsible for receiving and processing signals from the sensing unit and controlling the docking unit to disconnect or link after receiving signals from the sensing unit. The automatic connection is performed when the vehicle is switched from the highway mode to the railway mode to form the container vehicle group [6].

(4) Design of security system

Composed of locomotive sensors, information processing system, display screen, speed measuring system, speed comparison system and brake control section, this system is mainly used to prevent speeding, collision and other dangerous conditions that may be caused when the train is running too fast. In addition to the speed limit effect, it is equipped with dirt-proof jacket and sealing device, which are distributed in the steering shaft of the steering mechanism;

An ABS (anti-lock braking system) is provided in the highway mode. In railway mode, the system transmits the highest safe speed limit signal to the train via the rails and continues to compare with the actual speed of the train, so as to avoid the danger caused by the train speeding. When the train is in braking, the system can automatically identify the vehicle's safe braking distance and ensure vehicle braking [7].

(5) Design of bogie and wheel alignment system

The wheel alignment uses laser radar. The device is mainly composed of an emission system, a receiving system and information processing. The emission system is composed of various lasers, such as a carbon dioxide laser. The receiving system uses a combination of telescopes and various forms of photodetectors, such as photomultipliers, semiconductor photodiodes, and avalanche photodiodes, infrared and visible light multiple detectors. Through the automatic control system, the wheel and track can be accurately docked.

The train bogie is mainly composed of a frame, a vibration damping device, a motor drive device, a single stage suspension system, a secondary suspension device, a traction rod, a centre pin seat, a unit brake cylinder and a height adjustment valve, a speed sensor, and a grounding device. The design parameters meets the following requirements. The height of the vibration damper spring should be greater than the rise of the damper caused by the damper and friction plate. According to the axle weight, the allowable stress is 1050MPa . The height of the top surface of the side frame from the rail surface should be less than 775mm to ensure that it can pass the minimum curve. The position and size of the moving lever of the basic braking device shall be determined by the braking ratio and the position of the joint. It shall be ensured that the centre distance of the side frame is consistent with the center distance of the journal, and that the height of the side frame from the rail surface is less than 160mm .

(6) Design of vehicle power supply system

Double closed-loop control of voltage and current is adopted to realize constant current and constant voltage charging of storage battery. The soft switching technology is used to reduce the high frequency switching loss of IGBT with an efficiency

of 92% [8]. Advanced amorphous cores are used to make transformers and reactors, and to reduce the size of the charger.

(7) Fixing device of container corner piece

The device is installed at each top corner of the container, whose function is to stabilize the container to ensure that the force on the container is even during the transportation process, so as to prevent the vehicle body from losing the balance because of the huge collision force, avoiding the damage to the container [9].

(8) Composition and function design of other systems

The vehicle is mainly composed of automatic docking system, lifting system, central processing system, automatic guidance system, security system, power system, highway wheel set, railway wheel set and braking device [10]. The overall system structure of the vehicle will be described below.



Fig. 8. Illustration of vehicle parts

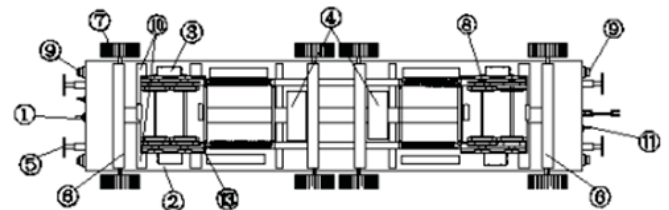


Fig. 9. Illustration of vehicle parts

Where, 1) and 5) automatic docking system and other electrical equipment information transmission power supply device inside the vehicle; 2) automatic guidance system; 3) automatic lifting system; 4) central processing system and power system; 6) security system; 7) highway wheel set and braking device; 8) railway wheel set and braking device; 9) automatic guidance device; 10) bogie and wheel alignment system; 11) highway traction device; 12) corner device; 13) braking device. [11]

FORCE ANALYSIS OF VEHICLE LIFTING DEVICE

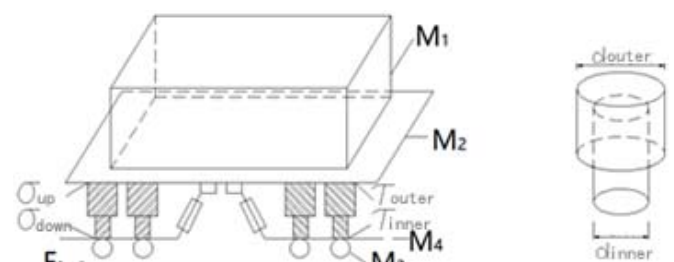


Fig. 10. Force analysis of vehicle lifting device

CALCULATION OF LOCAL NORMAL STRESS OF LIFTING HYDRAULIC JACK

The calculation of normal stress includes the following situations: rail wheel lowers in railroad mode and rail wheel rises in highway mode [12]. The thrust on a single jack, the local compressive stress at the outer guide tube joint during the elongation of the jack, and the local pushing stress at the inner guide tube joint are analysed for the two cases [13]. It is assumed that the acceleration of gravity is 9.81m/s^2 .

When the rail wheel is lowered to contact with the rail, the container and the floor rise, then:

$$\left\{ \begin{array}{l} F_t = \frac{(m_1 + m_2)g}{8} \\ \sigma_{up} = \frac{F_t}{A_{outer}} \\ \sigma_{down} = \frac{F_t}{A_{inner}} \end{array} \right. \quad (1)$$

Where, F_t —the pressure on the jack (N); m_1 —container mass; m_2 —body mass with removal of rail wheel mass; g —gravity acceleration; σ_{up} —local compressive stress at the outer guide tube joint during the hydraulic jack elongation process (MPa); σ_{down} —local pushing stress at the joint of inner guide tube (MPa); A_{outer} —circular cross-sectional area of outer guide tube of the hydraulic jack; and A_{inner} —circular cross-sectional area of inner guide tube of the hydraulic jack [14].

When the rail wheel rises and retracts, the force is:

$$\left\{ \begin{array}{l} F'_t = \frac{\left(m_3 + \frac{m_4}{4}\right)g}{8} \\ \sigma'_{up} = \frac{F'_t}{A_{outer}} \\ \sigma'_{down} = \frac{F'_t}{A_{inner}} \end{array} \right. \quad (2)$$

Where, F'_t —pulling force of the jack (N); m_3 —the mass of a single rail wheel; m_4 —the mass of single side lower panel; σ'_{up} —local tensile stress at the outer guide tube joint during the shortening process of the hydraulic jack (MPa); σ'_{down} —local tensile stress at the inner guide tube joint (MPa).

CALCULATION OF LOCAL SHEAR STRESS OF LIFTING HYDRAULIC JACK

The calculation of the local shear stress includes the shear stress of the inner and outer guide tubes. When the container carrier is transported on the rails, the rolling friction force on the rail wheel is analysed, and then the force received by the single jack can be obtained by balancing the force and ignoring the force exerted on the side lower plate, thereby obtaining the shear stress on the outer guide tube and inner guide tube of the hydraulic jack [15].

$$\left\{ \begin{array}{l} F_f = (m_1 + m_2 + 8m_3 + 2m_4)gu \\ F_\tau = \frac{1}{8}F_f \\ \tau_{outer} = \frac{F_\tau}{A_{outer}} \\ \tau_{inner} = \frac{F_\tau}{A_{inner}} \end{array} \right. \quad (3)$$

Where, F_f —rolling friction forces on all rail wheels (N); μ —rolling friction coefficient between iron wheel and rail, 0.05; F_τ —shear stress on a single jack (N); τ_{outer} —shear stress on the outer guide tube (MPa); and τ_{inner} —shear stress on the inner guide tube (MPa).

By substituting known data into the above formula, it is obtained that when the rail wheel set descends, the local compressive stress at the joint of the outer guide tube is 13.9MPa, and the local pushing stress at the joint of the inner guide tube is 55.5MPa; when the rail wheel set rises, the tensile stress at the joint of the outer guide tube is 1.8MPa, and the tensile stress at the joint of the inner guide tube is 7.1MPa; when the vehicle under load is in a railway mode, the shear stress of the outer guide tube of the hydraulic jack is 0.78MPa and the shear stress of the inner guide tube is 3.13MPa [16].

THE ANALYSIS OF THE OVERALL FORCE ON THE VEHICLE

The force on a single carriage is as shown below. The train is on the rails and during the start-up to transportation, there is:

$$F_{traction} - F_x - F_f = a(m_1 + m_2) \quad (4)$$

Where, $F_{traction}$ —traction force on the carriage; F_x —horizontal force of the rear compartment on the carriage; F_f —friction force on the carriage; m_1 —container mass; m_2 —mass of a single empty carriage; and a —train acceleration. When the total traction force of the train is $F_{overall}$ and there are n carriages in the process of transportation:

$$F_{traction} - F_x = \frac{F_{overall}}{n} \quad (5)$$

It can be obtained from the symmetry of carriages and containers:

$$F_y = F'_y \Rightarrow F_{N1} = F_{N2} = F_{N3} = F_{N4} \quad (6)$$

Where, F_y —the vertical force of the rear compartment on the carriage; F'_y —the vertical force of the front compartment on the carriage; and F_{Ni} —vertical support forces provided by a single rail wheel.

The maximum friction force on the train is:

$$(F_f)_{max} = (m_1 + m_2)gu \quad (7)$$

Where, μ –Friction coefficient of rail and train wheel.

Before acceleration, the frictional force experienced by the vehicle is static friction.

$$F_f = F_{traction} - F_x \Rightarrow F_y = (F_{traction} - F_f) \cdot \frac{a}{l} \quad (8)$$

At the critical point when the train just gets acceleration, then the frictional force of the train changes from static friction to sliding friction ($a = 0$):

$$F_{traction} - F_x = (F_f)_{max} = (m_1 + m_2)g \quad (9)$$

At this point, the moment of the o point is $\Sigma Mo = 0$.

$$F_y \cdot l = F_f \cdot a \Rightarrow F_y = (m_1 + m_2)g\mu \cdot \frac{a}{l} \quad (10)$$

Where, a –vertical height of train bottom plate to lower plate; and l –overall train length.

When the train obtains the maximum traction force, the maximum acceleration it obtains at this time is:

$$(F_{traction})_{max} - F_x - (m_1 + m_2)gu = (m_1 + m_2)a$$

$$\Rightarrow a_{max} = \frac{(F_{traction})_{max} - F_x - gu}{(m_1 + m_2)} \quad (11)$$

FINITE ELEMENT ANALYSIS

THE ESTABLISHMENT OF FINITE ELEMENT MODEL

THREE-DIMENSIONAL MODEL HYPOTHESIS

- (1) The vehicle is composed of three parts, namely, the loading board, the bearing and the tire.
- (2) The container acts on the vehicle with a uniform load.
- (3) The plate can be replaced by Q345 steel with the isotropic and homogeneous materials after conversion.
- (4) The bearing is replaced by Q420 after conversion.
- (5) The bearing is connected with the plate at the fixed end. The bearing can rotate but cannot move.

ESTABLISHMENT OF SAP FINITE ELEMENT MODEL

After simplification and substitution, the model in SAP is as shown in Figure 11.



Fig. 11. SAP model of the vehicle

DEFINITIONS OF MATERIAL AND CROSS SECTION ATTRIBUTE AND LOAD

FRAME SEGMENTATION

The tire model is processed by polyline. Divide the tire into 50 equal parts, that is, the number of rods is 50.

DEFINITION OF MATERIAL ATTRIBUTES

In the material definition of the loading board, the same Q345 steel after conversion is used; in the definition of the bearing, Q420 is used to define the material; and finally, in the material definition of the tire, the related parameters of the giant tire 2700R49 are used, as shown in Table 2.

Tab. 2. Material attributes data settings

Material attributes	Data settings
Weight density	10380(unit: N, cm, C)
Mass density	1058.4654(unit: N, cm, C)
Modulus of elasticity E	6.000E+9
Poisson ratio U	0.45
Coefficient of linear expansion A	6500E+06
Shear modulus G	2.069E+09

DEFINITION OF CROSS SECTION ATTRIBUTES

Q345 rectangular cross-section steel with equivalent weight of 3000×254 (mm) (width×height) is used according to the cross section attributes of the plate; the bearing is converted into Q420 (length×width) of 3000×600 (mm); and the tire is defined as a cylinder with an outer radius of 550 mm and an inner radius of 228 mm. With two tires in the same cross-section, the relevant area, resistance moment and mass have to be doubled, as shown in Figure 12.



Fig. 12. Cross section model after definition

LOAD DEFINITION

According to the assumption, the weight of the container is a uniform load acting on the board, the maximum weight of the load on the board is 70 t, and the uniform distribution force is 528.23 N/cm. When setting load conditions, its own weight shall be considered, and it shall be noted that the tire mass shall be doubled.

OUTPUT AND ANALYSIS OF THE RESULT

The actual deformation of the model is shown in Figures 13 and 14.



Fig. 13. Demo after model deformation

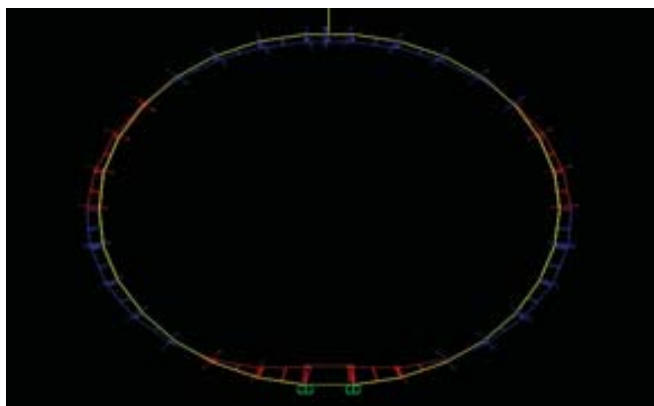


Fig. 14. ire shear diagram

According to the output analysis, the axial stress of the bearing and the shear force of the tire are the parts with the greatest stress. The maximum axial force of the bearing is 14.8MPa , and the bearing stress is required to be at least 15MPa upon consideration of the safety reserve. The tire design shall meet the above parameters.

SIMULATION ANALYSIS

The simulation model is established in Flexsim software and the input parameters are as shown in Table 3:

According to the analysis of the results, the number of standard containers in the model without the automatic transfer vehicle is 2,738, while that of the model with automatic transfer vehicle is 3,390. It can be seen that the container throughput of the automatic terminal has been increased by 23.813 % after the adoption of highway and railway ocean port containers.

CONCLUSIONS

The automatic transfer vehicle for highway and railway ocean port containers has the advantages of improving the efficiency of logistics transportation and reducing costs while solving “seamless connection” and market demand. In addition, the vehicle can be combined with the Internet platform to incorporate many services such as ocean port container insurance, finance, import and export business on the same platform, and integrate all business and transportation forces,

Tab. 3. Parameter settings of automatic terminal simulation model 2 after using unmanned transfer vehicles for highway and railway ocean port containers

Tag name	State/parameter
Container ship	the Number of Initial "BOXES", 4000
Quay crane	Maximum speed, 2.87m/s
Container parking platform 1	Processing time, 0
Container unmanned transfer vehicle 1	Maximum speed, 6.87m/s
Yard	Maximum capacity, 100000
Gantry crane 1	Maximum speed, 2.87m/s
Container parking platform 2	Processing time, 0
Container unmanned transfer vehicle 2	Maximum speed, 6.87m/s
Waiting area for train conversion	Maximum capacity, 20
Conveyor belt	Accumulated cargo flow 15: Transmission speed, 6.87m/s
Train	Processing time, 4s
Model running time	86400s

thus to make trade activities more efficient and convenient. Finally, it will promote the transformation and upgrading of ocean port container service mode to the “Internet +” mode, which will play a positive role in developing modern port logistics and serving “Belt and Road” strategy and economic development of China.

ACKNOWLEDGMENT

The project (cstc2016shmszx30017) is supported by Chongqing Social Career and People’s Livelihood Guarantee Science and Technology Innovation Special. The project (cstc2017jcyjA1754) is supported by Chongqing Basic research and frontier exploration.

REFERENCES

1. H. B. Li, *The Research and Development of Key Technology of Container Automatic Guide Vehicle in China*, Containerization, Vol. 11, pp. 25–27, 2011.
2. *Railway Vehicle Strength Design and Test Identification Code*, Beijing: Railway Publishing House, 1996.
3. Z. Yang. Research and Design of DC600/110V Charging Set Test Stand. Southwest Jiaotong University, 2010.
4. Y. T. Ruan, *Vehicle-borne 3D Laser Mapping radar*, Technology Development of Enterprise, Vol. 31, pp. 92–93, 2012.

5. S. Y. Zhu, "Guangzhou Metro Bogie. Railway vehicle, Vol. 38, pp. 67–68, 2000.
6. J. G. Yu, X. F. Hu, Q. T. Ye, *Strong Nonlinear Thermal-Mechanical Coupling Analysis of Subway Braker Resistance*, Journal of Mechanical Strength, Vol. 26, pp. 552–555, 2004.
7. G. C. Ning, Y. Zeng, *A New Type of Casing Pullout Machine for Oil Field Production*, Energy saving of petroleum and petrochemical, Vol. 3, pp. 47–47, 1996.
8. X. Yuan, *Discussion on Mode and Operation Mechanism of Railway Container Transportation Management*. Northern Jiaotong University, 2000.
9. Q. Gao, *Analysis of the Braking Performance of a Certain Brand Automobile*, Dalian University of Technology, 2013.
10. A. M. Youssef, *Operations of electric vehicle traction system, Mathematical Modelling of Engineering Problems*, Vol. 5, No. 2, pp. 51–57, 2018.
11. U. K. Hassan, S. Kasim, R. Hassan, H. Mahdin, A. A. Ramli, M. F. Md Fudzee, and M. A. Salamat, *Most Stationery Inventory Management System*, Acta Electronica Malaysia, Vol. 2, No. 2, pp. 10–13, 2018.
12. R. Hamzah, S. Kasim, R. Hassan, H. Mahdin, A. A. Ramli, M. F. Md Fudzee, and M. A. Salamat, *Taxi Reservation System of Batu Pahat Taxi Association*, Acta Electronica Malaysia, Vol. 2, No. 2, pp. 20–24, 2018.
13. X. Luo, *Static Characteristic Analysis of Concrete-filled Steel Tube Tied arch bridge*. Acta Mechanica Malaysia, Vol. 1, No. 1, pp. 21–24, 2017.
14. X. C. Tian, Q. H. Li, C. S. He, Y. G. Cai, Y. Zhang, and Z. G. Yang, *Design and experiment of reciprocating double Track Straight Line Conveyor*, Acta Mechanica Malaysia, Vol. 2, No. 2, pp. 01–04, 2018.
15. F. Qiao, *The Study on The Integration of Green Architecture and Appropriate Technology*, Engineering Heritage Journal, Vol. 2, No. 2, pp. 01–03, 2018.
16. S. Tao, *Evaluation of Technology Innovation in Hubei Province*, Engineering Heritage Journal, Vol. 2, No. 2, pp. 09–10, 2018.

CONTACT WITH THE AUTHORS

Gouhui Liu

e-mail: liuguohuimeng@163.com

College of Architecture and Urban Planning
of Chongqing Jiaotong University
Chongqing 400074
CHINA

STUDY ON OPTIMIZATION SIMULATION OF SCR DENITRATION SYSTEM FOR MARINE DIESEL ENGINE

Jun Du

Ruo Nan Li

Xin Wu

Yan Zhang

Jiangsu University of Science and Technology, Jingkou, Zhenjiang, China

ABSTRACT

With the rapid development of shipbuilding industry exhaust world is also very harmful one kind of environmental issues, and the ship marine diesel engine exhaust gas is mainly produced, so in recent years it has developed a diesel engine SCR system. SCR system can control emissions of nitrogen oxides in the exhaust of vessel, furthermore air pollution can be reduced. The main goal of article was using fluent software to correct SCR system selection and flue gas flow under different size best deflector arrangement is simulated. Next goal is further optimize the structure of the SCR system.

Keywords: marine diesel engine, SCR system, flue gas, flow deflector

INTRODUCTION

In order to control the pollution of marine diesel engine exhaust gas, in October 2008, the Marine Environment Protection Committee (IMO MEPC) of the International Maritime Organization (IMO) made a more stringent amendment to VI, a subsidiary of the MARPOL73/78 Convention. For marine diesel engines built on or after January 1, 2016, NO_x emission limits must be implemented in accordance with the third level Standard when navigating within the global emission limitation zones. At present, the proportion of NO_x pollution is increasing. In particular, in some large ocean-going ports, heavily traded straits and shipping routes, the source of pollution in the region comes mainly from emissions from these diesel engines [1,2]. Therefore, the NO_x emission control of marine diesel engine has become an unavoidable practical problem in air pollution control [3,4]. It is particularly important to develop a reasonable and feasible exhaust gas purification technology for marine diesel engine. In the experimental study of diesel

engine NO_x emission reduction, Koga, Raptotasios and so on have put forward the relevant solutions [5,6], such as Koga has given out the countermeasures that accord with the Nox emission regulation of marine diesel engine. Ma have carried out the experiment of reducing the NO_x emission of diesel engine by the method of inlet water injection [7]. The results show that when the fuel consumption rate of the diesel engine is maintained at a specific value, the intake port water injection can greatly reduce the emission of NO_x.

Magnusson also pointed out in the study that the marine SCR system has reached a certain technical maturity, is an efficient NO_x emission reduction technology, can meet the third layer and possibly more stringent nitrogen oxide regulations in the future [8]. Calvillo studied the characteristics of SCR at low temperature. The carbon materials with V catalyst were loaded on honeycomb support. The denitrification rate reached 59.8% -72.1% when the temperature was 150 °C[9]. Lv H treated the CeO₂ with NH₃, it was tested with BET, XRD, TPR and XPS . The results showed

that the NH_3 treated CeO_2 catalyst had excellent SCR activity and stability because of the decrease of crystallinity and the improvement of reductivity [10]. Daniel C Haworth simulate the evaporation, pyrolysis and hydrolysis of urea solution in Urea-SCR system of diesel engine by using CFD software model [11]. The swirl and turbulence in SCR reactor are helpful to enhance the evaporation, decomposition and mixing of urea solution with diesel engine exhaust. With the development of SCR technology, this technology has been widely used in the field of nitrogen oxide emission control. In 1989, MAN B & W Company first installed the SCR rear processor on the ship's two-stroke diesel engine [12], and controlled the NO_x emissions from the exhaust gas to about $2\text{g}/\text{kW}\cdot\text{h}$. At present, MAN B & W company diesel engine denitrification technology is mainly SCR technology, and the installation and layout of the SCR system, and the matching status of the engine and other aspects of a deeper study. The first installation of the SCR system on a ship by Vacelan Diesel Company of Finland in 1992 reduced NO_x by 85%, CO and HC by 70%. After 2005, H + H Environment and Industry Co., Ltd. in the shipboard SCR system technology and market gradually matured, became the main supplier of Wachelan Company [13]. Mitsubishi Corporation of Japan successfully developed a honeycomb denitrification catalyst with Ti-V-W as the active material, and more than 70% of the power plants began to use this catalyst [14]. In order to improve the activity of the catalyst, control the arrangement of the atomic components of the catalyst and promote the mixture of NO_x , reductant and catalyst to be more uniform, the catalyst for denitrification of SCR at low temperature was developed [15]. In 2011, on the basis of the working principle of reducing the NO_x emission of vehicle diesel engine by SCR system, Siemens Company of Germany continued to develop a SCR system suitable for the rear exhaust control of marine diesel engine, making the denitrification rate more than 90%.

Among the various post-treatment methods of NO_x emissions, SCR (Selective Catalytic Reduction) technology is the fastest developing, most widely used and most mature process for denitrification of marine diesel engines [16].

THE BASIC MODEL

SCR SYSTEM PRINCIPLE

Controlling nitrogen oxide emissions from ships exhaust gas, the diesel engine may be externally from exhaust or an internal combustion diesel engine control [17]. Diesel engine while the internal transformation process is very difficult, so that the external technique commonly used for processing a diesel engine exhaust gas (referred to as SCR technology) [18]. SCR technology is the use of a catalyst and ammonia as a reducing agent, the reaction after a certain nitrogen oxides in diesel exhaust gas is converted into water vapor and nitrogen gas, so that nitrogen oxides in the exhaust gas can be recycled, Greatly reduce the nitrogen oxide emissions

of diesel engines, thereby capable of reducing diesel exhaust pollution of the environment [19].

SCR SYSTEM COMPOSITION

Marine diesel engine SCR system is mainly composed of a catalytic reactor, a urea storage and injection system, a mixer, blowing system, the detection and control system components. among them The catalytic reactor is the core of SCR technology, It is the main place catalytic reduction of NO_x and a reducing agent [20]. Discharging the flue gas from the flue diesel engine, a reducing agent in a pipe system with injection ejected, entering the SCR catalyst chemical reaction. Throughout the process, control (e.g. reaction temperature, inlet and outlet NO_x concentration, main power, etc.) according to various types of signal detection of the detection system to regulate the injection system, the injection amount of reducing agent and adjusting the injection angle of the entire system running in good condition.

DESIGN OF SCR SYSTEM

To facilitate the simulation of the present Venter appropriately simplified overall structure of the SCR, as shown in Fig. 1 below:

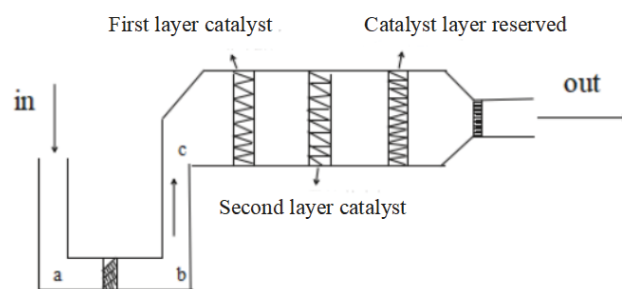


Fig. 1. Simplified diagram SCR catalytic reaction system

FLUE STRUCTURE SIMULATION ANALYSIS

SLANT FLUE DESIGN

After injection of NH_3 into the flue, the flue gas mixing with the SCR injection system, the structure of the turning of the flue at b at Fig [21]. 1 is designed to be oblique, using the inner chamfer ($150\text{mm} \times 45^\circ$) design, the corresponding structural shape, dimensioned below Fig. 2, The unit mm.

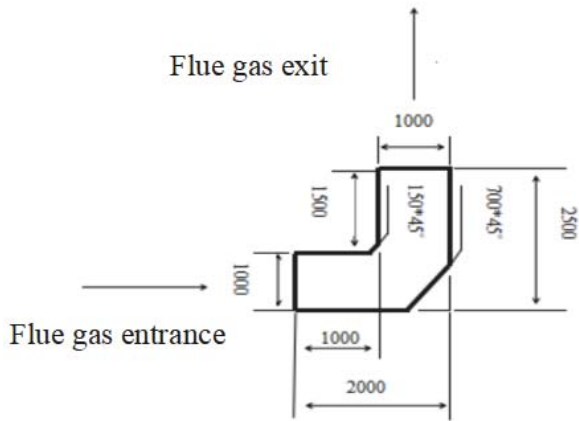


Fig. 2. Inclined type flue structure diagram (no guide plate)

Simulation results of the swash flue and analyzed as shown below.

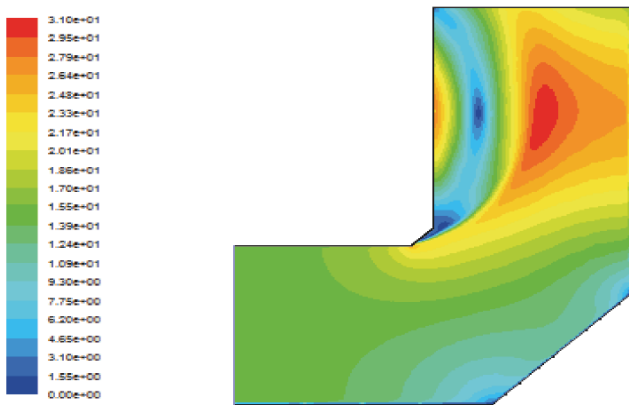


Fig. 3. The velocity distribution of the flue gas in the non-deflector plate

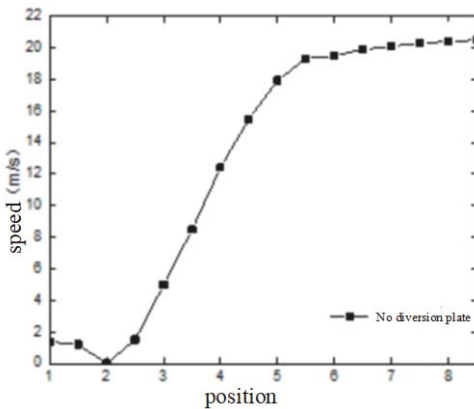


Fig. 4. A graph of the exit velocity of a flue without a deflector

As can be seen from Fig. 3, the flue gas flow in the flow channel, the outer side of the swash plate and the rear left corner of the flue are a large number of low-speed region, the area of the 1/3 vertical regions. Internal corner vortex due to gas generation, high-speed vertical apparent area, 2/3 vertical region, while a lot entrances significantly higher flow speed, and the formation of large vortices [22]. As can be seen

from Fig. 4, You can look at the flow rate fluctuation range of import and export greatly, not only high-speed zone speed is too large, and the minimum value of zero speed appears. The pressure at the entrances to the value to calculate the pressure drop can be obtained as 64.44Pa.

ARC FLUE DESIGN

The flue design arc, the radius of curvature of 1150mm outer, inner curvature radius of 150mm, other sizes as shown in Fig. 5.

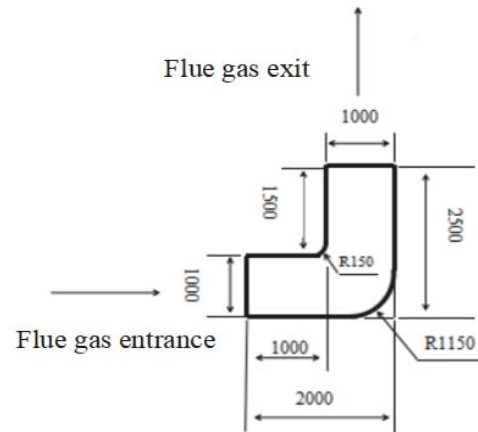


Fig. 5. Circular flue structure diagram (no guide plate)

Arc flue the simulation results and analysis:

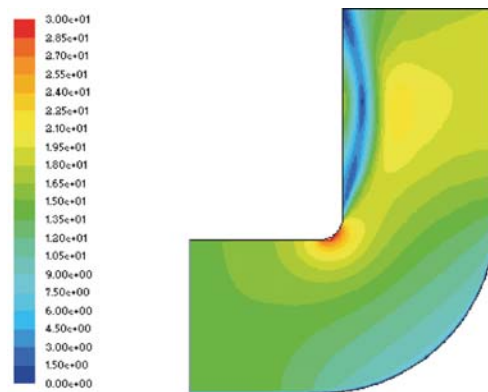


Fig. 6. The velocity distribution of the flue gas in the non-deflector plate

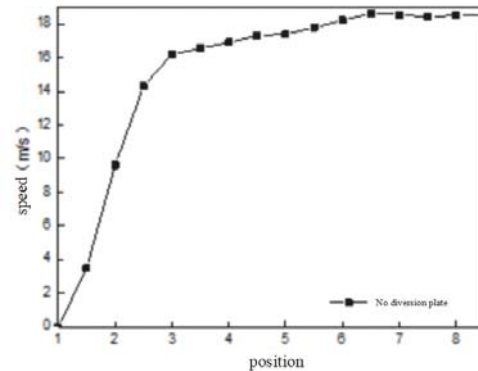


Fig. 7. A graph of the exit velocity of a flue without a deflector

As can be seen from the Fig. 6, the flue gas flows in an arcuate flow path, the outer corner appears a low speed region, area accounted Shui Angle 1/3, In the left corner of the smoke .Also a large number of low-speed channel region, and the speed was significantly much lower than the outer corner region accounts for less than 1/3 of the vertical part of the flue area. Internal corner vortex due to gas generation, high-speed region apparent, small footprint. From Fig. 7 in export to enlarge the flow rate fluctuation range, a large number of high-speed region, and the lowest velocity value of 0 m/s. The outlet pressure value, Computing system pressure to give difference of 30Pa.

Original gas flow path flowing suddenly encountered corner, swirls, so that the flow rate increases, Large amount of gas toward the vertical wall, impact damage to the wall easily, reducing its service life. Comparative simulation results of both analyzes of the flue, in order to reduce the flow rate and pressure range, reduce the impact force of the gas to reduce the wall damage, to reduce the loss of the flue, the flow channel design is more reasonable arc corner.

SIMULATION ANALYSIS OF ADDING FLUE DEFLECTOR UNDER DIFFERENT FLUE GAS FLOW IN ARC FLUE

According to the size of the flue, the circular arc deflector is arranged in turn. In order to reduce the energy loss of the system, six design schemes and sizes of the guide plate are filled in the flue, as shown in Table .1 below.

Tab. 1. Setting of reducing agent inlet parameters

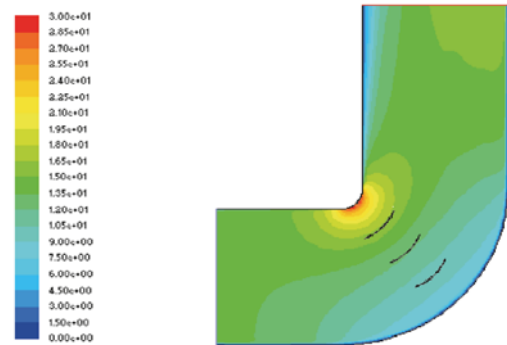
Six kinds Refinement parameters baffle								
No.	a	b	c	d	e	f		
(Piece)	3	4		5				
Arrangement	a row Arrangement	a row Arrangement	Disaggregated arrangement (2 + 2)	a row Arrangement	Disaggregated arrangement (2 + 3)	Disaggregated arrangement (3 + 2)		
Radius (R,mm)	210	210	210	210	210	210		
Arc length (L,mm)	281	281	281	281	281	281		
The distance (D,mm)	250	200	250	167	330	250	250	330

In the flue gas flow rate 43490kg/h, 61570kg/h, 102733kg/h, Under the simulation, respectively, to obtain the optimal solution.

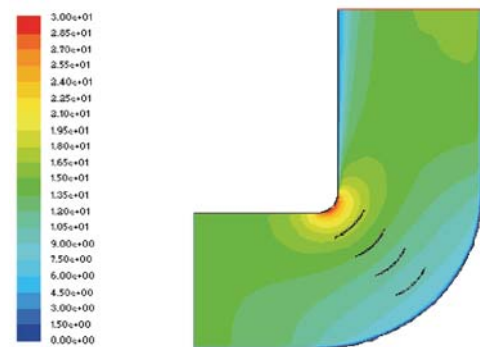
IN THE FLUE GAS FLOW 43490KG / H

After the addition of baffles, each of the arcuate baffle flue Six simulation arrangement shown in Fig. 8.

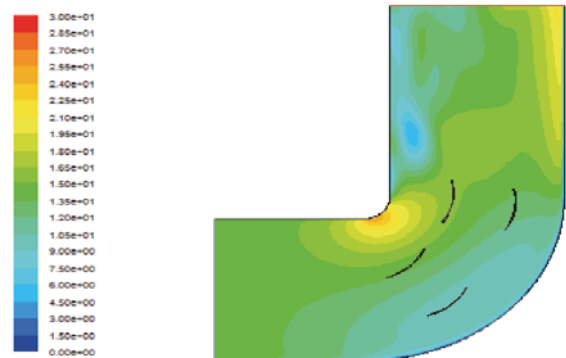
(a) Three baffles are arranged



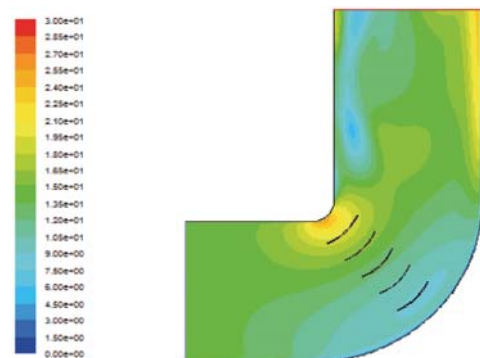
(b) Arranged in a four baffles



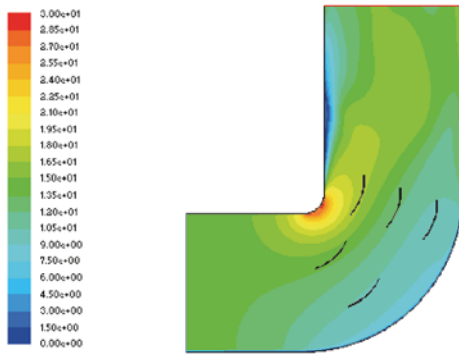
(c) Four baffles arranged disaggregated



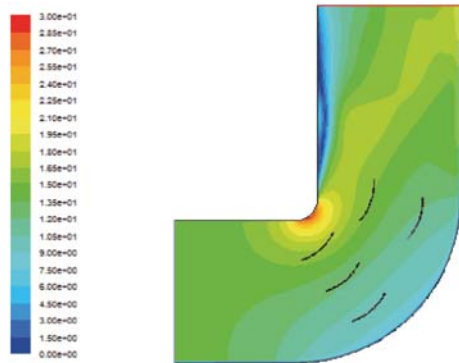
(d) Five baffles are arranged on



(e) Five points out baffle arrangement (after the first two three)



(f) Five points out baffle arrangement (two after the first three)

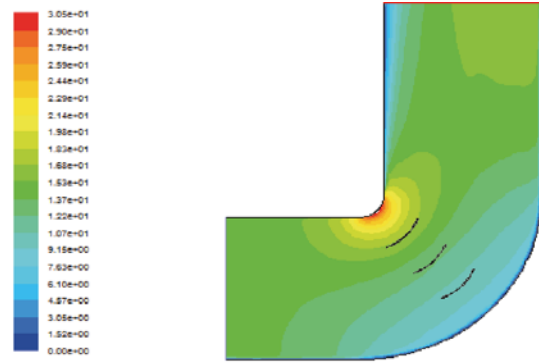


In summary, Simulation results of the six kinds of flue deflector according to the design, Binding design velocity field distribution within the flue six kinds of arcuate deflector, outlet cross-sectional flow graph, the pressure loss can be seen in FIG. Analysis: Accordingly, the simulation results can be seen in conjunction with the program: when flue gas flow rate 43490kg/h, When four baffle a baffle disposed best results.

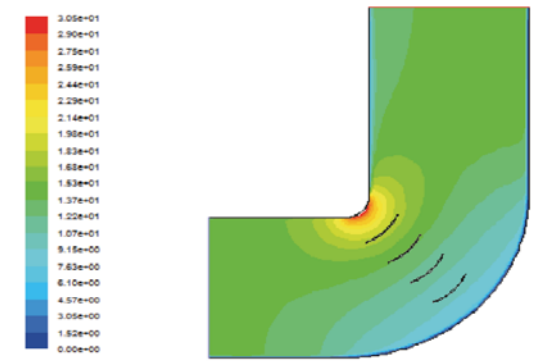
IN THE FLUE GAS FLOW 61570KG / H

After the addition of baffles, each of the six kinds of flue arcuate deflector arrangement simulation, shown in Fig .11.

(a) Three baffles are arranged



(b) Arranged in a four bafflesort



(c) Four baffles arranged disaggregated

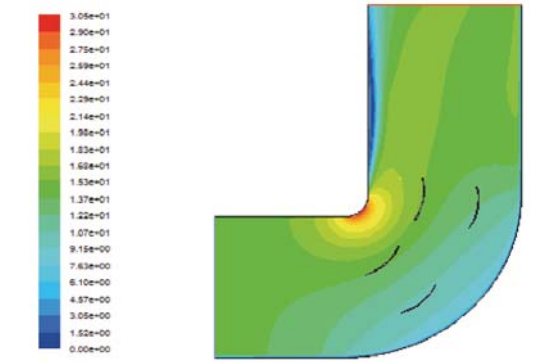


Fig. 8. The velocity field profile of the different deflector plates

The velocity curve at the exit is drawn according to the simulation process, as shown in Fig. 9.

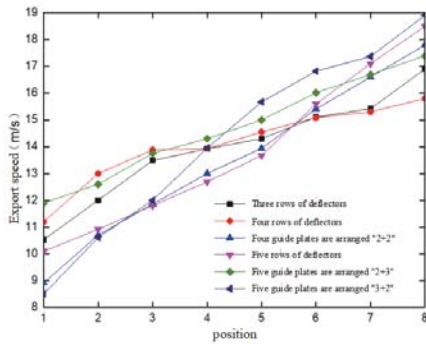


Fig. 9. The velocity diagram of the exit velocity of different guide plate is given

The pressure loss can be obtained by simulation programs such as Fig.10.

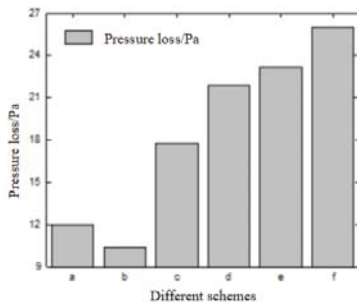
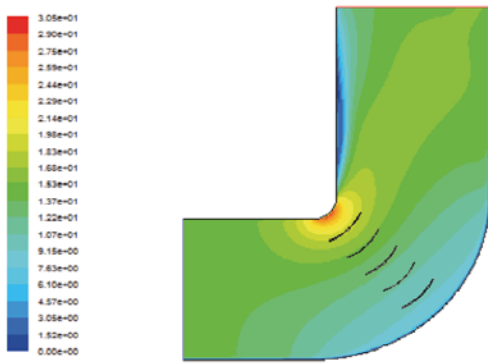
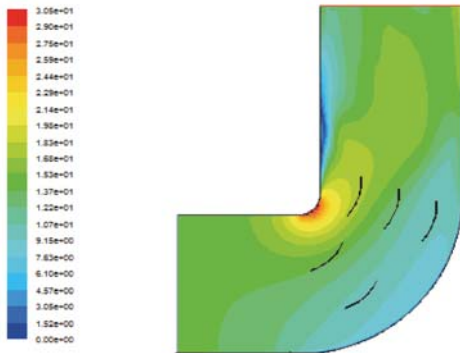


Fig. 10. Different design scheme of smoke pressure loss

(d) Five baffles are arranged one



(e) Five points out baffle arrangement (after the first two three)



(f) Five points out baffle arrangement (two after the first three)

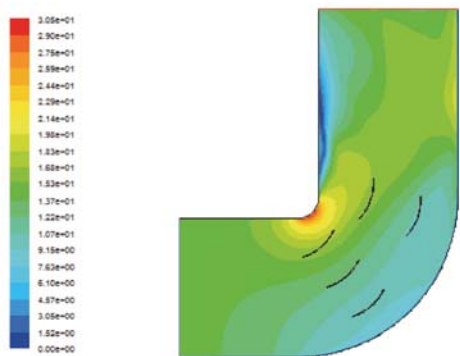


Fig. 11. The velocity field profile of the different deflector plates

The velocity curve at the exit is drawn according to the simulation process, as shown in Fig.12.

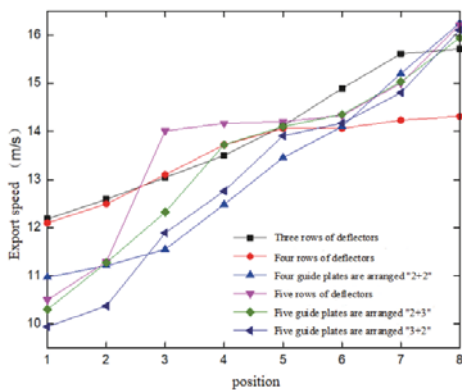


Fig. 12. The velocity diagram of the exit velocity of different guide plate is given

According to the simulation results, the pressure loss Fig.13 of different schemes is drawn as follows:

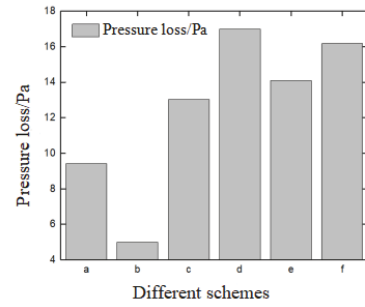


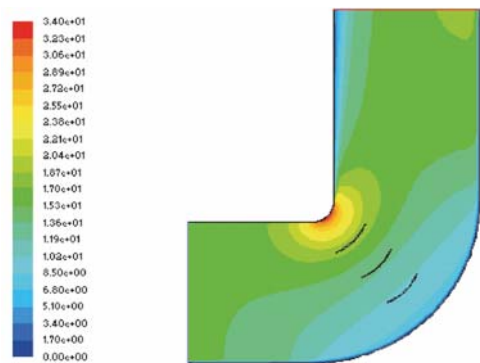
Fig. 13. Different design scheme of smoke pressure loss

In summary, Simulation results of the six kinds of flue deflector according to the design, Binding design velocity field distribution within the flue six kinds of arcuate deflector, outlet cross-sectional flow graph, the pressure loss can be seen in FIG. Analysis: Accordingly, the simulation results can be seen in conjunction with the program: when flue gas flow rate 61570kg/h, When four baffle a baffle disposed best results.

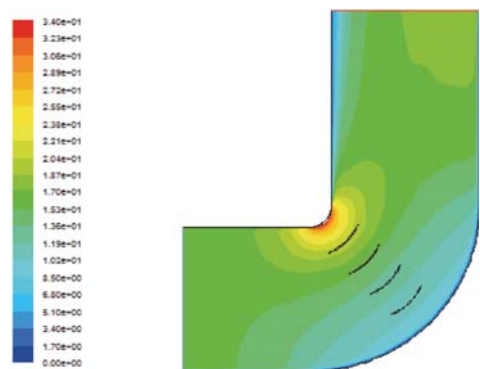
IN THE FLUE GAS FLOW 102733KG / H

After the addition of baffles, each of the six kinds of flue arcuate deflector arrangement simulation, shown in Fig.14.

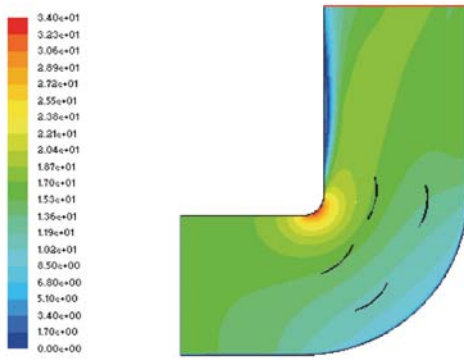
(a) Three baffles are arranged



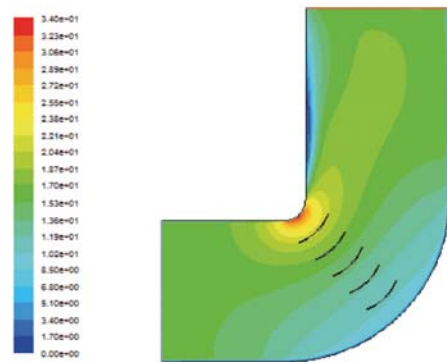
(b) Arranged in a four baffles



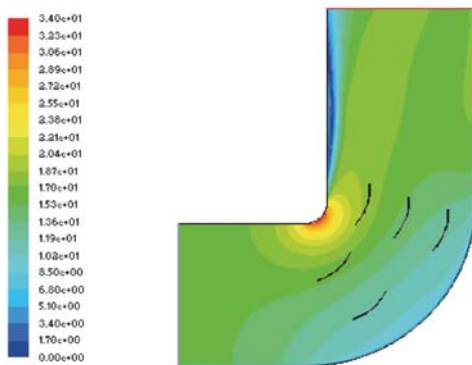
(c) Four baffles arranged disaggregated



(d) Five baffles are arranged one



(e) Five points out baffle arrangement (after the first two three)



(f) Five points out baffle arrangement (two after the first three)

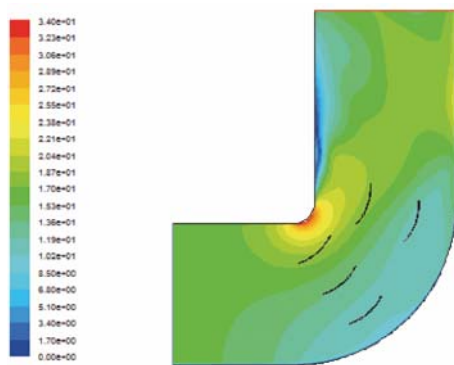


Fig. 14. The velocity field profile of the different deflector plates

The velocity curve at the exit is drawn according to the simulation process, as shown in Fig.15.

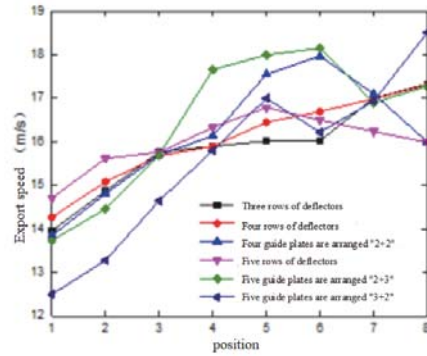


Fig. 15. The velocity diagram of the exit velocity of different guide plate is given

According to the simulation results, the pressure loss Fig.16 of different schemes is drawn as follows:

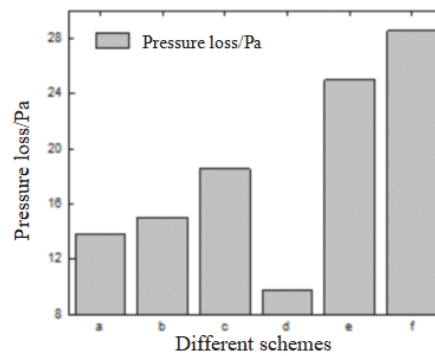


Fig. 16. Different design scheme of smoke pressure loss

In summary, Simulation results of the six kinds of flue deflector according to the design, Binding design velocity field distribution within the flue six kinds of arcuate deflector, outlet cross-sectional flow graph, the pressure loss can be seen in FIG. Analysis: Accordingly, the simulation results can be seen in conjunction with the program: when flue gas flow rate 102733kg /h Time, Five flow deflectors are arranged in columns best.

CONCLUSIONS

1. SCR system to simplify the structure, Analysis of the results of comparison of the two simulated flue sloping and curved, in order to reduce the wall damage, problems such as flue losses, the flow channel design is more reasonable arc corner.
2. Flue corner Office Developing the design arrangement of the baffles, the baffles simulate drainage effect in terms of velocity, pressure loss, etc., with a view to determine a flue Different flue gas flow Best baffle arrangement.
3. When flue gas flow rate 43490 kg/h Time, Program guide arc length becomes four baffles and arranged in an arc to reduce the pressure loss of the flue best; when flue gas flow rate 61570 kg/h Time, The arc length of

the arc flue four variant embodiment is preferably a baffle arrangement; when flue gas flow rate 102733 g/h Time, The arc length of the arc becomes five flue baffle disposed a best solution.

ACKNOWLEDGEMENTS

This project is partially supported by Jiangsu University of Science and Technology.

BIBLIOGRAPHY

- Wang, J., Chia, A., Menq, H.: Control of Diesel Engine Urea Selective Catalytic Reduction Systems. Etd.ohiolink.edu, 2010.
- Konstandopoulos, A.G., Zarvalis, D., Chasapidis, L.: Investigation of SCR Catalysts for Marine Diesel Applications. 2017.
- Fisher, C., Meech, R.: Bunkers an analysis of the technical and environmental issues. Petrosport Limited England, 2, 2013.
- Forzatti, P.: Present status and perspectives in de-NOX SCR catalysis. Applied Catalysis A: General, 2001, 222, Pp. 221-236.
- Koga, T., Kubo, T., Fukuya, S.: Countermeasures to Comply with Tier III NOx Emission Regulations for Marine Diesel Engines. Journal of the Marine Engineering Society in Japan, 2013, 48(1), Pp. 15- 20.
- Raptotasiou, S.I., Sakellaridis, N.F., Papagiannakis, R.G.: Application of a multi-zone combustion model to investigate the NOx reduction potential of two-stroke marine diesel engines using EGR. Applied Energy, 2015, 157, Pp. 814 -823.
- Ma, X., Zhang, F., Han, K.: Effects of Intake Manifold Water Injection on Combustion and Emissions of Diesel Engine. Energy Procedia, 2014, 61, Pp. 777-781.
- Magnusson, M.: NOx Abatement Technique for Marine Diesel Engines - Improved Marine SCR Systems. 2014.
- Garcia-Bordeje, E., Calvillo, L., Lazaro, M.J.: Vanadium supported on carbon-coated monoliths for the SCR of NO at low temperature: Effect of pore structure. Applied Catalysis B: Environmental, 2004, 50, Pp. 235- 242.
- Ly, H., Hua, X., Xie, W.: Promotion effect of H₂ pretreatment on CeO₂ catalyst for NH₃-SCR reaction. Journal of Rare Earths, 2018, 7.
- Bhattachajee, S., Haworth, D.C.: CFD Modeling of Processes Upstream of the Catalyst for Urea SCR NOX Reduction Systems in Heavy-Duty Diesel Applications. SAE Paper, 2012-0-13 (22).
- Selective Catalytic Reduction system for reducing NOX emissions installed on an MAN B & W 6S35MC diesel engine. News from MAN B & W Diesel.18 September 2001.
- Nesse, H.P.: Wartsila Low NOx Solutions.Wartsila.15 may 2008.
- Nojima, S., Lida, K., Kobayashi, N.: Development of NOX removal SCR Catalyst for low SO₂ oxidation. Technical Review, 2011, 38(2), Pp. 87-91.
- Hiromi, K.N., Toshiyuki, T.O., Chris, D.: Latest SCR technologies and experience on coal fired boilers [A] ICAC forum 98 "Cutting NOX Emissions" Durham North Carolina: 1998.
- Chong, P.C., Pyo, Y.D., Jin, Y.J.: NOx, reduction and N₂ O emissions in a diesel engine exhaust using Fe-zeolite and vanadium-based SCR catalysts. Applied Thermal Engineering, 2017, 110, Pp. 18-24.
- De'nan, F., Hasan, H., Choong, K.K.: The efficiency of structural steel section with perforated-corrugated web profile subjected to shear loading condition. Engineering Heritage Journal, 1(1), Pp. 29-35.
- Hassan, S.R., Zaman, N.Q., Dahlan, I.: Influence of Seed Loads on Start Up of Modified Anaerobic Hybrid Baffled (MAHB) Reactor Treating Recycled Paper Wastewater. Engineering Heritage Journal, 2017, 1(2), Pp. 05-09.
- Tu, C.X.: Research on the Multilevel Security Authorization Method Based on Image Content. Acta Electronica Malaysia, 2017, 1(1), Pp. 18-20.
- Luo, X.: Static Characteristic Analysis of Concrete-Filled Steel Tube Tied Arch Bridge. Acta Mechanica Malaysia, 2018, 2(1), Pp. 08-11.
- Li, B.Q., Li, Z.: The Design of Wireless Responder System Based on Radio Frequency Technology. Acta Electronica Malaysia, 2018, 2(1), Pp. 11-14.
- Luo, X.: Study on Pc Continuos Girder Mechanical Properties Based On Tendon Tensioning Pattern. Acta Mechanica Malaysia, 2018, 2(1), Pp. 12-15.

CONTACT WITH THE AUTHORS

Jun Du, *Master Student*
e-mail:dujun9988@163.com

Jiangsu University of Science and Technology
2 Mengxi, Jingkou
Zhenjiang 212003
CHINA

TECHNICAL APPLICATION OF PETROLEUM LOGGING INSTRUMENTS IN MARINE LOGGING

Caiyun Gu

Peng Zhao

Li Wang

Hongxia Guo

Yulin University, Shaanxi, China

ABSTRACT

To solve the problem of offshore oilfield development, based on the newly introduced pulsed neutron oxygen activation logging instrument, the application research of test design and interpretation method was carried out and applied to actual production. The structure, technical indicators and logging principles of pulsed neutron oxygen activation logging tools were introduced. The test design under different well conditions was studied, including general positive and negative injection, oil sleeve injection, single oil pipe configuration and multi-tubing configuration. A large amount of field test data was collected and analysed technically. A set of effective interpretation models was proposed. The corresponding interpretation software was developed. A set of test design methods and operating specifications for different well conditions were developed. Based on the conventional interpretation method, the peak selection, the double-tuber peak identification and the carbon dioxide flooding interpretation method were added. The results show that the test design and interpretation methods were applied well through a large number of field tests and production applications. Therefore, pulsed neutron oxygen activated injection profile logging technology is successfully applied in offshore oil fields.

Keywords: oil logging instrument, pulsed neutron oxygen activation, injection profile logging, application

INTRODUCTION

Oil logging can provide an effective basis for the exploration and development of petroleum resources, which runs through the whole process of oil well drilling to oil well production. Therefore, the application of logging tools directly affects oil exploration and development. To improve the level of oil logging and ensure the efficient development of petroleum resources, advanced technology should be applied in the logging process.

In the process of oil and gas field exploration and development, the continuous development of logging technology has become an important “helper” for the petroleum industry personnel to qualitatively and quantitatively evaluate oil and gas reservoirs. According to various logging principles, successful oil logging tools can be used to better understand the formation. Electromagnetic

flowmeters and ultrasonic flow have been used in other industries for many years, and the logging industry has been introduced for several years, but the application effect has not been very satisfactory. For example, the electromagnetic flowmeter can only measure the liquid flow rate of the conductive medium and cannot measure the flow rate of the non-conductive medium, and the sensor material problem of the ultrasonic flow meter. Those factors hinder its development. In addition, although turbine flow, ultrasonic flow, and electromagnetic flow logging techniques are relatively advanced, they are all contact flow logging devices that require downhole contact with the test fluid. Therefore, the loop and the flow outside the tube cannot be measured. The oilfield injection well has the characteristics of long section, large number of layers and small injection volume. Most of the logs are layered or multi-tube dispensing structures. Contact measurement method cannot play a full role in complicated

wells such as stratified water injection and multi-string water injection. Logging techniques such as well temperature and noise cannot quantitatively determine the flow rate, and the injection flow logging cannot be completed separately.

The pulsed neutron oxygen activation logging method is a nuclear logging method. The water flow is activated by a pulsed neutron tube, and the water flow velocity is determined by measuring the time that the activated water flow flows through the respective detectors to determine the injection amount. The logging method uses any radiotracer. There are no problems such as contamination, sedimentation and pollution. The measurement results are not affected by lithology and pore permeability parameters and the size of the perforation diameter. It is not only suitable for the measurement of polymer injection, ternary composite solution wells, but also for the measurement of general positive injection wells, general reverse injection wells, oil casing injection wells and layered injection wells. The method can determine the flow of fluid in the tube, outside the tube and in the annulus without direct contact with the fluid and can simultaneously measure the upper and lower streams. The field is quickly and intuitively explained, and the flow rate of the measuring point can be quickly obtained. Therefore, the oil field injection profile test is widely used.

STATE OF THE ART

At present, there are two types of non-renewable energy that people use most in their daily lives. One is natural gas and the other is oil. Over time, energy is being mined frequently, which has led to a decline in global oil and gas resources reserves. However, the demand for natural gas and oil is rising. For these reasons, scientists around the world are constantly exploring new oil and gas fields, and also increasing the exploration of high-tech exploration in oil and gas fields.

The distinctive feature of the product in 2004 is that on the basis of the four-shot and double-receiving symmetric distribution products, a set of emission spacing is added to form a six-shot double of T5---T3--T1-RR-T2--T4---T6. A symmetrically distributed antenna array is received. The operating frequency is still dual frequency: 400kHz and 2MHz. An apparent resistivity curve of 12 different depths of detection is obtained, which provides a wealth of formation information. Based on a study, a typical representative of this generation of products is Weatherford's MFR [1].

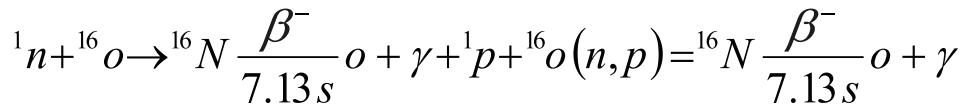
In 2005, a scholar introduced a new logging while drilling tool, that is, a directional electromagnetic logging tool. This generation of instruments mainly focuses on the depth and orientation of the instrument and optimizes the application effect in geo steering. The new directional electromagnetic wave LWD instrument uses tilt and lateral antennas with multiple source distances and frequencies to collect data as much as possible. The symmetry of the measurement makes the response sensitive to the distance to the interface and the resistivity contrast. It is not affected by resistivity anisotropy and relative tilt. In order to facilitate real-time decision making, real-time inversion software was developed [2].

In 2011, the SWFL-A pulse neutron oxygen activated water flow logging tool has been greatly upgraded and improved in technical design and performance indicators. The utility model has the advantages of various functions, simple and compact structure, various combination modes, large source distance and measurement range, higher precision, wider temperature range, reliability and convenience. The SWFL-B neutron oxygen activated water flow logging tool fully possesses the neutron lifetime logging function in the measurement function. In the neutron lifetime logging mode, the method of measuring the variable period neutron decay time spectrum of the equal width gate is adopted, and the equal-width neutron decay time spectrum is used [3].

In 2007, a scholar proposed a continuous measurement velocity model and a pulse measurement velocity model. During the measurement process, the pulsed neutron tube continuously emits a high-energy fast neutron pulse to activate the oxygen element in the fluid. The flow rate of the fluid can be determined based on the count rate measured by the instrument and the characteristic exponential decay rate [4].

PULSED NEUTRON OXYGEN ACTIVATION LOGGING

Oxygen activated water flow logging methods were proposed from the 1960s and 1970s. Until recently, a method for measuring the amount of water absorbed by each layer in a water injection well or an injection well was applied. This method is a non-contact measurement method that utilizes the activation reaction of fast neutrons to the surrounding medium. The principle is as follows: the neutron generator emits a fast neutron of 14 MeV, radiates the material around the wellbore and in the formation, and generates a radiation reaction, which can activate elements such as O, Si, and Al to generate a radioactive element with a half-life of seconds to a grade. After the reaction, ^{16}O was converted to ^{16}N (half-life 7.13S), ^{28}Si was converted to ^{28}Al (half-life 2.24min), and ^{27}Al was converted to ^{27}Mg (half-life 9.46min). All three radioactive elements emit high-energy β and γ rays. The β ray is easily absorbed by the formation rock, the surrounding medium and the logging steel shell, while the γ ray can be detected by the γ detector [5]. According to research, the oxygen nucleus produces a nitrogen isotope at 10 MeV of fast neutron activation, and the radioactive nitrogen isotope undergoes β decay with a half-life of 7.13S [6]. High energy γ rays are emitted after β decay. The energy is 6.13 MeV of radiation. The threshold energy of the ^{16}O reaction was 10.2 MeV. Therefore, the 14MeV neutron generator is suitable. Due to the high energy, 6.13 MeV γ rays can penetrate wellbore materials of several tens of centimetres, such as well fluids, tubing, casing, cement, etc. The Monte Carlo method can be used to calculate the activation profile of oxygen activation and the response function of the detector, so it is possible to predict the change in the detector count rate caused by water flow [7]. Study showed the reaction process of oxygen activation is as follows [8].



(1)

Pulsed oxygen activated water flow logging was proposed by Schlumberger in the United States in 1991 to detect vertical water flow and provide quantitative measurements of water flow velocity and flow, known as WFL logging methods.

When logging, the generator hits the neutron for a few seconds. The surrounding water is activated. Then, after a few seconds of rest, several detectors simultaneously record the time spectrum of the γ signal. If the water is flowing, after a period, the water reaches the detectors in turn, and a peak appears in the time spectrum of each detector. According to the position of the peak on the time spectrum, the time T of the water flow reaching each detector is known, and the distance travelled by the water during this time is the source distance L of each detector, and the speed of the water is $V=L/T$. Since the borehole and the tubing diameter D are known, the cross-sectional area S of the water can be calculated, and the flow rate $Q = VS$ [9].

If the neutron pulse time width is T_a , the time that the activated water flows from the neutron source to the detector can be obtained by the following equation [10]:

$$T_m = \frac{T_a}{2} + \frac{\int f(t)tdt}{\int f(t)dt} \quad (2)$$

INTERPRETATION AND APPLICATION OF PULSED NEUTRON OXYGEN ACTIVATION LOGGING

FEATURE ANALYSIS OF SPECTRAL PEAK RECOGNITION

The time peaks recorded by the pulsed neutron oxygen activation log show different forms with the flow velocity of the measured fluid. The spectral peak characteristics are generally described in terms of the amplitude, width and symmetry of the peak [11].

A single peak characteristic is produced when there is only one column space fluid flow at the measurement site. A single peak characteristic is also produced when the fluid flow direction and flow rate in the two column spaces are exactly the same, which is a special case. In actual production, it rarely happens.

The bimodal and the two peaks appear as a superposition of two single peaks on the time spectrum. According to the degree of overlap, it can be divided into non-overlapping, partial overlap and severe overlap. This situation is the performance of two kinds of column space fluid flow at the measuring point [12]. For example, the tubing and the loop space have fluids that flow simultaneously downward [13].

First, the non-overlapping bimodal. There is a significant bimodal on the time spectrum, and the points between the two peaks are more open. There is no overlap.

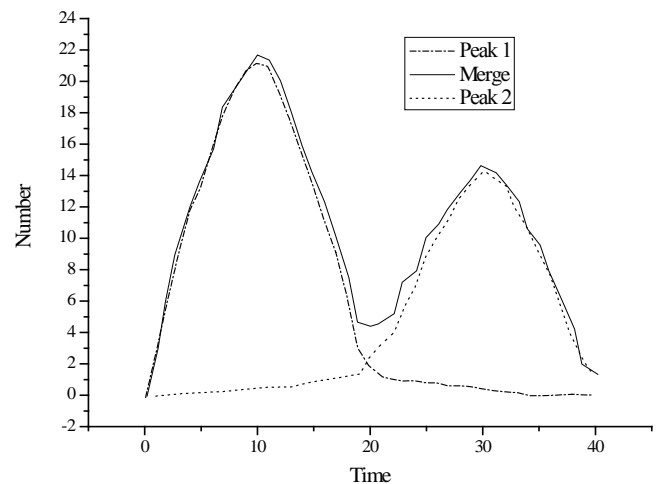


Fig. 1. Theoretical graph of non-overlapping bimodal

Second, partially overlapping bimodal. The time spectrum is shown as two peaks, and the lower half of the single peak overlaps.

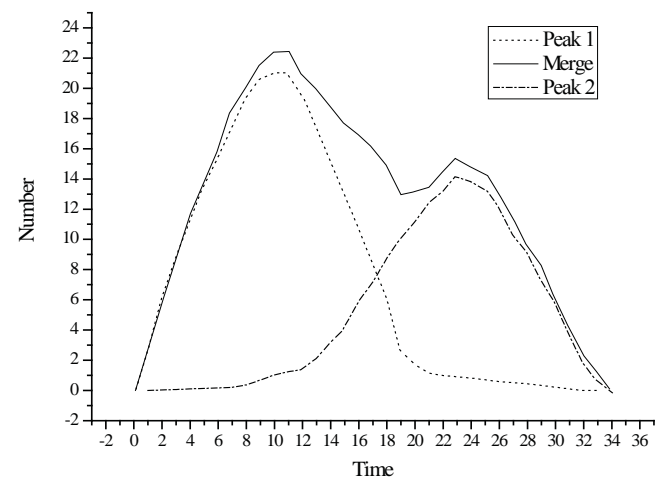


Fig. 2. Theoretical graph of partially overlapping bimodal

Third, the serious overlap of the bimodal. The two peaks overlap completely and only one peak can be seen on the time spectrum.

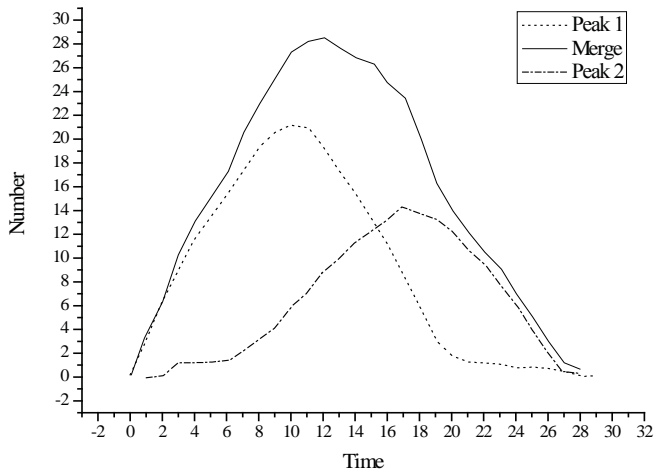


Fig. 3. Theoretical graph of seriously overlapping bimodal

BASIC FUNCTIONS OF THE SOFTWARE

The pulse neutron oxygen activation logging interpretation software is divided into three parts, namely, point measurement calculation, comprehensive calculation and profile result table generation, and result image electronic picture output and printing. The point measurement calculation is used to perform peak identification and flow calculation for a single measurement point. The software can display the measurement data of seven probes at the same time and can filter each curve. The flow rate in the tubing, inside the casing and the oil collar annulus of each peak is calculated.

The flow value of the measurement point is imported into the comprehensive calculation section. Combined with the perforation horizon, water distributor, packer, bell mouth and other structural positions, the suction profile is calculated, and the results graph and the results table data are produced. It also includes a carbon dioxide flooding calculation module and a single point calculation module. The density and mass flow of carbon dioxide are calculated [14]. The single point calculation module enables the mutual conversion of time, flow rate and flow for a specific source distance, which is used as a reference in identifying peaks.

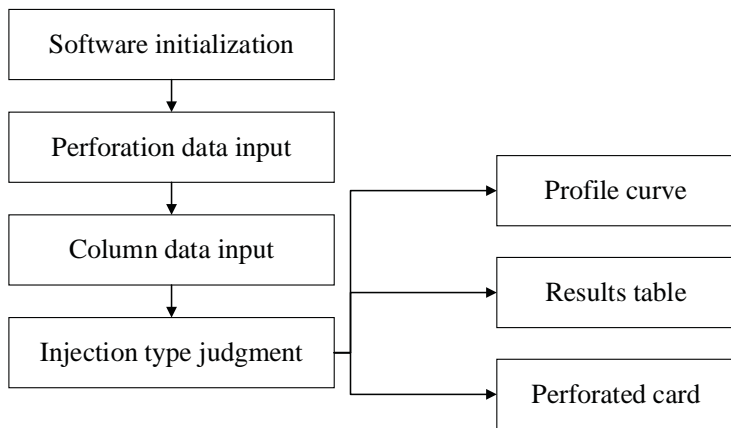


Fig. 4. Flowchart of integrated computation

The software first judges whether the water injection is positive or negative injection, compounding, general injection or double pipe layering according to the perforation interval and column structure data (water distributor, packer, bell mouth). The point flow data is imported to calculate the amount of injection for each layer. Finally, the injection profile curve (tubing flow profile, casing flow profile, reverse injection annulus profile, up flow and downflow separation), outcome data, conclusion cards, perforation cards were calculated. The specific process is shown in Figure 4 [15].

The single point calculation module enables the conversion of time, flow rate and flow to a specific source distance. Based on the column data and fluid space type, combined with the source distance, the software converts the three parameters of time, flow rate and flow. In the peak identification process, the time in the graph is determined based on the estimated flow value. The flow rate is determined based on the estimated flow rate and time. During construction, the selection of measurement points and the verification of the validity of the measurement results are guided.

DOUBLE PIPE LAYERED WATER INJECTION

The double-pipe layered water injection method is complicated, which makes the underground water flow form more complicated. To make the interpretation more intuitive, the multi-section form is used to show the interpretation of the results. The flow profile for interpreting the results graph is three lanes. They represent the inner tubing water flow, the tubing annulus water flow and the oil jacket space water flow, respectively.

The peak is determined by the relationship between flow, flow rate and time, as shown in Figure 5. The flow rate is different in different column structures. It is converted to time based on the distance between the neutron tube and the detector (source distance) [16]. According to the relationship between flow and time, the peak is judged. This method is generally used to determine the peak position of the total injected amount. In the double-tube stratified injection well, the peak position of the total water flow in the oil pipe, the oil pipe annulus and the oil jacket annulus can be judged, which provides a reference for determining the flow peaks of each layer in the next step.

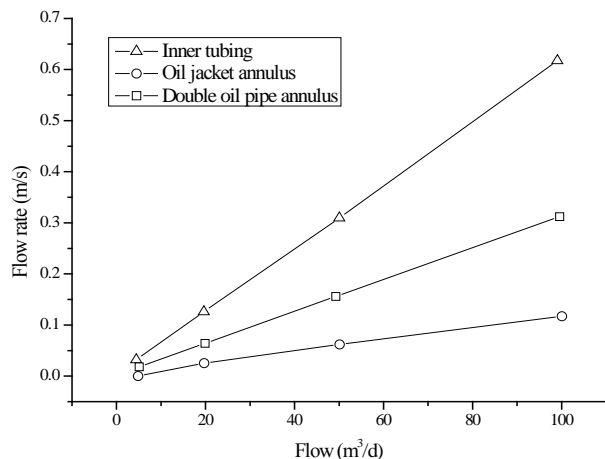


Fig. 5. The relationship between inner tubing, oil jacket annulus and double oil pipe annulus

Tab. 1. Log interpretation results

Layer number	Perforating section (m)	Relative water absorption (%)	Absolute water absorption (m ³ /d)	Degree of water absorption (m ³ /d/m)	Flow direction
12	1665.0-1669.9	6.68	3.21	0.68	Oil jacket up
13	1670.4-1678.9	14.16	6.81	1.49	Oil jacket up
		17.09	8.21	2.17	Oil jacket up
15	1684.0-1694.9	13.12	6.31	1.27	Oil jacket up
		16.05	7.69	1.34	Oil jacket up
16	1695.2-1701.7	6.45	3.09	1.12	Oil jacket up
		10.01	4.81	1.34	Oil jacket up
18	1711.0-1715.9	11.66	5.61	1.18	Oil jacket up
19	1716.6-1723.5	4.79	2.29	0.69	Oil jacket up
Total		100.00	48.03		

Tab. 2. Interpretation results of back injection logging

Layer number	Perforating section (m)	Relative water absorption (%)	Absolute water absorption (m ³ /d)	Degree of water absorption (m ³ /d/m)	Flow direction
25	2140.0-2153.0	-	Not absorbing	-	-
26	2180.0-2196.0	8.08	8.31	1.12	Oil jacket down
		91.92	94.49	11.13	Oil jacket down
27	2224.0-2228.9	-	Not absorbing	-	-
28	2228.9-2230.0	-	Not absorbing	-	-
29	2236.0-2252.0	-	Not absorbing	-	-
30	2258.0-2270.9	-	Not absorbing	-	-
31	2270.9-2280.0	-	Not absorbing	-	-

Tab. 3. Interpretation results of positive logging

Layer number	Perforating section (m)	Relative water absorption (%)	Absolute water absorption (m ³ /d)	Degree of water absorption (m ³ /d/m)	Flow direction
25	2140.0-2153.0	-	Not absorbing	-	-
26	2180.0-2196.0	-	Not absorbing	-	-
27	2224.0-2228.9	26.35	10.81	1.81	Oil jacket up
28	2228.9-2230.0				
29	2236.0-2252.0	5.35	2.19	0.64	Oil jacket up
		-	Not absorbing	-	-
30	2258.0-2270.9	2.45	1.01	0.26	Oil jacket up
		4.86	1.99	0.19	Oil jacket up
		40.99	16.81	4.55	Oil jacket up
31	2270.9-2280.0	15.60	6.39	1.20	Oil jacket up
		4.40	1.81	0.50	Oil jacket up

FIELD APPLICATION

The well depth is 1967.86m. The outer diameter of the casing is 139.7 mm and the outer diameter of the oil pipe is 73 mm. The target layer measurement section is 1630.0-1727.0m, and the daily water injection volume is 48.0 m³/d. The oil pressure is 8.0 MPa and the casing pressure is 0.0 MPa. The single oil pipe is used for general water injection, and the bell mouth is located at 1719.6 m, which is injected into the water and returned to each suction layer. The amount of inhalation at each horizon was determined by pulsed neutron oxygen activation logging. The water absorption of each layer is shown in Table 1.

The well depth of the well is 2490.02 m. The outer diameter of the casing is 177.8 mm and the outer diameter of the oil pipe is 73 mm. The target layer measurement section is 2020.0-2281.0 m, and the daily water injection volume is 120.2m³/d. The oil pressure is 23.5 MPa and the casing pressure is 19.5 MPa. Water is injected by means of oil sleeve. The packer position is 2207.0 m and the bell mouth position is 2300.0 m. According to the pulsed neutron oxygen activation logging, the total injection of the oil jacket annulus is 102.8 m³/d, and the total injection volume of the oil pipeline is 41.0 m³/d. The amount of inhalation of each layer is determined. The water absorption of each layer is shown in Table 2.

CONCLUSION

Aiming at the actual logging data of offshore oilfields, the interpretation methods are studied, including spectral peak identification feature analysis methods and interpretation model establishment. In particular, the spectral peak identification method and carbon dioxide flooding interpretation method for double-tube layered water injection are proposed. Oxygen activation logging can be implemented in oil fields. This interpretation method basically meets the existing logging requirements.

For the test design and interpretation method of the research, the corresponding interpretation software is written. The software includes point measurement calculation, comprehensive calculation, profile result table generation and electronic picture output and printing. After a period of practical application, this method has undergone a series of improvements. At present, the actual interpretation needs have been met. As the application deepens and the scope of application expands, the software needs to be continuously improved and expanded.

REFERENCES

1. C. Qing, X. Wu, X. Li, W. Zhu, C. Qiao, and R. Rao, *Use of weather research and forecasting model outputs to obtain near-surface refractive index structure constant over the ocean*, Optics Express, Vol. 24, No. 12, pp. 13303–13315, 2016.
2. M. Wang, X. Liu, L. Tan, L. Jiang S. Seunghyun, and S. Wei, *Impacts of viirs sdr performance on ocean color products*, Journal of Geophysical Research-atmospheres, Vol. 118, No. 18, pp. 10347–10360, 2016.
3. A. Camps, J. Font, M. Vall-Llossera, I. Corbella N. Duffo, and F. Torres, *Determination of the sea surface emissivity at l-band and application to smos salinity retrieval algorithms: review of the contributions of the upc-icm*, Radio Science, Vol. 43, No. 3, pp. 1–16, 2016.
4. W. D. Robinson, B. A. Franz, J. H. Ahn, and J. H. Ahn, *Cloud motion in the goci/coms ocean colour data*, International Journal of Remote Sensing, Vol. 37, No. 20, pp. 4948–4963, 2016.
5. R. H. Morin, G. E. Descamps, and L. D. Cecil, *Acoustic televiewer logging in glacier boreholes*. Journal of Glaciology, Vol. 46, No. 46, pp. 695–699, 2017.
6. W. S. Chan, M. L. Mah, R. C. Bay, and J. J. Talghader, *Long-wavelength optical logging for high-resolution detection of ash layers in glacier ice* Journal of Glaciology, Vol. 63, No. 237, pp. 17–21, 2016.
7. G. C. Hays, L. C. Ferreira, A. M. M. Sequeira, M. G. Meekan, C. M. Duarte, and H. Bailey, *Key questions in marine megafauna movement ecology*, Trends in Ecology & Evolution, Vol. 31, No. 6, pp. 463–475, 2016.
8. B. C. Bennett, *The sound of trees: wood selection in guitars and other chordophones*, Economic Botany, Vol. 70, No. 1, pp. 49–63, 2016.
9. S. Biancamaria, D. P. Lettenmaier, and T. M. Pavelsky, *The swot mission and its capabilities for land hydrology*, Surveys in Geophysics, Vol. 37, No. 2, pp. 307–337, 2016.
10. M. Glasius, and A. H. Goldstein, *Recent discoveries and future challenges in atmospheric organic chemistry*, Environmental Science & Technology, Vol. 50, No. 6, pp. 2754, 2016.
11. S. Kasim, N. A. Omar, N. S. Mohammad Akbar, R. Hassan, and M. A. Jabar, *Comparison Semantic Similarity Approach Using Biomedical Domain Dataset*, Acta Electronica Malaysia, Vol. 1, No. 2, pp. 1–4, 2017.
12. N. S. Ismail, S. Kasim, Y. Y. Jusoh, R. Hassan, and A. Alyani, *Medical Appointment Application*, Acta Electronica Malaysia, Vol. 1, No. 2, pp. 5–9, 2017.
13. Z. He, X. Gu, X. Y. Sun, J. Liu, and B. S. Wang, *An Efficient Pseudo-Potential Multiphase Lattice Boltzmann Simulation Model for Three-Dimensional Multiphase Flows*, Acta Mechanica Malaysia, Vol. 2, No. 1, pp. 01–03, 2018.
14. X. Luo, *Research on Anti-Overturning Performance Of Multi-Span Curved Girder Bridge with Small Radius*, Acta Mechanica Malaysia, Vol. 2, No. 1, pp. 04–07, 2018.
15. H. Farrajia, N. Qamaruzaman, S. K. Md Sa'ata, and A. F. Dashtia, *Phytoremediation of suspended solids and turbidity of palm oil mill effluent (POME) by Ipomea aquatic*, Engineering Heritage Journal, Vol. 1, No. 1, pp. 36–40, 2017.
16. F. De'nan, H. Hasan, and M. Mahzuz, *Behaviour of the beam to column connection for tapered steel section with perforation*, Engineering Heritage Journal, Vol. 1, No. 1, pp. 41–44, 2017.

CONTACT WITH THE AUTHORS

**Caiyun Gu
Peng Zhao
Li Wang
Hongxia Guo**

Yulin University
Shaanxi 719000
CHINA

APPLICATION OF EVALUATION ALGORITHM FOR PORT LOGISTICS PARK BASED ON PCA-SVM MODEL

Bianjiang Hu

School Of Business, Central South University, Changsha, Hunan, China

ABSTRACT

To predict the logistics needs of the port, an evaluation algorithm for the port logistics park based on the PCA-SVM model was proposed. First, a quantitative indicator set for port logistics demand analysis was established. Then, based on the grey correlation analysis method, the specific indicator set of port logistics demand analysis was selected. The advantages of both principal component analysis and support vector machine algorithms were combined. The PCA-SVM model was constructed as a predictive model of the port logistics demand scale. The empirical analysis was conducted. Finally, from the perspective of the structure, demand, flow pattern and scale of port logistics demand, the future logistics demand of Shenzhen port was analysed. Through sensitivity analysis, the main influencing factors were found out, and the future development proposals of Shenzhen port were put forward. The results showed that the port throughput of Shenzhen City in 2016 was 21,328,200 tons. Compared with the previous year, it decreased by about 1.74 %. In summary, the PCA-SVM model accurately predicts the logistics needs of the port.

Keywords: port logistics demand, support vector machine, principal component analysis, economic hinterland

INTRODUCTION

With the integration of the world economy, logistics has been widely valued by various countries and has achieved rapid development. At present, the logistics industry has become an important pillar industry and a new economic growth point in China. It is a strong support for the tertiary industry. As an important branch of logistics, urban logistics guarantees the continuous operation of various functions of the city. This is a new impetus to promote the healthy and rapid development of the regional economy. With the continuous deepening of economic transformation and the optimization and upgrading of industrial structure, the specialization of logistics and the process of socialization have obviously accelerated. The level of urban logistics services has been further improved. With the supply-side structural reform entering the tough stage, logistics companies must upgrade their own strength to adapt

to the development of the times. As of the end of 2015, the total cost of social logistics was approximately 11.1 trillion. It grew by 2.9 % compared to the previous year. Among them, the transportation cost is 6 trillion. Compared with the previous year, it increased by 3.3 %. The cost of storage is 3.7 trillion. Compared with the previous year, it increased by 1.3 %. The administrative fee is 1.4 trillion. Compared with the previous year, it increased by 5.6 %. This shows that the steady growth of the logistics industry is the fundamental guarantee for the sound development of the tertiary industry and social economy. In August 2015, policies such as “Multiple measures to promote the accelerated development of modern logistics” and “Notice on Accelerating the Implementation of Major Projects in Modern Logistics” were issued. The logistics industry has been promoted to an unprecedented height. A sound modern logistics service system can promote economic transformation and upgrading of industrial structure.

Based on the research status of port logistics demand at home and abroad, the internal relationship between port logistics demand and port economic hinterland is analysed. According to the corresponding construction principles, a set of quantitative analysis indicators for port logistics demand was established. Domestic and international common port logistics demand analysis methods are compared. Combined with the characteristics of port logistics demand, the advantages of support vector machine and principal component analysis are combined and the PCA-SVM model is established. It provides a new method and idea for port logistics demand analysis.

STATE OF THE ART

Lin et al. analysed the freight negotiations in France and assessed the effectiveness of the urban freight policy. The combination of qualitative and quantitative methods was used to analyse the negotiation of the institutional framework of the French region at three levels. Specific consultations on freight cost issues need to be implemented, and important consultation results are translated into effective policies and behaviours [1]. Taking Poland as an example, Fresno et al. analysed the role of government in the development of urban logistics. A collaborative process model for urban logistics policy makers was constructed. Studies have shown that government departments not only lack a comprehensive and effective plan to develop urban logistics, but also lack cooperation with urban logistics practitioners [2]. Hope et al. analysed the relationship between the construction of transportation infrastructure and employment growth in the region. The regression model was used to analyse the employment data from 1992 to 2008. The study showed that the transportation infrastructure construction increased the employment rate [3]. Taking the export of the Spanish region as an example, Wu et al. studied the logistics infrastructure and trade import and export volume. Data from 19 Spanish regions to 64 destinations for the period 2003–2007 were analysed using a bilateral export model. The survey results show that the level and quality of logistics infrastructure have a positive impact on trade export flows [4]. Qi et al. studied the relationship between logistics development and economic development for a long time and established an econometric model. WGDP represents economic growth. Transportation turnover and inventory represent logistics development. Tests prove that economic growth is positively related to logistics development [5]. Li et al. studied the relationship between traffic flow and economic growth in Indonesia from 1988 to 2010 to analyse the relationship between logistics and economic development. Shipping, air and rail freight volumes are used as logistics indices, and GDP is used as an economic index to build a series of models. Experiments show that logistics plays a supporting role in maintaining economic growth. Logistics infrastructure construction is one of the means to ensure sustainable economic development [6]. To reduce the inventory cost brought by the bullwhip effect, Feng

et al. used the DWT-ANN model to predict regional logistics demand. In contrast to the ARIM method, data from three different manufacturing companies were collected for analysis. Experiments show that the DWT-ANN model has higher precision [7]. Foraker et al. pointed out that the evaluation method of the effectiveness of logistics measures is crucial. The O-D matrix is established from three aspects of transportation service type, delivery time and vehicle type. The collected data was used for simulation and satisfactory results were obtained [8]. A scholar used the Delphi method to predict the gross domestic product of the road freight traffic from Finland and concluded that different economic developments would produce different transportation needs [9].

In general, developed countries such as Europe and the United States attach great importance to the forecasting of logistics demand, and the research time is much earlier than China. Foreign studies have achieved theoretical success. Relevant laws and regulations guarantee the healthy and sustainable development of the logistics industry [10].

PORT LOGISTICS DEMAND FORECASTING MODEL BASED ON PCA-SVM

The logic of the support vector machine learning process is expressed in mathematical formulas as follows:

If there is an unknown joint probability $F(x, y)$ between the input variable x and the output variable y , according to several independent and identically distributed samples $(x_1, y_1), (x_2, y_2), (x_3, y_3), \dots, (x_n, y_n)$, an optimal $f(x', y')$ is found in a set of functions to minimize the expected risk [11]:

$$R(X) = \int L(y, f(x', y')) dF(x, y) f(x', y') F(x, y) \quad (1)$$

In the formula (1), $L(y, f(x', y'))$ represents the loss function caused by the function performing regression prediction. In general, when the function is fitted, the calculation error of the least square difference is used to represent the loss function. Minimizing risk is the main purpose of machine learning. However, in many practical problems, the information available is very limited. It is difficult to calculate the expected risk. The principle of empirical risk minimization is as follows [12]:

$$R_{emp}(W) = \frac{1}{n} \sum_{i=1}^n L(y, f(x', y')) \quad (2)$$

The principle of empirical risk minimization has been used to replace the principle of expected risk minimization, which has achieved good application in many fields [13]. It provides a new way of thinking and perspective for problem solving and has gradually become a common guideline.

The operation steps of the PCA-SVM prediction model are shown in Figure 1:

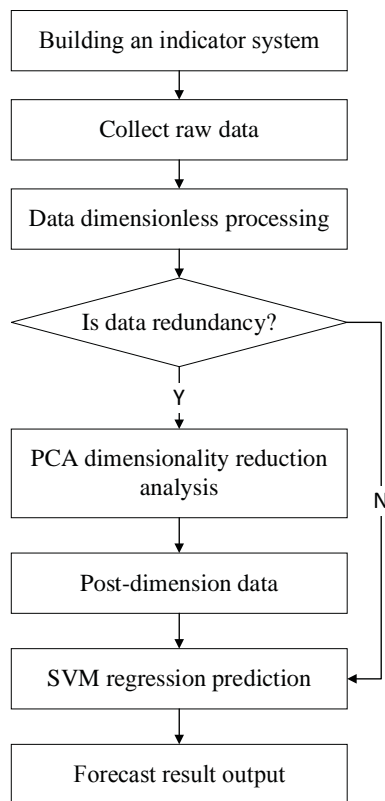


Fig. 1. Operation steps of the PCA-SVM model

In the PCA-SVM model, there is a problem of parameter optimization. The appropriateness of the parameter selection directly determines the prediction accuracy of the model. There are two parameters in the model that need to be optimized, namely the penalty parameter C and the kernel function selection parameter g . At present, the academic community generally uses the grid search method and the particle swarm algorithm to optimize the parameters.

EMPIRICAL ANALYSIS OF PORT LOGISTICS DEMAND

STRUCTURAL ANALYSIS OF PORT LOGISTICS DEMAND

Shenzhen port is the second largest port in China and the third largest container port in the world. It is a key location for China's foreign trade. With the transformation of economic growth mode and the continuous development of Shenzhen's economy, port logistics has become increasingly important in the logistics system of Shenzhen. In 2015, the container throughput of Shenzhen port increased by 0.7 % compared with the previous year, with a total of 24,240,600 TEU [14]. Among them, the export container throughput decreased by 0.9 %. The total number of standard boxes is 12.60 million. Compared to last year, it fell by 0.9 %. The cargo throughput of the port is 21,706,380 tons. Compared to last year, it fell by 2.8 %.

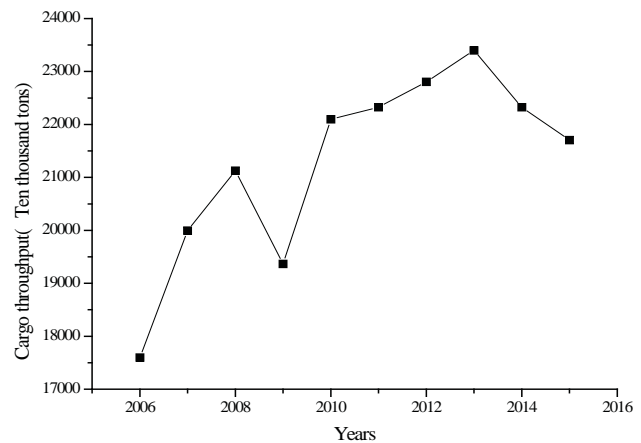


Fig. 2. Curve of port cargo throughput in Shenzhen from 2006 to 2015

In recent years, the total volume of imports and exports in Shenzhen has shown a downward trend. Since 2000, the total annual import volume of Shenzhen has been greater than the total export value. However, the growth rate of the import and export gap has continued to slow down. This shows that Shenzhen is in the transitional stage of "bringing in" and "going out". At present, Shenzhen's foreign trade is still dominated by imports. Port logistics demand will also be based on import logistics demand.

Hong Kong, the United States, and Taiwan account for the largest share of Shenzhen's imports, followed by South Korea and Japan. The main trading partners are concentrated in the Pacific Rim. With the continuous development of the global economy, the cooperation between Shenzhen and the major trading partners in the Pacific Rim continues to strengthen, which will inevitably strengthen the logistics needs of Shenzhen's foreign trade. Moreover, Shenzhen, as the largest port in South China, is the logistics point of import and export trade. With the continuous improvement of the transportation system, the connection between Shenzhen and the economic hinterland has been continuously strengthened. The development of the hinterland will inevitably provide a huge source of transit for Shenzhen. Such a large potential market will provide opportunities for the development of modern logistics in Shenzhen. It has obvious rules of logistics flow.

FORECAST OF LOGISTICS DEMAND OF BASIC PCA-GA-SVM

First, the gray correlation method is adopted. The following eight indicators were selected as input indicators for the forecast of Shenzhen port logistics demand. They are the gross domestic product of the hinterland, the gross agricultural production in the hinterland, the gross industrial production in the hinterland, the freight turnover in the hinterland, the transportation in Shenzhen, the fixed investment in warehousing and postal services, the gross domestic product of Shenzhen, total import and export volume and social freight volume in Shenzhen. Through the relevant literature research and the actual situation, the port throughput is selected as the output index to carry

out the target prediction. As can be seen from Table 1, the correlation of the sample data is generally above 0.8, which means that the sample data is highly correlated. It can be seen from Table 2 that the significance is 0, which is less than 0.05, indicating that it is less than the significance level. Therefore, the null hypothesis was rejected. It is significantly different from the identity matrix. The KMO index is 0.761. Therefore, the data can be analysed by principal component analysis.

Principal component analysis was performed using SPSS 22.0 software. The cumulative contribution rate is selected to be greater than 99 % as the main component. Since the cumulative contribution rate of the first, second and third principal components reached 99.369 %, the information of the original eight indicators was well retained. Three integrated variables were used to replace the eight variables in the original data. The coefficient matrix of each principal component can be calculated according to the factor score coefficient.

The 2-RBF function is selected. At this time, the penalty parameter C and the kernel function parameter g are determined. The choice of parameters C and g determines the performance of the SVR. Appropriate parameters allow the model to achieve more accurate predictions. After multiple experiments, grid search was used for parameter optimization. K-fold cross-validation was used to evaluate model performance to avoid overfitting.

There are two steps to improving the grid optimization method. First, the parameters are roughly selected, and the approximate range of the optimal parameters is selected using 0.5 steps to narrow the search range. Second, within the range of the optimal parameters determined by the rough selection of the parameters, the search is performed using a smaller step size. In this paper, 0.05 steps are used to find the final parameters. If multiple sets of parameters appear in the search results as the optimal result, the group with the smallest penalty parameter C is selected, because this can achieve a stronger generalization ability of the model. If the penalty parameter C is the same, the parameter that was first searched is taken as the optimal parameter.

The logistics demand structure of Shenzhen port and the main body of demand were analysed. With the continuous upgrading of the industrial structure, the proportion of high value-added and high-tech goods will increase in the logistics demand of Shenzhen ports. The logistics demand structure of Shenzhen port will be changed. In the case of slower port growth, the development of Shenzhen port has shifted from port throughput growth and traditional port industry layout to industrial chain and value chain. The port logistics service system is the main efficient industrial development model and establishes a new port and urban development relationship.

ANALYSIS OF FORECAST RESULTS AND FUTURE PREDICTIONS

The PCA-GA-SVM model is compared with four models to evaluate the prediction accuracy of the model. The PCA-PSO-SVM model is compared to the PCA-SVM model. The characterization of the training set is shown in Figures 3 and 4:

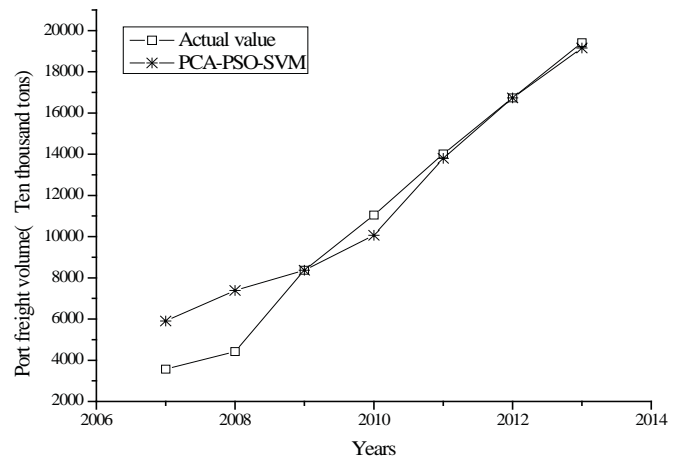


Fig. 3. The fitting of PCA-PSO-SVM model to the training set

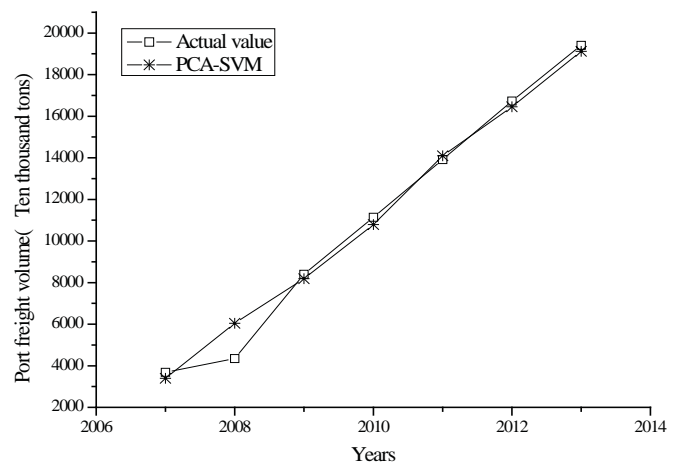


Fig. 4. The fitting of PCA-SVM model to the training set

The linear regression and BP neural network are used as the comparison model. The fitting of the training set is shown in Figures 5 and 6. The prediction results of the prediction set are shown in Table 2.

Tab. 1. Comparison of individual models

Years	Actual value	Predictive value					
		PCA-PSO-SVM	Error rate	PCA-SVM	Error rate	PCA-GA-SVM	Error rate
2014	24222	24261	0.1338	24231	0.000373	24311	0.00368
2015	24520	24517	0.1273	24517	0.000123	24520	0

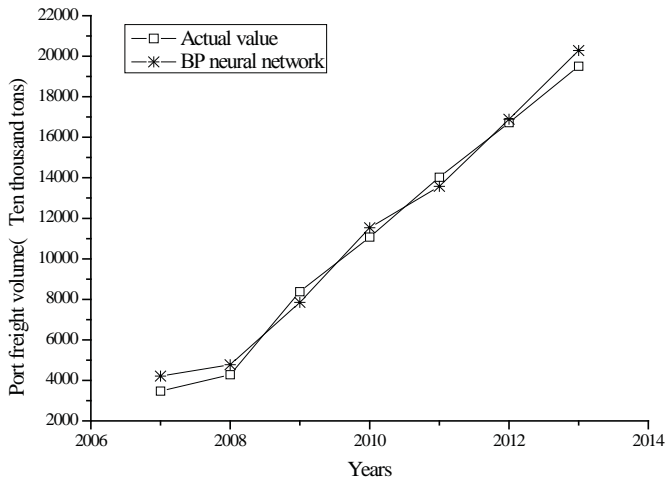


Fig. 5. The fitting of BP-Neural network model to the training set

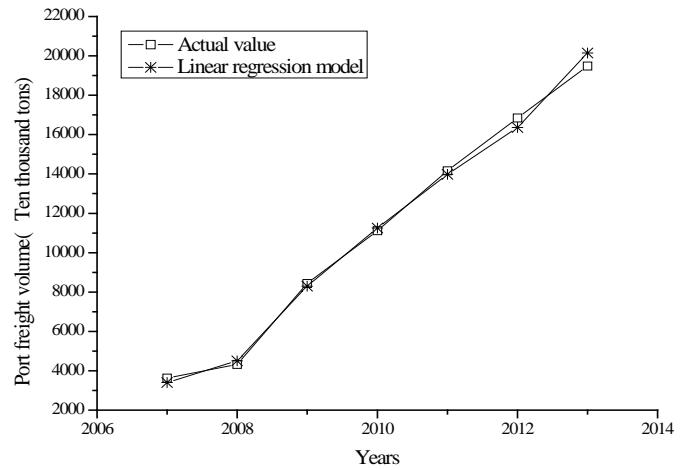


Fig. 6. The fitting of linear regression model to training set

Tab. 2. Comparison of individual models

Years	Actual value	Predictive value					
		Regression sequence	Error rate	BP model	Error rate	PCA-GA-SVM	Error rate
2014	24222	23996.94	0.00925	22791.85	0.06558	24311	0.00368
2015	24520	24520	$0.85 \cdot 10^{-5}$	24272.98	0.01098	24520	0

It can be seen from Table 2 that the error rate of the PCA-GA-SVM prediction model is the smallest, which is mainly controlled within 0.5 %. Its prediction accuracy is good. According to the results of the BP neural network model, the error rate is about 5 %. The degree of prediction is worse in the prediction model. The prediction accuracy of the PCA-GA-SVM model is good, which shows that this method has certain promotion value.

The PCA-GA-SVM model is used to forecast the port cargo volume of Shenzhen in the next three years. When making predictions, the value of the independent variables of the logistics demand in the next three years should be obtained first. By using the GM model, the influencing factors of the port freight volume demand for 2019–2011 are predicted. The PCA-GA-SVM model is used to predict the freight volume of Shenzhen port. The logistics demand in Shenzhen in 2019–2011 is:

Tab. 3. Logistics demand in Shenzhen from 2019 to 2011

2019	2010	2011
34857	41648	45149

As can be seen from Table 3, the port cargo volume of Shenzhen in 2019–2011 is increasing year by year. To meet the growing demand for logistics, logistics supply capacity must be accelerated, and the transportation system improved. Logistics resources are rationally allocated, and the logistics economy is coordinated.

CONCLUSION

Based on the basic theory of port logistics demand, the relationship between port logistics demand and economic hinterland is analysed. Combined with relevant literature research and data review, the quantitative analysis index system of port logistics demand was established. Based on the comparative study of port logistics demand analysis methods, a combination of qualitative and quantitative analysis methods was established. A predictive analysis model combining support vector machine and principal component analysis is proposed. The intrinsic drive between the development of port logistics and the hinterland economy was analysed. The factors of port logistics demand were analysed. According to the principle of effectiveness, relative independence, operability and strong correlation, the index set of port logistics demand analysis is established. Through the grey correlation analysis method, a specific index set suitable for Shenzhen port logistics demand analysis is selected. Analytical methods at home and abroad are studied and compared. Based on the advantages of principal component analysis and support vector machine (SVM), the PCA-SVM model is constructed as the forecast model of the port logistics demand scale, and an empirical analysis is carried out.

Changes in port logistics demand are closely related to the development of the economic hinterland. When conducting research and analysis, in addition to relying on historical data on port logistics demand, the link between the economic hinterland and the port should be combined to establish a scientific and rational quantitative indicator set. According to the characteristics of port logistics demand, the forecasting method is selected.

REFERENCES

1. Y. K. Lin, C. T. Yeh, and C. F. Huang, *A simple algorithm to evaluate supply-chain reliability for brittle commodity logistics under production and delivery constraints*, *Annals of Operations Research*, Vol. 244, No. 1, pp. 67–83, 2016.
2. C. Fresno, G. A. González, G. A. Merino, A. G. Flesia, O. L. Podhajcer, and A. S. Llera, *A novel non-parametric method for uncertainty evaluation of correlation-based molecular signatures: its application on pam50 algorithm*, *Bioinformatics*, Vol. 33, No. 5, pp. 693, 2017.
3. J. L. Hope, A. E. Sinha, B. J. Prazen, and R. E. Synovec, *Evaluation of the dotmap algorithm for locating analytes of interest based on mass spectral similarity in data collected using comprehensive two-dimensional gas chromatography coupled with time-of-flight mass spectrometry*, *Journal of Chromatography A*, Vol. 1086, No. 1, pp. 185–192, 2016.
4. J. Wu, J. Chu, Q. Zhu, P. Yin, and L. Liang, *Dea cross-efficiency evaluation based on satisfaction degree: an application to technology selection*, *International Journal of Production Research*, Vol. 54, No. 20, pp. 1–18, 2016.
5. X. Qi, G. Wu, K. Boriboonsomsin, and M. J. Barth, *Development and evaluation of an evolutionary algorithm-based online energy management system for plug-in hybrid electric vehicles*, *IEEE Transactions on Intelligent Transportation Systems*, Vol. 99, pp. 1–11, 2016.
6. M. W. Li, J. Geng, W. C. Hong, and Z. Y. Chen, *A novel approach based on the Gauss-vSVR with a new hybrid evolutionary algorithm and input vector decision method for port throughput forecasting* *Neural Computing and Applications*, Vol. 28, No. 1, pp. 621–640, 2017.
7. Y. C. Yang, and S. L. Chen, *Determinants of global logistics hub ports: Comparison of the port development policies of Taiwan, Korea, and Japan*, *Transport Policy*, Vol. 45, pp. 179–189, 2016.
8. J. Foraker, S. Lee, and E. Polak, *Validation of a strategy for harbor defense based on the use of a min-max algorithm receding horizon control law*, *Naval Research Logistics*, Vol. 63, No. 3, pp. 247–259, 2016.
9. J. Piao, S. Xu, Z. Wu, Y. Li, B. Qu, and X. Duan, *Su-f-t-619: dose evaluation of specific patient plans based on monte carlo algorithm for a cyberknife stereotactic radiosurgery system*, *Medical Physics*, Vol. 43, No. 6, pp. 3606–3606, 2016.
10. S. Y. Kim, H. Park, H. M. Koo, and D. K. Ryoo, *The Effects of the Port Logistics Industry on Port Citys Economy*, *Journal of Navigation and Port Research*, Vol. 39, No. 3, pp. 267–275, 2015.
11. J. Feng Jie, X. J. Liu Xiaojun, *Design of Upright Intelligent Vehicle Based on Camera*, *Acta Electronica Malaysia*, Vol. 1, No. 1, pp. 09–11, 2017.
12. M. S. Ibrahim, S. Kasim, R. Hassan, H. Mahdin, A. A. Ramli, M. F. Md Fudzee, and M. A. Salamat, *Information Technology Club Management System*, *Acta Electronica Malaysia*, Vol. 2, No. 2, pp. 01–05, 2018.
13. Z. G. He, X. N. Gu, X. Y. Sun, J. Liu, and B. S. Wang, *An efficient pseudo-potential multiphase lattice Boltzmann simulation model for three-dimensional multiphase flows*, *Acta Mechanica Malaysia*, Vol. 1, No. 1, pp. 08–10, 2017.
14. M. Elmnifi, M. Amhamed, N. Abdelwanis, and O. Imrayed, *Solar Supported Steam Production For Power Generation In Libya*, *Acta Mechanica Malaysia*, Vol. 2, No. 2, pp. 05–09, 2018.

CONTACT WITH THE AUTHOR

Bianjiang Hu

School Of Business
Central South University
Changsha, Hunan 410083
CHINA

SIMULATION MODEL AND STATE ANALYSIS OF SHIP TRANSMISSION LINE

Yanzhe Hu¹⁾

Mengjie Xu²⁾

Yang Li¹⁾

¹⁾ Institute of Water Resources and Hydro-electric Engineering, Xi'an University of Technology
& Shaanxi Electric Power Design Institute Co. Ltd., China

²⁾ State Grid Shaanxi Economic Research Institute, China

ABSTRACT

In order to discuss the simulation model of the ship transmission line and the state of the transmission line, an early fault model is built according to the evolution principle of the short circuit fault of the transmission line and combining with the fault characteristics of the early fault. A small distributed ship transmission line system is built in MATLAB/Simulink. Then, combined with the constructed fault module, the original short circuit module, and the load module, the various states (normal state, early fault state, severe early fault state, short circuit state) of the ship transmission line are stimulated, and the features of voltage signal in each state is analysed. It is concluded that, due to the normal operation of the ship transmission line system, the variation characteristics of the flow signal and voltage signal caused by the sudden load mutation, that is, the sudden load and the sudden increase load, are very similar to the changes caused by the early fault. Therefore, in order to find a more accurate early fault detection method, the state is divided into normal state, sudden load state, sudden increase and sudden decrease load state.

Keywords: ship power, transmission line, simulation model, insulation deterioration

INTRODUCTION

Based on a study, early failure of ship transmission line is an early manifestation of deterioration of insulation layer [1]. Because the line has an unavoidable defect in its own material, manufacturing technology, and laying process, it is affected by the environmental factors such as power supply pressure, oil mist, water vapour and temperature on the line insulation layer or line junction, resulting in the gradual aging of the insulating layer and the appearance of the local arc. As the environment of the ship is relatively humid and there is more oil pollution, it is easier to generate

the eliminating arc, causing current leakage, partial discharge and other phenomena [2]. According to research, early failures usually occur near the peak of the voltage waveform and stop at the first zero crossing point of the current waveform [3]. And after the first early failure, this early fault event will occur repeatedly. With the further deterioration of the insulation layer of the transmission line, the early fault will gradually deteriorate to the serious early fault, and the serious early fault will appear repeatedly. Then the insulation fails, and the short-circuit fault is easily generated. According to a scholar, early fault is the early embodiment of short circuit fault, and early fault identification to early fault monitoring data is

important information for the realization of the short circuit prediction of the ship transmission line [4].

The early fault of the ship transmission line is very similar to the intermittent arc fault. Its early fault resistance is a nonlinear time-varying resistance. The nonlinear and time-varying characteristics of the intermittent arc can well simulate its early fault. Shariatzadeh built an arc model through the study of the principle of the energy balance of the arc column. The model is used to simulate the early fault of the transmission line [5], and the simulation signal fits the actual situation. This model constructed is applied to simulate the early fault of the ship transmission line.

STATE OF THE ART

Compared with the early fault detection methods on the shore transmission lines, the main related research at home and abroad is focused on the diagnosis, identification and positioning after the line fault, among which the detection of the early fault of the ship transmission line is less. In the study of early fault in China, the usual method is the analysis based on waveform rather than vector, and the detection of the voltage and current characteristics in time domain and voltage and current characteristics in frequency domain. For the early fault detection, a scholar monitored the early faults of the long time series from two aspects of time domain and frequency and analysed the content of the harmonic in the frequency range. In the time domain, the amplitude transformation of the voltage and current and the duration of each barrier were detected mainly [6].

In the field of early fault detection, the characteristics of signal time and frequency, neutral point current signal and its change characteristics are studied and analysed, and the characteristics of transient overcurrent are detected. Some methods have been applied to relay, and the protection of feeder is improved. A scholar took the two-level distribution network as the test object, used the wavelet transform to analyse the time frequency state of the voltage and current in the time domain and frequency domain, and analysed the feasibility of the detection of the arc fault in the underground line [7]. A previous scholar proposed to use the consistency of superposition current and the neutral point current before and after using the monitoring fault. In this way, the initial phase and duration of the fault can be detected, and the warning or trip signal can be set accordingly [8]. Using the detection method based on neutral line current and neutral line current change rate, the transient fault and the judgment fault of the line with self-recovery are detected. As a result, it can distinguish normal system conversion or other system faults, such as fast fuse operation. Other scholar also put forward a detection method for the fault of the line joint. By detecting the transient overcurrent, recording the times and frequency of the fault, the alarm or the trip is carried out [9].

Model-based fault prediction techniques normally require that special analytical mathematical models for describing systems (or devices) and their physical models of faults are

known. And this kind of technology is used for grasping the evolutionary process of the state model of the predicted system (or equipment and components), predicting system (or equipment and components) failure state or evaluating residual life and damage degree of equipment and components. The grey model includes GM (1, 1) model, grey Verhulst model and MGM (1, m) model, among which the most commonly used models in power system fault prediction are GM (1, 1) model. A scholar used comprehensive probability theory, grey system theory and fuzzy mathematics to apply the component life samples or test data of known probability distribution law. In order to predict the reliability series with unknown distribution rules, the development of the small sample system with unknown rules was completed [10]. Grey prediction has the advantages of small sample and few data modelling, which is suitable for fault prediction of power system or electric power equipment with few historical data and lack of information. Study showed an improved non-equal interval grey prediction method for transformer in view of non-equal interval characteristics in test transformer time. The main idea is to improve the original model by using the Lagrange interpolation method to reconstruct the background value to construct the equal-interval series. The accumulative generating series of grey model was assumed, and the reduction method of GM (1, 1) model was modified, and achieved good results [11]. A scholar, from the actual situation of electrical insulation, put forward constructing a new sequence by the original data sequence according to its own law, and then replaced by GM (1, 1) model. The experiment proved that this could effectively improve the prediction precision [12]. In practical application, the application of GM (1, 1) model only considers the characteristic behaviour or makes characteristic behaviour independent of each other, but it lacks the comprehensive consideration of characteristic behaviour [13]. Therefore, in order to realize the tracking of multiple characteristic parameters of the system, the precision that is difficult to be realized by using multiple GM (1, 1) models is achieved. A multivariable grey prediction model MGM (1, m) model is needed [14].

To sum up, the above research work is mainly focused on the early fault diagnosis technology of the power system and the model-based fault prediction technology. However, there are few researches on the simulation model of the ship transmission line and the analysis of the status of the transmission line [15]. Therefore, based on the above research status, an early fault model is built based on the evolution principle of the short-circuit fault of the transmission line and combined with the fault characteristics of the early fault [16]. In addition, the various states of the ship transmission line are simulated and analysed combined with the early fault module, the original short circuit module and the load module [17, 18].

METHODOLOGY

EVOLUTION MECHANISM OF SHORT CIRCUIT FAULT OF SHIP TRANSMISSION LINE

The short-circuit fault of ship transmission line is mainly caused by the deterioration of insulation layer. The insulating layer of a ship transmission line is usually made of rubber type materials. Because the physical and mechanical properties of the vulcanized rubber will change with the oxidative decomposition of the rubber, it becomes harder and more brittle. In this way, many cracks will occur on the rubber, and the entry of air and water will make the deterioration of insulation layer faster. Due to the decrease of insulation capacity, the partial discharge arc and flashover arc will cause the insulation layer deteriorating further, resulting in insulation breakdown and entering short circuit fault prone period. According to the different deterioration of the ship transmission line and better analysis of the evolution process of the short circuit fault, the operating status of ship transmission line can be divided into four periods: the safety period, the partial discharge prone period, the early fault prone period, and the short circuit fault prone period. Among them, the early fault is the early embodiment of the short circuit fault, and it is due to the deterioration of the insulating layer to a certain extent.

From Figure 1, it can be seen that the resistance value of the insulation will slow down with the increase of the use time of the line. At this time, the condition of the insulating layer is further deteriorated, and the running state of the line changes from the safe state to the sub-health state. At this time, it is prone to have the condition of the partial discharge. With the occurrence of local discharge, the insulation layer will continue to deteriorate, resulting in early failure. When the value of insulation resistance is decreasing, the early failure will continue to occur. Eventually, it will enter short circuit fault prone period.

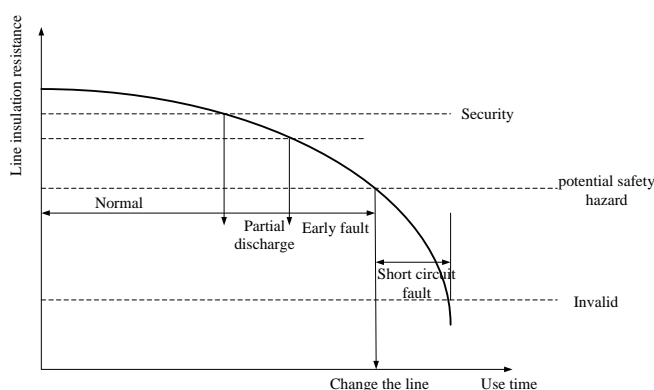


Fig. 1. Sketch map of the evolution of the short circuit fault of the ship transmission line

OCCURRENCE AND CHARACTERISTICS OF THE EARLY FAULT OF THE SHIP TRANSMISSION LINE

There are unavoidable defects in the material, manufacturing technology and laying process of the ship transmission line. It is influenced by external environmental factors in the line insulating layer or line junction, such as power supply pressure, oil mist, water vapour, and temperature. As a result, it is extremely easy to have water branches or partial discharge, and this situation will be further developed. Thus, the electrical branches are eventually generated, resulting in insulation breakdown and short circuit faults. According to the above analysis, the relationship between deterioration factors and deterioration modes of transmission lines is shown in Figure 2.

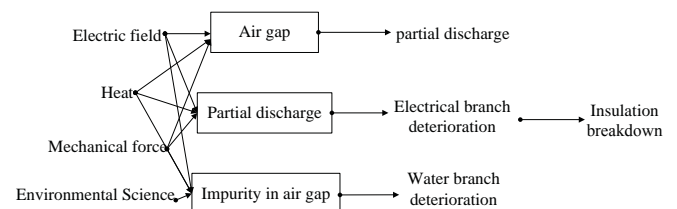


Fig. 2. The relationship between deterioration factors and deterioration modes of transmission lines

The early fault of the ship transmission line is an early manifestation of the insulation deterioration process, which usually accompanied by the generation of the arc. Due to the change of the fault resistance, the magnitude of the instantaneous current becomes a variable in a period of time, and the continuous process of the occurrence of the early fault is random. As a result, it may occur several times in a few seconds, or it may not happen again for a long time and maintains at normal level. If the traditional current protection device is used to detect the change of the early fault current, even if the threshold is set low enough, it is still unable to carry out effective detection. The main reason is that the state of the current mutation is various, the randomness is too strong, and the duration of the single early barrier is very short. Therefore, this failure may not be solved for a long time. Transmission lines will be "ill" (sub-health) running for several days, months or even years, eventually causing a short circuit fault.

In the early fault of the transmission line, the early fault of single-phase grounding is the most frequent, and most of the early fault of the interphase grounding is caused by the early fault of the single-phase grounding. Therefore, the early fault of the single-phase grounding is studied. According to the difference of the number of cycles, typical early failures can be divided into two types: one is the half cycle wave early fault, and the other is the multi periodic wave early fault. The arc is produced during the early fault of the transmission line, in which the arc of the half cycle fault is usually produced at the peak of the voltage. At the beginning of the fault, the phase current of the fault phase rises instantaneously. On the contrary, the phase voltage of the fault phase drops instantaneously, and the duration is 1/4 of the period. When

the current passes through the zero point, the early fault ends, the arc will also disappear automatically, and the current and voltage will return to normal.

ANALYSIS OF ARC MATHEMATICAL MODEL

Intermittent arc fault model is an essential condition for effective early failure analysis of ship transmission lines. Moravej discussed a series of arc models. Through theoretical analysis and practical verification, it is widely recognized that the arc has the nonlinear and time-varying characteristics, and it has high frequency components, and the arc voltage waveform is similar to a square wave. The realization of the arc model built in Cano is simple and capable of showing the nonlinear and time-varying characteristics of the arc very well, and it is applied to the arc fault analysis. Therefore, this model is used for subsequent analysis. The arc model is built based on the energy balance principle of arc column, and Formula (1) is the conductance differential expression.

$$\frac{dg}{dt} = \frac{1}{\tau}(G - g) \quad (1)$$

In Formula (1), τ represents the time constant of arc; g indicates the instantaneous electric arc conductance; G suggests fixed arc conductance.

Formula (1) is a generalized arc equation, which is suitable for representing arcs between terminals of a circuit. In the resonant grounding system, the variation of the parameters of the small current arc depends on the arc length, that is, the arc elongation. The definition of arc extension is shown as follows:

$$elongspd = \frac{dl_{arc}}{dt} = \frac{7I_0}{\frac{0.2}{v_{th}} + 0.2} \quad (2)$$

In Formula (2), v_{th} refers to transient initial voltage transient value; v_{max} is the maximum of normal voltage; I_0 indicates the initial length of the arc, which can be obtained by measuring.

The arc length is defined as a time function before simulation. The arc time constant is defined as:

$$\tau = \tau_0 \left(\frac{I_{arc}}{I_0} \right)^a \quad (3)$$

In Formula (3), τ_0 suggests the initial time constant; I_0 denotes the arc initial length; a indicates the negative coefficient, which generally takes -4.

RESULTS AND DISCUSSION

ESTABLISHMENT AND SIMULATION OF EARLY FAULT RESISTANCE MODULE

Because the early fault of the transmission line is usually accompanied by the appearance of the arc, the fault resistance size has the nonlinear time-varying characteristics. In the single-phase early failure, the core conductor of the transmission line is constructed by a time-varying resistance and a fixed resistance grounding. As shown in Figure 1, the arc resistance r_{arc} in the module is jointly determined by the initial arc length l_0 , the arc stretching rate $elongspd$, and the time constant τ_0 three parameters. It is combined with a fixed resistor r to form an early fault resistance. The effect of initial time constant τ_0 , initial arc length l_0 , arc extension $elongspd$ and fixed resistance r value change on early fault module is simulated and analysed for the simple power system model based on early access fault module. According to Formula (2), the arc extension rate $elongspd$ is jointly determined by the ratio of the transient initial voltage instantaneous value to the normal voltage peak value and the initial arc length l_0 . The simulation results can be obtained by setting the fault phase as A phase and altering the value of τ_0 , l_0 , $\cos\beta$, and series connected fixed resistance r .

When the initial time constant τ_0 is changed, $r=0.1$ is taken. When the parameters are set $l_0=0.1m$, and $\cos\beta=1$, that is, when $elongspd=1.75m/ms$, τ_0 changes between 0.01ms-1ms, and 10 sets of sample data are obtained. The fault phase current transient peak I_{max} and its increment ΔI_{max} are compared. It is seen from Table 1 that, with the increase of τ_0 , the peak I_{max} of fault current and its increment ΔI_{max} gradually decrease, but the decline rate of the peak value of fault current is 13.1% and the decrease rate of its increment ΔI_{max} is 32.9%, which shows that the impact of the peak current peak and its increase is small.

Tab. 1. Sample parameters changed by the initial time constant τ_0

Parameter	1	2	3	4	5	6	7	8	9	10
τ_0	0.01	0.02	0.05	0.1	0.2	0.4	0.6	0.8	0.9	1.0
I_{max}	47.98	47.95	47.75	47.55	46.68	45.99	44.56	42.89	42.11	41.74
ΔI_{max}	19.09	19.05	18.85	18.65	17.78	17.10	15.66	13.21	13.21	12.84

When the initial length l_0 of the arc is changed, $r=0.1$ is taken. When the parameters are set $\tau_0=0.1ms$, $\cos\beta=1$, l_0 is changed between 0.01ms-1ms. Formula (2) shows that $elongspd$ is changed between 0.175/ms-17.5m/ms, and 10 sets of sample data are obtained. The fault current transient peak I_{max} and its increment ΔI_{max} are compared. From Table 2, it is seen that, with the increase of l_0 , the peak value of the fault current and its increment gradually decrease, and the rate of change decreases with the increase of l_0 . The peak decrease rate of the fault current is I_{max} 45.6% and the decrease rate of its increment ΔI_{max} is 99.5%. It can be seen that the initial arc length has a great influence on the fault current peak and its increase, which has a decisive effect on it.

Tab. 2. Sample parameters changed by initial arc length l_0

Parameter	1	2	3	4	5	6	7	8	9	10
l_0	0.01	0.02	0.05	0.1	0.2	0.3	0.4	0.6	0.8	1.0
I_{max}	56.47	55.49	52.33	47.55	41.38	38.02	35.98	33.39	31.22	29.05
ΔI_{max}	27.55	26.59	23.43	18.65	12.48	9.11	7.11	4.49	2.32	0.15

When the arc extension rate $elongspd$ is changed, $r=0.1$ is taken and when the parameters are set $\tau_0=0.1ms$, $l_0=0.1m$, $cos\beta$ is changed between 0.01-1. Formula (2) shows that $elongspd$ is changed between 3.465/ms-1.75m/ms, and 10 sets of sample data are obtained. The fault current transient peak I_{max} and its increment ΔI_{max} are compared. From Table 3, it is seen that, with the increase of $elongspd$, the peak value of fault current and its increment gradually increase. The peak decrease rate of the fault current is I_{max} 3.56% and the decrease rate of its increment ΔI_{max} is 8.85%. The influence of the arc extension on the fault current peak and its increase is small.

Tab. 3. Sample parameters changed by arc extension rate $elongspd$

Parameter	1	2	3	4	5	6	7	8	9	10
$cos\beta$	0.01	0.02	0.05	0.1	0.2	0.3	0.4	0.6	0.8	1.0
$elongspd$	3.455	3.432	3.332	3.183	2.912	2.693	2.498	2.189	1.945	1.652
I_{max}	46.49	46.49	46.59	46.92	46.92	47.17	47.36	47.73	47.99	48.09
ΔI_{max}	17.59	17.58	17.69	18.03	18.02	18.27	18.27	18.83	19.08	19.21

When the fixed resistance r in the early fault module is changed, when the parameters are set $\tau_0=0.1ms$, $l_0=0.1m$, $cos\beta=1$, and $elongspd=1.750m/ms$, r is changed between 0.01-500, and 10 sets of sample data are obtained. The fault current transient peak I_{max} and its increment ΔI_{max} are compared. Table 4 shows that with the increase of l_0 , the peak value of fault current and its increase gradually decrease, and the rate of change gradually decreases. The change rate of r is larger between 0.01-50, and the change rate is almost zero when $r>100$. The peak decrease rate of the fault current is I_{max} 39.4% and the decrease rate of its increment ΔI_{max} is 99.9%. It can be seen that the fixed resistance in the early fault module has a great influence on the peak value of the fault current and the increment of the fault current, and it has a decisive effect on it.

Tab. 4. Sample parameters changed by the fixed resistor r in the early fault module

Parameter	1	2	3	4	5	6	7	8	9	10
r	0.01	0.1	0.5	1	5	10	20	50	100	200
I_{max}	47.78	47.55	46.75	45.85	41.08	38.08	35.11	31.78	30.32	29.30
ΔI_{max}	8.84	8.55	17.23	16.88	12.18	9.24	6.21	2.98	1.43	0.48

SIMULATION MODEL OF SHIP TRANSMISSION LINE STATE

At present, the dry-feed hybrid transmission network is basically used in ship power system. This power supply mode is a combination of trunk and feeder. The power grid is equipped with a number of pivot longitudinal connections to supply power to some sections of distribution boards or sub boards, and then the power distribution boards are supplied to the load. Therefore, MATLAB/Simulink is used to build

a simulation model of the state of a ship transmission line based on the hybrid transmission network structure, as shown in Figure 3, which consists of the power supply system, the transmission system, and the load. The transmission system includes dry-feed distribution board, current and voltage data monitoring, load mutation module, early fault module, and short circuit fault module.

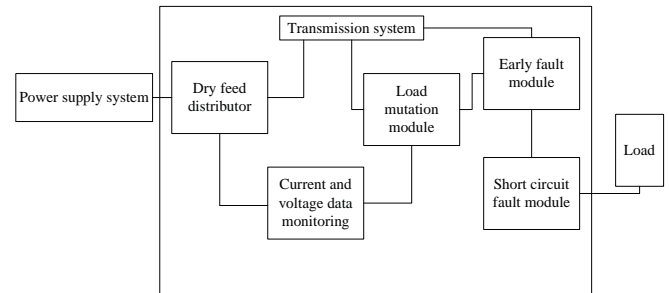


Fig. 3. Simulation model of ship power system

ANALYSIS OF THE STATE OF THE SHIP TRANSMISSION LINE

In the simulation experiment, the state of the transmission line system includes normal state, normal suddenly added load state, normal sudden increase and sudden decrease load state, mild early failure state, severe early fault state, and short circuit fault state. In the ship transmission system, the single-phase early fault and the single-phase short circuit fault are most common, and the phase-phase early fault is also derived from the single-phase early fault. Then, the single-phase state of the system is analysed one by one (in Figure 4~ Figure 6, the transverse coordinate is time, the ordinate is the amplitude, and the starting point of the state mutation is 0.065 seconds):

Normal state: the normal operation state of the system without normal sudden increase load or normal sudden decrease load, and no sudden change of voltage waveform.

Normal sudden increase load: the state of the sudden increase load in the normal operation of the system. The voltage waveform is the dotted line as shown in Figure 4. The voltage decreases quickly at the sudden increase load and then quickly recovers to the original state.

Normal sudden increase and decrease load state: the state of a sudden increase and decrease load in the normal operation of the system. The voltage waveform is the solid line shown in Figure 4. The voltage decreases quickly at the sudden increase load and then quickly recovers to the original state. The load is withdrawn immediately after the 1/4 cycle, the voltage slightly and slowly increases and then decreases, and returns to normal after about 1/2 cycle.

CONCLUSION

Based on the early fault mechanism of the ship transmission line and its mathematical model, the early fault module of the line is built, and the characteristics of the electric arc resistance module are simulated and analyzed. The influence of the change of the different initial parameters on the early fault is studied, and then a simple dry-feed distribution system of the ship transmission line is built. Moreover, the system, early fault module, and short circuit fault module are used to simulate the operation states of the transmission line. Finally, the states are compared and analyzed, and the characteristics of each operation and the differences between them are summarized.

REFERENCES

1. G. F. Lauss, M. O. Faruque, K. Schoder, C. Dufour, A. Viehweider, and J. Langston, "Characteristics and design of power hardware-in-the-loop simulations for electrical power systems," *IEEE Transactions on Industrial Electronics*, Vol. 63, No. 1, pp. 406-417, 2016.
2. H. Park, J. Sun, S. Pekarek, P. Stone, D. Opila, R. Meyer, and R. DeCarlo, "Real-time model predictive control for shipboard power management using the IPA-SQP approach," *IEEE Transactions on Control Systems Technology*, Vol. 23, No. 6, pp. 2129-2143, 2015.
3. S. Y. Kim, S. Choe, S. Ko, and S. K. Sul, "A Naval Integrated Power System with a Battery Energy Storage System: Fuel efficiency, reliability, and quality of power," *IEEE electrification magazine*, Vol. 3, No. 2, pp. 22-33, 2015.
4. A. P. N. Tahim, D. J. Pagano, E. Lenz, and V. Stramosk, "Modeling and stability analysis of islanded DC microgrids under droop control," *IEEE Transactions on Power Electronics*, Vol. 30, No. 8, pp. 4597-4607, 2015.
5. F. Shariatzadeh, C. B. Vellaithurai, S. S. Biswas, R. Zamora, and A. K. Srivastava, "Real-time implementation of intelligent reconfiguration algorithm for microgrid," *IEEE Transactions on sustainable energy*, Vol. 5, No. 2, pp. 598-607, 2014.
6. N. C. Coops, F. M. A. Fontana, G. K. A. Harvey, T. A. Nelson, and M. A. Wulder, "Monitoring of a national-scale indirect indicator of biodiversity using a long time-series of remotely sensed imagery," *Canadian Journal of Remote Sensing*, Vol. 40, No. 3, pp. 179-191, 2014.
7. J. Ma, W. Ma, D. Xu, Y. Qiu, and Z. Wang, "A power restoration strategy for the distribution network based on the weighted ideal point method," *International Journal of Electrical Power & Energy Systems*, Vol. 63, No. 2, pp. 1030-1038, 2014.

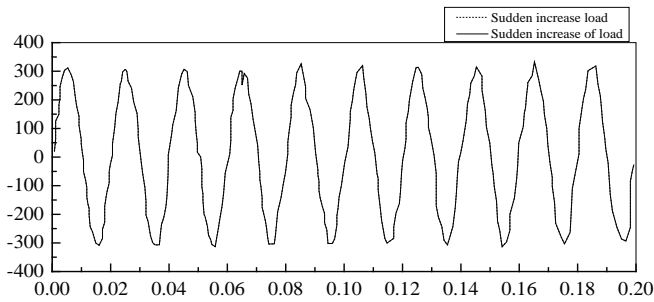


Fig. 4. Normal sudden increase and normal sudden increase and decrease load state diagram

Mild early fault state and severe early fault state: the operation state of the early fault of the system. According to the deterioration of the insulation layer, the size of the arc current is differentiated, which is realized by changing the early fault module. The comparison of the state waveform is shown in Figure 5. In the initial stage of the half-period wave early fault, the voltage drops rapidly. With the gradual decrease of the arc current, the voltage is slowly restored, and maintained at the 1/4 cycle. The normal state value will be restored at the zero point of the voltage wave. The difference between mild early fault state and severe early fault state is that the sudden decrease of severe early fault state is greater than that of mild early fault state.

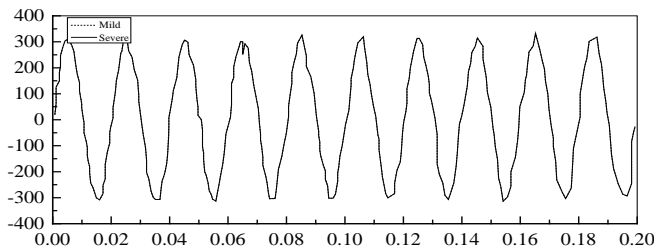


Fig. 5. Voltage comparison diagram for mild early failure and severe early failure

Short circuit fault state: the operating state of a system with short circuit faults. The contrast diagram of the state waveform of the severe early and short circuit faults is shown in Figure 6. The voltage mutation is zero after the short circuit fault occurs.

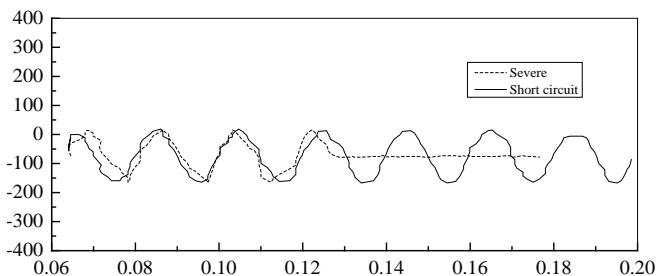


Fig. 6. Comparison of severe early fault and short-circuit fault state waveform

8. S. Z. Jamali, M. O. Khan, S. B. A. Bukhari, M. Mehdi, G. H. Gwon, and C. H. Noh, "Short-circuit fault protection of a low voltage dc distribution system using superimposed current components," *Journal of the Korean Institute of Illuminating & Electrical Installation Engineers*, Vol. 31, No. 10, pp. 86-94, 2017.
9. Y. Wang, G. Xu, L. Lin, and K. Jiang, "Detection of weak transient signals based on wavelet packet transform and manifold learning for rolling element bearing fault diagnosis," *Mechanical Systems & Signal Processing*, 54-55, 259-276, 2015.
10. H. Li, K. Dong H. Jiang, R. Sun, X. Guo, and Y. Fan, "Risk assessment of china's overseas oil refining investment using a fuzzy-grey comprehensive evaluation method," *Sustainability*, Vol. 9, No. 5, pp. 696-713, 2017.
11. M. D. Francesco, S. Fagioli, M.D. Rosini, and G. Russo, "Deterministic particle approximation of the Hughes model in one space dimension," *Kinetic & Related Models*, Vol. 10, No. 1, pp. 215-237, 2016.
12. N. Hozumi, K. Frusawa, H. Ooba, and F. Aono, "The actual situation and problem of a diagnosis, the evaluation technique in an insulation electric wire, the cable for the supply of electric power," *Ieej Transactions on Power & Energy*, Vol. 137, No. 5, pp. 339-343, 2017.
13. J. Feng Jie, X. J. Liu Xiaojun, "Design of Upright Intelligent Vehicle Based on Camera," *Acta Electronica Malaysia*, Vol. 1, No. 1, pp. 09-11, 2017.
14. Z. C. Yu, "An Improved Infrared and Visible Image Fusion Algorithm Based on Curvelet Transform," *Acta Electronica Malaysia*, Vol. 1, No. 1, pp. 12-14, 2017.
15. Z. G. He, X. N. Gu, X. Y. Sun, J. Liu, and B. S. Wang, "An efficient pseudo-potential multiphase lattice Boltzmann simulation model for three-dimensional multiphase flows," *Acta Mechanica Malaysia*, Vol. 1, No. 1, pp. 08-10, 2017.
16. X. Luo, "Research on Anti-Overturning Performance of Multi-Span Curved Girder Bridge with Small Radius," *Acta Mechanica Malaysia*, Vol. 1, No. 1, pp. 11-15.
17. F. De'nan, N. Naa'im, and C. L. Lai, "Behaviour of flush end-plate connection for perforated section," *Engineering Heritage Journal*, Vol. 1, No. 1, pp. 11-20, 2017.
18. N. S. Abdul Sukor, and A. F. Mohd Sadullah, "Addressing the road safety results impasse through an outcome-based approach in the state of Penang, Malaysia," *Engineering Heritage Journal*, Vol. 1, No. 1, pp. 21-24, 2017.

CONTACT WITH THE AUTHORS

Yanzhe Hu

Institute of Water Resources and Hydro-electric
Engineering
Xi'an University of Technology & Shaanxi Electric Power
Design Institute Co. Ltd.
Xi'an710048
CHINA

Mengjie Xu

State Grid Shaanxi Economic Research Institute
Xi'an710065
CHINA

Yang Li

Institute of Water Resources and Hydro-electric
Engineering
Xi'an University of Technology & Shaanxi Electric Power
Design Institute Co. Ltd.
Xi'an710048
CHINA

STUDY OF THE FORCE AND DEFORMATION CHARACTERISTICS OF SUBSEA MUDMAT-PILE HYBRID FOUNDATIONS

Desen Kong^{1,2}

Meixu Deng^{1,2}

Yi Liu^{1,2}

Xiaoyan Tan³

¹ College of Civil Engineering and Architecture, Shandong University of Science and Technology, China

² Shandong Provincial Key Laboratory of Civil Engineering Disaster Prevention and Mitigation,
Shandong University of Science and Technology, China

³ Shandong Xingke Intelligent Technology Co., Ltd., China

ABSTRACT

To study the force and deformation characteristics of subsea mudmat-pile hybrid foundations under different combined loads, a project at a water depth of 200 m in the South China Sea was studied. A numerical model of a subsea mudmat-pile hybrid foundation is developed using the numerical simulation software FLAC3D. The settlement of the seabed soil, the bending moments of the mudmat, and the displacements and bending moments along the pile shaft under different load combinations, including vertical load and horizontal load, vertical load and bending moment, and horizontal load and bending moment load, are analyzed. The results indicate that settlement of the seabed soil is reduced by the presence of piles. The settlement of the mudmat is reduced by the presence of piles. Different degrees of inclination occur along the pile shaft. The angle of inclination of pile No. 1 is greater than that of pile No. 2. The dip directions of piles No. 1 and No. 2 are identical under the vertical load and bending moment and are opposite to those under the other combined loads. The piles that are located at the junctions between the mudmat and the tops of the piles are easily destroyed.

Keywords: Subsea Mudmat-pile Hybrid Foundations, force characteristics, deformation characteristics, combined loads

INTRODUCTION

In recent years, traditional fossil energy sources have been increasingly exhausted, and the environment has been deteriorating. Marine resources have made significant progress as a renewable energy source, and the technology for developing marine resources has matured [1-2]. Deepwater resources have been discovered, and offshore oil and gas engineering equipment has progressed from the shallow sea to the deep ocean. The deep ocean has gradually become the main area for the development of global marine resources [3-4]. As a common component in the development of deepwater oil and gas resources, subsea anti-sinking plate foundations

are used as the supporting structures for wellheads, pipe sink nodes, umbilical cord cables and other components of underwater production systems. These foundations bear the load of each block of the underwater production system and transfer it to the foundation. They form the foundation of each block in the underwater production system, and they are rarely subjected to a single load during operations [5-8]. Due to the complex environmental conditions of the seabed, these foundations are usually subjected to two or more loads simultaneously. Because of the limitations of the anti-horizontal load and anti-overturning capabilities of anti-sinking plates, their bearing capacity is low. To overcome the limitations in the application of anti-sinking plates, piles

are added under them to form composite foundations, which bear part of the horizontal load and overturning bending moment to reduce the size of the anti-sinking plate.

Foreign scholars have conducted numerous studies on anti-sinking panels, and several results have been achieved. Yun simplified the seabed as a homogeneous soil and analyzed the bearing capacity envelope lines of three types of anti-sinking plate foundations in the V-H-T load space using a numerical method [9]. Bransby studied the bearing characteristics of a skirt plate of an anti-sinking plate foundation in the V-H-M composite load space by means of numerical calculations [10-11]. However, few domestic studies have focused on subsea anti-sinking plates; in particular, mudmat-pile hybrid foundations have rarely been studied. Based on practical engineering, provide examples of using industry standards to design anti-sinking plate foundations [12-14].

Using the FLAC3D finite difference software, numerical models of subsea mudmat-pile hybrid foundations can be developed to study their force and deformation characteristics under different load combinations. By applying combined loads to the model, such as a vertical load and a horizontal load, a vertical load and a bending moment, and a horizontal load and a bending moment, analyses of the seabed soil settlement, the bending moments of the anti-sinking plate, and the displacements and bending moments along the pile shaft can be performed, which have theoretical significance.

DEVELOPMENT OF THE NUMERICAL MODEL

Taking a 200 m water depth project in the South China Sea as an example, a separation-type mudmat-pile hybrid foundation is simplified as an anti-sinking plate and angle piles. A numerical simulation model of the subsea mudmat-pile is developed using the FLAC3D numerical simulation software, which is also used to determine the constitutive model of the seabed soil, the unit types of the anti-sinking plate model and the pile model, and their various physical and mechanical parameters.

The FLAC3D finite difference equation is as follows:

$$\int_S n_i f ds = \int_A \frac{\partial f}{\partial x_i} dA \quad (1)$$

In Eq (1):

\int_S – The integral around the boundary of the closed surface;

n_i – The unit normal vector of s ;

f – A scalar, vector, or tensor;

x_i – The coordinate vector; ds is the incremental arc length;

\int_A – The integral of the surface area A .

CONSTRUCTION OF THE SOIL BODY MODEL

The soil body model is built as a six-sided block body with a built-in grid. The model is 50 m long, 25 m wide and 20 m deep. The lower left corner of the model is taken as the coordinate origin. Considering the accuracy of the numerical calculations and the size requirements of the grid, the elements of the soil body model are all constructed with 1 m×1 m×1 m positive-cube cells, and the entire model includes 25,000 zones and 27,846 grid points. The three-dimensional numerical calculation model is shown in Fig. 1.

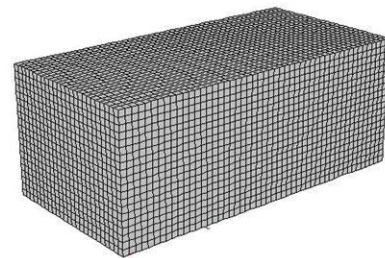


Fig. 1. Model of the seabed soil

Based on the actual conditions of the South China Sea, the seabed soil body is modeled as saturated soft clay. To utilize few parameters and simplify the measurements, the Mohr-Coulomb model is adopted for the seabed soil body model, and the material parameters are listed in Tab. 1. In the model, the boundary parallel to the x axis limits the velocity in the x direction, the boundary parallel to the y axis limits the velocity in the y direction, the bottom boundary limits the velocity in the z direction, and the top boundary is free.

Tab. 1. Material parameters of the seabed soil

bulk modulus /Pa	shear modulus /Pa	cohesion /Pa	internal friction angle /($^{\circ}$)	saturatd density /kg·m ⁻³
4.2×10^7	1.83×10^7	12×10^3	23	2000

DEVELOPMENT OF THE MODEL OF THE MUDMAT-PILE STRUCTURE SYSTEM

In the numerical model, structural units were used to build the mudmat-pile structure model, lining structures were used to build the anti-sinking plate model, pile structures were used to build the pile models, and point to point connections were established between the anti-sinking plate and the piles. The model, size of the anti-sinking plate and pile layout are shown in Fig. 2

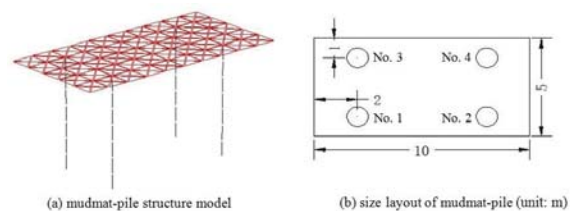


Fig. 2. Model of the mudmat-pile structure

The lining structural unit is shown in Fig. 3. It consists of a flat shell unit with three joints and can resist surface loads and bending loads. Thin plate theory is adopted in the analysis, and the deformation caused by transverse shear is ignored. The mechanical properties of the lining unit can be divided into the response of the lining material itself to the structure and the interaction between the lining and the mesh. The lining unit can consider tangential friction and normal compressive (tensile) action with the rock and soil body, and it can be detached (or embedded) from the rock and soil body. The lining structure unit is mainly used to simulate the structure with normal and tangential forces on the rock and soil body, which can withstand tension in the normal direction and simulate separation between the anti-sinking plate and the seabed soil body. Frictional slip between the anti-sinking plate and the seabed soil in the tangential direction can be simulated [15].

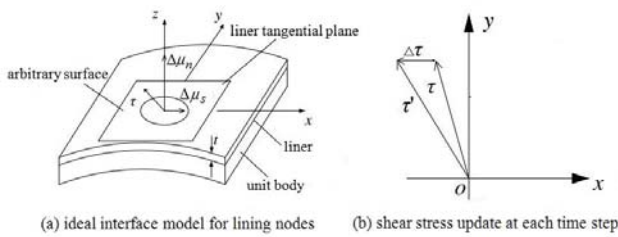


Fig. 3. Diagram of the liner structural element

The apparent stiffness of the unit in the normal direction to the lining surface is:

$$\max \left[\frac{\left(K + \frac{4}{3} G \right)}{\Delta Z_{\min}} \right] \quad (2)$$

In Eq (2):

K and G – The volume modulus and bulk modulus, respectively;

ΔZ_{\min} – The minimum size of the adjacent unit normal to the lining.

As shown in Fig. 4, the pile unit is a two-node slender unit with 6 degrees of freedom at each node and anti-bending and axial anti-tensile (anti-pressure) characteristics. It is composed of a combination of a beam element and a bar element. The interaction between the pile element and the soil grid is realized by nonlinear, sliding tangential and normal coupling springs. The tangential spring can simulate the tangential action of the grouting anchor rod, the normal spring can simulate the extrusion between the pile and the soil, and the force and displacement can be transmitted between the pile and the foundation soil by unit nodes.

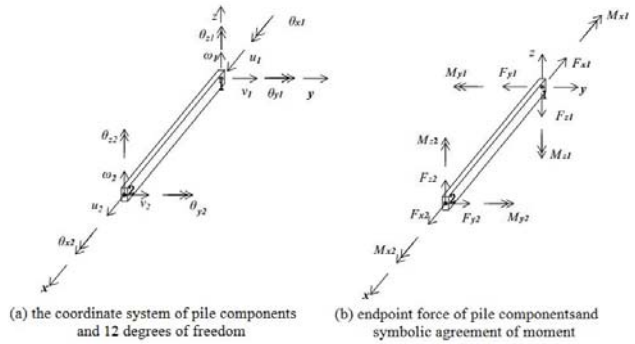


Fig. 4. Diagram of the pile element

The shear characteristics of the model pile and the mesh contact surface are mainly its natural cohesive force and friction force. The characteristics of the tangential coupling spring include the stiffness k_s , cohesion C_s , internal friction angle ϕ_s , and radius of the pile's external boundary. As shown in Fig. 5, the action of the tangential spring around the pile body is reflected by these parameters and the effective stress around the pile body.

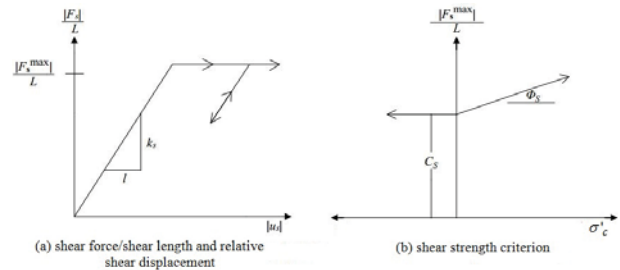


Fig. 5. Shear material behavior of piles

The shear force of a unit length pile [16] is:

$$\frac{F_s}{L} = k_s (u_p - u_m) \quad (3)$$

In Eq (3):

k_s – The shear stiffness of the connecting spring;

u_p – The axial displacement of the pile;

u_m – The axial displacement at the interface between the rock and soil.

The maximum shear force per unit length is:

$$\frac{F_{s\max}}{L} = c_s + \sigma'_c \times \tan \phi_s \times l \quad (4)$$

In Eq (4):

c_s – The bonding strength of the shear coupling spring;

σ'_c – The average effective lateral stress perpendicular to the pile unit;

ϕ_s – The friction angle of the shear coupling spring;

l – The exposed perimeter of the unit.

The average effective lateral limit stress perpendicular to the unit is:

$$\sigma'_c = -\left(\frac{\sigma_n + \sigma_m}{2} + p\right) \quad (5)$$

In Eq (5):

- $\sigma_n = \sigma_x v_1^2 + \sigma_y v_2^2 + 2\sigma_{xy} v_1 v_2$;
- v_i – is the unit vector;
- σ_m – is the stress outside the plane;
- p – is the pore pressure.

As shown in Fig. 6, the characteristic parameters of the normal coupled spring include the stiffness k_n , cohesion C_n , internal friction angle ϕ_n , gap and effective stress. These parameters reflect the normal mechanical action of the pile-soil interface when the pile and soil move in the normal direction. When piles are subjected to horizontal loads, cracks will form between the pile and soil [17]. If the reverse load is applied, the gap must close first before the soil can withstand the force in the opposite direction. If the gap parameter is set to be on, the influence of the gap on the lateral load pile can be considered.

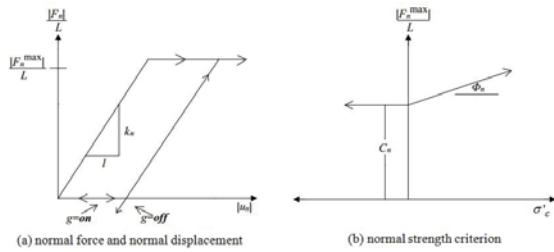


Fig. 6. Normal-direction material behavior of piles

In the model, the anti-sinking plate is 10 m long, 5 m wide and 0.2 m thick. It is simulated by lining structural units, is located in the middle of the soil body model and is in contact with its upper surface. The piles are 4 m long and 0.6 m in diameter [18]. They are simulated by pile units and are located at the four corners of the anti-sinking plate. Each pile foundation consists of 7 pile members. The top nodes of the pile and the mudmat are set as point-to-point connections. The bottom node limits the translational freedom in the three directions, and the pile has rotational freedom [19]. The mudmat-pile model includes 228 structural elements and 48 points, and the structural elements are listed in Tab. 2.

Tab. 2. Parameters of the structural elements

name	pile	mudmat
elastic modulus/GPa	206	206
Poisson's ratio	0.3	0.3
density/kg·m ⁻³	7850	7850
tangential coupling spring stiffness/GPa	13.9	0.8
normal coupling spring stiffness/GPa	1.39	0.8
tangential coupling spring bond strength/kPa	67.4	4000
normal coupling spring bond strength/kPa	67.4	—
tangential coupling spring friction angle/(°)	17.6	20
normal coupling spring friction angle/(°)	0	—

ANALYSIS OF THE NUMERICAL CALCULATION RESULTS

Using the FLAC3D numerical simulation software, a rectangular anti-sinking plate foundation is used to investigate the force and deformation characteristics of the seabed soil, the anti-sinking plate and the pile under three load combinations (vertical load and horizontal load, vertical load and bending moment, and horizontal load and bending moment load). The load conditions are listed in Tab. 3.

Tab. 3. Load conditions of mudmat-piles hybrid foundations

load name	structure self-weight/kN	vertical load/kN	horizontal load/kN	bending moment M_x /kN·m	bending moment M_y /kN·m
numerical value	470	175	345	201	305

CHARACTERISTIC ANALYSIS OF THE COMPOSITE FOUNDATION UNDER A VERTICAL LOAD AND HORIZONTAL LOAD

SETTLEMENT ANALYSIS OF THE SEABED SOIL

The settlement characteristics of the seabed soil are shown in Fig. 7. The normal surface is the section at the corner pile, and the amount of settlement of the soil decreases radially with distance from the anti-sinking plate. The maximum settlement of the soil body is 0.772 mm, and it occurs in the middle of the bottom of the anti-sinking plate [20]. The maximum positive vertical displacement of the soil body is 0.0235 mm, and it occurs at the edge of the long side of the model of the seabed soil body, which indicates that the soil far from the anti-sinking plate is slightly uplifted. As a result of the action of the angular piles, the settlement of the soil body near the piles is significantly less than that far from the piles at the same depth [21]. With increasing distance from the angular piles, their effect decreases gradually, and the settlement of the soil body caused by the piles essentially disappears at a depth of approximately 7 m. The results show that the angular pile influences the settlement of the seabed soil in a region approximately twice the length of the piles.

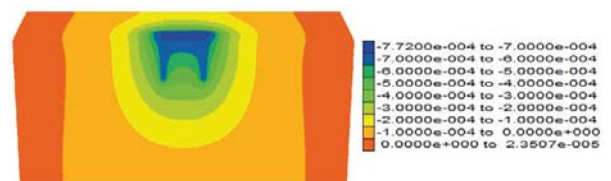


Fig. 7. Settlement of the seabed soil (units: m)

ANALYSIS OF THE BENDING MOMENTS OF THE ANTI-SINKING PLATE

The bending moment of the anti-sinking plate is shown in Fig. 8. The bending moment diagram of the anti-sinking plate is also symmetric about the y axis because of the structural symmetry and because the load is applied on the y axis. Due to the simple structure and load, the bending moment diagram of the anti-sinking plate has a clear pattern.

As shown in Fig. 8(a), the maximum positive bending moment of the anti-sinking plate in the x direction is 4.437 kN-m, and it is located in the middle of the long edge of the anti-sinking plate and has a semicircular distribution. The maximum negative bending moment is 19.401 kN-m and is located at the positions of the corner piles. The maximum bending moment occurs at the locations of the corner piles, which indicates that it is easy to cause damage at these locations; that is, damage to the anti-sinking plate can easily occur at the junctions between the piles and the anti-sinking plate [22]. As shown in Fig. 8(b), the maximum positive bending moment of the anti-sinking plate in the y direction is 1.151 kN-m, and it is located on the long edge of the anti-sinking plate and has an elongated distribution. The maximum negative bending moment is 15.376 kN-m, and it occurs at the positions of piles No. 1 and No. 2. The maximum bending moment of the anti-sinking plate is a negative bending moment that occurs at the junctions between piles No. 1 and No. 2 and the anti-sinking plate. The bending moments at piles No. 3 and No. 4 are negative and are much greater than the maximum positive bending moment, which indicates that damage to the anti-sinking plate can easily occur at the junctions between the anti-sinking plate and the piles; this is consistent with the pattern in the x direction bending moment diagram.

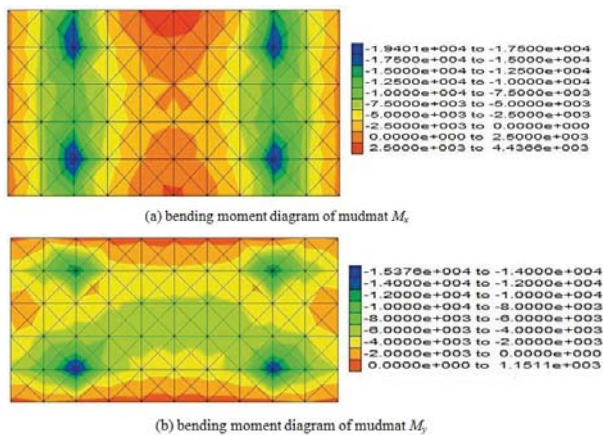


Fig. 8. Bending moments of the mudmat (unit: N-m)

ANALYSIS OF THE DISPLACEMENTS ALONG THE PILE SHAFTS

Four piles are set up in the mudmat-pile hybrid foundation model, which are symmetrical to the xoz surface and the yo z plane. Piles No. 1 and No. 2 are investigated. Eight

displacement monitoring positions were set from the tops of the piles to the bottoms, and 7 shear force, axial force and bending moment monitoring positions were analyzed.

The horizontal displacements of piles No. 1 and No. 2 are shown in Fig. 9. Under the combined action of the vertical and horizontal loads, pile No. 1 moves negatively along the x axis, and pile No. 2 moves forward along the x axis. The top of pile No. 1 moves 0.61×10^{-6} m in the positive direction along the x axis, and the bottom moves 13.11×10^{-6} m in the negative direction. The top of pile No. 2 moves 1.07×10^{-6} m in the negative direction along the x axis, and the bottom moves 9.914×10^{-6} m in the positive direction. The maximum displacement of pile No. 1 is 19.03×10^{-6} m, and that of pile No. 2 is 16.15×10^{-6} m, both of which occur in the middle of the piles. This may be because the pile is held fixed by the anti-sinking plate and the soil at the bottom of the pile, and the soil pressure between the corner piles under the anti-sinking plate is greater than that outside the corner piles. The horizontal displacement lines of piles No. 1 and No. 2 are smooth curves, which indicates that the pile bodies buckle. Piles No. 1 and No. 2 move in the negative horizontal direction. Pile No. 1 leans in the negative direction along the x axis, and pile No. 2 leans in the positive direction. The differences in displacement between the tops and bottoms of the piles are 12.5×10^{-6} m and 8.841×10^{-6} m, respectively, and the inclination angle of pile No. 1 is greater than that of pile No. 2.

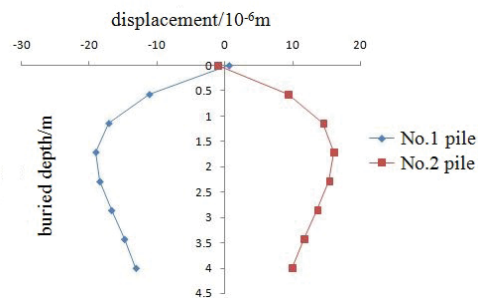


Fig. 9. Horizontal displacements along the pile shafts

The vertical displacements of piles No. 1 and No. 2 are shown in Fig. 10. The pile foundations move downward as a whole due to the combined action of the vertical and horizontal loads. The vertical displacement of the top of pile No. 2 is greater than that of pile No. 1, which indicates that the composite foundation is inclined. The vertical displacement at the top of pile No. 1 is 0.6758×10^{-3} m, and that at the bottom is 0.6768×10^{-3} m. The vertical displacement at the top of pile No. 2 is 0.6872×10^{-3} m, and that at the bottom is 0.6881×10^{-3} m. The vertical displacements of the pile bodies are greater in the middle of the piles, which is mainly caused by the stress on the bottom of the piles caused by the soil, which generates axial compression on the piles.

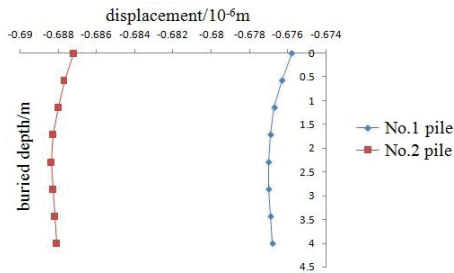


Fig. 10. Vertical displacements along the pile shafts

ANALYSIS OF THE BENDING MOMENTS ALONG THE PILE SHAFTS

The bending moments along the bodies of piles No. 1 and No. 2 are shown in Fig. 11 and Fig. 12. The bending moments of the pile bodies in the x direction are 0, so they are not analyzed. Due to the symmetry of the structure and the applied load, the bending moments of the two piles in the y direction are symmetric, and the bending moments in the z direction vary little.

The bending moments of the pile bodies in the y direction are shown in Fig. 11. Pile No. 1 has a negative bending moment of 19.58 kN·m at the junction between the pile top and the anti-sinking plate, and the bottom of pile No. 1 has a positive bending moment of 0.232 kN·m. Pile No. 2 has a positive bending moment at the junction between the pile top and the anti-sinking plate of 18.19 kN·m, the bottom of pile No. 2 has a positive bending moment of 0.185 kN·m. The bending moments of the two piles at a depth of 2.8 m are 0. The positive and negative signs of the bending moments at the pile tops are the same as those in the horizontal displacement diagram of the piles.

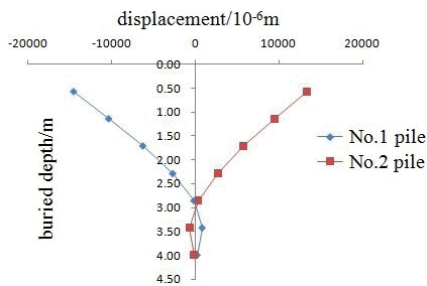


Fig. 11. Bending moments along the pile shafts in the y direction

The bending moments of the pile bodies in the z direction are shown in Fig. 12. The maximum negative moments of piles No. 1 and No. 2 are located at the tops of the piles and are 8644 N·m and 6406 N·m, respectively. The bending moments of pile No. 1 are greater than those of pile No. 2. The maximum positive bending moments of the two piles are located at a depth of 2.3 m and are 3260 N·m and 3302 N·m, respectively. The maximum positive bending moments of the two piles are relatively similar. The maximum bending moments are

located at the tops of the piles, and the bending moments at the bottoms of the piles are approximately zero, which indicates that the confining effect of the soil at the bottoms of the piles is much less than the effect of the anti-sinking plate on the stabilization of the piles.

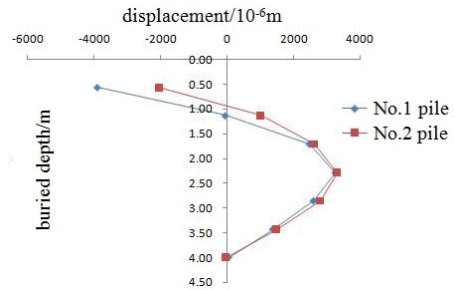


Fig. 12. Bending moments along the pile shafts in the z direction

CHARACTERISTIC ANALYSIS OF THE COMPOSITE FOUNDATION UNDER A VERTICAL LOAD AND BENDING MOMENT

SETTLEMENT ANALYSIS OF THE SEABED SOIL

The settlement characteristics of the seabed soil are shown in Fig. 13. In the figure, the normal surface is the section at the corner pile, and the settlement of the soil decreases radially with distance from the anti-sinking plate. The maximum soil settlement is 0.85 mm, and it occurs at the locations of piles No. 2 and No. 4. The vertical displacement of the seabed soil at the edge in the x axis direction is 0.027 mm, which indicates that the soil far from the mudmat-pile hybrid foundation is uplifted. The displacements at piles No. 2 and No. 4 pile are greater than those at piles No. 1 and No. 3, which indicates that the mudmat-pile hybrid foundation is inclined. As a result of the action of the angular pile, the soil settlement around the piles is significantly less than that far from the piles at the same depth. The effect of the angular piles decreases gradually with increasing distance from the piles, and the difference in the soil settlement caused by the pile essentially disappears at a depth of approximately 8 m. The results show that the presence of corner piles significantly reduces the settlement of the seabed soil body.

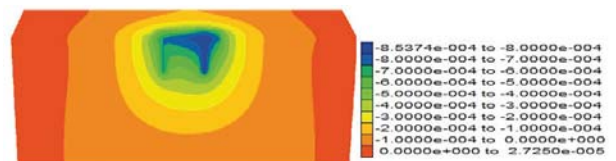


Fig. 13. Settlement of the seabed soil (unit: m)

ANALYSIS OF THE BENDING MOMENTS OF THE ANTI-SINKING PLATE

The bending moment of the anti-sinking plate due to the combined action of the vertical load and bending moment is shown in Fig. 14. Although the structure and the applied load are symmetrical, the bending moment diagram of the anti-sinking plate is not symmetric, and the bending moment distribution is complex.

As shown in Fig. 14(a), the maximum negative bending moment of the anti-sinking plate in the x direction is 21.282 kN·m, and it is located at the junction between pile No. 3 and the anti-sinking plate. The maximum positive bending moment is 6.75 kN·m and occurs in the middle of the long side of the anti-sinking plate. The area of the maximum positive bending moment is small and has little influence, whereas the area of the second highest positive bending moment is large and is located in the middle of the anti-sinking plate. The bending moments at the junctions between the four angle piles and the anti-sinking plate are between 15 kN·m and 21.282 kN·m, which are significantly greater than those at the other locations; this indicates that damage to the anti-sinking plate will occur at the junctions between the anti-sinking plate and the piles. As shown in Fig. 14(b), the maximum negative bending moment of the anti-sinking plate in the y direction is 14.444 kN·m, and it occurs at the connections between piles No. 3 and No. 4 and the anti-sinking plate. The maximum positive bending moment is 5.23 kN·m and is located along the long side of the anti-sinking plate. The bending moments of the anti-sinking plate are concentrated between 2 kN·m and 6 kN·m; only small areas of the edges and the junction between the corner piles and the anti-sinking plate are outside this range. The bending moments at the junctions between the corner piles and the anti-sinking plate are significantly greater than those at other locations, which indicates that damage to the anti-sinking plate can easily occur at the junction between the anti-sinking plate and the corner piles, which is the same as in the x direction bending moment diagram.

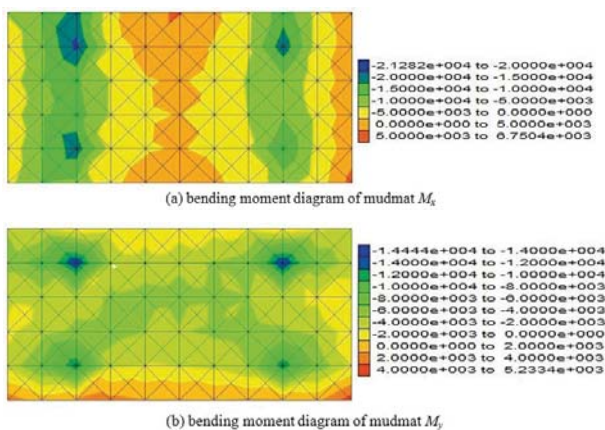


Fig. 14. Bending moments of the mudmat (unit: N·m)

ANALYSIS OF DISPLACEMENTS ALONG THE PILE SHAFTS

The horizontal displacements of piles No. 1 and No. 2 are shown in Fig. 15. Due to the combined action of the vertical load and bending moment, piles No. 1 and No. 2 move in the negative direction along the x axis at the bottom and forward along the x axis at the top. The top of pile No. 1 moves 5.143×10^{-6} m in the positive direction along the x axis, and the bottom moves 58.77×10^{-6} m in the negative direction. The top of pile No. 2 pile moves 3.97×10^{-6} m in the positive direction, and the bottom moves 16.88×10^{-6} m in the negative direction. The horizontal displacement lines of both piles are smooth curves, which indicates that the pile bodies are buckling. Piles No. 1 and No. 2 move in the same direction horizontally and tilt toward the x axis. The difference in displacement between the top and bottom of pile No. 1 is 63.91×10^{-6} m, and that of No. 2 pile is 20.85×10^{-6} m. The inclination angle of pile No. 1 is greater than that of pile No. 2.

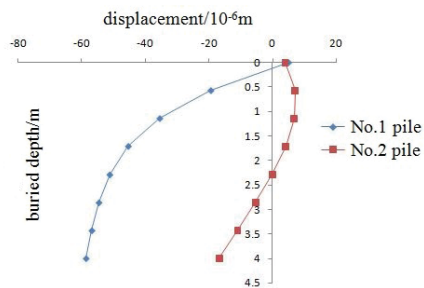


Fig. 15. Horizontal displacements along the pile shafts

The vertical displacements of pile No. 1 and No. 2 are shown in Fig. 16. The pile foundations move downward as a whole under the combined action of the vertical load and bending moment. The vertical displacements of the two piles form straight lines; the vertical displacement at the top of pile No. 1 is 0.7×10^{-3} m, and that at the top of pile No. 2 is 0.85×10^{-3} m. The displacements of the two pile tops are different, which indicates that the composite foundation is inclined.

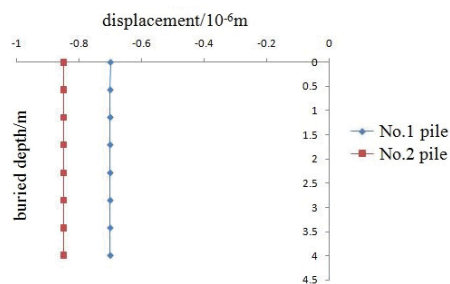


Fig. 16. Vertical displacements along the pile shafts

ANALYSIS OF THE BENDING MOMENTS ALONG THE PILE SHAFTS

The bending moments of the bodies of piles No. 1 and No. 2 are shown in Fig. 17 and Fig. 18. The bending moments of the pile bodies in the x direction are 0, so they are not analyzed. The bending moments of the pile bodies in the y direction are shown in Fig. 17. The maximum bending moments are located at the junctions between the pile tops and the anti-sinking plate, and the minimum bending moments are located at the bottoms of the piles, which indicates that pile damage can easily occur at the junctions between the pile tops and the anti-sinking plate. The bending moment at the top of pile No. 1 is 27.67 kN·m, and that at the bottom is 90.18 N·m. The bending moment at the top of pile No. 2 is 12.16 kN·m, and that at the bottom is 91.39 N·m. The bending moments of both piles decrease gradually from the top to the bottom and have opposite signs. The bending moments of pile No. 1 are greater than those of No. 2.

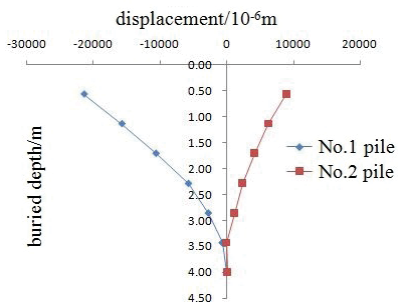


Fig. 17. Bending moments along the pile shafts in the y direction

The bending moment of the pile bodies in the z direction are shown in Fig. 18. The bending moment at the top of pile No. 1 is 11.26 kN·m, and that at the bottom of the pile is 0.72 N·m. The bending moment at the top of pile No. 2 is 6.67 kN·m, and that at the bottom of the pile is 42.79 N·m. The bending moment are largest at the tops of both piles, those at the bottoms are the smallest, and the signs are the same. The bending moment of pile No. 1 are greater than those of pile No. 2.

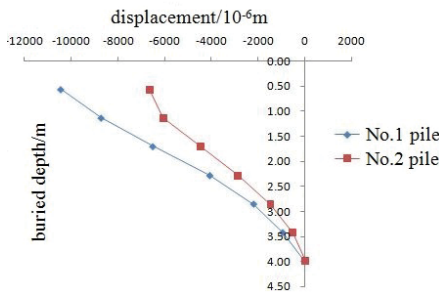


Fig. 18. Bending moments along the pile shafts in the z direction

CHARACTERISTIC ANALYSIS OF THE COMPOSITE FOUNDATION UNDER A HORIZONTAL LOAD AND BENDING MOMENT

SETTLEMENT ANALYSIS OF THE SEABED SOIL

The settlement characteristics of the seabed soil are shown in Fig. 19. In the figure, the normal surface is the section at the corner pile, and the amount of settlement decreases radially with distance from the composite foundation. The maximum settlement is 2.36 mm, and it occurs in the middle of the bottom of the anti-sinking plate. As a result of the action of the angular piles, the settlement of the soil around the piles is significantly less than that far from the pile at the same depth. With increasing distance from the angular piles, the effect of the piles decreases gradually, and the horizontal difference in the soil settlement caused by the piles essentially disappears at a depth of approximately 8 m. The angular piles influence the settlement of the seabed soil over a certain area, which is approximately twice the length of the piles.

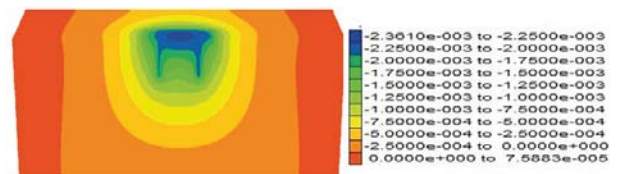


Fig. 19. Settlement of the seabed soil (unit: m)

ANALYSIS OF THE BENDING MOMENTS OF THE ANTI-SINKING PLATE

The bending moments of the anti-sinking plate due to the combined action of a horizontal load and bending moment are shown in Fig. 20. In general, the bending moments of the anti-sinking plate are not symmetrical, and the distribution pattern is not obvious.

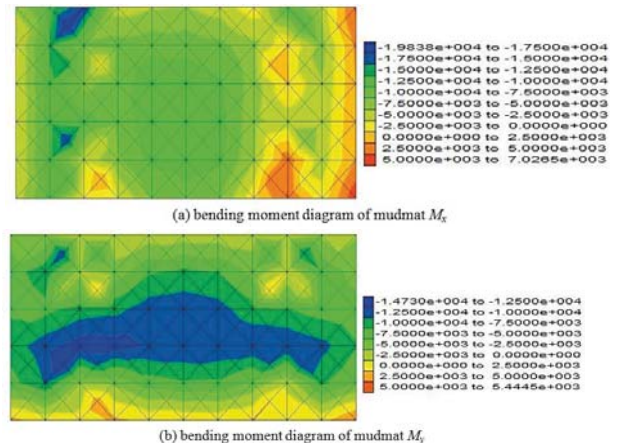


Fig. 20. Bending moments of the mudmat (unit: N·m)

As shown in Fig. 20(a), the maximum negative bending moment of the anti-sinking plate in the x direction is 19.838 kN·m, and it is located near piles No. 1 and No. 3. The maximum positive bending moment is 7.0265 kN·m, and it occurs at the corner of the anti-sinking plate along the x axis. The area of the maximum positive bending moment is small and has little influence. The bending moments of the anti-sinking plate are mainly between 10 kN·m and 12.5 kN·m, and they are located in the middle of the anti-sinking plate. The bending moments at the junctions between the piles and the anti-sinking plate are large. As shown in Fig. 20(b), the maximum negative bending moment of the anti-sinking plate in the y direction is 14.73 kN·m, and it is located between piles No. 1 and No. 3. The maximum positive bending moment is 5.4445 kN·m, and it occurs at the corner of the anti-sinking plate along the x axis. The area of the maximum positive bending moment is small, and its influence is not significant. The bending moments of the anti-sinking plate are mainly between 10 kN·m and 12.5 kN·m; they are located in the middle of the anti-sinking plate and are distributed in long strips in the x direction.

ANALYSIS OF DISPLACEMENTS ALONG THE PILE SHAFTS

The horizontal displacements along piles No. 1 and No. 2 are shown in Fig. 21. Due to the combined effects of a vertical load and horizontal load, pile No. 1 moves in the negative direction along the x axis, and pile No. 2 moves forward along the x axis. The top of pile No. 1 moves 4.139×10^{-6} m in the positive direction along the x axis, and the bottom moves 171.5×10^{-6} m in the negative direction. The top of pile No. 2 moves 0.2374×10^{-6} m in the negative direction, and the bottom moves 120×10^{-6} m in the positive direction. The horizontal displacements of piles No. 1 and No. 2 form smooth curves, which indicates that the pile bodies are buckling. Piles No. 1 and No. 2 move backward horizontally, the body of pile No. 1 pile leans in the negative direction along the x axis, and the body of pile No. 2 leans forward along the x axis. The difference in displacement between the top and bottom of pile No. 1 is 175.639×10^{-6} m, and that between the top and bottom of pile No. 2 is 120.24×10^{-6} m. The inclination angle of pile No. 1 is greater than that of pile No. 2.

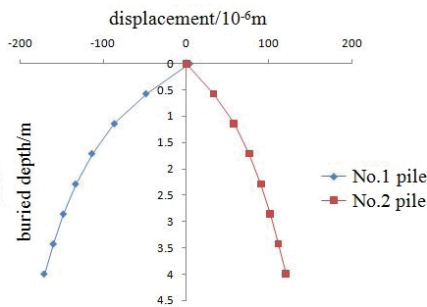


Fig. 21. Horizontal displacements along the pile shafts

The vertical displacements of piles No. 1 and No. 2 are shown in Fig. 22. The pile foundations move downward as a whole under the combined effects of the vertical load and horizontal load. The vertical displacement at the top of pile No. 1 is 2.037×10^{-3} m, and that at the top of pile No. 2 is 2.112×10^{-3} m. The vertical displacements at the tops of the two piles are different, which indicates that the composite foundation is inclined. The vertical displacements at the bottoms of the two piles are 2.032×10^{-3} m and 2.107×10^{-3} m, respectively. The vertical displacements of the pile bodies decrease, which indicates that the pile body is inclined; this is consistent with the results of the horizontal displacement analysis. The vertical displacements of the two piles form inclined nearly linear curves, which is mainly because the soil under the pile imparts a stress at the bottom of the pile, so the pile body experiences axial compression.

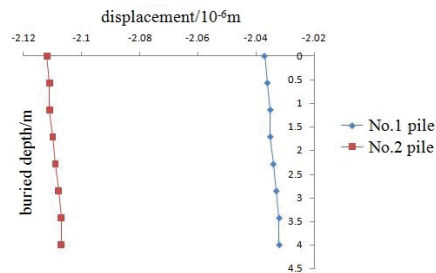


Fig. 22. Vertical displacements along the pile shafts

ANALYSIS OF THE BENDING MOMENTS ALONG THE PILE SHAFTS

The bending moments on the bodies of piles No. 1 and No. 2 are shown in Fig. 23 and Fig. 24. The bending moments of the pile bodies in the x direction are 0, so they are not analyzed.

The bending moments of the pile bodies in the y direction are shown in Fig. 23. The maximum bending moment of pile No. 1 is 49.11 kN·m, and it is located at the junction between the pile top and the anti-sinking plate. The minimum bending moment of pile No. 1 is 25.31 N·m, and it occurs at the bottom of the pile. The maximum bending moment of pile No. 2 pile is 28.49 kN·m, and it is located at the junction between the top of the pile and the anti-sinking plate. The minimum bending moment of pile No. 2 is 36.72 N·m, and it occurs at the bottom of the pile. The bending moments of pile No. 1 are greater than those of No. 2 pile body. The positive and negative signs of the bending moments at the bottom of the pile are the same as those shown in the horizontal displacement diagram of the piles; the results are the same as those of the horizontal displacement.

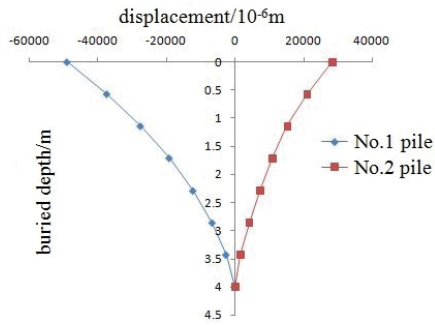


Fig. 23. Bending moments along the pile shafts in the y direction

Fig. 24 shows the bending moment of pile body in the z direction. The maximum bending moment of pile No. 1 is 26.54 kN·m, and it is located at the junction between the pile top and the anti-sinking plate. The minimum bending moment of pile No. 1 is 13.91 N·m, and it occurs at the bottom of the pile. The maximum bending moment of pile No. 2 is 22 kN·m, and it is located at the junction between the top of the pile and the anti-sinking plate. The minimum bending moment of pile No. 2 is 30.66 N·m, and it occurs at the bottom of the pile. The bending moments of pile No. 1 are greater than those of No. 2. Both piles have positive and negative bending moments in the vertical direction, and the positive bending moments are located in the lower half of the pile. The point of 0 bending moment on pile No. 1 is located at a depth of 1.7 m, and that on pile No. 2 is located at a depth of 1.5 m.

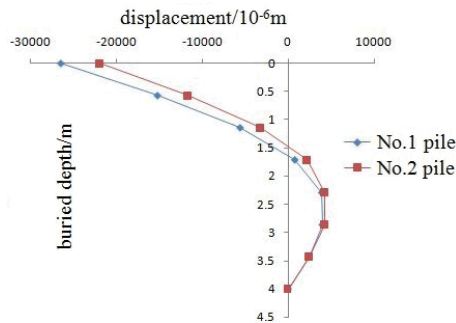


Fig. 24. Bending moments along the pile shafts in the z direction

CONCLUSION

A numerical model of a subsea mudmat-pile hybrid foundation is developed using the numerical simulation software FLAC3D, and the force and deformation characteristics of the model under different load combinations, including a vertical load and horizontal load, a vertical load and bending moment, and a horizontal load and bending moment, were analyzed. The main conclusions are as follows:

1. Due to the effect of the combined load, the seabed soil near the mudmat-pile hybrid foundation experiences settlement, whereas the soil far from the foundation is slightly uplifted. The presence of the pile foundation affects

the settlement of the seabed soil, and the range of influence is approximately 2 times the length of the pile body.

2. Due to the effect of the combined load, the bending moment distribution of the anti-sinking plate is complex, and there are patterns under a vertical load and horizontal load but no clear patterns under the other load combinations. The maximum bending moments of the anti-sinking plate occur at the junctions between the anti-sinking plate and the piles, which indicates that damage can occur easily in these locations.
3. Horizontal displacements along the pile shaft are produced by the combined loads. The horizontal displacement directions of piles No. 1 and No. 2 are opposite under a vertical load and horizontal load and under a horizontal load and bending moment load. The horizontal displacement directions of piles No. 1 and No. 2 under a vertical load and bending moment are the same. The pile bodies are inclined to varying degrees, and the tilt angle of pile No. 1 is greater than that of pile No. 2. The inclination directions of piles No. 1 and No. 2 are opposite under a vertical load and horizontal load and under a horizontal load and bending moment, whereas they are the same under a vertical load and bending moment.
4. The analysis of the bending moments along the pile shafts shows that the maximum bending moments occur at the junctions between the anti-sinking plate and the pile tops, which indicates that under a combined load, the piles are most vulnerable to damage at the junctions between the pile tops and the anti-sinking plate. Under a vertical load and horizontal load and a horizontal load and bending moment load, the pile bodies have points with a zero-bending moment.

ACKNOWLEDGMENTS

This study was financially supported by the National Natural Science Foundation of China (nos. 41372288).

BIBLIOGRAPHY

1. Bransby, M.F., Brown, M.J., Knappett, J.A.: Vertical capacity of grillage foundations in sand. *Revue Canadienne De Géotechnique*, 2011, 48(8), Pp. 1246-1265.
2. Brown, M.J., Bransby, M.F., Knappett, J.A.: The vertical capacity of grillage foundations. *Géotechnique*, 2012, 62(3), Pp. 201-211.
3. Chen, G.S., Liu, R.: Upper bound solutions of horizontal bearing capacity of skirted mudmat in sand. *Journal of Tianjin University (Natural science and Engineering Technology Edition)*, 2018, 53(3), Pp. 264-270.
4. Guan, W.W., Chen, L.: International vision of marine renewable energy management. *Modern Economic Information*, 1, Pp. 20-22.

5. He, Q., Wang, P.: Current Situation and prospect of deep-sea energy development. *Ocean Development and Management*, 2017, 34(12), Pp. 66-71.
6. Liu, B., Han, Y.H.: FLAC principles, examples and application guides. *Communications Press, Beijing*, 2005, pp. 67-68.
7. Lian, J.J., He, W., Wu, M.D.: Experimental study of bearing characteristic of bucket foundation of offshore wind turbine with bulkheads. *Rock and Soil Mechanics*, 2016, 37(10), Pp. 1-8.
8. Liu, R., Chen, G.S.: Upper bound solutions of vertical bearing capacity of skirted mudmat in sand. *The Ocean Engineering*, 2015, 34(4), Pp. 45-52.
9. Liu, R., Liu, M.M., Yang, S.G.: Bearing capacity of different shape mudmat foundations for subsea production system on undrained clays. *Acta Oceanologica Sinica*, 2016, 38(3), Pp. 131-144.
10. Liu, Y.M., Xu, D.P.: FLAC/FLAC3D foundation and engineering examples. *Water Conservancy and Hydropower Press, Beijing* 2008, Pp. 172-173.
11. Tan, Y., Liu, M.: Structure analysis of mudmat foundation for subsea production system. *Ship & Ocean Engineering*, 2012, 41(4), Pp. 133-135,141.
12. Xu, M.: Study of structural improvement of Mudmat in deep sea subsea system. *Master's thesis, Tianjin University, Tianjin, China*. 2015.
13. Xu, M., Yang, S.G., Wang, H.: Study of structural improvement of mudmat in the subsea system. *Marine Science Bulletin*, 2016, 35(4), Pp. 436-442.
14. Yun, G.J., Alasdair, M., John, O.: Undrained capacity of surface footings subjected to combined V-H-T loading. *Proceedings in the Nineteenth International Offshore and Polar Engineering Conference. Osaka*. 2009, Pp. 9-14.
15. Zhou, L., Liu, R., Guo, S.Z.: A dynamic simulation method for continuous spud can penetration. *Journal of Earthquake Engineering*, 2015, 37(2), Pp. 460-466.
16. Zhao, W.G., Liu, Y.T., Wang, W.S.: Current situation and development of marine renewable energy power generation. *Smart Grid*, 2015, 3(6), Pp. 493-499.
17. Ku Mohd Razali, K.H.N.S., Kasim, S., Hassan, R., Mahdin, H., Ramli, A.A., Md Fudzee, M.F., Salamat, M.A.: Lensalyza Photography Studio Reservation System. *Acta Electronica Malaysia*, 2018, 2(2), Pp. 06-09.
18. Li, B.Q., Li, Z.: Design of Automatic Monitoring System for Transfusion. *Acta Electronica Malaysia*, 2018, 2(1), Pp. 07-10.
19. Luo, X.: Research on Anti-Overturning Performance of Multi-Span Curved Girder Bridge with Small Radius. *Acta Mechanica Malaysia*, 2017, 1(1), Pp. 11-15.
20. Luo, X.: Study on PC Continuous Girder mechanical properties Based on Tendon Tensioning Pattern. *Acta Mechanica Malaysia*, 2017, 1(1), Pp. 16-20.
21. De'nan, F., Hasan, H., Mahzuz, M.: Behaviour of the beam to column connection for tapered steel section with perforation. *Engineering Heritage Journal*, 2017, 1(1), Pp. 41-44.
22. Kumar, R.: Comparison of Instruction Scheduling And Register Allocation For Mips And Hpl -Pd Architecture For Exploitation Of Instruction Level Parallelism. *Engineering Heritage Journal*, 2018, 2(2), Pp. 04-08.

CONTACT WITH THE AUTHORS

Desen Kong, Ph.D.

e-mail: skd992012@sdust.edu.cn

College of Civil Engineering and Architecture
Shandong University of Science and Technology
Qingdao Shandong
266590
CHINA

EXPERIMENT ON PRESSURE CHARACTERISTICS OF SUBMERGED FLOATING TUNNEL WITH DIFFERENT SECTION TYPES UNDER WAVE CONDITION

Qinxi Li¹

Shuping Jiang²

Xiang Chen³

¹ School of Civil Engineering, Chongqing Jiaotong University, Chongqing, China

² China Merchants Chongqing Communication Research & Design Institute Co., Ltd., Chongqing, China

³ School of Civil Engineering, Chongqing Three Gorges University, Chongqing, China

ABSTRACT

Submerged floating tunnel (SFT for short) is a special underwater traffic structure, and wave load is one of the main environmental loads of SFT structure. In this paper, the 1:60 physical model test of three kinds of SFT in a two-dimensional wave flume is tested. The effects of random irregular waves on the SFT structure under different wave heights and periods are discussed. The study shows that: (1) Compared with circular and polygonal sections, there are multiple local peaks in the elliptical section during the period. with the increase of wave height, the number of local peaks also increases. It suggests that the rotational moment plays an important role in the elliptical section which has a relatively small depth-width ratio. (2) The position of the maximum and minimum pressure in the three kinds of SFT sections is consistent. Their vertical wave forces are all larger than their horizontal wave forces. The increase of vertical wave force relative to horizontal wave force in polygon section is larger than that in elliptical section, and the difference in the circular section is the smallest. (3) Under the same traffic condition, the wave force of the elliptical and polygon section is smaller, but they are more sensitive to the change of wave height, and the increase is obvious. The distribution of wave force in the circular section is more uniform.

Keywords: Submerged floating tunnel, section type, irregular waves, pressure characteristics, physical test

INTRODUCTION

Submerged floating tunnel (SFT for short) is the only way to maintain the dynamic balance of the water structure by the buoyancy and the cable tension. In some places where it is difficult to build a tunnel or bridge to cross. SFT can be used as a transportation scheme to solve narrow and deep Straits, lakes and rivers. So far, there is still no real SFT in the world.

Although scholars at home and abroad are almost sure that it must be buried under a certain depth of water, the effect of wave force on SFT is negligible. However, there is still a need to study the wave force of the SFT structure. From the project plan, the structure of pure SFT scheme has the water entry section, the transition section and the deep buried section. The first two sections of the SFT structure are affected by the wave force. If the combination of “shield method + submerged floating

tunnel method” or “immersed tube method + submerged floating tunnel method” is adopted, the connection position will inevitably exist. The determination of the best connection position also needs to study the exact influence of the depth range on the wave force of the SFT structure. In addition, it is necessary to study the response of the deep fjord wave to the SFT structure, which had great damage and deep influence.

The study of the engineering scheme of the submerged floating tunnel is the first problem in front of the engineer, especially the problem of the type selection of the submerged floating tunnel. Around the form of a submerged floating tunnel section, many countries are aimed at different sea area characteristics and project conditions, a variety of cross section forms are put forward, it includes circular, ellipse and polygons [1]. In 1966, British engineer Mr. Grant proposed the basic idea of building a water submerged floating tunnel in

the water. He proposed a submerged floating tunnel structure with 3 circular concrete pipes with diamond shaped steel shells. In 1984, Italy Archimedes company designed a prestressed concrete pipe structure for the eight sides of Messina strait [2]. Then, a variety of structural schemes have been put forward, such as steel concrete steel sandwich tube section, outer steel tube + inner shell section and pipe joint structure of steel –concrete – steel circular structure section. In 1996, four Norway companies proposed four different submerged floating tunnels with different Anchorage and buoy structures. In 1996, Japan [3] proposed an up and down two highways and rail traffic submerged floating tunnel for the Funka Bay. At the same time, a submerged floating tunnel scheme is proposed for the traffic line of North Japan [4], with circular section of inner concrete and external elliptical shell structure. In 2009, a submerged floating tunnel with an oblique anchorage was put forward in the Sulafjord fjord. In 2016, Norway also designed a double cylindrical structure of submerged floating tunnel in the Sognefjord fjord. Therefore, we have designed three kinds of SFT sections, round, ellipse and polygon, as the alternative for the SFT physical model test.

In the physical model experiment of SFT, The SFT's static water load test was first carried out by a scholar [5–7], he tested the spatial stress distribution of the tube section under the hydrostatic load. A previous researcher [8, 9] carried out the SFT structure section model test and studied the spatial stress and the distribution of the axial force of the anchor cable in the SFT structure under pure flow, but the flow rate in the pool space is not easy to control. The SFT structure test under the uniform flow condition of Venkataramana [10] is more refined, and the random vibration of the SFT model is observed. Japan and South Korea are the long and multi island countries of the coastline. Scholars of the two countries are mainly devoted to the study of the motion characteristics of SFT under the action of waves in the fjord or shallow sea area. A Japanese scholar carried out a model test of a shallow water submerged floating tunnel [11, 12]. It is believed that the tension of the anchor cable increases with the increase of the regular wave period. South Korea's S-H. a group of scholars [13, 14] also studied the hydrodynamic characteristics of SFT under the action of waves through a regular wave physical test in a wave flume. It is found that the anchorage system has an important influence on the movement displacement of the structure. The model test of SFT experienced the development of static water test to pure flow, regular wave and random irregular wave. The test conditions also advance to the single flow to wind and wave water flume, and the large wave water pool test in deep water. Because the regular wave has only one specific period, the test result is generally unstable. Sometimes the resonance result is large, sometimes the result is small, and the irregular wave period has certain distribution, the test result rule is usually relatively stable. Therefore, based on the above three types of SFT section, the structure response of SFT structure under random irregular waves is studied. It provides a reference for the optimization and development of new structural type SFT in the future.

PHYSICAL TEST

TEST EQUIPMENT AND MODEL STRUCTURE

Based on the consistent consideration of the traffic volume, three kinds of bi-directional six lane highway traffic SFT cross section prototype are selected. Figure 1 shows the design sketch of the SFT. SFT is fixed to the bottom of the seabed by the tension leg. The test wave flume is 60 m long, 1.9 m high, and 2 m wide.

In order to obtain reliable wave sequence, the wave elements were calibrated first. In the width of 2.0 m, the flume was divided into two 1.0 m wide flume. The test area was located in the lower half, and the upper half diffuses the reflected waves, as shown in figure 2. When the wave propagates to the test area, a part of the wave will be reflected back after the structure is encountered. A part of the reflected wave is diffused in the parallel flume in the upper half, and finally the energy of the reflected wave is dissipated by the gravel. And the other part is reflected back to the vicinity of the wave-maker. The wave height of the reflected wave is measured by the wave height instrument, and the wave elimination treatment is carried out on the wave guide plate controlled by the computer. Similarly, reflected wave which propagating through the test area are shattered and its energy dissipated by the gravel. Therefore, whether the wave propagated through the test area or not, the waves are well treated with wave elimination, which will not cause the reflection and superposition of the waves.

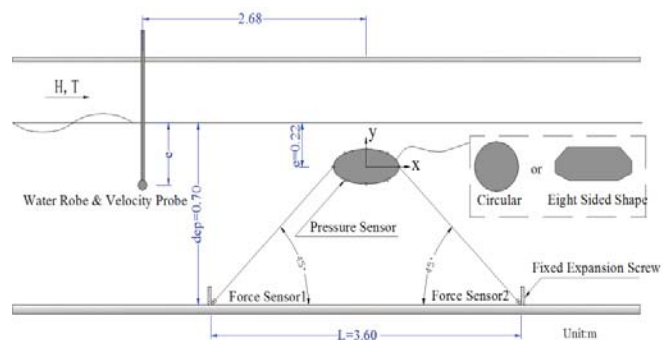


Fig. 1. Experimental parameters and design sketch of the SFT

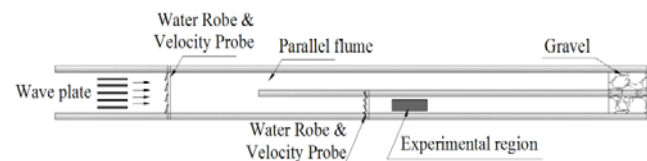


Fig. 2. Schematic diagram of experimental flume arrangement



(a) Top view

(b) Elevation view

Fig. 3. General situation of experimental device (circle as example)

Tab. 1. Dimensions of main sections of three structural types

Section type	The primary parameter value of the prototype (m)	Prototype section area (m ²)	The main parameter value of the model (cm)	Model section area (cm ²)	Traffic volume
Circular	Diameter = 41.5	1355.0	69.2	3763.9	Bi-directional six lane
Ellipse	Long axis * short axis = 45.0 x 19	671.5	75.0x31.7	1865.3	Bi-directional six lane
Polygon	Height * width = 41.2x13.6	514.2	68.7x22.7	1428.3	Bi-directional six lane

Considering the dimension of the wave flume and the size effect of the hydraulic test, the model test scale is 1:60. The length of the single tube section of the prototype is determined to be 51 m, so the length of the SFT test tube section is determined to be 85 cm. In order to prevent water from entering the pipe section, the pipe joint is in a sealed state during the test. The section parameters of three structural types are given in Table 1. Figure 3 is the general situation of experimental device (circle as example) in the test flume. In order to test the pressure of the surface of the SFT structure under the random wave load, eight pressure sensors are evenly arranged in the circumference of each section. At the same time, in order to test the tension of the anchor cable, four total force sensors are arranged, and the transverse distance between the anchor cables is 70 cm, as shown in Figure 4.

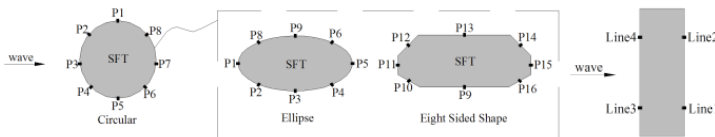


Fig. 4. Measurement point arrangement of sectional pressure and notations of tension legs

SIMILARITY CRITERION

Suspended pipe in water is mainly affected by wave force, ocean currents and earthquakes. The wave force calculated according to the Miroson equation is mainly the inertial force and the damping force. To simulate the above two types of wave forces, similar designs for dynamic experiments should satisfy Froude similarity and Reynolds similarity. In fact, it is difficult to meet both of them at the same time. According to the ship hydrodynamics experiment and the traditional hydrodynamic experiment experience, the experimental pipe section and the anchor cable should meet the following condition:

PIPE SECTION SIMILARITY

The experimental section is geometrically similar to the prototype of SFT through the 1:60 scale. According to Ge Fei [15]'s study, there exist a suitable range of buoyancy-weight ratio (BWR) value which will lead to less dynamic response and more stability for the SFT, it's called "synergetic range of BWR". Meanwhile BWR determines the range of influence of inclined mooring angle (IMA). When IMA is 45°, BWR=1.3 is adopted to counterweight the structure so that the quality of the

pipe section is similar. According to the ship fluid mechanics experiment and the traditional hydrodynamics experiment experience, the experimental material adopts plexiglass.

ANCHOR CABLE SIMULATION

The anchor cable belongs to the non-rigid structure and is simulated by deformation similarity and mass similarity.

The model of anchor rope should be similar to the tension-elongation relationship of the prototype. According to "the wave model test procedure" (Chinese Standard JTJ/T234-2001), the tension-elongation relation of the anchor cable is determined by the following formula (1):

$$T_m = \frac{C_p d_p^2 (\Delta S / S)^n}{\lambda^3} \quad (1)$$

Where T_m is model anchor cable tension(N), d_p is diameter of prototype anchor cable(m), C_p is elastic coefficient of prototype anchor cable and usually takes a value of 26.97×10^4 MPa for the anchor cable; $\Delta S / S$ represents relative elongation of prototype anchor cable, S is Initial length of prototype anchor cable; n is the index, and the n value of the cable is recommended for $n = 1.5$; λ is the model scale, which is 60 in this experiment.

The model of anchor rope is simulated by the combination of steel wire ropes which is basically inelastic (this test range of force measurement) and multi-stage spring steel plates. By varying the length of the spring steel plates to simulate the different tensile – elongation curve, tensile-elongation similarity can be achieved. Meanwhile, the length of anchor cable, the position of the tension legs and anchor angle (45 degrees) of the anchor cable are similar to those of the prototypes. The initial tension of anchor cable is 30kN.

According to "wave model experiment regulations", the quality of cables is similar to that calculated by the following formula (2):

$$W = \frac{C_p d_p^2}{\lambda^2} \quad (2)$$

Where W is the mass per unit length of anchor cable (kg/m), d_p is diameter of prototype anchor cable(m), λ is the model scale, which is 60 in this experiment. C_p is mass proportion coefficient of prototype anchor cable in air, and the C_p value of the cable is 3670 [kg/(m².m)].

WAVE SIMULATION

The wave simulation satisfies the gravity similarity condition, and the irregular wave spectrum adopts JONSWAP spectrum. Thus $s(f)$ is calculated by using formula (3):

$$s(f) = \alpha H_s^2 T_p^{-4} f^{-5} \exp\left[-\frac{5}{4}(T_p f)^{-4}\right] \gamma^{\exp[-(T_p f - 1)/2\sigma^2]} \quad (3)$$

Where H_s is significant wave height (m), T_p is the peak period of spectrum (s); γ is the spectral peak parameters, take $\gamma = 3.3$;

$$\alpha = \frac{0.0624}{0.230 + 0.0336\gamma - 0.185(1.9 + \gamma)^{-1}}, \quad \sigma = \begin{cases} 0.07 & f \leq f_p \\ 0.09 & f \geq f_p \end{cases}$$

Before wave test, the characteristic wave elements are input into the computer to control the wave generator to produce the corresponding irregular wave sequence, so that wave elements meet requirements at the place of model placement.

The experiment adopts the intermittent wave generating method to eliminate the multiple reflections of the wave maker. In this test, each regular wave train has a wave number of about 120, then stops. After the water surface is calm, the next test is carried on. Each trial was repeated 3 times to ensure the reliability of the experimental data.

TEST CONDITIONS AND METHODS

In order to test the effect of wave force on SFT, we assume that the SFT structure is at a shallow water level. We take the immersion depth of the prototype SFT is 6 m. Therefore, the pipe-top of the model is 10 cm from the surface of the water (Immersion depth 10 cm), and the rest of the test parameters is shown in Table 2. The experiment is carried out vertically to the SFT structure in the direction of wave motion, and the test wave is set as a series of irregular wave sequences with different wave heights and different period. The main test parameters of the pressure testing system and the tension test system are shown in Table 3.

Tab. 2. Experimental conditions

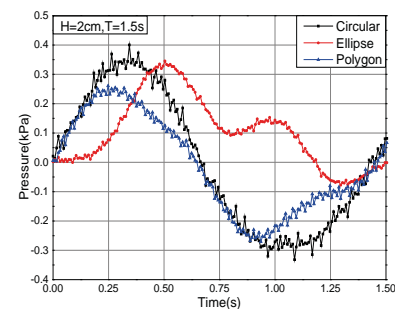
Class	parameter	parameter value
Model	Immersion depth	0.1m
	Length of pipe section	0.85m
	Support mode	Flexible anchor cable
	Anchor cable type	steel wire rope
Anchor cable	Diameter of wire rope	2.5mm
	Inclined mooring angle (IMA),	45°
	Wave period	1.5s~2.1s
Wave	Wave height	2cm~6cm

Tab. 3. Main parameters of measurement system

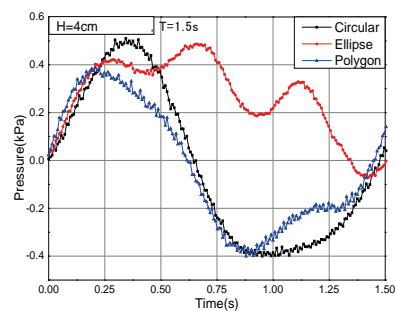
type	Sensor range	Resolution accuracy	Frequency of sampling
Pressure measurement system	10~20/kPa	1%	0.008 seconds / times
Total force measurement system	2~30/kg	1%	0.03 seconds / times

TEST ANALYSIS

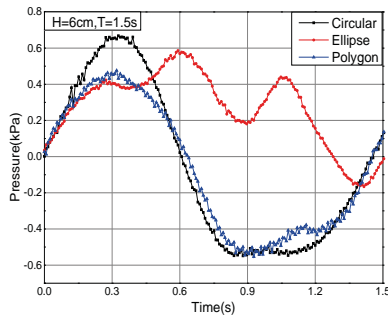
Under the same period and different wave heights, wave pressure at wave ward side – time diagram of the three SFT cross sections is shown in Figure 5. When the bi-directional six lanes are adopted, which means that the traffic volume is consistent, the three kinds of cross sections can be compared. Due to the difference of section area, the wave force time history curves of three kinds of cross section show significant difference. The circular section has the largest section area, and its peak pressure in the time history curve is also the largest. Compared to the circular and polygonal sections, the elliptical section has several obvious local peaks in the period. Moreover, with the increase of wave height, the number of local peaks also increases. It suggests that the rotational moment plays an important role in the elliptical section which has a relatively small depth-width ratio. Therefore, the rotation moment of the cross section should be paid more attention to in the structural design.



(a) $H=2\text{cm}, T=1.5\text{s}$

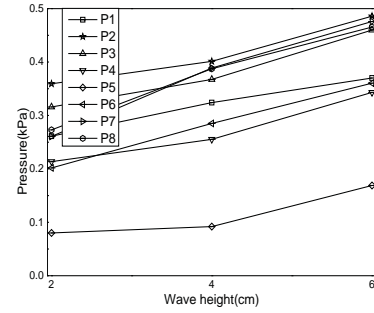


(b) $H=4\text{cm}, T=1.5\text{s}$



(c) $H=6\text{cm}$, $T=1.5$

Fig. 5. Wave front pressure at different wave cross sections

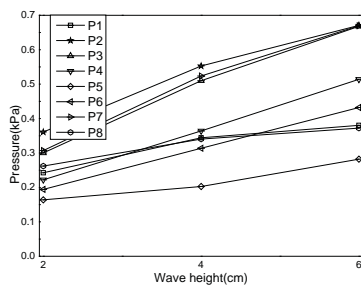


(c) Polygonal cross section

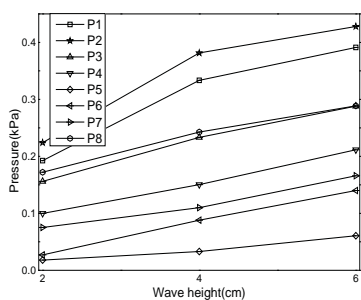
Fig. 6. Circumferential pressure of three cross sections

After changing the experimental period T of the wave, the pressure value will change. It suggests that the pressures still vary with the wave heights. Therefore, we take the period $T = 1.5\text{s}$ as an example to illustrate. We select eight measuring points on each section, and then measure the peak value of the pressure at each measuring point. The measurement results are shown in Figure 6. Overall, the peak value of pressure of three SFT sections shows a positive correlation with wave height. Because the position of each sensor on the cross section is different, there is a significant difference the value of pressure. For the circular section, the maximum pressure appears at P2 on the wave front (clockwise 315 degrees), and the minimum pressure appears at P5 (clockwise 180 degrees). The maximum pressure at the elliptical and polygonal sections also occurs at P2, and the minimum pressure appears at P5.

Based on a study, the wave force was evaluated based on the diffraction theory by Boundary Element Method [15, 16]. We got inspiration from it and evaluated vertical and horizontal the wave force by the circumferential pressure obtained experimentally. Taking the period $T = 1.5\text{s}$ as an example, the vertical and horizontal wave forces of three kinds of SFT cross sections are given in Figure 7. The vertical and horizontal wave force of three kinds of SFT cross sections are positively correlated with wave height. For circular section, vertical force is larger than horizontal force, 2%~12% [17]. For elliptical section, vertical force is larger than horizontal force, 52%~55%. For polygon section, the vertical force is larger than horizontal force, 67~69%. It suggests that the vertical wave forces of the three kinds of cross sections are larger than the horizontal wave forces [18]. Thus, the vertical force should be paid more attention to in the structural design [19]. By comparing the increase values of vertical wave force relative to horizontal wave force on three kinds of cross sections, it is found that the increase of polygon cross section is greater than that of ellipse section while the increase of circular section is the smallest [20]. It is indicated that wave height is one of the important factors affecting wave force, and the sensitivity of elliptical and polygonal sections to wave height change is more obvious than that of circular section [21].



(a) Circular cross-section



(b) Elliptical cross section

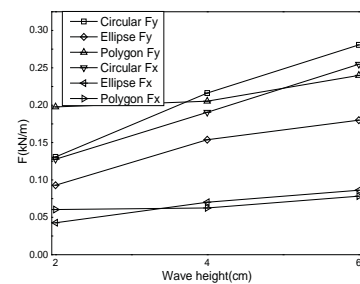
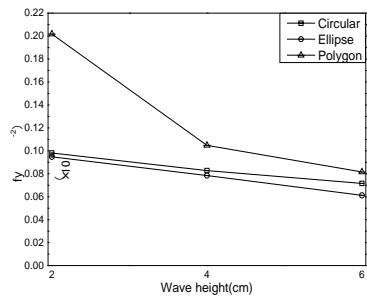
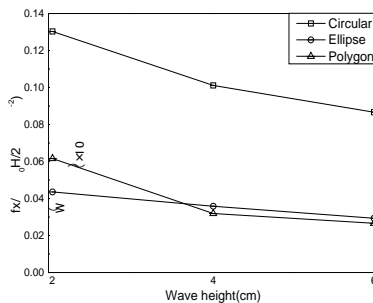


Fig. 7. Vertical and horizontal wave forces of three SFT sections



(a)



(b)

Fig. 8. Dimensionless wave forces of three SFT sections

In the analysis of wave forces, a scholar proposed the method of dimensionless wave force, that is, the wave force is divided by the water mass and half of the wave height. In Figure 8, the dimensionless results of vertical and horizontal wave forces of three kinds of cross sections are given respectively, and the transverse axis is wave height [22]. As shown in Figure 8, with the increase of wave height, the dimensionless wave force is not linearly increased. On the other hand, the increase of the dimensionless wave force decreases gradually when the wave height is equivalent increased, and the rate of the decrease of the vertical dimensionless wave force and the horizontal dimensionless wave force is almost the same.

CONCLUSIONS

This study carried out physical experiments to investigate the effects of random irregular waves on the SFT structure under different wave heights and periods. This creative result of physical experiment has been summed up as the following aspects.

The pressure of the three SFT sections all increases with the wave height, and the position of the maximum and minimum pressure in the three kinds of SFT sections is consistent. The maximum value appears at P2, the minimum value appears at P5. For elliptical section, there are multiple local peaks during the period. And with the increase of wave height, the number of local peaks also increases. It suggests that the rotational moment plays an important role in the elliptical section which has a relatively small depth-width ratio.

By evaluating the wave force, it is found that the wave forces of the three SFT sections also increases with the wave height.

Their vertical wave forces are all larger than their horizontal wave forces. The increase of vertical wave force relative to horizontal wave force in polygon section is larger than that in elliptical section, and the difference in the circular section is the smallest.

Under the same traffic condition, the wave force of the elliptical and polygon section is smaller, but they are more sensitive to the change of wave height, and the increase is obvious. The distribution of wave force in the circular section is more uniform

ACKNOWLEDGMENT

This work was financially supported by the National Ministry of Transport Major Construction Technology Projects "Preliminary Study on Key Technologies of Deep Sea Submerged Floating Tunnel" (Grant No. 2013318740050).

REFERENCES

1. F. Perotti, G. Barbella, and M. D. Pilato, *The dynamic behavior of Archimede's Bridges: Numerical simulation and design implications*, Procedia Engineering, No. 4, pp. 91–98, 2010.
2. G. Martire, B. Faggiano, F. M. Mazzolani, A. Zollo, and T. A. Stabile, *Seismic analysis of a SFT solution for the Messina Strait crossing*, Procedia Engineering, Vol. 4, No. 6, pp. 303–310, 2010.
3. B. Jakobsen, *Design of the Submerged Floating Tunnel operating under various conditions*, Procedia Engineering, Vol. 4, No. 6, pp. 71–79, 2010.
4. S. Kanie, T. Mikami, and Y. Kakuta, *Dynamic Characteristics of Submerged Floating Tunnels Due to Wave Force*, Proceedings of the Japan Society of Civil Engineers, No. 556, pp. 159–168, 2010.
5. B. Faggiano, G. Martire, and F. M. Mazzolani, *Cable Supported Immersed Inverted Bridge: A challenging proposal*, Procedia Engineering, Vol. 4, No. 6, pp. 283–291, 2010.
6. S. Kanie, *Feasibility studies on various SFT in Japan and their technological evaluation*, Procedia Engineering, Vol. 4, pp. 13–20, 2010.
7. Y. Gan, X. Xu, *Three-dimensional degenerate beam element method for stability analysis of thin-walled members*, Journal of Zhejiang University (Engineering Edition), Vol. 37, No. 3, pp. 337–340, 2003.
8. G. Wang, *Numerical analysis and experimental study of SFT structure response under wave current*, Southwest Jiao Tong University, 2008.

9. Y. Qin, *Key technologies of SFT stability under ocean eddy currents*, Southwest Jiao Tong University, 2009.
10. K. Venkataramana, S. Yoshihara, S. Toyota, and Y. Aikou, *Current-induced vibrations of submerged floating tunnels*, Proceedings of the Six International Offshore and Polar Engineering Conference, Vol. 28–31, pp. 111–118, 1996.
11. H. Kunisu, S. Mizuno, Y. Mizuno, and H. Saeki, *Study on Submerged Floating Tunnel Characteristics Under the Wave Condition*, International Society of Offshore and Polar Engineers, 1994.
12. R. Fujita, T. Mikami, T. Yamashita, N. Kawai, and H. Sasaki, *Development of Submerged Floating Tunnels in Shallow Water*, Doboku Gakkai Ronbunshuu B, Vol. 16, pp. 263–268, 2000.
13. S. H. Oh, W. S. Park, S. C. Jang, D. H. Kim, and H. D. Ahn, *Physical experiments on the hydrodynamic response of submerged floating tunnel against the wave action*, Hasanuddin University Press, 2013.
14. S. I. Seo, H. S. Mun, J. H. Lee, and J. Kim, *Simplified analysis for estimation of the behavior of a submerged floating tunnel in waves and experimental verification*, Marine Structures, Vol. 44, pp. 142–158, 2015.
15. Y. Hong, and F. Ge, *Dynamic response and structural integrity of submerged floating tunnel due to hydrodynamic load and accidental load*, Procedia Engineering, Vol. 4, pp. 35–50, 2010.
16. H. Kunisu, *Evaluation of wave force acting on Submerged Floating Tunnels*, Procedia Engineering, Vol. 4, No. 6, pp. 99–105, 2010.
17. B. Q. Li, Z. Li, *The Implement of Wireless Responder System Based on Radio Frequency Technology*, Acta Electronica Malaysia, Vol. 2, No. 1, pp. 15–17, 2018.
18. M. S. Ibrahim, S. Kasim, R. Hassan, H. Mahdin, A. A. Ramli, M. F. Md Fudzee, and M. A. Salamat, *Information Technology Club Management System*, Acta Electronica Malaysia, Vol. 2, No. 2, pp. 01–05, 2018.
19. Z. He, X. Gu, X. Y. Sun, J. Liu, and B. S. Wang, *An Efficient Pseudo-Potential Multiphase Lattice Boltzmann Simulation Model for Three-Dimensional Multiphase Flows*, Acta Mechanica Malaysia, Vol. 2, No. 1, pp. 01–03, 2018.
20. C. Adrian, R. Abdullah, R. Atan, and Y. Y. Jusoh, *Theoretical Retical Aspect in Formulating Assessment Model Of Big Data Analytics Environment*, Acta Mechanica Malaysia, Vol. 2, No. 1, pp. 16–17, 2018.
21. N. Abd Rahman, H. Halim, H. Gotoh, and E. Harada, *Validation of Microscopic Dynamics of Grouping Pedestrians Behavior: From Observation to Modeling and Simulation*, Engineering Heritage Journal, Vol. 1, No. 2, pp. 15–18, 2017.
22. M. A. Hassan, and M. A. Mohd Ismail, *Literature Review for The Development of Dikes's Breach Channel Mechanism Caused by Erosion Processes During Overtopping Failure*, Engineering Heritage Journal, Vol. 1, No. 2, pp. 23–30, 2017.

CONTACT WITH THE AUTHORS

Qinxi Li

e-mail: 494974130@qq.com

School of Civil Engineering
Chongqing Jiaotong University
Chongqing 400074
CHINA

EXPLORATION OF LAND DEVELOPMENT INTENSITY INDEX OF PORT CONTAINER LOGISTICS PARK BASED ON QUANTITATIVE ALGORITHM AND PENT ANALYSIS METHOD

Nan Lyu^{1,2)}

Jingyuan Zhao¹⁾

Minghua Lyu³⁾

¹⁾School of Architecture, Chang'an University, China

²⁾Xi'an City Planning & Design Institute, China

³⁾Xi'an Aerospace Base Municipal Public Utilities Development Co. Ltd., China

ABSTRACT

To give full play to the circulation function of the port container logistics park, it is urgent to study the development intensity of the land in the port container logistics park and to guide the scientific development of the port logistics park with reasonable development intensity control index. The current situation of land development intensity control index of container logistics park at home and abroad is analysed, the PENT (politics, economy, society and technology) analysis method is used to analyse the factors influencing the land development intensity control index of container logistics park, and the index system structure of influencing factors is constructed. Finally, index value is obtained quantitatively with the proposed calculation method of the land development intensity index of the port container logistics park. Its practicability is verified in case analysis.

Keywords: development intensity, logistics park, container; indicator, land, port

INTRODUCTION

The research and construction of logistics park in China started late, but the development is very rapid. Although the development and construction of China's port container logistics park is commendable, there are also serious problems. First of all, in the case that the country's available land resources are becoming scarcer, the explosive growth of the number of logistics parks and land scale inevitably raises concerns. Based on a study, due to its large size and low development intensity, port container logistics park has become a hot topic in the field of logistics and urban planning [1, 2]. Secondly, some port logistics park projects are rushed to start without detailed feasibility study, which makes the logistics demand,

functional positioning and planning layout unclear. Finally, the construction of some port container logistics parks seeks to be large and complete, which is inconsistent with local economic conditions, resulting in a large number of idle lands in the logistics park, low development intensity and serious resource waste [3, 4]. Study showed to fully implement the scientific concept of development, realize the conservation of land resources, promote the optimized allocation and intensive use of industrial land, and improve the management level of construction land for logistics projects, it is urgent to scientifically and reasonably determine the land scale and land development intensity control indicators of the port logistics park to guide the development and construction of the port container logistics park [5].

LITERATURE REVIEW

At present, domestic and foreign scholars don't directly calculate and study the land development intensity control indicators of the port container logistics park, the research on the port container logistics park mainly focuses on the scale of the park, the layout of the internal facilities of the park and the prediction of the logistics quantity in the park. Foreign researches on the land scale of port container logistics park are mainly conducted quantitative analysis by building mathematical models, as well as qualitative analysis from the relevant factors affecting the scale of logistics parks. Some researchers proposed a mathematical model based on bi-level programming to quantitatively analyse the scale and location of logistics park; based on the analysis of port location factors and port operational quantities, some scholars proposed the model of optimal port size and site location with integer programming [6, 7]. There are many researches on the prediction of the logistics quantity, and many mathematical prediction models are proposed. In particular, there are many research achievements on the combined prediction. In addition, Multiple Probability Model (MNP) is also studied to solve the high spatiotemporal variability in the process of cargo demand, and Monte Carlo method is adopted to evaluate the accuracy of the prediction results [8].

There are many methods for predicting the logistics quantity of logistics parks. Domestically, it is mainly based on quantitative calculation, supplemented by qualitative analysis. The mathematical methods used include Grey Forecast Model, Multiple Linear Regression (MLR), Exponential Smoothing, Neural Network Forecasting Method and combination prediction. For example, grey system theory is used to study the logistics quantity of logistics park scale, and the quantity demand of logistics is determined by establishing Grey Forecast Model and the qualitative modification of predicted value [9]. The calculation of logistics land scale is mainly carried out from three aspects: one is to get the

total scale of regional logistics land through the calculation of social logistics quantity, and then calculate the land scale of a certain direction or specific logistics park. Secondly, start with the functional layout inside the logistics park, measure and calculate the area of each functional land, and then summarize. The third is to conduct an analogy analysis of relevant regulations and other mature logistics parks. At present, there are many studies on the urban land development intensity in China, but there is little research on the land development intensity for logistics, especially for port logistics park [10].

METHODOLOGY

PENT ANALYSIS OF INFLUENCING FACTOR OF THE DEVELOPMENT INTENSITY CONTROL INDICATORS

Based on a study, the PENT analysis method is adopted to analyse the influencing factor of the land development intensity control indicators of port logistics park [11]. And the index system structure as shown in the following figure is constructed through the refinement of the indicators of policy and regulation, economic environment, natural environment and technical environment.

Policy and regulation factors: the continuous improvement and innovation of policies related to the logistics industry is the basic guarantee for the development and prosperity of the port logistics park, and the prosperity of the logistics park is also the prerequisite for the improvement of its land development intensity [12]. Under the new situation of logistics development, it is necessary to focus on the impact of land policy, tax revenue policy and expense of taxation policy on the land development intensity index of port container logistics park [13].

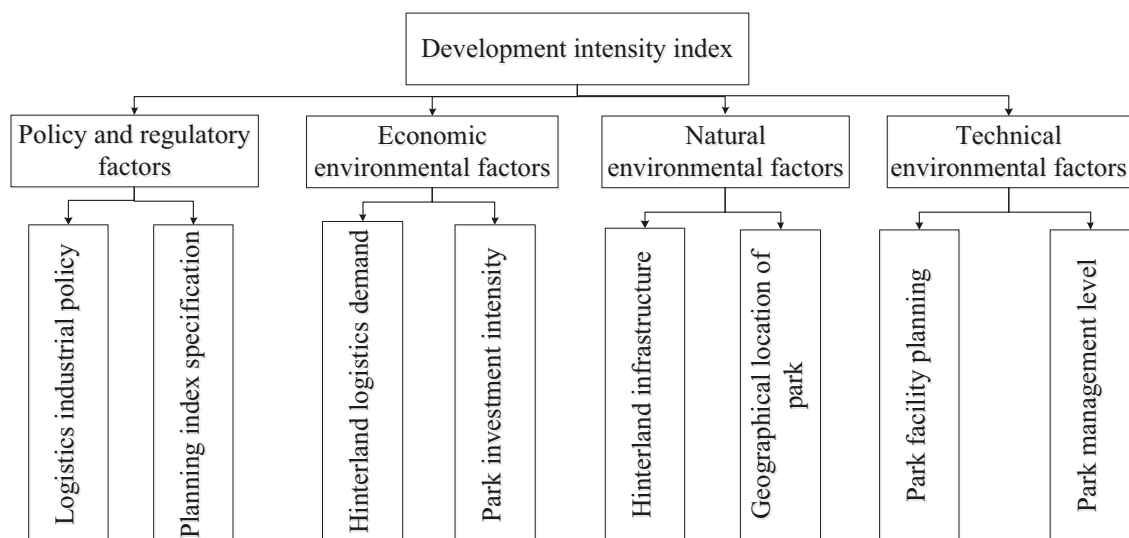


Fig. 1. The structure of index system of PENT analysis method

In terms of environmental factors, the improvement of economic development level of port hinterland will generate big logistics quantity and huge logistics demand, thus promoting the development intensity of port logistics park [14]. Therefore, the prosperity of hinterland economy in port area is an important factor to improve the development intensity of port logistics park. The investment intensity is widely applied to the land approval system, which reflects the scale operation and intensive utilization level of land. However, there is a lack of relevant regulations in China to adjust the investment intensity of logistics land. Since China's fixed asset investment statistics include the relevant fees paid for land acquisition, the investment intensity included here includes land price and infrastructure investment [15].

Natural environmental factors: the infrastructure of the hinterland of the port logistics park will also have an extremely important impact on the development intensity of the port logistics park. As the geographical location of each industrial land is different, there are differences in infrastructure conditions, traffic conditions, resources and environmental conditions, resulting in land grade differences. Therefore, there are different levels of land rent, different industries have different requirements on the bearing capacity of land rent and specific location, and different types of industrial land have different location choice.

Technical environmental factors: whether the planning and design of the facilities in the port logistics park is reasonable will affect the operational efficiency and the development intensity of the park [16]. The management level of the logistics park is directly reflected in whether it can respond to the market quickly and efficiently, and whether it can complete various logistics operations in the shortest time. Therefore, the management level affects the operational efficiency of the park, and the operational efficiency under the market economy conditions often becomes a key factor for enterprises to win.

RELEVANT THEORETICAL METHODS AND MODELS FOR DETERMINING DEVELOPMENT INTENSITY CONTROL INDICATORS

Container throughput prediction method: assume that the time series observed value of a predicted object is x_t , $t=1, 2, \dots, N$. There are m feasible single prediction methods, and x_{it} is called the fitting value (predicted value) of the i -th prediction method at time t . Among them, $i=1, 2, 3, \dots, m$, $t=1, 2, 3, \dots, N$. Let $L = (l_1, l_2, \dots, l_m)$ be the weighting coefficient of the m kinds of single-term predictions in the combined prediction, and $\sum_{i=1}^m l_i = 1, l_i \geq 0, i=1, 2, \dots, m$. Then, the IOWGA combined prediction value at the t -th moment generated by the prediction precision sequence $p_{1t}, p_{2t}, \dots, p_{mt}$ is:

$$IOWGA_L(\langle p_{1t}, x_{1t} \rangle, \langle p_{2t}, x_{2t} \rangle, \dots, \langle p_{mt}, x_{mt} \rangle) = \prod_{i=1}^m x_{p-index(it)}^{l_i} \quad (1)$$

Taking the square sum of logarithmic error as the criterion, the combined prediction model based on the Induced Ordered

Weighted Geometric Averaging (IOWGA) operator can be expressed as the following model:

$$\min S(L) = \sum_{i=1}^m \sum_{j=1}^m L_i L_j \left(\sum_{t=1}^N e_{a-index(it)} e_{a-index(jt)} \right) \quad (2)$$

$$S \cdot t = \begin{cases} \sum_{i=1}^m L_i = 1 \\ L_i \geq 0 \end{cases}$$

Calculation method of the total area of the park: at present, the typical research on the calculation method of the scale of logistics parks in China is the proportional summary method and the space-time consumption method. The model of the proportional summary method is shown in figure 2. As the logistics quantity (container throughput) of the port container logistics park is directly measured, the model formula of the proportion summary method can be simplified as:

$$S_j = S \times \beta_j = (L_i i_2 \alpha / 365) \times (L_j / L) = (L_j i_2 \alpha) / 365 = qa / 365 \quad (3)$$

Among them: q is the logistics quantity of port container logistics park, unit: t

α is the land parameter of unit production capacity, the unit is m^2/t , and its value ranges from 30 to 50.

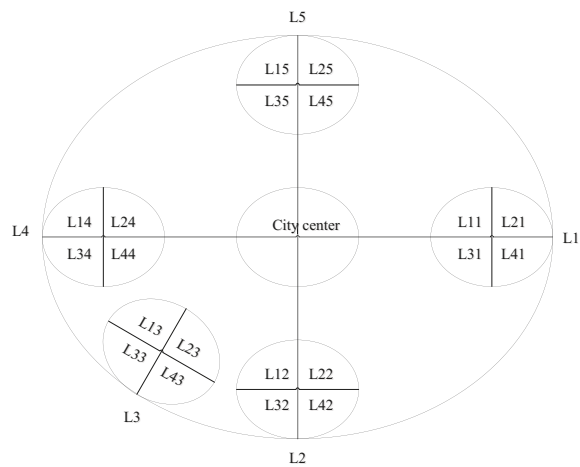


Fig. 2. The collecting of proportion

The model of the improved space-time consumption method is shown in the following figure. As the main business of the port container logistics park is the storage and distribution of containers and cargo, the type of cargo in the park can be considered as a kind of container. Meanwhile, the revised parameters β and γ , as well as the modified mathematical model formula are introduced:

$$A = \beta(VTQF / 365S) / \gamma \quad (4)$$

Among them, β is the utilization factor of the warehouse area, and its value ranges from 1.7 to 2.0. And γ is the ratio of warehouse area to total park size, which ranges from 0.3 to 0.4.

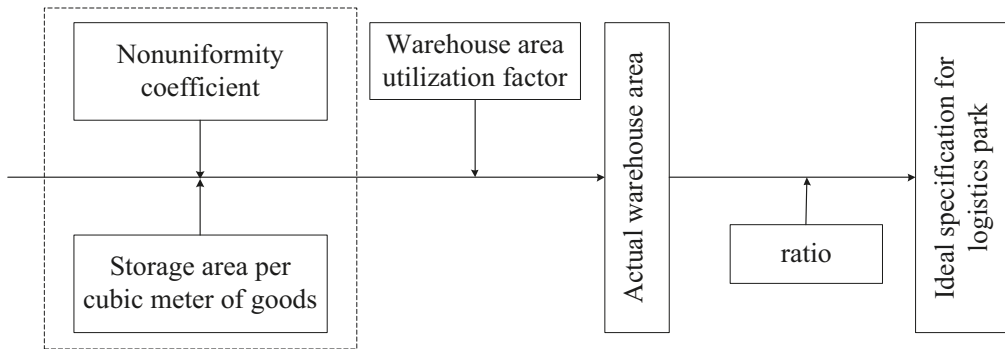


Fig. 3. The structure of improving mathematical model

Calculation model of yard area of container: the actual area of container, the land area of the gantry crane operation and the area of corridor make up the yard area of container. Factors such as stacking height, average stacking period of container, and area of unit container determine the yard area of container. The calculation formula is as follows:

$$S_1 = Q_1 \times D_1 \times kt_1 / (T \times H_1 \times k_H) \times S^1 \quad (5)$$

Among them:

- S_1 – The yard area required for the container, unit: m^2
- Q_1 – Annual container throughput of container yards entering the logistics park, unit: TEU
- D_1 – Average storage period of container, unit: d
- k_{t1} – Yard imbalance coefficient
- T – Annual operating days of the yard, unit: d
- H_1 – Stacking layer of container
- k_H – The utilization factor of the height
- S^1 – Area required for unit plane box, unit: m^2/TEU

Estimation model of the site area of the freight station: the site area of the freight station is determined by factors such as the amount of disassembly and assembly of container into and out of the site, the floor area of the unit cargo, the operating days and the average storage period of containers. The following calculation formula is adopted:

$$S_2 = Q_2 \times D_2 \times kt_2 \times S^2 \times f_2 / T \quad (6)$$

Among them:

- S_2 – The area required for the freight, unit: m^2
- Q_2 – The annual total amount of containers entering the freight station, unit: TEU
- D_2 – Average stockpiling period of container, unit: d
- k_{t2} – Stockpiling imbalance coefficient
- T – Annual operating days of freight station, unit: d

- f_2 – The utilization coefficient of the site area
- S^2 – Area required for unit container cargo, unit: m^2/TEU

Calculation model of the floor area of circulating warehouse: generally, for a stable container logistics park, its warehouse area accounts for about 30–40% of the total park scale. The size of warehouse area is influenced by factors such as quantity of work, utilization rate of area and turnover cycle of the warehouse. The following calculation formula is adopted:

$$S_3 = Q_3 \times D_3 \times kt_3 / T \times S^3 \times f_3 \times \eta_3 \quad (7)$$

Among them:

- S_3 – The floor area of the circulating warehouse, unit: m^2
- Q_3 – The amount of cargo entering the circulating warehouse, unit: t
- D_3 – Average storage period of warehouse cargo, unit: d
- k_{t3} – Unbalance coefficient of storage yard of warehouse
- T – Annual operation days of logistics warehouse, unit: d
- f_3 – The area utilization coefficient of logistics warehouse site
- S^3 – Average stockpiling area per unit cargo, unit: m^2/t
- η_3 – Influence coefficient of cargo operation

Calculation model of building area of the park: the size of the building area is directly related to the logistics quantity in the park. The more cargo, the larger the required building area. Just like the principle of the space-time consumption method established by Cheng Shidong, the following calculation formula is adopted:

$$S = \frac{Q}{q} \times \frac{1}{a} \times \frac{T}{365} \quad (8)$$

Among them:

- S – Building area of the park, unit: m^2
- q – volume of unit cargo in storage, unit: t/m^2
- T – Cycle time of warehouse cargo, unit: d
- a – Utilization coefficient of building area

RESULTS AND DISCUSSION

PREDICTION OF CONTAINER THROUGHPUT

The container throughput is used to replace the logistics quantity of the park. The investigation of the logistics quantity

of the Cuntan port logistics park from 2003 to 2011 is as follows:

Tab. 1. Logistics quantity from 2003 to 2011(TEU)

Year	2003	2004	2005	2006	2007	2008	2009	2010	2011
Quantity	49321	79726	109901	150154	204171	241467	203048	250034	321000

According to the weighting idea of the IOWGA operator algorithm, calculate the combined predicted value based on the combined prediction model, and the above combined predicted value is substituted into the combined prediction model based on IOWGA operator according to the criterion of sum of squares of logarithm error, the optimal weight coefficients of the combined prediction model based on IOWGA operator calculated with the quadratic programming model are $L_1=0.8662771$ and $L_2=1337229$. By substituting L_1 and L_2 into the combined prediction model, the combined predicted value from 2003 to 2011 is obtained, and the obtained mean mean square error is 2144.64.

MEASUREMENT AND CALCULATION OF THE TOTAL AREA OF THE PARK

According to the formula of proportional summary method and space-time consumption method, based on the predicted value of the combined forecast for the target year's logistics quantity, the land scale of Cuntan port logistics park in different years is calculated. The scale measured by the space-time consumption method is the lower limit, and the scale measured by the proportional summary method is the upper limit. The total theoretical scale of the park takes the average of the upper and lower limits. The results are shown in the table below.

Tab. 2. Total scale of park land using of target year (square meter)

Measure	2015	2020	2030
Proportional summary method	879611.08	1580878.55	3946733.2
Space time consumption method	431052.52	774707.93	1934092.62
Total theoretical scale	655331.80	1177793.24	2940412.92

METHOD FOR CALCULATING THE AREA OF THE CORE FUNCTIONAL AREA

Based on the predicted value of the combined forecast for the target year's logistics quantity, the relevant formula is used to calculate the yard area, the area of the container freight station, the area of the circulating warehouse of the Cuntan port logistics park and the total floor area of the park. The calculation results are shown in the following table.

Tab. 3. The prediction of scale of functional areas (square meter)

Year	2015	2020	2030
Yard area	157878.91	283747.43	708388.01
Cargo terminal area	19937.85	35833.25	89459.29
Warehouse	134580.50	241874.42	603850.18
Construction area	270250.88	485707.63	1212590.60

CALCULATION OF INDEX CORRECTION COEFFICIENT

The container throughput obtained above only reflects the logistics demand volume factor which belongs to the economic influencing factors. To correct the development intensity index of park obtained by container throughput, firstly, the ranking weights that are relatively important to the target layer are used as the weights of the factors in the factor layer, and it is determined by the analytic hierarchy process, namely:

$$A = (0.0461, 0.0092, 0.4238, 0.1413, 0.1967, 0.0656, 0.0294, 0.0881)$$

On this basis, the evaluation on whether all the influencing factors are favourable for improving the land development intensity of Cuntan port logistics park is conducted, and the normalization is carried out to obtain the evaluation matrix R.

$$R = \begin{bmatrix} 0.30 & 0.40 & 0.20 & 0.05 & 0.05 \\ 0.20 & 0.30 & 0.30 & 0.10 & 0.10 \\ 0.70 & 0.30 & 0.00 & 0.00 & 0.00 \\ 0.50 & 0.45 & 0.05 & 0.00 & 0.00 \\ 0.60 & 0.35 & 0.05 & 0.00 & 0.00 \\ 0.35 & 0.45 & 0.15 & 0.05 & 0.00 \\ 0.25 & 0.35 & 0.25 & 0.10 & 0.05 \\ 0.40 & 0.45 & 0.10 & 0.05 & 0.00 \end{bmatrix} \quad (9)$$

The most common matrix multiplication method is used for fuzzy operations:

$$B = A * R = (0.56655, 0.360225, 0.05488, 0.01385, 0.004695).$$

According to the principle of maximum membership degree, the corresponding evaluation is very favourable, and the correction coefficient is 10%.

DETERMINATION AND APPLICATION OF DEVELOPMENT INTENSITY INDEX

To calculate the development intensity index, firstly, the lower limit value of relevant indicators is determined based on the predicted total scale (parcel area) of theoretical land in the park in 2020; secondly, for the guiding and operational principles of the indicators, the upper limit of the development intensity index is calculated based on the relevant land data of Cuntan port logistics park in 2030; finally, the theoretical development intensity index obtained is revised, and a reasonable land development intensity control index of the Cuntan port logistics park is obtained to guide the future development and construction of the park.

Tab. 4. The related land scale of port logistics park of Cuntan port (square meter)

Year	2015	2020	2030
Total theoretical scale	655331.80	1177793.24	2940412.92
Yard area	157878.91	283747.43	708388.01
Cargo terminal area	19937.85	35833.25	89459.29
Warehouse	134580.50	241874.42	603850.18
Construction area	270250.88	485707.63	1212590.60

According to the proportion of the land with various functions, the theoretical land development intensity control index of Cuntan port logistics park is calculated, and the obtained 10% of the correction coefficient of the land development intensity control index of the Cuntan port logistics park is adopted to calculate the revised land development intensity control index of the Cuntan port logistics park, as shown in table 5.

Tab. 5. The revised index of land development intensity of logistics park of Cuntan port

Average plot ratio of the park	0.45~1.13	Average building density (%)	32~60
Storage function area volume rate	0.45~2.20	Building density of warehouse function area (%)	52
Vegetation rate (%)	6~20	Construction coefficient (%)	65

The revised land development intensity control index is also valuable for the planning and construction of other port container logistics parks. Among them, the plot ratio and building density of the warehouse functional area can be directly applied to control the development intensity of specific plot of land; the average plot ratio, building density and ratio of green space of the park can control the development intensity of the whole land; and the index of greening rate also applies to the control of specific plot of land.

CONCLUSION

On the basis of comparing the land development intensity index of port container logistics park at home and abroad, a three-level index system structure for the analysis of the influencing factors of the land development intensity index of port container logistics park is constructed, and the PENT analysis method is adopted to analyse the influencing factor of the land development intensity index in the park from four aspects: policy and regulation, economic environment, natural environment and technical environment. On this basis, the research method to measure the land development intensity control index of port container logistics park is proposed. By referring to and improving the relevant models, the land development intensity control index of the port container logistics park is finally calculated with an example.

Although the feasibility of the method is verified by a special case, the method for calculating the development intensity control index and the results calculated therefrom have general applicability.

ACKNOWLEDGMENT

The research described in this paper was financially supported by the National Natural Science Foundation of China (No.51678058), The National Key Research and Development Program of China (2016YFC0700401).

REFERENCES

1. D. Zhou, L. Zhang, and L. Hao, "Spatiotemporal trends of urban heat island effect along the urban development intensity gradient in China," *Science of the Total Environment*, Vol. 544, No. 2, pp. 617-626, 2016.
2. S. Fang, X. Jia, and Q. Qian, "Reclamation history and development intensity determine soil and vegetation characteristics on developed coasts," *Science of the Total Environment*, Vol. 586, No. 6, pp. 1263, 2017.
3. J. C. J. Bonzongo, A. K. Donkor, and A. Attibayeba, "Linking landscape development intensity within watersheds to methyl-mercury accumulation in river sediments," *Ambio*, Vol. 45, No. 2, pp. 196-204, 2016.
4. H. Chen, K. Wang, and J. M. Wang, "A case study on the sensitivity of downstream development to typhoon intensity and its initial location," *Meteorological Applications*, Vol. 24, No. 3, pp. 444-456, 2017.
5. M. Zare, "Recent development of the earthquake strong motion-intensity catalog and intensity prediction equations for Iran," *Journal of Seismology*, Vol. 21, No. 4, pp. 1-23, 2016.
6. Y. Guo, Z. Zeng, and J. Tian, "Uncovering the strategies of green development in a Chinese province driven by reallocating the emission caps of multiple pollutants among industries," *Science of the Total Environment*, Vol. 607-608, pp. 1487, 2017.
7. S. Choo, D. Sohn, and M. Park, "Mobility characteristics of the elderly: A case for Seoul Metropolitan Area," *Ksce Journal of Civil Engineering*, Vol. 20, No. 3, pp. 1023-1031, 2016.
8. Y. S. Kang, I. H. Park, and S. Youm, "Performance Prediction of a MongoDB-Based Traceability System in Smart Factory Supply Chains," *Sensors*, Vol. 16, No. 12, pp. 2126, 2016.

9. S. S. Lee, S. I. Park, and J. Seo, "Utilization analysis methodology for fleet telematics of heavy earthwork equipment," *Automation in Construction*, Vol. 92, pp. 59-67, 2018.
10. B. K. Lee, R. Zhou, R. D. Souza, "Data-driven risk measurement of firm-to-firm relationships in a supply chain," *International Journal of Production Economics*, Vol. 180, pp. 148-157, 2016.
11. N. F. Basir, S. Kasim, R. Hassan, H. Mahdin, A. Ramli, M. F. Md Fudzee, and M. A. Salamat, "Sweet8bakery Booking System," *Acta Electronica Malaysia*, Vol. 2, No. 2, pp. 14-19, 2018.
12. R. Hamzah, S. Kasim, R. Hassan, H. Mahdin, A. A. Ramli, M. F. Md Fudzee, and M. A. Salamat, "Taxi Reservation System of Batu Pahat Taxi Association," *Acta Electronica Malaysia*, Vol. 2, No. 2, pp. 20-24, 2018.
13. S. Sathishkumar, and M. Kannan, "Design and Fatigue Analysis of Multi Cylinder Engine and Its Structural Components," *Acta Mechanica Malaysia*, Vol. 2, No. 2, pp. 10-14, 2018.
14. A. Abugalia, M. Shaglouf, "Analysis of Different Models of Moa Surge Arrester for The Transformer Protection," *Acta Mechanica Malaysia*, Vol. 2, No. 2, pp. 19-21, 2018.
15. R. Kumar, "Comparison of Instruction Scheduling and Register Allocation for Mips And Hpl -Pd Architecture for Exploitation Of Instruction Level Parallelism," *Engineering Heritage Journal*, Vol. 2, No. 2, pp. 04-08.
16. S. Tao, "Evaluation of Technology Innovation in Hubei Province," *Engineering Heritage Journal*, Vol. 2, No. 2, pp. 09-10, 2018.

CONTACT WITH THE AUTHORS

Jingyuan Zhao
e-mail: zjyqtt@163.com

School of Architecture
 Chang'an University
 Xi'an 710061
CHINA

NUMERICAL SIMULATIONS OF LINEARLY STRATIFIED FLOW PAST SUBMERGED BODIES

Weizhuang Ma¹

Yunbo Li²

Yong Ding¹

Kaiye Hu¹

Linxin Lan¹

¹ College of Shipbuilding Engineering, Harbin Engineering University, China

² College of Ocean Science and Engineering, Shanghai Maritime University, China

ABSTRACT

In this study, a methodology was presented to predict density stratified flows in the near-field of submerged bodies. The energy equation in temperature form was solved coupled with momentum and mass conservation equations. Linear stratification was achieved by the definition of the density as a function of temperature. At first, verifications were performed for the stratified flows passing a submerged horizontal circular cylinder, showing excellent agreement with available experimental data. The ability of the method to cope with variable density was demonstrated. Different turbulence models were used for different Re numbers and flow states. Based on the numerical methods proposed in this paper, the stratified flow was studied for the real scale benchmark DAPRA Suboff submarine. The approach used the VOF method for tracing the free surface. Turbulence was implemented with a $k - \omega$ based Detached Eddy Simulation (DES) approach. The effects of submarine speed, depth and density gradient on the free surface wave pattern were quantitatively analyzed. It was shown that, with the increasing of the speed of the submarine, the wavelength and wave height of the free surface wave were gradually increasing. The wave height of the free surface wave was gradually reduced as the submarine's depth increased. Relative to the speed and submarine depth, the changes of the gradient density gradient have negligible effects on the free surface wave field.

Keywords: Stratified flow, circular cylinder, internal wave, Suboff, equation of state

INTRODUCTION

As is known to us all, the ocean is density stratified especially in the vertical direction. When a submerged body moves in the ocean, it can leave a lot of wake features because of the stratification effect. It also can produce some singular flow phenomena which are different from those in the uniform flow environment. For instance, lee waves can be observed clearly in the wake of the submerged bodies when they are moving at low speeds. These characteristic wakes will cause some changes in the wind waves on the free surface. For example, the wave amplitude on the free surface may be converged and diverged for a long time [1-3]. Besides, a lot of researchers describe the formation of lee waves for

the flows around cylinders with different Froude number (Fr) based on the methods of asymptotic analysis [4-6]. Many other researchers also study the linearized density stratified flow passing a circular cylinder by experimental methods [7-10]. Meunier showed experimentally and numerically that vortices can be emitted for strong stratifications at moderate Reynolds numbers [11].

There are fewer numerical works on the flow around a cylinder in a linear stratified fluid. Meunier described numerically how the three-dimensional instabilities of a cylinder wake are modified by the presence of a linear density stratification [12]. Boyer has founded a large number of regimes when the Fr varies from 0.02 to 13 and the Reynolds number (Re) varies from 5 to 4000. For the condition of being

strongly stratified, the study revealed the presence of internal waves, of an accelerated flow on the centerline. Winters and Armi studied the recirculation bubble upstream of the cylinder, which is known as the blocking effect [13]. The stratification seemed to prevent the appearance of vortices, due to the stabilization of the stratification. Stratified wakes of other real scaled submerged body have received less attention. Esmailpour has studied the stratified flow around naval vessels. It is shown that the generation of internal waves requires energy that results in an increase in resistance [14]. Chang presented the CFD computations for a vessel in a stratified fluid. They computed the internal and surface waves generated by the DARPA Suboff submarine advancing in a two-layer fluid, for different Froude numbers, and studied the wave pattern [15].

In this paper, the continuity equation and the momentum conservation equation were solved for the motion of the flow. The energy equation was used to introduce the temperature into the numerical method. The equations were closed by the 1980 international standard seawater equation of state in order to realize the density stratification of the fluid. Numerical simulations of stratified flow passing a cylinder were conducted in order to verify the validity of the methods. The simulations cover from low *Fr* number to the high *Fr* number. The numerical results agree well with the experimental results of Boyer. Then, the established method was used to analyze the stratified flow past the real-scale Suboff submarine flow. The influences of speed, depth and stratification characteristics on the free surface wave of the submarine are analyzed.

NUMERICAL METHOOD

GOVERNING EQUATIONS

Since the speed of the submerged body is comparatively very low, the flow is still in the category of incompressible fluid. The continuity equation and the momentum conservation equation can be used to solve the fluid motion. The energy conservation equation in terms of temperature is used to introduce the density anomaly into the numerical method. Finally, the 1980 standard seawater equation of state is used to realize the closure of the equations. The basic governing equations for numerical solution are expressed as follows.

$$\frac{\partial \rho}{\partial t} + \nabla \cdot (\rho \vec{v}) = 0 \quad (1)$$

$$\frac{\partial}{\partial t}(\rho \vec{v}) + \nabla \cdot (\rho \vec{v} \vec{v}) = -\nabla p + \nabla \cdot (\tau) + \rho \vec{g} \quad (2)$$

$$\frac{\partial(\rho T)}{\partial t} = -\nabla \cdot (\rho \vec{u} T) + \nabla \cdot \left(\frac{k}{c} \nabla(T) \right) \quad (3)$$

In the above formula, *T* is the temperature, and the unit is K. According to the 1980 standard seawater state equation, the water density can be expressed as a function of temperature and salinity. This study only discusses the effect of temperature on density. In the calculation process, only the linear part of the temperature in the equation of state was taken into account. The detailed functional relationship between temperature and density is:

$$\rho(T, S) = \rho_0 + AS + BS^{3/2} + CS \quad (4)$$

$$A = 8.24493 \times 10^{-1} - 4.0899 \times 10^{-3}(T - 273.15) \quad (5)$$

$$B = -5.72466 \times 10^{-3} + 1.0227 \times 10^{-4}(T - 273.15) \quad (6)$$

$$C = 4.8314 \times 10^{-4} \quad (7)$$

$$\rho_0 = 999.842594 + 6.793952 \times 10^{-2}(T - 273.15) \quad (8)$$

In order to verify the accuracy of the numerical method in this paper, the flow characteristics around the cylinder in the stratified flow are first analyzed. The computational domain diagram and mesh of this study is shown on Figure 1. Some dimensionless parameters used in this paper are:

Internal Froude number,

$$Fr = \frac{U}{ND} \quad (9)$$

Reynolds number,

$$Re = \frac{UD}{\nu} \quad (10)$$

Dimensionless time,

$$t'_n = \frac{t_n U}{d} \quad (11)$$

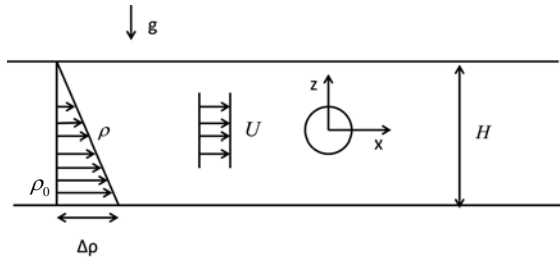
$$t'_e = \frac{t_e U}{d} \quad (12)$$

Where U is the flow velocity, and d is the diameter of the cylinder, t_n is the flow time in numerical simulation and t_e is the flow time in the experimental conditions, t'_n is the dimensionless time for numerical simulations, t'_e is the

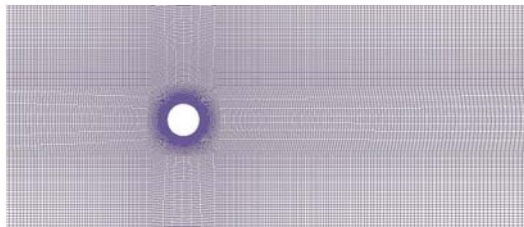
dimensionless time for the experiments, ν is the kinematics viscosity coefficient of water, N is the buoyancy frequency:

$$N = \sqrt{-\frac{g}{\rho_0} \frac{\Delta\rho}{H}} \quad (13)$$

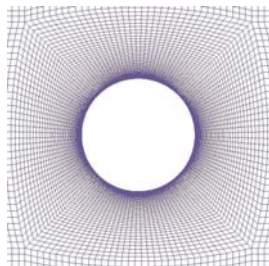
g is the acceleration of gravity, and other parameters for N are shown in Figure 1(a).



(a) Computational domain diagram



(b) Mesh around the cylinder



(c) O-block around the cylinder

Fig.1. Computational domain

Through the above process, the density of the fluids is linearly stratified. In order to be consistent with the experimental conditions of Boyer, the height of the fluid field is 0.2m, the cylinder diameter is 0.024m, and the inlet and outlet boundaries are far enough. The reference density is $\rho_0 = 998 \text{ kg/m}^3$, and density change is $\Delta\rho = 20.58 \text{ kg/m}^3$, then the buoyancy frequency is $N = 1.0 \text{ (1/s)}$.

According to the theory research of Boyer, when the Fr number is small, there are lee waves in the wake, and when the Fr number is large, the vortex structure in the wake plays a key role. Through the test of Boyer, when the Fr reaches to 0.4, the main features in the wake are already not the lee wave, and then the vortex structure in the wake is getting the upper hand. According to this conclusion, we define the $Fr > 0.4$ is high, and the $Fr < 0.4$ number is low.

The main operating conditions and specific settings are shown in Table 1. The numerical results are compared with the experimental results of Boyer.

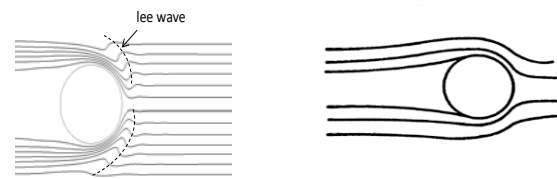
Tab. 1. Conditions of stratified flow around a cylinder

Index		Fr	Re
1	Low Fr	0.018	12
2		0.08	1500
3	High Fr	0.88	480
4		1.77	960

NUMERICAL RESULTS OF THE STRATIFIED FLOW AROUND THE CYLINDER

THE NUMERICAL RESULTS FOR LOW Fr

In this paper, the numerical simulation of the stratified flow around a circular cylinder at low Fr is performed. The streamline pattern of the numerical simulation and the experimental results are shown in Figure 2.



(a) numerical result

(b) experimental result of Boyer

Fig.2. Streamline for $Fr=0.018$, $Re=12$

It can be seen that the numerical results are consistent well with the experimental results. There are also some differences in the numerical results, and the lee wave wake pattern of the cylinder is symmetric due to the volume effect of the cylinder. Also, the lee wave peak line is asymmetric up and down. There is no new lee wave generation in the direction of flow. Figure 3 shows the velocity profile of the numerical results at $x = \pm 7.5d$ when $t'_n = 11, 22$ and 54. Figure 3(a) is the velocity profile curve for the upstream and Figure 3(b) is the velocity profile curve for the downstream. The flow diagram shows that the velocity crest value of upstream velocity profile and the velocity trough value of the downstream velocity profile are all increasing with time. The flow formed in the stratified flow is a quasi steady state, and the velocity profile is slightly different at different time.

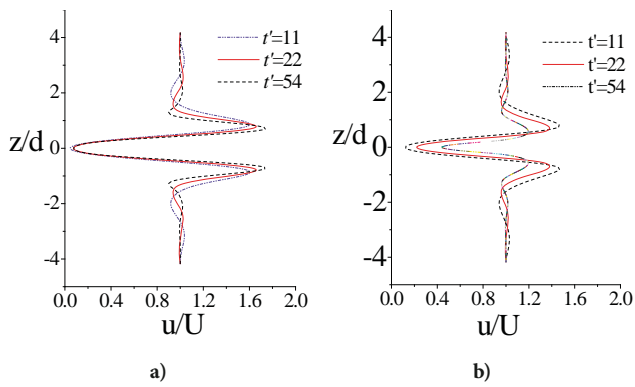


Fig. 3. Numerical results of velocity profiles upstream and downstream of cylinder at $x = \pm 7.5d$ for $Fr=0.018$, $Re=12$, $t'_n = 11, 22, 54$.

Figure 4 is the velocity profile curve at $t'_e = 21, 42$ and 62 , in which Figure 4(a) is the velocity profile curve for the upstream and Figure 4(b) is the velocity profile curve for the downstream. The study shows that the downstream speed profile curve is “two sections curve” with the relative speed less than 1.0 in the near of the axis. The velocity profile of the numerical results is qualitatively consistent with the experimental results.

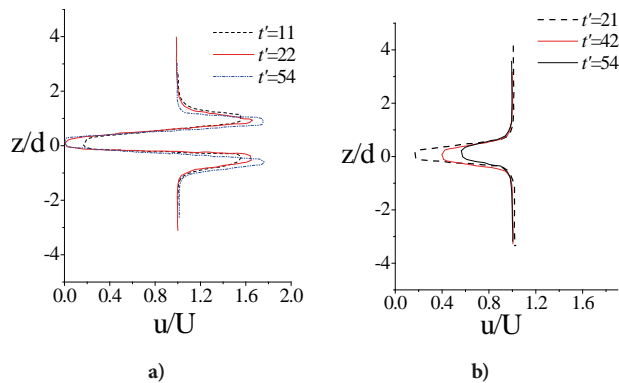


Fig. 4. Experimental results of velocity profiles upstream and downstream of cylinder at for $Fr=0.018$, $Re=12$, $t'_e = 21, 42, 62$

The numerical time is not corresponding to the experimental time in the beginning. However, in a numerical moment, if the upstream velocity profile is corresponding to the test time, then the downstream velocity profile of the numerical results will bring into correspondence with the test results at the same time during the subsequence. Figure 5 shows the numerical results of $x = \pm 7.5d$ at $t'_n = 15$ and $t'_n = 67$. The comparison of the numerical results to the experimental velocity profile at $t'_e = 21$ and $t'_e = 62$ can verify this rule. The extreme of the velocity profile represents the maximum or minimum value of the velocity somewhere. The relative error of the trough is less than 2%. This proves that the numerical results agree well with experimental results quantitatively. This proposed model is an effective method for the simulation of the internal wake at low Fr number.

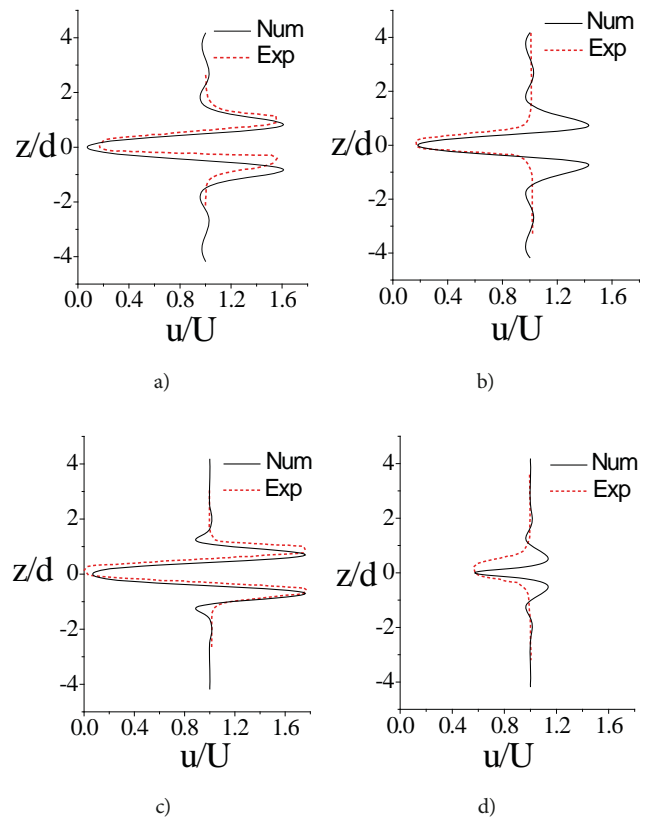


Fig. 5. Velocity profiles upstream and downstream of cylinder under numerical and experimental conditions. (a, c) upstream; (b, d) downstream

THE INFLUENCE OF TURBULENCE MODEL ON NUMERICAL RESULTS

Based on the previous work for low Fr , keeping the same $Fr=0.08$, we change the speed and the characteristic length of the cylinder in order to get different numerical simulation results for Reynolds number varying from 240 to 6000. It was found that the wake characteristics are similar below the $Re=98.7$. It shows that the flow line is “calabash shape” near the axis and also the lee wave is generated behind the cylinder. The results for different turbulence models at $Re=1500$ are shown in Figure 6.

We can find that the characteristics of the wake and the “calabash shape” streamline feature in the wake of the RSM model results are the closest to that in the laminar flow model. The SST $k-\omega$ model is more similar to the laminar state [17]. The $k-\varepsilon$ model results are relatively largely different with the laminar model. For the lee wave characteristics in the wake, the results under RSM model are in good agreement with the laminar model results. There is only one pair of lee wave in the results of $k-\varepsilon$ model. The lee wave of the SST $k-\omega$ model decays very quickly, and there are only two pairs of lee waves. In fact, the turbulence model is based on the assumption of the eddy viscosity hypothesis and isotropic [18]. But in the density stratified fluids, the density is not isotropic, so it is more reasonable to use the RSM model which is not restricted by isotropy assumption. It is worth

mentioning that in the implementation of the RSM model, we use the wall function to deal with the near wall. If it uses the enhanced wall function and the result is similar to that of the SST $k-\omega$ model under the same condition. When it comes to the $k-\varepsilon$ model, there is no difference between the results of the SST $k-\omega$ model using the wall function and the enhanced wall function. It has the same conclusion between the $Re=6000$ and the $Re=1500$ [19].

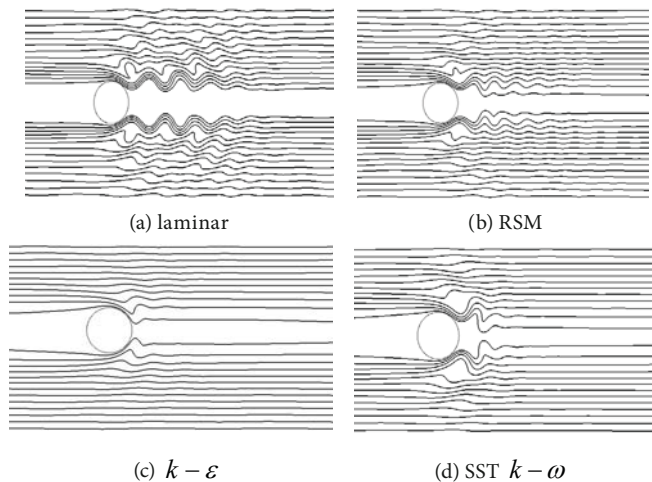


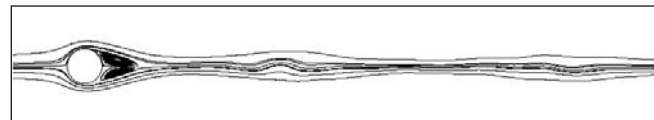
Fig. 6. The numerical results under different turbulence models

THE NUMERICAL RESULTS FOR HIGH Fr

This paper uses the $k-\omega$ based DES model to study the wake of the cylinder at high Fr in the stratified flows. Figure 7 shows the experimental results and numerical results of the flow around a circular cylinder under the condition of $Fr=0.88$ and $Re=480$. The two results are roughly the same for the wake streamline shape. Also, they both have a pair of vortices in the wake behind the cylinder [20]. The first wave packet generates at a distance of 6 times than the diameter of the cylinder center. The second wave packets generates at a distance of 16 times than the diameter of the cylinder center. The difference is that wave package amplitude of numerical results is smaller than the experimental results. In fact, in order to keep consistent with experiment, the distance from the center of the cylinder to the upper and lower bound is $4.17d$. Thus, there is a non-negligible effect for the boundary conditions during the numerical simulations [21]. Also, the experiment takes the manner of dragging a cylinder, so the boundary conditions of the physical tank are relatively small. Figure 8 shows the experimental results and numerical results of the flow around a circular cylinder under the condition of $Fr=1.77$ and $Re=960$. The typical characteristics of the wake in this condition are that the wake presents fully turbulent wake state. There is a strong vortex structure near the cylinder wake. Obviously, the numerical method successfully simulates these features.

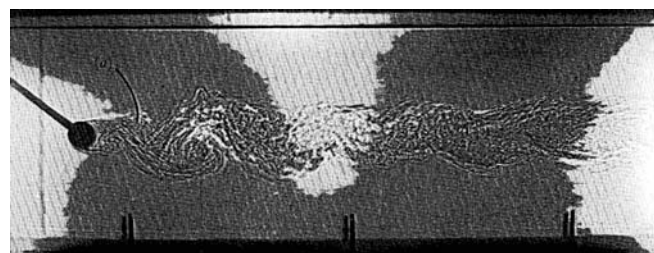


(a) Experiment result (Boyer,1989)

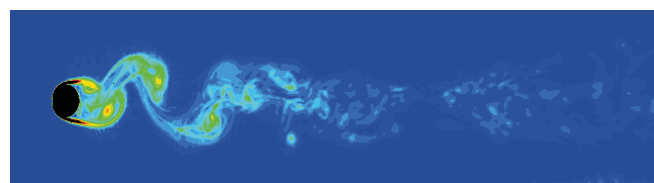


(b) Numerical result

Fig.7. Experimental and numerical results for $Fr = 0.88, Re = 480$



(a) Experiment result (Boyer,1989)



(b) Numerical result

Fig. 8. Experimental and numerical results for $Fr = 1.77, Re = 960$

NUMERICAL RESULTS OF THE STRATIFIED FLOW AROUND SUBOFF

Based on the numerical method established above, the numerical simulations of the flow field of the moving submarine in the mixed stratified flow are carried out. The simulated submarine uses the well-known DARPA Suboff full-appended model, and the model is magnified 20 times to obtain a real-scale submarine. The main particulars of the Suboff model and the simulated real scale model are shown in Table 2.

Tab. 2. Main particulars of the Suboff model

	Suboff Model	Simulation Model
L_{OA} (m)	4.356	87.12
L_{BP}	4.261	85.22
D_{max}	0.508	10.16
S (m ²)	5.989	2395.6
∇ (m ³)	0.699	5592

In order to accurately capture the flow field details and flow in the turbulent state, this paper uses the turbulence model of $k-\omega$ based detached eddy simulation (DES) method to numerically simulate the stratified flow around the Suboff submarine. The convective item discrete format adopts the bounded center difference format. The diffusion item discrete format uses a central difference format, and the time item discrete format uses a second order up wind format [22]. At the same time, because the flow around the Suboff is a transient problem, the discrete equation is solved by PISO algorithm. The computational geometry models related to this paper have a variety of absolute dimensions. Each calculation case uses three sets of grids to perform the correlation verification process on grid independence, confirming the convergence of the grid. The geometric model and the 3-D view of the Suboff model with full appendages is shown in Figure 9.



Fig. 9. The 3-D view of the Suboff model

Since the calculations are implemented on the real scale submarine, the calculation domain needs to be large enough in order to fully capturing the hydrodynamic phenomenon in the wake field. Figure 10 is a schematic diagram of the calculation domain. The extension of the incoming flow direction is 200m, and the distance of the wake direction behind the Suboff is 1000m. The calculation domain lengths of the right and left side are 500m.

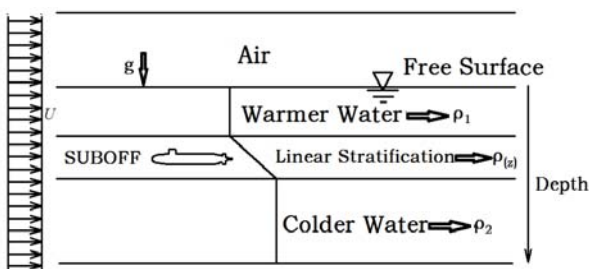


Fig.10. The stratification of the fluid

In the depth direction, the fluid of the upper layer is air, the second layer is warmer water, the middle layer is pycnocline, and the bottom layer is colder water. The thickness of each layer of water is shown in Table 3.

Tab. 3. Thickness of the different layers

	Thickness (m)
Air layer	20
Warmer water layer	20
Pycnocline layer	10
Colder water layer	40

The free surface between the air and water is located at $z=25m$. The vertical 3D geometry of the computational domain is shown in Figure 11.

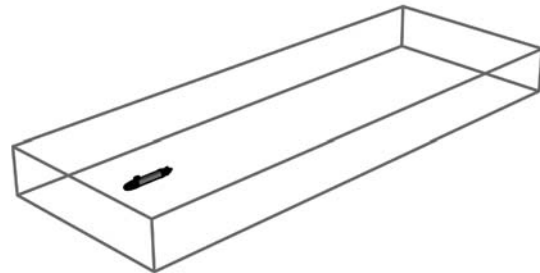


Fig.11. Calculation domain diagram of the Suboff

Tab. 4. Different cases of the simulations

Cases	Speed(kn)	Depth(m)	Density gradient(kg·m ⁻⁴)
1	10	25	0.5
2	20	25	0.5
3	30	25	0.5
4	20	15	0.5
5	20	35	0.5
6	20	25	0.1
7	20	25	1.0

In the simulations, the depths of the submarine are 15m, 25m and 35m respectively. This can be satisfied that the submarine positions are located in the upper, middle and lower of the pycnocline layer. So that the influence of the position of the pycnocline layer relative to the submarine on the wake field can be studied. Therefore, the combinations of the speed, submarine depth and density gradient are shown in Table 4. The comparative analysis of working conditions 1, 2 and 3 can be used to study the influence of submarine speed on the internal wave and free surface wave field. The comparison of working conditions 2, 4 and 5 can be used to analyze the influence of submarine depth on the wave field. The comparative analysis of working conditions 2, 6, and 7 can study the influence of ocean environmental parameters, i.e., the strength of the pycnocline layer on the wake field.

The basic principle when meshing the computational domain is to meet the requirements of the wall $y+$ of the submarine. Then the grid is gradually transiting outwards. There are also separately refined at the appendage of the submarine. The free surface is refined with a custom anisotropic cutting body mesh to ensure at least 10 grids in the wave height direction. The wavelength can be estimated by the surface ship wave-making empirical formula in wave

analysis theory. It shows that when the speed of the submarine is 10, 20 and 30 knots, the wavelength is about 16.95m, 67.79m and 152.53m separately. The computational domain size is enough to capture several wave patterns. In addition, simple refines is performed near the pycnocline layer which has a height of 10 m in order to capture the internal wave field. The final grid number is about 10 million. Figure 11 is the schematic diagram of the meshes in the bow and stern of the Suboff submarine.

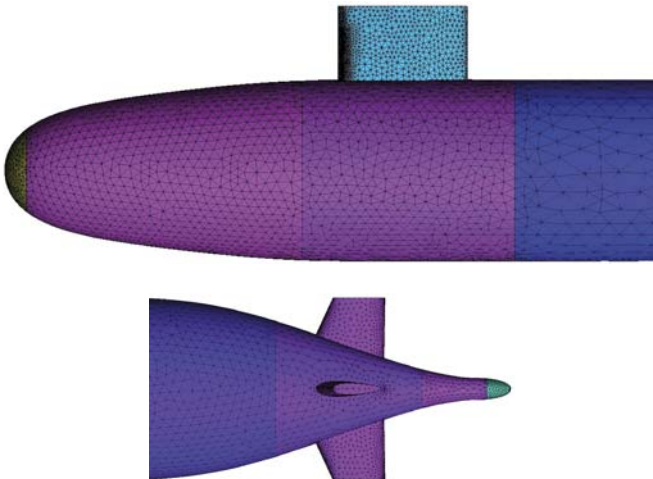


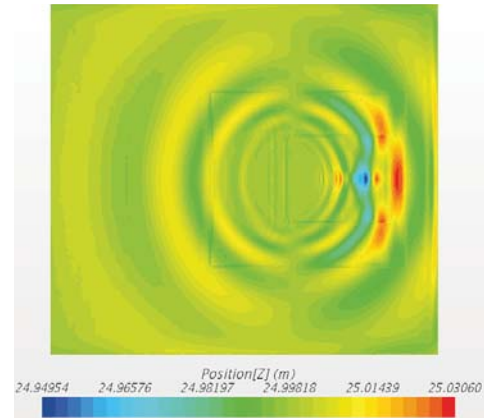
Fig. 12. Meshes around the bow and stern of the Suboff

INFLUENCE OF THE SUBMARINE SPEED ON THE FREE SURFACE

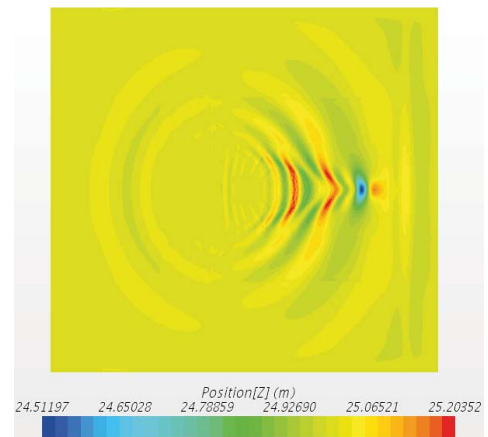
Simulations are conducted for the conditions 1, 2, and 3 in Table 4. The submarine depth is 25m, the density gradient is about $0.5\text{kg}\cdot\text{m}^{-4}$, and the speeds of the submarine are 10kn, 20kn and 30kn respectively. The simulation results are compared with each other and the influence of the submarine speed on the free surface waves is analyzed. The free surface wave pattern at different speed is shown in the Figures 13.

In summary, when the submarine sails in the stratified flow, obviously waves are generated on the free surface. The shape of these waves is similar to the Kelvin wave of a ship. As the speed of the ship increases, the wavelength of the surface wave increases gradually, which can reach to 118.49m at a speed of 30kn. At the same time, the wave height is gradually increased. The height of the waves at the speed of 10kn is on the order of centimeters. At the speed of 20kn, the wave height can be the order of decimeter. When the speed is 30kn, the maximum height of the surface wave is 1.3m. The Kelvin angle gradually decreases with the increase of the speed. When the speed is 10kn, the lateral propagation range of the scattered wave reaches 350m. When the speed is 30kn, the longitudinal propagation range of the transverse wave reaches 473.97m. At the same time, the pycnocline at the stern of the Suboff will form a catastrophic region, the thickness becomes smaller, and the length is equivalent to the length of the submarine. As the speed increases, the catastrophic region will form

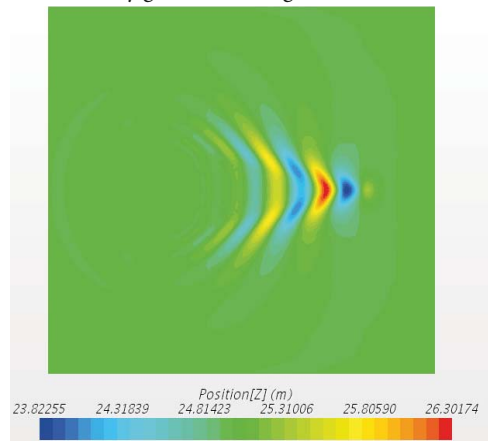
faster and faster. When the speed is 10kn, it uses 20 seconds to form a complete mutation area. But at the speed of 20kn and 30kn, the time to form complete catastrophic region can be reduced to 10s and 5s respectively. As the speed of the Suboff increases, the divergence intensity of the free surface flow field also gradually increases, showing a similar shape to the surface wave, and the roughness changes of the free surface are different.



(a) Density gradient $=0.5\text{kg}\cdot\text{m}^{-4}$, $v=10\text{kn}$, $t=40\text{s}$



(b) Density gradient $=0.5\text{kg}\cdot\text{m}^{-4}$, $v=20\text{kn}$, $t=40\text{s}$



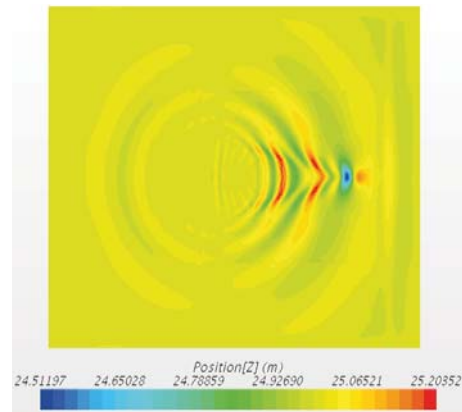
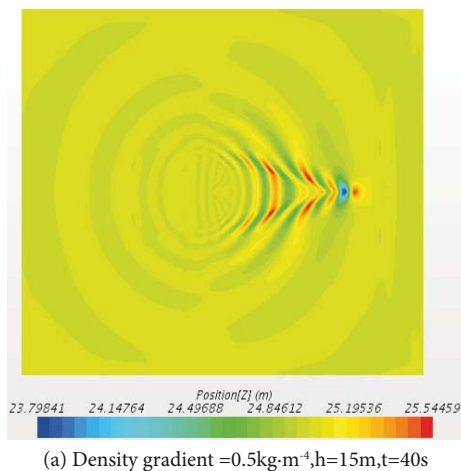
(c) Density gradient $=0.5\text{kg}\cdot\text{m}^{-4}$, $v=30\text{kn}$, $t=40\text{s}$

Fig.13. Wave pattern of the free surface at different speed

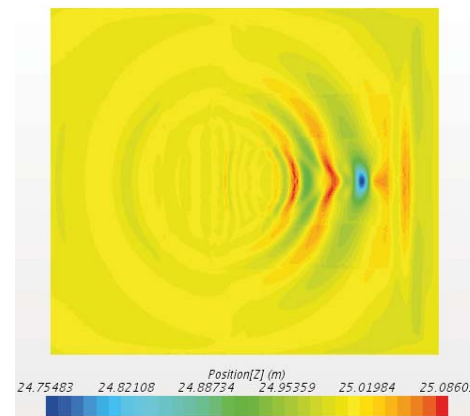
INFLUENCE OF THE SUBMARINE DEPTH ON THE FREE SURFACE WAVES

In the cases of 2, 4 and 5 in Table 4, the speed of the Suboff submarine are all 20kn, the gradient density of the pycnocline is $0.5\text{kg}\cdot\text{m}^{-4}$, and the depths of submarine are 25m 15m, and 35m respectively. As a result, the impact of the submarine depth on the wake field is studied.

Fig. 14a is a wave pattern diagram of the free surface wave-making with a depth of 15m and the time $t=40\text{s}$. At that time, about 5 complete waveforms are formed on the free surface. The longitudinal propagation distance reaches to 323.1m, and the lateral propagation distance reaches to 152.3m. In the case of 35m depth, there are about three complete waveforms on the free surface at $t=40\text{s}$, but compared to the depth of 25m and the depth of 15m, since the submarine is located below the pycnocline, the free surface waveform is greatly affected by the internal wave. The wave pattern is domain by the scattered waves. The Kelvin angle is relatively large. The longitudinal propagation distance is about 276.8m, and the lateral propagation distance is about 370.6m. In summary, as the submarine depth increases, the wave height of the free surface wave is gradually reduced. When the depth is 15m, the maximum crest is 1.02m. When the submarine depth is increases to 25m, the maximum crest is 0.36m. When the depth of the submarine continues to increase to 35m, the maximum crest is reduced to 0.15m. At the same time, when the submarine is below the pycnocline, the free surface wave pattern is greatly affected by the internal wave, which is mainly the scattered wave. The propagation distance is large. In the scale which is equivalent to the length of the submarine, the pycnocline becomes thicker behind the submarine and forms a bulge downward. When the submarine is above the pycnocline, the free surface wave pattern is mainly determined by the surface wave mode. The Kelvin angle is relatively smaller. The longitudinal propagation distance is larger and the pycnocline behind the submarine will formed a uplift.



(b) Density gradient = $0.5\text{kg}\cdot\text{m}^{-4}$, $h=25\text{m}$, $t=40\text{s}$



(b) Density gradient = $0.5\text{kg}\cdot\text{m}^{-4}$, $h=35\text{m}$, $t=40\text{s}$

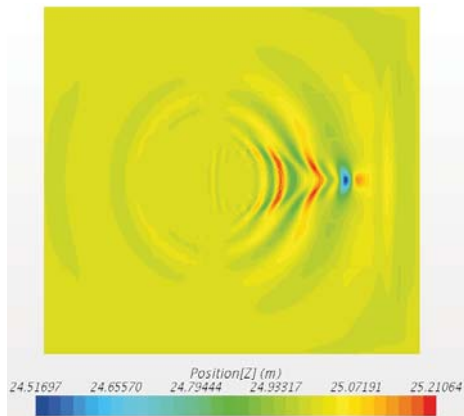
Fig. 14. Wave pattern of the free surface at different submarine depth

INFLUENCE OF THE GRADIENT DENSITY GRADIENT ON THE FREE SURFACE WAVE FIELD

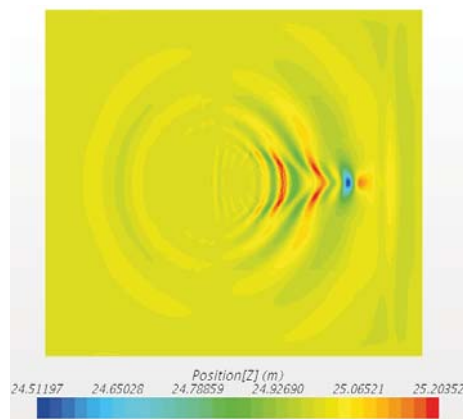
Comparison between the cases of 6, 2 and 7 in Table 4 can examine the effect of different density gradients on surface wave pattern. The speed of the submarine is 20kn, the submarine depth is 25m, and the gradient density gradient are $0.1\text{kg}\cdot\text{m}^{-4}$, $0.5\text{kg}\cdot\text{m}^{-4}$ and $1.0\text{kg}\cdot\text{m}^{-4}$ respectively.

Fig. 15(a) is a diagram showing the free surface wave pattern at $t = 40\text{s}$ in the case of a density gradient of $0.1\text{kg}\cdot\text{m}^{-4}$. The figure shows that there are about four complete wave patterns appearing on the free surface. The longitudinal propagation distance is 307m, and the lateral propagation is about 257.6m. The distance between the second crest and the third crest is far. Fig. 15(c) is a wave pattern of the free surface at $t = 40\text{s}$ in the case of a density gradient of $1.0\text{kg}\cdot\text{m}^{-4}$. When the time $t=40\text{s}$, about four wave patterns appear on the free surface. The longitudinal propagation distance is about 298m, and the lateral propagation distance is about 261.3m. In summary, the change of the density gradient of the pycnocline has little effect on the free surface wave pattern and the dispersion intensity of the free surface. When the speed and the depth of the submarine are constant, the wave height and wavelength of the surface wave and the Kelvin angle

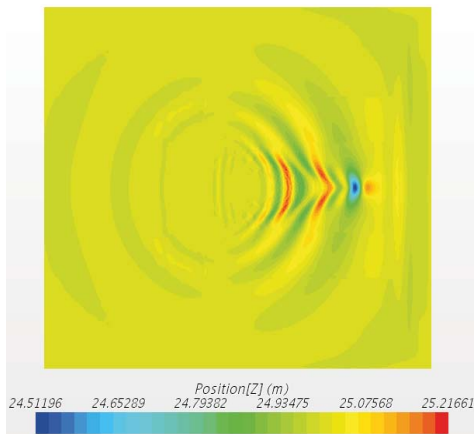
remain unchanged. Yet the effect of the change in density gradient is weak.



(a) Density gradient = $0.1 \text{ kg}\cdot\text{m}^{-4}$, $v=20 \text{ kn}$, $t=40 \text{ s}$



(b) Density gradient = $0.5 \text{ kg}\cdot\text{m}^{-4}$, $v=20 \text{ kn}$, $t=40 \text{ s}$



(c) Density gradient = $1.0 \text{ kg}\cdot\text{m}^{-4}$, $v=20 \text{ kn}$, $t=40 \text{ s}$

Fig.15. Wave pattern of the free surface at different pycnocline

CONCLUSIONS

This study has presented a methodology for the numerical simulation of the stratified flows. Then, using the established numerical simulation method, the stratified flows around a cylinder and the real-scale Suboff submarine are analyzed. The problem of free surface wave-making of the Suboff

submarine moving in a stratified flow is investigated. The effects of speed, submarine depth and density gradient on the free surface wave are investigated.

1. At the condition of $Fr=0.018$ and $Re=12$, the wake streamlines of the numerical results for the cylinder are qualitatively consistent with the experimental results. The velocity profile of the upstream and the downstream with the time are the same between the numerical results and experimental results. The peaks and troughs of the velocity are similar for the tow results and the error ratio is less than 2%.

2. When it comes to the turbulent model, it is most reasonable to simulate the stratified flow by using the RSM model which is not restricted by the isotropy assumption. The use of $k-\omega$ based DES model to simulate the flow around the cylinder and under the condition of high Fr number can get results of good agreements with the experiments. This fully shows that the proposed model for stratified flow based on the DES model can well simulate the stratified wake at high Fr number.

3. When the Suboff submarine is proceeding in the density mixed stratified flow, the Kelvin ship wave is formed on the free surface. The crests and troughs gradually propagate to the far fields from the corresponding position above the submarine. Both transverse wave and scattered wave exist. The divergence intensity distribution of the free surface exhibits a shape similar to the wave pattern. The roughness at different positions is different. At the same time, due to the disturbance of the submarine, the thickness of the pycnocline near the submarine tail will change to a certain extent, forming a catastrophic area or a raised area corresponding to the length of the submarine. These changes can be propagated to the far wake field.

4. With the increase of the speed of the submarine, the wavelength and wave height of the free surface wave are gradually increasing. The Kelvin angle gradually decreases. With the increase of the submarine's depth, the wave height of the free surface wave is gradually reduced, and the waves pattern also change greatly. Relative to the speed and submarine depth, the change of the gradient density has little effect on the free surface wave field. The wavelength, wave height and shape of the Kelvin wave on the free surface remain basically the same, and the amplitude of the divergence intensity of the flow field is nearly the same. The variation characteristics of the pycnocline at the submarine tail are mainly determined by the relative positions of the submarine and the layer, which are also less affected by the density gradient.

ACKNOWLEDGEMENTS

This paper is supported by National Natural Science Foundation of China (No. 51779053).

REFERENCES

1. Wang, J., You, Y.X., Hu, T.Q.: The Characteristics of Internal Waves Generated by a Revolution Body in a Stratified Fluid

- with a Pycnocline. *Acta Physica Sinica*, 2012, 61(7), Pp. 074-701.
2. Ouchi, K.: Recent Trend and Advance of Synthetic Aperture Radar with Selected Topics. *Remote Sensing*, 2013, 5(2), Pp.716-807.
 3. Spedding, G.R.: Wake Signature Detection. *Annual Review of Fluid Mechanics*, 2014, 46, Pp. 273-302.
 4. Miles, J.W.H.: Lee Waves in a Stratified Flow. Part 2. Semi-Circular Obstacle. *Journal of Fluid Mechanics*, 1968, 33(4), Pp. 803-814.
 5. Long, R.R.: Some Aspects of the Flow of Stratified Fluids. *Tellus*, 1955, 7(3), Pp. 341-357.
 6. Lighthill, M.J.: *Hyperbolic Equations and Waves*, Springer, New York, 1970.
 7. Stevenson, T.N.: Some Two-Dimensional Internal Waves in a Stratified Fluid. *Journal of Fluid Mechanics*, 1968, 33(4), Pp.715-720.
 8. Stevenson, T.N., Chang, W.L., Laws, P.: Viscous effects in lee waves. *Geophysical and Astrophysical Fluid Dynamics*, 1979, 13(1), Pp. 41-151.
 9. Boyer, D.L., Davies, P.A., Fernando, H.: Linearly Stratified Flow Past a Horizontal Circular Cylinder. *Philosophical Transactions of the Royal Society of London A: Mathematical, Physical and Engineering Sciences*, 1989, 328(1601), Pp. 501-528.
 10. Xu, Y., Fernando, H.J., Boyer, D.L.: Turbulent Wakes of Stratified Flow Past a Cylinder. *Physics of Fluids*, 1995, 7(9), Pp. 2243-2255.
 11. Meunier, P.: Stratified Wake of a Tilted Cylinder. Part 1. Suppression of a Von Kármán Vortex Street. *Journal of Fluid Mechanics*, 2012, 699, Pp.174-197.
 12. Bosco, M., Meunier, P.: Three-dimensional instabilities of a stratified cylinder wake. *Journal of Fluid Mechanics*, 2014, 759, Pp.149-180.
 13. Winters, K.B., Armi, L.: Hydraulic control of continuously stratified flow over an obstacle. *Journal of Fluid Mechanics*, 2012, 700, Pp. 502-513.
 14. Esmaeilpour, M., Martin, J.E., Carrica, P.M.: Near-Field Flow of Submarines and Ships Advancing in a Stable Stratified Fluid. *Ocean Engineering*, 2016, 123, Pp.75-95.
 15. Yu, C., Feng, Z., Jun, Z.: Numerical Simulation of Internal Waves Excited by a Submarine Moving in the Two-Layer Stratified Fluid. *Journal of Hydrodynamics, Ser. B*, 2006, 18(3), Pp. 330-336.
 16. Frank, J.M., Alain, P.: International one-atmosphere equation of state of seawater. *Deep Sea Research*, 1981, 28(6), Pp. 625-629.
 17. Yaacof, N.A., Qamaruzzaman, N., Yusup, Y.: Comparison method of odour impact evaluation using calpuff dispersion modelling and on-site odour monitoring. *Engineering Heritage Journal*, 2017, 1(1), Pp. 01-05.
 18. Yue, X.G., Ashraf, M.A.: Analysis of The Function Relations Between the Depth Of Gap Or Slot And The Speed Of Vibra tion In Millisecond Multiple-Row Holes Blasting. *Engineering Heritage Journal*, 2018, 2(1), Pp. 01-04.
 19. Tian, X.C., Li, Q.H., He, C.S., Cai, Y.G., Zhang, Y., Yang, Z.G.: Design and experiment of reciprocating double Track Straight Line Conveyor. *Acta Mechanica Malaysia*, 2018, 2(2), Pp. 01-04.
 20. Yan, Z.H.: Modeling and Kinematics Simulation Of Plane Ten-Bar Mechanism Of Warp Knitting Machine Based On Simcape/Multibody. *Acta Mechanica Malaysia*, 2018, 2(2), Pp. 15-18.
 21. Yu, Z.C.: An Improved Infrared and Visible Image Fusion Algorithm Based on Curvelet Transform. *Acta Electronica Malaysia*, 2017, 1(1), Pp. 12-14.
 22. Zamanian, P., Kasiri, M.: Investigation of Stage Photography In Jee Lee's Works And Comparing them With The Works Of Sandy Skoglund. *Acta Electronica Malaysia*, 2018, 2(1), Pp. 01-06.

CONTACT WITH THE AUTHORS

Kaiye Hu, Ph.D.

email: hukaiye@126.com

College of Shipbuilding Engineering
Harbin Engineering University
Harbin Heilongjiang
150001
CHINA

EXPLORATION AND MINING LEARNING ROBOT OF AUTONOMOUS MARINE RESOURCES BASED ON ADAPTIVE NEURAL NETWORK CONTROLLER

Lisheng Pan

School of Management, Hefei University Of Technology, Hefei, China

ABSTRACT

To study the autonomous learning model of the learning robot for marine resource exploration, an adaptive neural network controller was applied. The motion characteristics of autonomous learning robots were identified. The mathematical model of the multilayer forward neural network and its improved learning algorithm were studied. The improved Elman regression neural network and the composite input dynamic regression neural network were further discussed. At the same time, the diagonal neural network was analysed from the structure and learning algorithms. The results showed that for the complex environment of the ocean, the structure of the composite input dynamic regression network was simple, and the convergence was fast. In summary, the identification method of underwater robot system based on neural network is effective.

Keywords: adaptive neural network, marine resources, learning robot

INTRODUCTION

Based on a study, the total area of the ocean accounts for 70.8 % of the total area of the Earth, and it is an important part of the global life support system [1]. According to research, rich marine life resources, marine mineral resources, water resources and marine energy are contained, which is a valuable asset to help achieve sustainable development. Marine resources play a vital role in the sustainable development of mankind [2–3]. Marine development requires advanced technology and equipment. Underwater robots are currently the only equipment that can work in the deep sea, which has an irreplaceable role in deep sea development. Underwater robot technology is a high-tech that has been developed with the deepening of marine research and development. It is an important part of marine high technology.

The exploration and mining learning robot of marine resources is taken as the research object, and the neural network is used as a tool to systematically identify its motion characteristics. The forward and predictive models of the robot are established separately. Taking the neural network as the

starting point, the nonlinear system identification method based on neural network and the network characteristics commonly used for identification are discussed. Study showed the neural network is optimized from two aspects of network topology and learning algorithm [4]. The neural network identification model of multi-layer forward neural network and dynamic regression neural network based on improved Elman algorithm is studied. Through comparison, an effective method to improve the identification effect is proposed.

STATE OF THE ART

The research of underwater robots has been more than 20 years old. Many coastal countries, especially developed countries, are committed to underwater robot technology research and product development. Countries such as the United States, Canada, the United Kingdom, Japan, Russia, and China have established specialized institutions or established research laboratories in universities to study underwater robot technology, such as Centre for Autonomous Underwater

Vehicle Research, Marine Systems Engineering Laboratory at Maine State University, The Autonomous Undersea Systems Institute, British Maritime Technology Center, Underwater Robot Application Laboratory of the University of Tokyo, Japan, Shenyang Institute of Automation and Harbin Engineering University, National Key Laboratory of Underwater Robots [5]. Some professional associations established internationally, such as IEEE Marine Engineering Association, IEEE Robotics and Automation Association, Maritime Technology Association, etc. have contributed to the development of underwater robot technology [6].

The research of neural network can be divided into two aspects: theoretical research and applied research. Theoretical research can be divided into neurophysiological and cognitive science research human thinking and intelligent mechanism. The research results and mathematical methods of neural basic theory are more complete. The performance of the neural network model is superior [7]. Network algorithms and performance are studied in depth, such as stability, convergence, fault tolerance, and robustness. New network mathematical theory has been developed, such as neural network dynamics, nonlinear neural fields, and so on. Application research can be divided into the following two categories: software simulation of neural networks and hardware implementation research and application of neural networks in various fields. These areas include system identification, pattern recognition, signal processing, knowledge engineering, expert systems, optimization combinations, and robot control [8]. With the development of neural network theory itself and related theories and related technologies, the application of neural networks will be more in-depth and extensive.

METHODOLOGY

ONLINE IDENTIFICATION OF NONLINEAR SYSTEMS

Based on a study, the neural network is used to model the nonlinear dynamic system, which mainly reflects the nonlinear mapping ability of the neural network [9]. However, if the external environment of the system changes, the output of the system will also change, so that the dynamic response to the network has higher requirements. From the structure of the network, learning algorithms, identification structure and other aspects, the adverse effects are eliminated. In view of this, online recognition was introduced. The parameters of the online identification neural network model are determined by a certain online learning algorithm. Thus, a controlled object model that satisfies a certain precision needs to be established. The initial information of the network is obtained through offline learning. Then, by embedding the identification structure in series and parallel form into the system, the

model can be modified in time by adjusting the weight and threshold of the neural network model online. The model has good robustness.

SBPTT (simplified backpropagation through time) is developed based on the BPTT algorithm combined with the requirements of online identification. The algorithm takes into account the online learning ability of the BPTT algorithm and the small amount of online learning. The learning of the model requires a condition that enables it to jump out. Because online learning has certain requirements for the learning time of the network, the logical or relationship of the precision and the number of learning is used as a condition. Once the accuracy meets the requirements or the number of learnings of the network reaches a predefined number of times, the network ends the current learning process.

A series-parallel identification structure is adopted between the controlled system and the identification network. The identification network uses a modified Elman network. The learning algorithm uses a BPTT algorithm suitable for online identification. However, online identification has strict requirements on the amount of calculation, convergence speed and consumption time of the network. The online learning method uses the SBPTT algorithm. For the nonlinear system with multiple inputs and multiple outputs, on the one hand, the mapping capability of the system is higher; on the other hand, there are certain requirements for the coupling and decoupling of the identification system.

In many practical problems, the identification may not always be performed in an open loop state, such as learning the speed experiment of the robot. If the difference in motor performance of the learning robot is not very large, it can be done by direct open-loop experiment. However, if the experiment of the robot is carried out, it is almost impossible to learn the robot based on different control amounts and to obtain the desired angle of inclination. There are many reasons, such as robot inertia, hydrodynamics, and robot energy. In some cases, if the feedback channel is disconnected, the system will be unstable, and some systems or most systems will not allow or cannot disconnect the feedback channel [10].

ESTABLISHMENT OF NONLINEAR SYSTEM PREDICTION MODEL

The plane motion output information of the learning robot includes information such as longitudinal speed and slant angle. They are chronologically ordered and have some statistical relationship [11]. The information can be statistically described by a probability distribution function or a function group. The fitted mathematical model is used to predict future possible values, which is one of the main application purposes of the time series analysis method [12]. Thus, the output prediction of the learning robot can be performed using a time series analysis method.

The representation of the nonlinear system uses the following structure:

$$y(k+1) = f[y(k), y(k-1), \dots, y(k-n+1); u(k), u(k-1), \dots, u(k-m+1)] \quad (1)$$

Neural network prediction of time series is usually based on existing sample data to train the network. If the past N ($N \geq 1$) data is used to predict the value of the future M ($M \geq 1$) moments, the M -step prediction is performed. The sequence of N adjacent samples is a sliding window and maps them to M values. These M values represent the predicted values of the samples at the M moments after the window. The training data is divided into data segments with K segments of length $N+M$, and the first N data of each segment is used as the input of the network, and the last M data is used as the output of the network [13].

The method of neural networks to describe nonlinear systems is maturing. Therefore, a method of constructing a multi-step predictive model with a neural network has emerged. In summary, there are two options, one is the recursive multi-step prediction model, and the other is the non-recursive multi-step prediction model [14].

The recursive multi-step prediction model is used as a one-step prediction model, which is obtained after offline or online training. According to the network structure, the input link can be increased or decreased. This requires relatively more system information when applying multiple layers of forward static networks [15]. When using dynamic regression network for modelling, the dynamic mapping of the network itself can be utilized to reduce the structure of the network. It facilitates the implementation of programs for online identification and generalized predictive control.

According to the longitudinal motion of the learning robot to simplify the model and the relationship between thrust and voltage, equation (2) is obtained:

$$5.64V_c - 3.1 - D_{Q,x} |v_x| v_x - D_{L,x} v_x = M_x v_x \quad (2)$$

Nonlinear system identification requires a computer to process, while a computer can only process discrete time models. Therefore, it is necessary to digitally discretize the above formula. The parameters obtained by longitudinal identification and the control period and sampling period are both 0.1s. Equation (4) is obtained:

$$v_x(k+1) = v_x(k) + \frac{5.64v_c(k) - 146.8857|v_x(k)|v_x(k) - 22.2157v_x(k) - 3.1}{2365.319} \quad (3)$$

According to the actual input and output of the learning robot, the input allowable range is -5V~5V. However, the model between the thrust and voltage of the propeller here is derived from the forward data. The relationship between the voltage and the thrust when learning the robot back is different from the parameter at the time of advancement [16]. Therefore, the amount of control should be in the range of 0 to 5V when performing longitudinal experiments.

EXPERIMENTAL DESIGN

A set of sinusoidal curves of amplitude-frequency variation distributed in the range of 0~5V is designed as an excitation signal for learning the robot model. However, due to the presence of the pull-wire sensor at the rear of the learning robot and the static resistance of the robot, there is a dead zone in the starting voltage. When the starting control voltage satisfies $V_c > 0.55V$, the learning robot can generally generate the forward thrust.

This model is a nonlinear system with a certain time lag. The learning robot model is identified by using multi-layer forward neural network, improved Elman neural network and composite input dynamic regression neural network. The recognizer uses a series-parallel structure, that is, the output of the model is used as an input to identify it. The convergence speed of the nonlinear identification system is effectively improved.

RESULT AND DISCUSSION

IDENTIFICATION OF MULTI-LAYER FORWARD NEURAL NETWORKS

There are many learning algorithms for multi-layer forward networks. The earliest algorithm was the standard back propagation (BP). The input vector u of the network is n -dimensional, the output vector y is m -dimensional, and the input/output sample length is N . The BP learning algorithm consists of two phases: forward propagation and back propagation. In forward propagation, the input signal passes from the input layer through the hidden layer to the output layer. If the output layer gets the desired output, the learning algorithm ends; otherwise, it goes to backpropagation. Backpropagation is to calculate the error signal (the difference between the sample output and the network output) in the reverse direction of the original connection path. The gradient descent method adjusts the weight and threshold of each layer of neurons to reduce the error signal.

The neural network structure of $N(2,6,1)$ is designed, and the serial-parallel identification structure is adopted. The input of the network is $V_c(k)$ and $v(k-1)$, and the output of the network is $v(k)$. The network learning algorithm uses an improved BP learning algorithm with momentum terms. After the trained network, the square wave of the input variable amplitude frequency is obtained as shown in Figure 1.

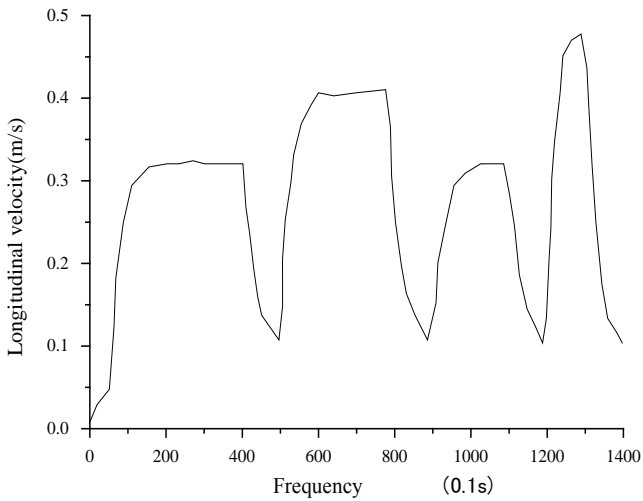


Fig. 1. Identification results of multilayer feedforward networks

IDENTIFICATION OF IMPROVED ELMAN NEURAL NETWORK

The nonlinear system has hysteresis, and the order of the nonlinear system is difficult to determine. Therefore, the Elman algorithm is improved. Based on the basic Elman structure, a self-feedback link is added to the structural elements of the network. The self-gain factor generally takes a fixed value α . The network can map higher order nonlinear systems. The structure is shown in Figure 2.

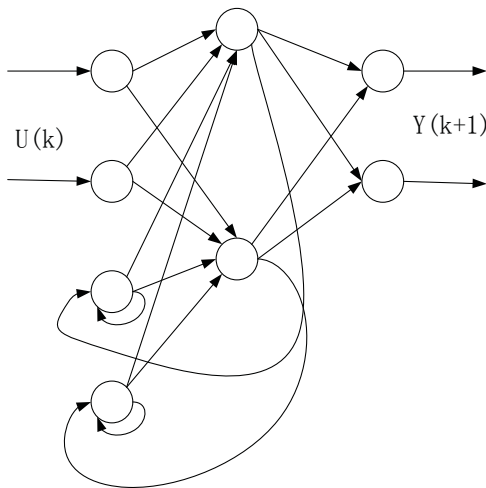


Fig. 2. Improved Elman neural network

The weight learning algorithm of Elman network can be performed by standard BP learning algorithm. However, since $Xc(k)$ is a dynamic recursive process, and the BP algorithm only uses a step, it will lead to poor stability of the structural unit connection weight. To ensure learning convergence, for high-order systems, the learning rate must be minimal, resulting in poor approximation accuracy. Therefore, the Elman network can only identify first-order linear dynamic systems. To overcome this shortcoming, a dynamic backpropagation learning algorithm was used to train the Elman network. The

improved Elman neural network uses an N(1,3,1) structure. The initial value of the state layer of the network has a large impact on the convergence of the network. Therefore, the method of simulating data is used to obtain the initial value of the state layer, that is, the neural network is used to learn the state layer value of the offline learning to initialize the initial state layer of the recognizer.

The network learning algorithm uses a variable-step error feedback learning algorithm. In the improved Elman network, the learning method can identify higher-order nonlinear systems. Using the state layer of the Elman network, only three neurons are selected in the middle layer, and the learning memory parameter is 0.1. If the memory parameters are too large, the system learning is prone to oscillation. The step size from the input layer to the hidden layer and the step size from the hidden layer to the output layer are both 0.8, which can improve the learning adjustment speed of the state layer to the hidden layer unit. The historical information of the system can be easily input into the network. The output of the network approaches the output of the actual system. The identification effect of the network is shown in Figure 3.

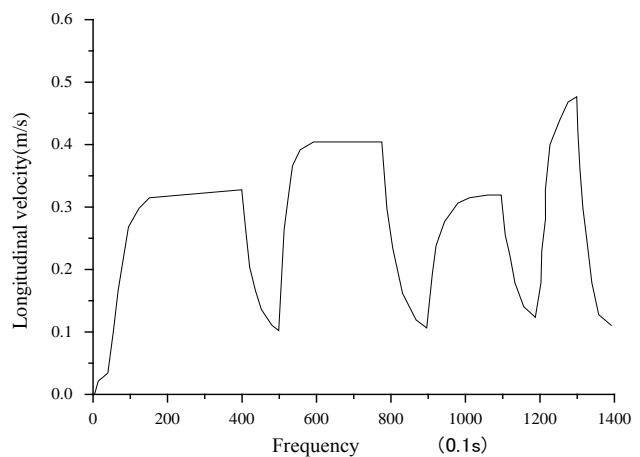


Fig. 3. Identification results of improved Elman neural network

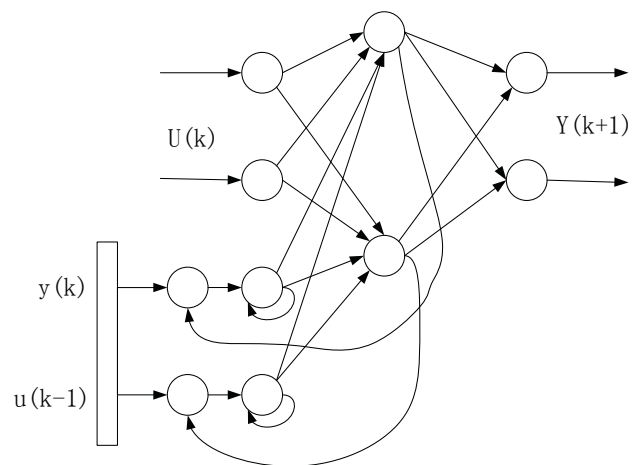


Fig. 4. Characteristics of compound input dynamic neural network

IDENTIFICATION OF COMPLEX INPUT DYNAMIC NEURAL NETWORKS

Compound input dynamical recurrent neural networks (CIDRNN) takes into account the more information of the input system of the BP network and the dynamic characteristics of the Elman network. The structure is shown in Figure 4.

Composite input neural networks can be trained using standard BP algorithms. Compared with the Elman network, CIDRNN's generalization ability and convergence speed have been improved due to the use of more system resources, but this also brings the characteristics of large structure. The composite input neural network was developed based on Elman. It inputs certain historical information of the network into the network as an augmented input to the network. The inputs of the recognizer network include $V_c(k)$, $V_c(k-1)$, and $v(k-1)$. Among them, $V_c(k-1)$ and $v(k-1)$ are the augmented inputs of the network. The output of the network is $v(k)$. The weight of the network is adjusted by learning the output of the robot model as an error. The network adjustment algorithm uses an improved error back propagation learning algorithm.

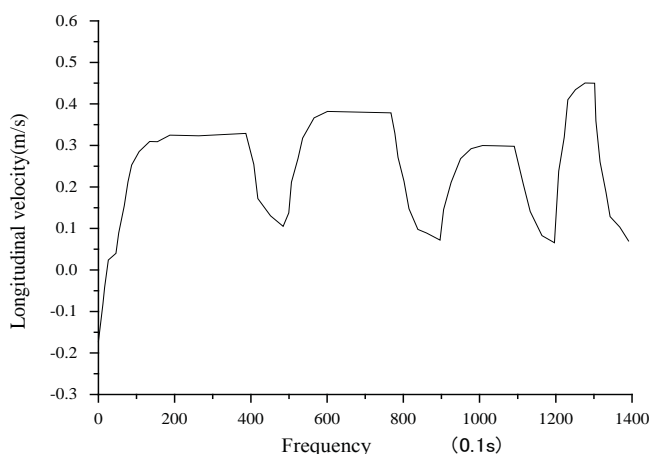


Fig. 5. Identification effect of compound input dynamic regression neural network

ANALYSIS OF SIMULATION EXPERIMENT RESULTS

The training error curves of the three networks were analyzed. It can be seen that the improved Elman network is initially oscillating because the initial value of the state layer is not optimal.

The recognition effects of the learning robot models of the above three networks are compared. It can be found that the overall accuracy of the multilayer forward neural network is relatively high. The model system has no noise. From the perspective of static network mapping, the model can be well identified. An improved Elman neural network and a composite input dynamic regression neural network were compared. It can be seen that the turning point is mainly due to the memory function of the network, which is closely related to the characteristics of the input quantity. The data analysis is shown in Table 1.

Tab. 1. Comparison of neural network identification effects

Parameter name	Multi-layer forward network	Improved Elman network	Composite input dynamic network
Structure	N(1,6,1)	N(1,3,1)	N(3,6,1)
Training error	8.968e-005	2.083e-004	8.946e-005
Number of iterations	4000	2500	1000
Mean value of test error	-7.475 e-004	-0.0213	0.0011
Variance of test error	1.1608 e-005	0.002	8.386e-005

CONCLUSION

The identification of nonlinear dynamic systems based on neural networks is introduced. The structure, algorithm, and convergence of neural network identification are analysed. At the same time, the differences between the identification of open-loop system and closed-loop system are analysed, and the methods commonly used to construct one-step prediction model and multi-step prediction model are discussed. In addition, combined with the learning robot model, the model identification experiment was designed by applying multi-layer forward network and regression network respectively. By learning robot simulation experiments, the performance between different networks is compared. The composite input dynamic regression network has a simple structure and fast convergence.

REFERENCES

1. M. Rahmani, and A. Ghanbari, *Hybrid neural network fraction integral terminal sliding mode control of an Inchworm robot manipulator*, Vol. 80, pp.117–136, 2016.
2. H. N. Nguyen, and J. Zhou, *A calibration method for enhancing robot accuracy through integration of an extended Kalman filter algorithm and an artificial neural network*, Vol. 151, pp. 996–1005, 2015.
3. W. He, and A. O. David, *Neural network control of a robotic manipulator with input dead zone and output constraint*, Vol. 46, No. 6, pp. 759–770, 2016.
4. M. Beyeler, and N. Oros, *A GPU-accelerated cortical neural network model for visually guided robot navigation*, Vol. 72, pp. 75–87, 2015.
5. P. K. Panigrahi, and S. Ghosh, *Navigation of autonomous mobile robot using different activation functions of wavelet neural network*, Vol. 25, No. 1, pp. 21–34, 2015.

6. I. V. Serban, and A. Sordoni, *Building End-To-End Dialogue Systems Using Generative Hierarchical Neural Network Models*, Vol. 16, pp. 3776–3784, 2016.
7. P. Van Cuong, and W. Y. Nan, *Adaptive trajectory tracking neural network control with robust compensator for robot manipulators*, Vol. 27, No. 2, pp. 525–536, 2016.
8. A. Pandey, and D. R. Parhi, *New algorithm for behaviour-based mobile robot navigation in cluttered environment using neural network architecture*, Vol. 13, No. 2, pp. 129–141, 2016.
9. T. Wang, and H. Gao, *A Combined Adaptive Neural Network and Nonlinear Model Predictive Control for Multirate Networked Industrial Process Control*, Vol. 27, No. 2, pp. 416–425, 2016.
10. A. Graves, and G. Wayne, *Hybrid computing using a neural network with dynamic external memory*, Vol. 538, No. 7626, pp. 471, 2016.
11. P. Zamanian, and M. Kasiri, *Investigation of Stage Photography in Jee Lee's Works and Comparing them With the Works of Sandy Skoglund*, Acta Electronica Malaysia, Vol. 2, No. 1, pp. 01–06, 2018.
12. B. Q. Li, and Z. Li (). *Design of Automatic Monitoring System for Transfusion*, Acta Electronica Malaysia, Vol. 2, No. 1, pp. 07–10, 2018.
13. Z. H. Yan, *Modeling and Kinematics Simulation of Plane Ten-Bar Mechanism of Warp Knitting Machine Based on Simcape/Multibody*, Acta Mechanica Malaysia, Vol. 2, No. 2, pp. 15–18, 2018.
14. A. Abugalia, M. Shaglouf, *Analysis of Different Models of Moa Surge Arrester for The Transformer Protection*, Acta Mechanica Malaysia, Vol. 2, No. 2, pp. 19–21, 2018.
15. F. De'nan, F. Mohamed Nazri, and N. S. Hashim, *Finite Element Analysis on Lateral Torsional Buckling Behaviour Of I-Beam with Web Opening*, Engineering Heritage Journal, Vol. 1, No. 2, pp. 19–22, 2017.
16. M. A. Hassan, and M. A. Mohd Ismail, *Literature Review for The Development of Dikes's Breach Channel Mechanism Caused by Erosion Processes During Overtopping Failure*, Engineering Heritage Journal, Vol. 1, No. 2, pp. 23–30, 2017.

CONTACT WITH THE AUTHOR

Lisheng Pan

School of Management
Hefei University Of Technology
Hefei, 230009

CHINA

DEVELOPMENT OF “4E” LEVEL RIVER-SEA-GOING SHIP

Zhiyong Pei

Qingning Yuan

Weiguo Wu

Wuhan University of Technology, Wuchang District, Wuhan, Hubei Province, China

ABSTRACT

In order to effectively promote the construction of the Yangtze River economic belt, it has become China's national strategy to vigorously develop the river-sea-going transportation. In the present paper, theoretical analysis, numerical simulation and model test are combined together to develop flat-type river-sea-going ship which is characterized with larger loading capacity, lower fuel consumption, better performance on energy-saving and environmental-friendly, excellent economy and higher transportation efficiency. Key technologies on hydrodynamic performance, structural safety, energy-saving technology and green ship technology are investigated to develop the river-sea-going ship. The developed “4E” level ship has great significance to the implementation of national strategic deployment.

Keywords: Energy-saving, Environment-friendly, high performance ship, “4E” level ship, flat-type river-sea-going ship.

INTRODUCTION

The Yangtze River is a natural channel connecting national strategies such as coastal opening in eastern China, rising of central China and developing of western China. It supports the logistics, comprehensive transportation system, economic and social development of the seven provinces and two cities within its valley. At present, the Chinese Government has established national development strategy for the golden waterway of Yangtze River. Relying on the golden waterway running through east and west, it will drive the development of the hinterland locating at the middle and upper reaches of Yangtze River and promote the orderly undertaking of the industrial transfer from the eastern coastal areas to the central and western regions so as to create a new economic belt for the Chinese economy. In the traditional transportation system, the cargoes are transported from deep-sea port such as Ningbo or Zhoushan to Nanjing or Ma'anshan via sea-going vessels, and then transported to the middle and upper reaches such as

Wuhan by inland ships. Such kind of transportation not only takes quite a long time and increases operating cost, but also leads to cargo damage and shortage. It is hard to improve the transportation efficiency which cannot satisfy the requirement of the economic and social development of the Yangtze River Valley. On the June 11, 2014, the Premier instructed to deploy comprehensive traffic corridor, create the Yangtze River economic belt, promote the standardization of inland vessels, research and popularize river-sea-going ships, and encourage developing energy-saving and environment-friendly ships at the executive meetings of the State Council.

In 2016, the Yangtze River freight volumes exceeded 2.3 billion tons which persists the first rank for 12 years in the world's inland river [1]. Large-scale ships are required by the development of the present economy and society. Such ships have higher transportation efficiency, lower energy consumption and better economic so that they have competitive advantage in the harsh shipping market. However, as the Yangtze River is the natural navigable waterway, ship length and draft are limited, and depth is restricted by the

clearness height of bridge. The possible way to actualize large-scale ships is to increase ship's width and develop flat-type ship which can adapt to natural condition of the Yangtze river [2]. The rapidity, navigability and structural safety of flat-type vessel have always been the key technologies for the academia and industry.

Based on extensive shipping market investigation, the flat-type river-sea-going ships which can adapt to the channel of Yangtze River and the corresponding port condition are developed through economic analysis and research on navigability and structural safety. Theoretical analysis, numerical simulation and model test are combined together to solve the key technologies on resistance performance of flat-type ship with shallow water, structural safety in the sea, energy-saving technology and green ship technology [3]. The developed ship having the characteristics of Energy-saving, Environment-friendly, Economy and Efficiency is considered as "4E" level river-sea-going ship.

1. Energy-saving: It is the key technology for the developing ship. Fuel consumption is decreased effectively by applying advanced technology to improve the competitiveness of the production.
2. Environment-friendly: It is the demand of social sustainable development.
3. Economy: It is the foundation for survival and development. It helps to occupy the shipping marketing the present harsh situation.
4. Efficiency: It is fundamental for efficient transportation to promote the implementation of national strategy.

The development of the "4E" level river-sea-going ship has great significance for the implementation of the national strategies such as the construction of the Yangtze River golden waterway, the strategy of rising of midland, the construction of Yangtze River shipping center and river-sea-going transportation service center.

THE DEVELOPMENT THOUGH OF "4E" LEVEL RIVER-SEA-GOING SHIP

CURRENT SITUATION OF RIVER-SEA-GOING SHIP

The current river-sea-going ships navigating in the Yangtze River are designed according to both the rules for sea-going vessels and the rules for inland ships which lead to the heavy structural weight. The hydrology and weather conditions of the river-sea-going navigating route are not comprehensively considered so that the ship has neither the advantage of sea-going vessel, nor the inland ship. With the improvement of the channel condition of Yangtze River and the loading/unloading capacity of the port, the requirement of large-scale river-sea-going ship is becoming more and more intense. The existing ships cannot satisfy it and be capable of supporting the construction of the "golden waterway".

KEY TECHNOLOGIES OF RIVER-SEA-GOING SHIP

Based on extensive shipping market research, river-sea-going ships are designed through economic analysis, seaworthiness research and structural safety research. Larger loading capacity, lower fuel consumption, energy-saving and environment-friendly, better economy and higher transportation efficiency are considered as objective. The developed ship has the characteristics of Energy-saving, Environment-friendly, Economy and Efficiency, regarding as "4E" level ship.

Comprehensive analysis system: The Yangtze River route is considered as the principal research objective. The freight distribution and the freight market are predicted and analyzed based on the status of the channel and the port condition. Key technology and economic model are researched so as to establish a comprehensive evaluation system on ship performance, economy in all life cycle and environmental effect. The system is adopted to perform comprehensive analyses so that the main dimension of developing ship is determined [4].

Mold line optimization: Numerical simulation and model test are combined together to perform the research on low resistance stem and energy-saving stern. Hydrodynamic performance including rapidity, sea-keeping and maneuverability is comprehensively considered to optimize the mold line [5]. Thus, the green ship with the Energy-saving and Environment-friendly can be designed.

Wake-adaption high efficient propeller design: For flat-type river-sea-going ship, the wake is uneven in both axial direction and radial direction. Circulation theory is used to design the wake-adaption high efficient propeller considering the actual wake distribution. Key technologies such as highly skewed blade, unloading at the tip of blade and anti-cavitation section are considered when the propeller is designed. Rapidity prediction of the designed ship can be performed by model self-propulsion test [6].

Development of energy-saving appendage: The stern wake field of flat-type river-sea-going ship is comparatively complex. The energy-saving appendage is designed by considering pre-rotation in front of the propeller and energy recovery behind the propeller. Theoretical analysis, numerical simulation and model test are combined together to research the energy-saving effect of pre-shrouded vanes, boss cap fins and thrust fin.

Application technology of LNG: Risk analysis on the processes of LNG storage, supplying and usage is performed and assessed. Key technology on LNG supplying system is carried out to obtain the technical design plan which makes it possible to use LNG safely and effectively. Furthermore, gas circuit is imported to collect the gas from spontaneous evaporation in the storage tanks well as the remaining gas in the pipeline during the fuel converting. The steady and dynamic characteristics analysis of LNG dual-fuel Main Engine system is conducted to ensure the stable power supplying.

Integration of energy-saving and environment-friendly technology: Integrated design model for energy-saving and environment-friendly is established taking comprehensive

energy management as the principal line and the minimization Energy Efficiency Design Index as the objective. The optimization of main propulsion system, the design of new non-pollution stern tube system and low noise shaft system reperformed to solve the key technologies such as Ship-Engine-Propeller matching, proper selection of Main Engine and generator and smart power station management system.

CHARACTERISTICS OF DEVELOPED RIVER-SEA-GOING SHIP

Large-scale ship satisfies the requirement of the present shipping market which has better economy and higher transportation efficiency. The ship length, depth and draft are constrained by the natural condition of the channel, port and clearness height. So, the developed river-sea-going ship is characterized with flat (lager ratio of breadth to depth), shallow draft and large block coefficient. In the present research, theoretical analysis, numerical simulation and model test are combined to solve the key technologies of flat-type ship form with large block coefficient, energy-saving and emission-reduction. Thus, the flat-type river-sea-going ship with Energy-saving, Environment-friendly, Economy and Efficiency ship is developed. The principal dimension of the developed ship is compared with that of existing ship in Table 1.

Tab. 1. Principal dimension comparison

Item	designed ship	existing ship
Length overall (m)	139.8	137.6
Length between perpendiculars (m)	137.0	133.2
Depth (m)	10.0	10.25
Breath (m)	25.6	22.8
Design draft/Structural draft (m)	5.5 / 6.3	5.5 / 6.25
Loadingcapacity (TEU)	940	810
Design speed (kn)	11.5	11.5
Main Engine power (kW)	2 x 1324	2 x 1470
Crew (Person)	11	14

The numerical tank for rapidity is constructed through the secondary development of commercial CFD software. The parameters on bow type, longitudinal and transversal curvature of the bow, distance between tail fins and pre-rotation angle of tail fin are discussed. Mold line optimization on more than 200 hull forms is carried out in the numerical tank to obtain the flat-type river-sea-going ship form [7]. The optimized mold line shows 8.0 % energy-saving efficiency comparing with the original one when the model test is carried

out in the towing tank. Circulation theory is adopted to design wake-adaption high efficient propeller considering the actual wake distribution anti-cavitation and vibration performance. The developed wake-adaption propeller indicates 4.0 %energy-saving improvement comparing with the traditional propeller obtained by propeller design charts through open-water test and self-propulsion test. Flow features of stern in typical loading condition are analyzed and the diversion fins system is installed in the propeller hub in order to improve the quality of incoming flow. Thus, the propeller efficiency can be improved. The optimization of section, angle and installation position of diversion fins are performed to develop the energy-saving appendage in front of the propeller. The energy-saving appendage behind the propeller, for example boss cap fin, is designed to recover the energy loss in radial direction of the propeller. The results of towing tank test indicate that the energy-saving appendages can achieve 3.0 % effect. The compositive management on heat recovery device in Engine room, exhaust gas boiler, fuel conversion device and smart power station system is carried out by energy-saving and environment-friendly integrated management system. The waste heat, idle energy and the fuel with low carbon conversion coefficient are fully utilized to minimum the Energy Efficiency Design Index. The energy-saving effect can reach 5.0% through the integrated energy management system.

The general technology of LNG supplying system, including risk analysis on LNG storage, supplying and usage as well control measures of ineffective dissipation, is investigated. The quantity, pressure and temperature of LNG supplying are determined according to the performance parameters of the Main Engine so that the proper LNG supplying control system and security system are chosen. The process of fuel supplying is analyzed for dual-fuel Main Engine to ensure the fuel conversion automatically. The steady and dynamic characteristics of power system are analyzed to ensure the stable power supplying. When LNG fuel is adopted, the exhaust emission can be remarkably reduced, in which the emission of CO₂ can be reduced by 25%, the emission of NOx can be decreased by 80 % and the SOx•PM can be reduced by 98 %.

The unit cost of transportation is defined as the cost for accomplishing unit transport volume (one standard container)⁴. It can be expressed as following,

$$C_T = C/Q_T \quad (1)$$

where C_T is the unit cost of transportation, and C is the annual total cost, and Q_T is the annual freight volume. C can be calculated by $Y + F_z$ where Y is the annual operating expenses, and F_z is the depreciation cost, $F_z = (K - L)/N_z$ where K is the investment amount, L is the residual value, N_z is the period of depreciation. Q_T is expressed as $2f_D \cdot C_D \cdot R_T$ where f_D is the loadingcoefficient, and C_D is the maximum allowable loading capacity, and R_T is the number of annual navigations. Unit cost of transportation of the designed ship is compared with the existing ship in table 2.

Tab. 2. Comparison of unit cost of transportation

Item	designed ship	existing ship
Annual operating expenses Y (ten thousandRMB/year)	600	650
Investment amount K (ten thousandRMB)	5700	5000
Residual value L (ten thousandRMB)	285	250
Period of depreciation N_z (year)	25	25
Depreciation cost F_z (ten thousandRMB/year)	216	190
Annual total cost C (ten thousandRMB/year)	816	840
Loading factor f_D	0.60	0.6
Maximum loadingcapacity C_D (TEU)	940	810
Annual navigations R_T (number/year)	25	25
Annual freight volume Q_T (TEU/year)	28200	24300
Unit cost of transportation C_T (RMB/TEU)	289	346
Percentage reduction	16.5 %	

The unit cost of transportation is the principal indicator to evaluate the ship's economic performance. Comparing with the existing ship, the unit cost of transportation of designed ship can be reduced 16.5 %, as shown in Table 2.

The transportation efficiency is the output value (cargo weight multiple transportation distance) through consuming unit energy. So, the transportation efficiency can be expressed as following,

$$\eta = \frac{1}{H_f S_{foc}} \frac{W_p \cdot V}{P} \quad (2)$$

where S_{foc} : Consumption rate of fuel, g/(kW·h);

H_f : Fuel caloricity, J/kg;

P : Main Engine power, kW;

V : Speed, kn;

W_p : Dead weight of vessel, t.

When comparing transportation efficiency, the same fuel should be adopted to ensure the comparability. The value of H_f shall keep the same one. So, the part of

$$\frac{1}{S_{foc}} \frac{W_p \cdot V}{P}$$

shall be compared, as shown in Table 3.

Comparing with the existing best performance ship, the designed ship improves 25.6 % in transportation efficiency⁴⁾.

Tab. 3. Comparison of transportation efficiency

Item	designed ship	existing ship
Deadweight, WP (t)	11605	9615
Main Engine power P (kW)	1324	1470
Main Engine number	2	2
Main Engine fuel consumption (g/kW·h)	205	205
Design speed V(kn)	11.5	11.5
$\frac{1}{S_{foc}} \frac{W_p \cdot V}{P}$	0.246	0.183
Percentage increment of transportation efficiency	25.6 %	

THE DEVELOPMENT OF ENERGY-SAVING MOLD LINE AND APPENDAGE

Theoretical analysis, numerical simulation and model test are combined together to perform the research of hydrodynamic performance on flat-type sea-river-going ship. The hydrodynamic performance of different stem type such as vertical bow, watermelon bow, and bulbous bow is discussed and researched comprehensively considering rapidity, sea-keeping in the sea and inland maneuverability. Both the longitudinal curvature and transverse curvature of the bow are optimized to obtain the vertical bow with lower resistance and better anti-slamming performance [8].

The development of stern line shall consider the propeller inflow and the maneuverability in shallow water. Numerical simulation and model test are carried out for the optimization of the length, distance and shape of tail fins. More than 200 stern lines are calculated to develop the outward rotation twin tail fins with low resistance, low thrust deduction and high propulsion efficiency. Model test demonstrates that the optimized mold line of flat-type river-sea-going ship can achieve about 8.0 % energy saving.

Flow field of river-sea-going ship in typical working conditions is analyzed to obtain the flow details at the location of propeller. Self-propulsion test is carried out in towing tank to get the components of propulsion as well the three-dimensional flow field at the propeller disk. The propeller design platform based on circulation theory is used to conduct the wake-adaption high efficient propeller design considering the efficiency, cavity, vibration and the actual axial and radial wake field. The technologies such as large skewed blade, unloading at the tip of blade and anti-cavitation section are also applied. The open water test and self-propulsion test illustrate that the developed propeller can improve 4.0 % energy saving than traditional one designed by atlas.

The diversion fins, a kind of energy saving device before the propeller, are proposed by analyzing the stern flow field to improve the flow quality so as to improve the propeller efficiency. The best angle and length of diversion fins are determined by considering the pre-whirled flow effect and resistance increment. Furthermore, thrust fins installed on the rudder, a kind of energy saving device behind the propeller, are developed by considering the recycling of circumferential energy loss to improve the propeller efficiency. Thus, the energy saving appendage for flat-type river-sea-going ship is determined by combining diversion fins before the propeller and thrust fins on the rudder. The propeller open water test and self-propulsion test show the proposed energy saving appendage can save energy 3.0 %.

STRUCTURAL LIGHTWEIGHT DESIGN

With the development of global economy, the shipping industry has entered into a new era which requires the larger capacity, higher transportation efficiency and lower emission. The researchers in shipping industry try their best to achieve such objective. It becomes consensus by international maritime the structural lightweight design can improve the transportation efficiency and decrease the emission. Thus, it is meaningful to minimize the structural weight under the premise of the structural safety and reliability.

It is possible for structural lightweight design by performing rational general arrangement design to decrease the external force which is calculated by the difference between gravity and buoyancy under various loading conditions. Structural direct calculation on supporting structures is performed. The lightweight design can be carried out in accordance with the calculation results on the premise of safety and reliability. The structural optimization on typical cross section is conducted to search for lightweight structural configuration.

Theoretical analysis, numerical simulation and model test are combined to analyze and evaluate the structural safety of flat-type river-sea-going ship [9]. According to the wave scatter diagram of navigating route, the long-term prediction of external force acting on the ship hull is carried out to obtain the equivalent design wave height [10]. Wave loads calculation for typical loading condition is performed to obtain the external force acting on the hull with time instantaneous. Then, structural nonlinear response analysis is conducted so that the ultimate strength of ship structure is achieved. Furthermore, the collapse test of ship structures in wave is carried out to obtain the external force subjected to the ship and the ultimate structural strength simultaneously [11]. Thus, the structural safety margin under specific loading condition and wave situation is understood [12].

For river-sea-going ship, the external force in sea part and Inland River is quite different [13]. The research on fatigue characteristic of typical structural joints under variable amplitude force is meaningful to reveal the fatigue mechanism of river-sea-going ship [14]. The fatigue test on longitudinal stiffener crossing the hold and hatch corner under variable

amplitude force is carried out to establish the assessment system on fatigue strength. The fatigue research makes the foundation for the safety and reliability of ship structures of river-sea-going ships [15].

Under the premise of structural safety, the structural lightweight design is conducted by the application of lightweight design technology. The structural weight can be reduced, and the ship economy can be improved. The shipbuilding material and the energy consumption can be reduced. Thus, the core competitiveness of China ship products can be improved.

THE DESIGN OF POWER INTEGRATED SYSTEM

Marine power system provides power for ship and determines the ability of ship navigation and operation. Power is generated by Main Engine and transmitted to propeller through driving device and shafting system so as to realize the purpose of ship propulsion. Reasonable design on marine power system can realize the comprehensive energy management so as to decrease the energy consuming effectively and realize the purpose of energy-saving and emission-reducing.

In the present research, the integrated design platform of marine power system is established based on the comprehensive energy management. A set of energy-saving and environmental-friendly management system is adopted to monitor and manage the marine power devices such as the recycling device of heat in engine room, exhaust gas boiler, diesel and LNG conversion device, shaft generator and main generator [16]. Make full use of the ship's residual heat, waste heat, idle energy and give priority to the usage of low-carbon conversion factor fuel so that the energy efficiency design index (EEDI) is controlled to a minimum one. Thus, the marine power design plan for energy-saving and environmental-friendly can be made.

The optimization of stern structures is carried out. The vibration isolation and absorption technology are adopted for installation of Main Engine and shaft system in order to reduce the vibration and noise of propulsion system so that the energy-saving and environmental-friendly can be achieved. Moreover, new type watertight stern tube is used and the optimization of sealing performance is performed to avoid the pollution caused by lubricant oil.

Smart substation management system is proposed to adjust and control the frequency generated by shaft generator and achieve parallel locomotive of diesel generator. The idle energy of Main Engine in underload condition can be transferred to electric power supplying which can reduce or replace the fuel consumption of diesel generator. The carbon emission can be effectively reduced by the above methods [17].

The power integrated system such as integrated design, comprehensive energy management, idle/waste heat usage, vibration isolation and absorption design, water lubrication and smart substation is adopted to manage the energy effectively so that the developed river-sea-going ship can achieve the energy-saving 5.0 %.

APPLICATION TECHNOLOGY OF LNG

The inland waterway takes more than 80 % of the total voyage for the developed river-sea-going ship where both sides are densely populated and economically developed areas. The carbon emission can be reduced and the emission of NO_x and SO_x•PM can be drastically reduced if the LNG is taken as the fuel. This can provide the fundamental supporting for the construction of the Yangtze River golden waterway and the sustainable development strategy for the Yangtze River shipping. In order to use LNG as fuel safely and effectively, the follows risk analysis and key technologies on LNG fuel powered ship are carried out.

LNG supplying system design technology: Risk analyses and key technologies on LNG fuel powered ship are performed to solve the balance of LNG supplying safely and effectively and the cargo hold capacity. The LNG storage tank, the supplying system and the protection system shall be scientifically arranged to reduce the loss of cargo hold capacity as little as possible. Simulation analyses are used to optimize the process of LNG supplying system to ensure its safety and reliability.

Invalid dissipation control measurement: The working condition of mode converting on dual-fuel Main Engine is investigated and researched to provide a reliable basis for the collection of the residual natural gas in the pipeline. Reasonable measurement is proposed to collect the gas from spontaneous evaporation in the storage tank as well the remaining gas in the pipeline during the fuel mode converting through simulation analyses. The proper arrangement of control system devices is conducted to solve the invalid dissipation of LNG effectively.

Control and security technologies: Control system of dual-fuel Main Engine is analyzed to determine the plan of LNG fuel control system. Flow, pressure and temperature of LNG are determined according to the performance parameters of dual-fuel Main Engine. Then, the proper control system and security system of LNG supplying are selected.

Matching technology of power system for dual-fuel Main Engine: The fuel supplying process for various working conditions of the Main Engine is analyzed to ensure the safe operation. The process of fuel mode converting is investigated to ensure the automatic converting and stable power output. The steady and dynamic characteristics of power system are studied to ensure the stable power supplying. The research on matching characteristic of Ship-Engine-Propeller is performed to improve the dynamic characteristics of the power system for dual-fuel Main Engine in various working conditions.

CONCLUSION

In the present research, theoretical analysis, numerical simulation and model test are combined together to solve the key technologies on flat-type river-sea-going ship with shallow water. The research on application of energy-saving

and environment-friendly technology is focused to develop the ship with characteristic of Energy-saving, Environment-friendly, Economy and Efficiency, regarding as “4E” level river-sea-going ship.

The main indicators for the developing ship are as follows:

1. The average daily fuel consumption per container can reduce 23.97% comparison with the existing best performance ship.
2. The application of LNG as fuel can reduce the 25 % CO₂ emissions, the 80 % NO_x and 98 % SO_x•PM emissions.
3. The application of watertight stern tube can effectively avoid the water pollution caused by lubricating oil.
4. The unit transportation cost of developed ship can be decreased by 16.5 % comparing with the existing best performance ship.
5. The transportation efficiency can be improved by 25.6 % comparing with the existing best performance ship.

The development of “4E” level flat-type river-sea-going ship is the requirement of current strategic development in China which has great significance to the implementation of national strategic deployment.

REFERENCES

1. *Current Situation Investigation and Development Prospect Analysis Report of Inland River Water Transportation Market in China*, China Industry Research, 2016.
2. Z. Y. Pei, S. Y. Wu, and W. G. Wu, *Key Technology of Flat-type Large-scale River-sea-going Container Ship*, China Water Transport, Vol. 37, pp. 11–12, 2016.
3. Z. Y. Pei, Z. H. Zhu, and W. G. Wu, *Design on Flat-type River-Sea-Going Multi-Purpose Ship*, 25th International Ocean and Polar Engineering Conference, ISOPE 2015, pp. 1229–1235, 2015.
4. W. Cai, H. Z. Gong, Z. K. Liu, J. Y. Yang, *Environmental Load Analysis and Scheme Optimization of Green Sea-river-through Ship Based on Practical LCA*, Ship Engineering, Vol. 39, pp. 5–10, 2017.
5. J. T. Qin, *Study on Rapidity performance of next-generation river-sea going ship*, Doctoral thesis, Wuhan University of Technology, 2014.
6. T. Yang, Y. S. Lin, W. G. Wu, J. T. Qin, W. He, and S. J. Qin, *Numerical prediction of pressure fluctuation included by propeller on hull surface*, Journal of Wuhan University of Technology (Transportation Science & Engineering), Vol. 41, pp. 97–103, 2017.
7. H. J. Cao, M. Rivoal, Z. Y. Pei, J. T. Qin, P. Sergent, and A. Droue, *Parametric Study of the Impact of Hull Form Deformations of an Inland Ship on its Hydrodynamic Performances in Shallow Water Using CFD*, 9th fluid mechanic academic conference, pp. 154–163, 2016.

8. C. Xie, J. He, and J. Qin, *Numerical simulation and model test on resistance performance for vertical stem*, China Water Transport, Vol. 15, pp. 13–14, 2015.
9. Z. Y. Pei, Z. H. Zhu, and W. G. Wu, *Research of load and structural direct calculation on flat-type river-sea-going ship*, Journal of Traffic and Transportation Engineering, Vol. 3, pp. 266–276, 2015.
10. W. H. Zhang, G. M. Liu, and W. G. Wu, *Investigation on the wave load for river-sea bulk carriers*, Journal of Wuhan University of Technology (Transportation Science & Engineering), Vol. 35, pp. 752–755, 2011.
11. Z. Y. Pei, T. Xu, S. L. Zhang, and W. G. Wu, *Collapse Test of Ship Hull Girder in Waves*, Proc. of the 31st Asian Technical Exchange and Advisory Meeting on Marine Structure, TEAM 2017, pp. 417–423, 2017.
12. Z. H. Yan, *Artificial Bee Colony Constrained Optimization Algorithm with Hybrid Discrete Variables And Its Application*, Acta Electronica Malaysia, Vol. 2, No. 1, pp. 18–20, 2018.
13. N. F. Basir, S. Kasim, R. Hassan, H. Mahdin, A. Ramli, M. F. Md Fudzee, and M. A. Salamat, *Sweet8bakery Booking System*, Acta Electronica Malaysia, Vol. 2, No. 2, pp. 14–19, 2018.
14. Z. He, X. Gu, X. Y. Sun, J. Liu, and B. S. Wang, *An Efficient Pseudo-Potential Multiphase Lattice Boltzmann Simulation Model for Three-Dimensional Multiphase Flows*, Acta Mechanica Malaysia, Vol. 2, No. 1, pp. 01–03, 2018.
15. S. Sathishkumar, and M. Kannan, “*Design and Fatigue Analysis Of Multi Cylinder Engine And Its Structural Components*,” Acta Mechanica Malaysia, Vol. 2, No. 2, pp. 10–14, 2018.
16. N.Y. Zainun, M.S. Abdul Rahman, A.R. Alias, and F.E. Mohamed Ghazali, *Significant factors of key parameters for low medium cost housing demand in Malaysia*, Engineering Heritage Journal, Vol. 1, No. 1, pp. 25–28, 2017.
17. S. R. Hassan, N. Qamaruz Zaman, I. Dahlan, *Influence of Seed Loads on Start Up of Modified Anaerobic Hybrid Baffled (MAHB) Reactor Treating Recycled Paper Wastewater*, Engineering Heritage Journal, Vol. 1, No. 2, pp. 05–09, 2017.

CONTACT WITH THE AUTHORS

Zhiyong Pei

e-mail: zhiyong_pei@whut.edu.cn

Wuhan University of Technology
 No. 1178, Heping Avenue
 Wuchang District
 Wuhan 430063
 Hubei Province
CHINA

PROGRESSIVE COLLAPSE TEST OF SHIP STRUCTURES IN WAVES

Zhiyong Pei^{1,2)}

Tao Xu¹⁾

Weiguo Wu^{1,2)}

¹⁾ Departments of Naval Architecture, Ocean and Structural Engineering, School of Transportation, Wuhan University of Technology, China

²⁾ Key Laboratory of High Performance Ship Technology of Ministry of Education, Wuhan University of Technology, China

ABSTRACT

The external loads and structural ultimate strength are two important aspects for the safety of ship hull girder. It may collapse in case the structural capacity is less than the external forces in extreme seas. In the present research, progressive collapse test is performed to investigate the collapse mechanism of ship structure in waves. External load with time history and corresponding structural collapse behavior are measured and discussed to demonstrate the interaction of fluid and structures.

Keywords: Ship hull girder, Progressive collapse behavior, Ultimate strength, External force, Collapse test

INTRODUCTION

Based on a study, with the development of society and the progress of economy, the international trade supported by shipping becomes more and more common. According to the statistical document, there are more than 1200 ship accidents all over the world from 2005 to 2014 [1], which caused not only loss of lives and properties but also seriously environmental problem such as pollution due to spilled oil. The main reason of these accidents is the ship structural ultimate strength is insufficient to resist the external loads acting on the ship hull in extreme seas. Ship wrecks and rules of related ship organizations make it necessary to study the progressive collapse behavior of ship structures in waves.

In traditional, ship structural ultimate strength is evaluated considering the structure itself. One frame space model or hold model is usually adopted imposing forced rotation on end cross-sections assuming that the cross-section remains plane. The bending moment is calculated by integrating the axial force multiplied by a lever in each element. The ultimate strength is defined as the maximum moment along the equilibrium path obtained by the above-mentioned static analysis. Direct calculation method, Smith method, Idealized Structural Unit Method and nonlinear

finite element method can be used to carry out such analyses. However, the natural world is not controlled by pathways or curvatures, but by pressure and/or force. Bending moment-curvature relationship obtained by forced displacement method or arc length method could be far from the reality after the working bending moment has exceeded the hull girder capacity, as pointed out by Lehmann [2-6].

Considering the fluid-structure interaction and its influence on collapse behavior of ship structures, a scholar proposes a total computation system combining three-dimensional Singularity Distribution Method with Idealized Structural Unit Method [7]. The three-dimensional Singularity Distribution Method is adopted to calculate the ship motion and pressure distribution. The calculated loads including inertia forces with time history are transferred to structural model and progressive collapse behavior can be obtained. According to research, the collapse characters of a bulk carrier under alternate loading condition are demonstrated and discussed [8-9]. A scholar combined computational fluid software STAR-CCM+ and the structural analysis software ABAQUS to carry out the coupling analysis of fluid and solid of a barge, in which the hull structure is regarded as an elastic beam [10]. Other scholar calculated structural ultimate capacity of several typical ship sections

considering both hydrostatic and hydrodynamic pressure to investigate the influence of lateral pressure on ultimate strength of ship hull girder [11]. To investigate the character of bending moment, a model test is carried out to describe the post-ultimate behavior of ship hull girder in waves [12]. Two rigid bodies are connected with a plastic hinge which is designed to measure the vertical bending moment caused by the fore and aft body.

In this paper, progressive collapse test in waves is carried out to investigate the collapse characteristics and ultimate capacity of ship structures. A stainless-steel test model with three holds is designed. The pressure of typical points in the bottom is measured through pressure sensor. The ship motion acceleration is recorded by acceleration sensor and inclinometer sensor. The strain distribution of three typical sections is measured by dynamic strain gauge. The weight of test model is small so that steel blocks are put in the fore and last section to form the proper still water bending moment. The wave maker produces the wave in towing tank in the condition that the wave length equals to the length of test model. With the increase of wave height, the force subjected to the test model increases so as to the structures collapse finally. The test results are discussed and compared with FEM results. The pressure, motion and stress distribution during the collapse test are demonstrated.

MODEL DESIGN

To explore the collapse mechanism of ship structures in extreme seas, the model collapse test in waves is carried out. The external forces should be larger than the structural ultimate capacity, otherwise the structural collapse cannot be happened. Due to the capacity limitation of wave maker, the wave bending moment is also limited. The test model shall be weak enough so as to be collapsed under the still water bending moment and wave bending moment [13, 14].

Nonlinear finite element method is used to estimate the ultimate capacity of preliminary designed test model. Double-span section model is adopted and forced rotation angle is added in the end section. As the increase of rotation angle, the relationship between vertical bending moment

and rotation angle can be achieved. The maximum bending moment represents the structural ultimate strength. The ultimate strength of test model is designed a little smaller than external loads including still water bending moment and wave bending moment. The procedure of model design is summarized in Fig. 1.

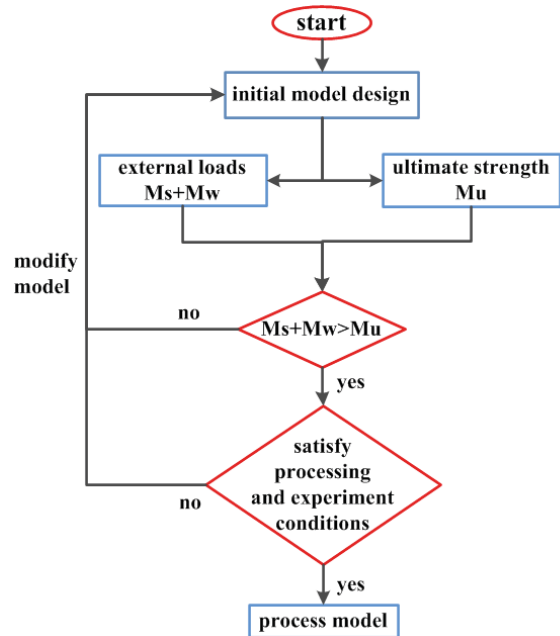


Fig. 1. Model design procedure

There are three holds for the test model. The fore and aft hold can be considered as loading part and the middle hold is the test one. There is deck opening at the end of loading hold in order to put mass block to enlarge the still water bending moment. The length of each hold is 2.25m so the length of test model is 6.75m. The width and depth are 1.25m and 0.3m, respectively. The space of bottom longitudinal is 0.25m and that of side longitudinal is 0.15m. The plate thickness of loading holds is 3mm and the stiffener size is -20x3mm. The plate thickness of the middle hold, namely test part, is 0.5mm and the stiffener size is -20x0.5mm. The dimensions of test model are shown in Fig. 2 [15].

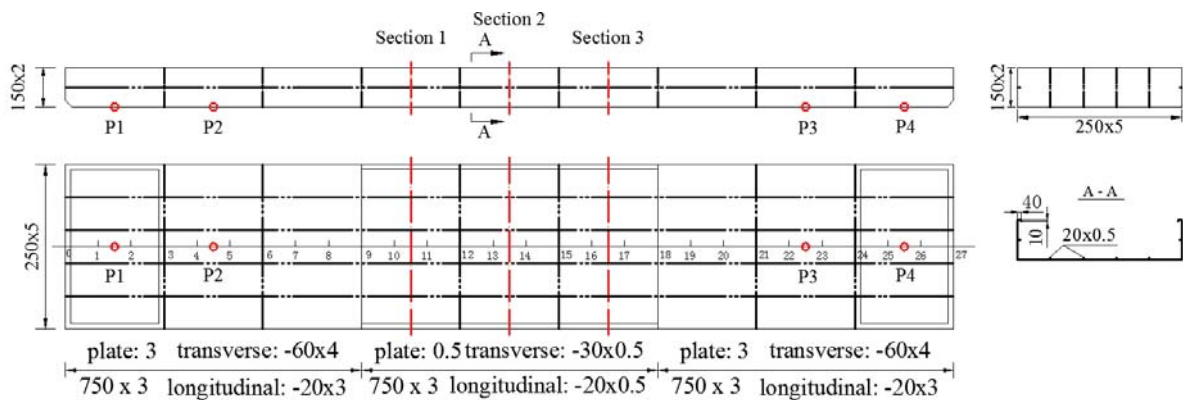


Fig. 2. Model dimensions and Measurement point of lateral pressure

MODEL TEST

Not only the external forces subjected to the test model but also the structural progressive collapse procedures are included in the test. The pressure distribution, the ship motion and the strain distribution in the still water and in the wave are recorded.

TEST CONTENT

The encountered wave length equals to the length of test model. The position of the crest is different with the movement of waves. So, the lateral pressure value of typical position in the bottom can represent the wave situation which can be used to calculate the wave bending moment.

The ship motion includes three translational motions and three rotational motions. The acceleration sensors are used to measure the translational motions such as surge, sway and heave and inclinometer sensors are adopted to test the rotational motions such as roll, pitch and yaw. The inertia forces are obtained by multiplying the mass by the corresponding acceleration [16].

The structural stress distribution during the collapse is the important affairs. In order to get the bending moment, the strain test points shall be distributed in the typical section of test part. There are test points in the stiffener position and the panel center of the middle section where the bending moment shall be the largest. The test points in neighbor section are also distributed to validate and/or eliminate incorrect data.

TEST POINTS

The pressure test points shall be able to represent the wave situation. The wave length is basically equal to the model length. There are totally four test points locating at the bottom center of two end sections in the loading hold, as shown in Fig. 2.

The elastoplastic deformation is comparatively smaller than the movement of rigid body. Two acceleration sensors are enough to describe the translational motion situation. They are arranged in the deck at the center of each loading hold [17]. The rotational motion of test part is interesting and worth measuring. Two inclinometer sensors are placed at fore and aft end of test part to record the rotational situation during the collapse test. The arrangement of sensors is shown in Fig. 3.

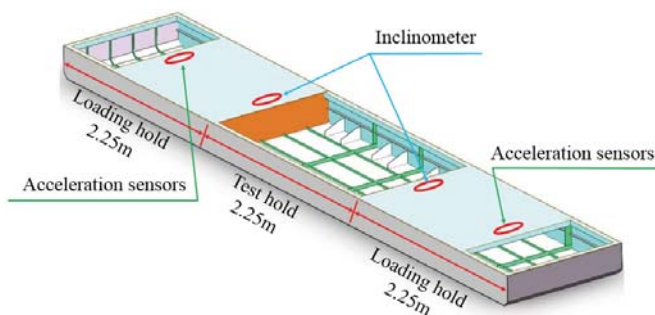


Fig. 3. Measurement point of ship motion

In order to realize the structural response during the collapse test in waves, the strain test points are distributed in the typical section of test part. The midst section will suffer the largest vertical bending moment so that all the positions of stiffener and center of panel are considered as stress test point. To describe the strain distribution in depth direction, seven test points are arranged in the same distance in the side shell from bottom to the upper deck. In the fore or aft section of the midst section, there are strain test points at the position of stiffener and the joints between side shell and bottom and deck. The position of sections for strain test points is schemed in Fig. 2 and the distribution of strain test points is shown in Fig. 4.

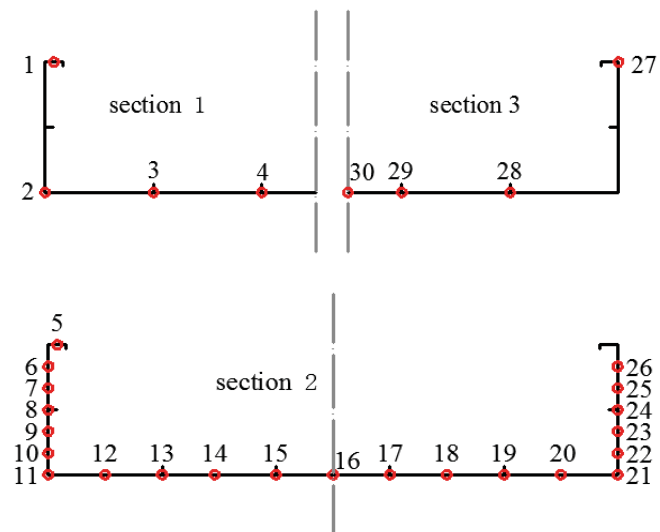


Fig. 4. Strain test points distribution

TEST PROCEDURE

To verify the character of test model, the test under hydrostatic condition is performed firstly. The mass block is put to the end section and thus the still water bending moment is produced. The stress distribution is measured with different weight of mass block to check the fundamental character of test model such as neutral axis, stress distribution and deformation distribution.

Considering the capacity of wave maker, the structural response of the hull structures under different loading conditions in wave is analyzed to determine the weight of mass block and the test wave parameters. In the test, a total of five cases are conducted, as shown in Table 1. The pressure with time history is measured for each pressure test point. The translational acceleration and rotational acceleration with time history and the strain distribution are measured under every loading condition and wave condition.

TEST RESULT

HYDROSTATIC TEST

In order to verify the fundamental character of test model, the test on hydrostatic pressure is performed firstly. The different weight of mass block is acted in the model to produce the different vertical bending moment. The structural response shall be in elastic range so that the weight of mass block is limited to less than 200kg. The relationship between draught and mass block weight is summarized in Table 2. The longitudinal stress distribution of test points in side shell is plotted in Fig. 5. The depth of zero longitudinal stress distribution represents the position of neutral axis. So, the neutral axis of test model locates at the position of depth 100mm. The tangential stiffness of above and below the neutral axis is different because the structures below the neutral axis are subjected to not only the longitudinal bending moment but also the lateral pressure [18]. The lateral pressure causes the bending of plating which leads to the bending stress components. The stress of structures below the still water surface includes the bending stress components caused by lateral pressure and in-plane stress components caused by the longitudinal bending moment. So, the tangential stiffness of lower structures becomes weak.

Tab. 1. Test cases

Case No.	Mass block (kg)	Wave height (mm)	Wave frequency (rad/s)	Wave length (mm)	period (s)
D1-1	200	50	2.92	7225	2.151
D1-2	200	100	2.92	7225	2.151
D2-1	600	40	2.98	6937	2.107
D2-2	600	80	2.98	6937	2.107
D2-3	600	120	2.98	6937	2.107

Tab. 2. Draught with different weight of mass block

Case No.	Mass block (kg)	Draught (mm)
H1	0	72.79
H2	50	78.82
H3	100	84.85
H4	150	90.89
H5	200	96.92

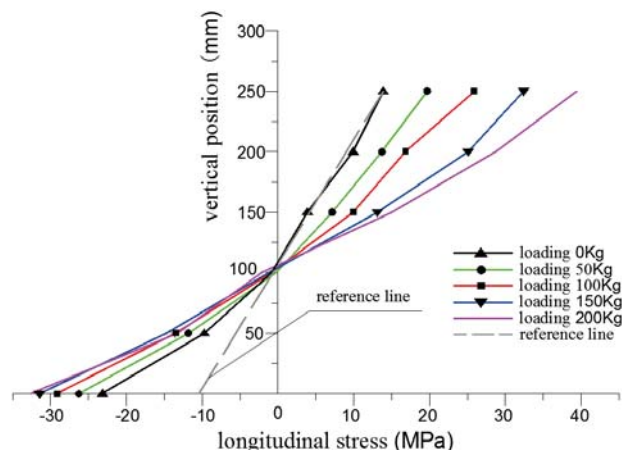


Fig. 5. Longitudinal stress with different weight of mass block

COLLAPSE TEST

According to the preliminary numerical analysis, the ship structures will be collapsed when the weight of mass block is 600kg and the wave height is 120mm. In order to demonstrate the structural response characteristics in waves, the pre-test is carried out for the weight of mass block 200kg and wave height of 50 mm and 100 mm respectively. Then, the collapse test is conducted under the conditions of weight of mass block 600kg and wave height 40 mm, 80 mm and 120 mm respectively. The pressure distribution with time history, ship motion characteristics and the corresponding structural condition are measured.

When the weight of mass block is 200kg and wave height is 50mm and 100mm, the ship structures are in the elastic situation. The test results demonstrate that the test system works well, and the response of test model satisfies the requirement. In case the weight of mass block is 600kg, the loads acting on the ship structures will increase with the increase of the wave height. When the wave height reaches to 120mm, the collapse of ship structures will be taken place. Due to page limitation, the results in elastic stage are not described and only those of structural collapse are shown in the paper. In fact, the results in elastic stage can be considered as the primary stage of collapse behavior.

The schematic diagram of the position of the model and the wave under the conditions of collapse test is shown in Fig. 6. The wave crest locates at the middle of test model so that the ship hull is in hogging condition. With the movement of the wave crest, the loads acting on the ship structures are also different and so as the ship motion and structural response. A wave-height gauge is placed in front of the test model and the sampling frequency is set to 50Hz. The measured wave height distribution with time history is shown in Fig. 7. To facilitate the analysis of various test results, the sampling frequencies of other instruments such as pressure sensor, acceleration sensor, inclinometers sensor and dynamic strain gauges are also set to 50Hz. The variation of the lateral

pressure with time history at the pressure test points in the bottom can represent the relative position of the wave and the test model. The lateral pressure distribution of the typical measuring point (No. 4 test point locating at the fore hold) is shown in Fig. 8. The average vertical acceleration of the fore and aft acceleration test points is expressed in Fig. 9. The relative rotation angle measured by the inclinometers is demonstrated in Fig. 10. All measured results are sinusoidal distribution with time history and the period is 2.107s which is consistent with the characters of wave.



Fig. 6. Collapse test of ship hull

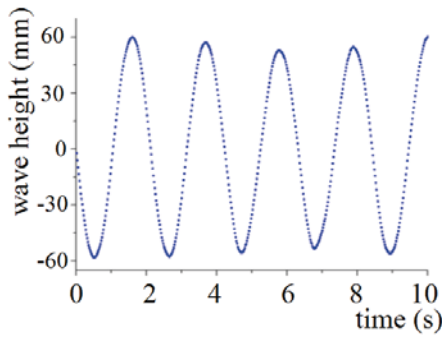


Fig. 7. Wave height

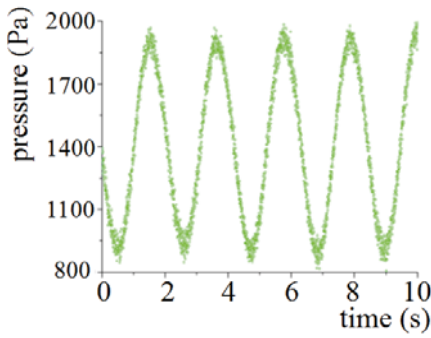


Fig. 8. Lateral pressure

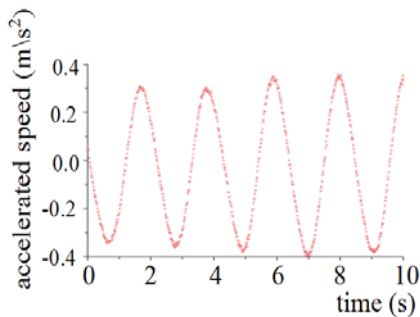


Fig. 9. Vertical acceleration

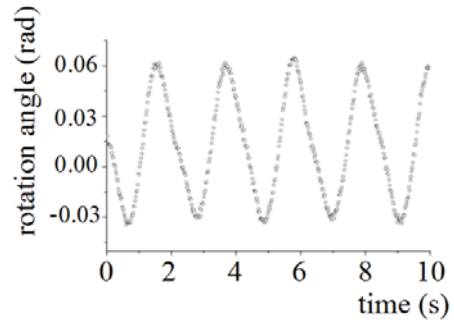


Fig. 10. Relative rotation angle

During the collapse test, the dynamic strain of test points is also measured. The dynamic stress can be calculated according to the stress-strain relationship of the specimen. The dynamic stress distribution of typical test points in the central section, such as test point 5 (locating at the deck), test point 11 (locating at the intersection between side shell and bottom), test point 19 (locating at the bottom longitudinal stiffener) and measuring point 26 (locating at the upper side of side shell) is plotted in Fig. 11. The dynamic stress of each test point demonstrates sinusoidal distribution and the period is same as wave period.

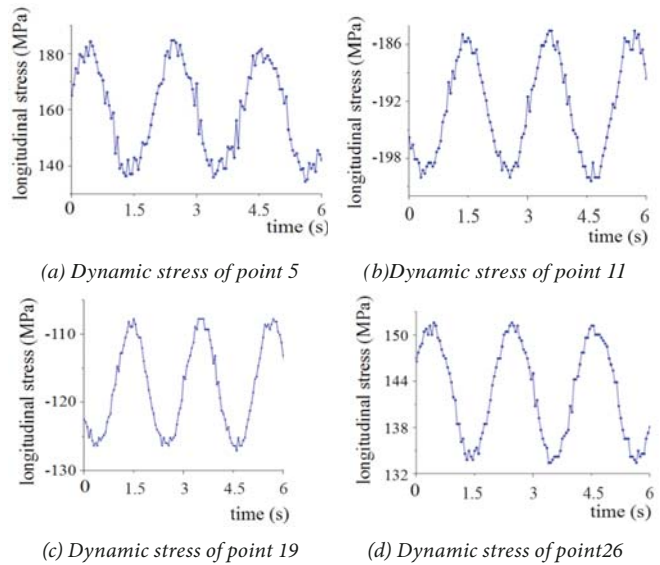


Fig. 11. Dynamic stress of typical points

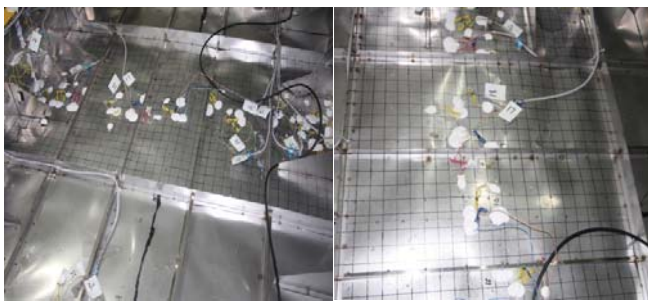
RESULT ANALYSIS

COLLAPSE BEHAVIOR

The ship is a large floating structural system which is subjected to both hydrostatic load and wave load. The bottom structures of test model are subjected to lateral pressure and thus the bending stress component is generated. When

the wave trough is locating in the mid length, the bottom structures are simultaneously subjected to compression caused by hogging and the bending caused by lateral pressure.

The wave load increases with the increase of wave height. When the wave crest is locating in the mid length, the buckling of bottom plating happens firstly under the compression and lateral pressure. With the movement of wave, the buckling of deck plating and the top plating of side shell are also taken place when the wave trough is locating in the mid length. Then, the load is re-distribution between the structural components. The longitudinal stiffener of bottom is buckled and yielded successively due to the compression and lateral pressure. The collapse of ship structures happens so as to loss the load-carrying capacity. The collapse mode of bottom structures is the stiffener tripping and plating buckling, as demonstrated in Fig. 12.



(a) test hold (b) collapse part

Fig. 12. Collapse mode of bottom structures

VERTICAL BENDING MOMENT-CURVATURE RELATIONSHIP

In the present research, the longitudinal bending moment can be obtained by performing secondary integration of the stress of each test point in the midst section. The relative rotation angle of test hold can be computed by the measured angle value at both end sections. The curvature is calculated by the relative rotation angle divided by the length of test hold. Then, the relationship of vertical bending moment and curvature can be achieved. To explore the fluid-structural interaction effect, the moment-curvature relationship obtained by structural calculation, fluid- structural interaction calculation and collapse test is compared in Fig. 13.

For structural calculation, double-span section model, namely longitudinal hull girder segment extending a half frame spacing in fore and aft directions from a transverse frame, is considered. A forced rotational angle is applied to both end cross-sections assuming that the cross sections remain plane. The obtained ultimate strength represents the structural itself capacity which is no relationship with the external force.

For fluid-structural interaction calculation, the wave induced load calculation is firstly performed on the test model to obtain the external loads. Then, they are converted into equivalent nodal forces and applied to the structural model.

The progressive collapse analysis is performed to obtain the corresponding bending moment and curvature. The ultimate strength calculated by such method is not only related to the hull structures, but also related to the external loads.

It can be seen from Fig. 13 that the ultimate strength calculated by structural calculation is larger than that by fluid-structural interaction calculation. The structure shall deform due to the action of fluid/water pressure which lead to the bending stress component. The structural buckling occurs earlier as well as initial yielding so that the ultimate strength is reduced. The traditional structural calculation, considering the structural model itself and not considering the influence of the fluid, will cause larger ultimate capacity. The shipwreck may be happened when the actual external load is smaller than the ultimate capacity calculated by traditional structural model but larger than actual structural capacity. In addition, the test result is about 10% smaller than that of fluid-structural interaction calculation. This is because the initial deformation and welding residual stress are not considered in the fluid-structural interaction calculation. Thin plate and small stiffener are adopted in the test hold of test model so that larger initial deformation and welding residual stress are produced during the course of processing.

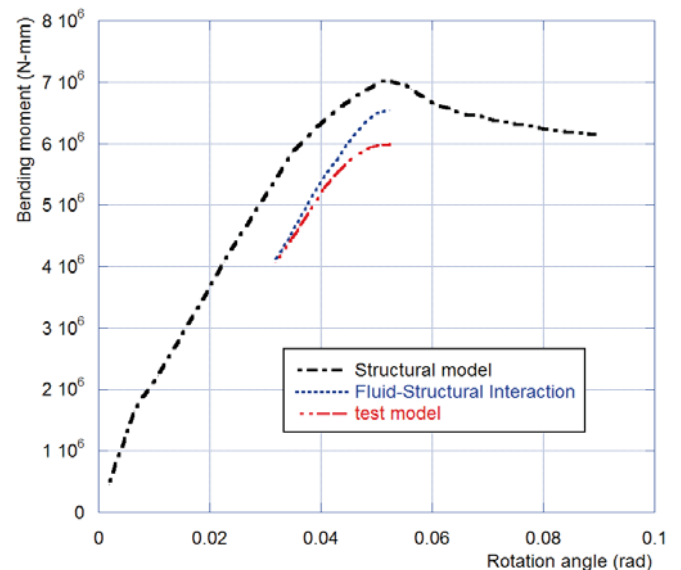


Fig. 13. Comparison on relationship of bending moment and rotation angle

CONCLUSION

In the present research, the collapse test of ship model is performed to investigate the collapse behaviour of ship structures in wave. The moment-curvature relationship obtained by collapse test is compared with that by structural calculation and fluid-structural interaction calculation. The calculation model and the influence of lateral pressure are discussed. The conclusions can be summarized as follows.

For the traditional structural calculation, the cross-section is assumed to remain plane. A forced rotational angle is applied to both end cross-sections and the maximum bending moment is defined as the structural ultimate strength. The ultimate strength obtained by such method is a little larger than actual one which may lead to dangerous situation.

The structures below the still waterline deflect under the effect of lateral pressure so as to produce the bending stress component. The structural buckling and initial yielding occur earlier and thus the ultimate strength is reduced. It is better to consider the effect of lateral pressure when structural ultimate strength is calculated.

The stiffener tripping and plating buckling of bottom structures are taken place under the longitudinal compression caused by vertical bending moment and out-of-plane bending caused by lateral pressure. With the happening of initial yielding and the spreading, the structural section loses its load-carrying capacity and reaches ultimate strength.

REFERENCES

1. <https://www.statista.com/chart/3354/large-ship-losses-reach-lowest-point-in-a-decade/>
2. J. Caldwell, "Ultimate longitudinal strength," *Trans Royal Inst Nav Arch*, Vol. 107, pp. 411-430, 1965.
3. C. Smith, "Influence of Local Compressive Failure on Ultimate Longitudinal Strength of a Ship's Hull," *Proc. Int. Symp. On Practical Design in Shipbuilding (PRADS)*, pp. 73-79, 1977.
4. Z. Pei, and M. Fujikubo, "Application of idealized structural unit method to progressive collapse analysis of ship's hull girder under longitudinal bending," *International Society of Offshore and Polar Engineers*, pp. 766-773, 2005.
5. H. K. K. Amlashi, and T. Moan, "Ultimate strength analysis of a bulk carrier hull girder under alternate hold loading condition – A case study: Part 1: Nonlinear finite element modelling and ultimate hull girder capacity," *Marine Structures*, Vol. 21, No. 4, pp. 327-352, 2008.
6. E. Lehmann, "Discussion on report of Committee III. 1: ultimate strength," In: *Proceedings of 16th ISSC*. 3, Southampton, UK, pp. 121-131.
7. T. Yao, M. Fujikubo, and K. Iijima, "Total system including capacity calculation applying ISUM/FEM and loads calculation for progressive collapse analysis of ship's hull girder in longitudinal bending," *Renaissance Quarterly*, Vol. 53, No. 2, pp. 706-713, 2009.
8. Z. Pei, K. Iijima, M. Fujikubo, Y. Tanaka, S. Tanaka, S. Okazawa, and T. Yao, "Collapse Analysis of a Bulk Carrier under Alternate Heavy Loading Conditions," *Int. Journal of Offshore and Polar Engineering*, pp. 224-231, 2013.
9. Z. Pei, K. Iijima, and M. Fujikubo, "Simulation on progressive collapse behavior of whole ship model under extreme waves using idealized structural unit method," *Marine Structures*, Vol. 40, pp. 104-133, 2015.
10. P. A. Lakshminarayanan, P. Temarel, and Z. Chen, "Hydro elastic analysis of a flexible barge in regular waves using coupled CFD-FEM modelling," *Marine Structures*, pp. 95, 2015.
11. D. K. Kim, H. P. Dong, and B. K. Han, "Lateral pressure effects on the progressive hull collapse behavior of a Suezmax-class tanker under vertical bending moments," *Ocean Engineering*, Vol. 63, No. 4, pp. 112-121, 2013.
12. W. Xu, W. Duan, and D. Han, "Investigation into the dynamic collapse behavior of a bulk carrier under extreme wave loads," *Ocean Engineering*, Vol. 106, pp. 115-127, 2015.
13. L. Chen, and C. X. Wang, "Green Development Assessment of Smart City Based on PP-BP Intelligent Integrated and Future Prospect of Big Data," *Acta Electronica Malaysia*, Vol. 1, No. 1, pp. 01-04, 2017.
14. Z. G. He, X. A. Gu, X. Y. Sun, J. Liu, and B. S. Wang, "A coupled immersed boundary method for simulating multiphase flows," *Acta Electronica Malaysia*, Vol. 1, No. 1, pp. 05-08, 2017.
15. X. N. Gu, Z. G. He, X. Y. Sun, J. Liu, and B. S. Wang, "Algebraic dynamic multilevel (ADM) method for compositional multi-phase flow simulation," *Acta Mechanica Malaysia*, Vol. 1, No. 1, pp. 01-03, 2017.
16. X. N. Gu, Z. G. He, X. Y. Sun, J. Liu, and B. S. Wang, "A Two-dimensional lattice Boltzmann method for compressible flows," *Acta Mechanica Malaysia*, Vol. 1, No. 1, pp. 04-07, 2017.
17. N. A. Yaacof, N. Qamaruzzaman, and Y. Yusup, "Comparison method of odour impact evaluation using calpuff dispersion modelling and on-site odour monitoring," *Engineering Heritage Journal*, Vol. 1, No. 1, pp. 01-05, 2017.
18. M. R. Rozainy, M. A. Z. Khairi, A.W. I. Abustan, S. S. Rahim, and M. N. Nasehir Khan, "A study on the selection of suitable sites for integrated smart trapper system installation (InSmarts)," *Engineering Heritage Journal*, Vol. 1, No. 1, pp. 06-10, 2017.

CONTACT WITH THE AUTHORS

Zhiyong Pei

Departments of Naval Architecture
Ocean and Structural Engineering
School of Transportation
Wuhan University of Technology
Wuhan 430063

CHINA

Key Laboratory of High Performance Ship Technology
of Ministry of Education
Wuhan University of Technology
Wuhan 430063

CHINA

Tao Xu

Departments of Naval Architecture
Ocean and Structural Engineering
School of Transportation
Wuhan University of Technology
Wuhan 430063

CHINA

Weiguo Wu

Departments of Naval Architecture
Ocean and Structural Engineering
School of Transportation
Wuhan University of Technology
Wuhan 430063

CHINA

Key Laboratory of High Performance Ship Technology
of Ministry of Education
Wuhan University of Technology
Wuhan 430063

CHINA

CALCULATION AND MEASUREMENT OF TIDE HEIGHT FOR THE NAVIGATION OF SHIP AT HIGH TIDE USING ARTIFICIAL NEURAL NETWORK

Li Qiang¹,
Yang Bing-Dong²,
Hong Bi-Guang¹

¹ Navigation College, Dalian Maritime University, Dalian, Liaoning, China

² Pilot Station of Huanghua Port, Huanghua, Hebei, China

ABSTRACT

Accurate tide height is crucial for the safe navigation of large deep-draft ships when they enter and leave the port. We have proposed an accurate forecasting method for the tide heights from the observation data and neural networks, which can easily calculate the tidal window period of large deep-draft ships' navigation through long channels at high tide. Moreover, an artificial neural network is established for the tide height from the observation of tide heights before their current time node. For an ideal forecast, the neural network was optimized for one year with the tide height data of Huanghua Port. In case of large ships, their tidal characteristics of channels for are complex. A new method is proposed for the observation of multiple stations and artificial neural networks of each observation station. When ships are navigating through the port, the tide height is predicted from the observed data and forecast tide heights of multiple observation stations. Thus, a valid tidal window period is secured when the ships enter the port. Comparative analysis of the ship's tidal window period with that of the measured one can lead us to conclude that the forecasted data has a strong correlation with the measurement. So, our proposed algorithm can accurately predict the tide height and calculate the node timing when the ship enters and depart the port. Finally, these results can be applied for the safe navigation of large deep-draft ships when the port is at high tide.

Keywords: Deep-draft ships, neural network, intelligent navigation, multi-observation stations

INTRODUCTION

The draught of large deep-draft ships has been continuously increasing due to their recent demand. The length and depth of the channels should high for the frequent entering and departure of the ships from the ports [1]. For instance, the channel length of the Comprehensive Port area of Huanghua Port [2] and Lanshan Port in Rizhao [3] reach 60.5 and 48.9 km, respectively. At certain ports, the tide timing for a ship can be obtained from the tide table. However, in case of a long channel with a high variation of tidal changes, tide table cannot calculate the tide timing when the ships enter

or depart and under keel clearance. At the same time, it will also calculate the tide height during the high tide time period which meets the conditions of entering the river fail and the requirements of the ship's entering the port at high tide. This dramatically affects the efficiency of large-scale deep-draft ships when entering the port, reduces the passage capacity of the port channel, and affects the navigation safety of the ships.

To date, only theoretical research is conducted on the water level when the ships enter the port at high tide and other related plans. Furthermore, this topic has become one of the hot topics for researchers in the field. Tang et al.

investigated the adaptability of a 400 thousand dwt bulk cargo ships with the water depth when the ships enter Dongjiakou Port. They thoroughly investigated the node time of ships while entering the ports by the tide. Moreover, they also proposed methods for keel clearance of large ships from the observation of tidal records at Dongjiakou Port [4]. Zhang et al. proposed a method for the depth calculation of artificial long channel. Actually, they proposed this method from the tide forecast at a single station and the characteristics of channels in Lansshan Port District of Rizhao Port. However, their method cannot adequately differentiate in tide heights of different channel sections [3]. On the other hand, Huang et al. have proposed another method for the calculation of tide height at Yamen Channel in Jujiang. The value of tide height is required for the ships when they enter the port and the channels have high tide. This method can rarely be applied to those ports which have small differences in the tide period but large differences in the tide height [5]. In 2012, Xu et al. proposed a multi-station joint method for the calculation of tide height, especially, when the ships enter the port at high tide in the tidal estuary of the long channel [6]. It can be observed from the trial calculations that this method still needs to be optimized such as for the optimal process of entering the port at high tide and the optimal tide height for each tidal process. Furthermore, to get the tide height when the ships enter the port at high tide corresponding to different cumulative frequencies. So, the calculation process is realized by the program, but the results are not intuitive enough. On the other hand, this method can only be applied to those channels which have constant tide height, means cannot consider the different tide heights in different sections of the long channel.

The above analysis led us to conclude that for the safe navigation of large deep-draft ships and to clear the ports, accurate measurement of the tide height is required. The tide height is primarily related to the ship's navigation time while entering the port. Secondly, it is related to the mileage of the channel and the accuracy of the tide height forecast. In this paper, we are using the feedback neural network algorithm and the measured data of the tides in the port, to achieve the goals in the following two aspects: (1) using the measured tidal data to forecast the tide at the position of each station; (2) calculation of tidal window of the ships when entering the port.

MODEL FOR THE CALCULATION OF TIDAL WINDOW

Draughts of ships have been continuously increasing as the size of ships becomes larger and larger. The draught of 200 thousand dwt bulk cargo ship has reached 18.3 m. For a 300 thousand bulk cargo ship, its draught has reached to 21.5 m. In case of 400 thousand dwt ships, their draughts have reached 22 m. The high number of draught means, we need a deeper depth of channel for the safe navigation of ships. However, the depth of the channel cannot be increased unrestrictedly

during the construction of channels for large ships due to the following three reasons.

1. High-depth channel requires high construction and maintenance cost;
2. There is enough time for large bulk cargo ships to wait for the tide raise as these ships have a longer sailing period. Moreover, there are more chances that they can enter the port at high tide;
3. A number of large ships that navigate through the port is limited. To deepen the depth of channel are waste of resources.

Therefore, the constructors are trying to employ those methods which can allow the ship's navigation through the channels at high tides to lower the depth of channels. When ships navigate through this type of channels, the tide height must reach a certain level to allow safe navigation through the port. In case of insufficient tide height, the short of under keel clearance will cause the risk of ships being stranded and also increase the difficulty of handling the ships. The time period for the appropriate tide height, where the ships can navigate through the port is called tidal window. Obviously, the tidal window is related to the draught and speed of ships, the tide height, and the under-keel clearance. Traditionally, the tidal window can be calculated from the typical tide curve method [7]. This method does not consider the effects of water level fluctuation, caused by meteorological factors, so, cannot be applied to those ports which have prominent water level fluctuation.

When a ship navigates, then its velocity depends on the following factors such as depth of water, navigation obstacles, and the distance from the port. Thus, the velocity tends to be not a fixed value [8, 9]. In this study, the velocity of the ship at time t is presented by function $V(t)$ ($t \in [t_0, t_1]$), t_0 and t_1 are the nodes time while navigating through the port at high tide at the beginning and end, respectively. The location of the ship in the channel can be expressed by the following equation:

$$M(t) = \int_{t_0}^t V(t) dt \quad (1)$$

When the ships navigate in the port, they produce water pressure which led to ship squat. The higher the velocity, the higher the amount of the ship squat. In addition, other factors such as tidal current, waves, the heel and trim of the ship are also responsible for the ship squat. To avoid ships from stranded and touching the bottom of the sea, a certain amount of abundant depth between the keel of the ship and the bottom of the sea is required. This extra depth is called under-keel clearance.

When the ships navigate through the channel, the water depth is required for the draught of the ship and the under-keel clearance. The following conditions are required for the safe navigation of ships through the port.

$$\begin{cases} D_T \geq d + UKC \\ D_T = D_0 + T \end{cases} \quad (2)$$

where D_i is the actual water depth; D_0 is the deigned depth; T is the tide height at high tide; d is the draught of the ship; UKC is the under-keel clearance.

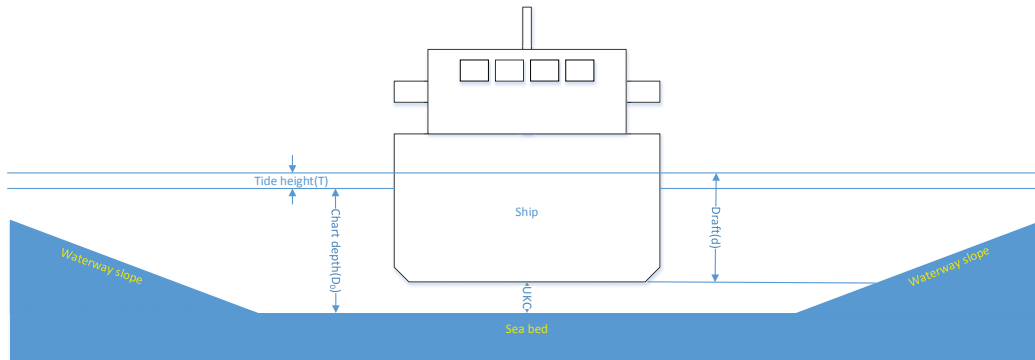


Fig. 1. The UKC during the ship's traversing the channel

Figure 1 shows the relation between water depth, tide height, draught, and under-keel clearance when the ships navigate through the channel. From Figure 1, we can see that the tide height, required for the ships' navigation, has a direct relation with the draught, the under-keel clearance, and the actual water depth of the channel. The time period of tide height in which large deep-draft ships can enter the port is called tidal window. So, the actual tide height for the ship's location should meet the following requirements as specified in Equation 2.

Under-keel clearance is a vital factor which affects the safe navigation of the ships through the port. The calculation method for the UKC, has already been reported [10]. Once UKC is fixed, then the tide height can determine and ensure the safe navigation through the channel of ships. For the tidal window, the tide height in the port should be precisely calculated when the ship navigates through the channel at high tide. In case of the small area of the port, the tide heights remain the same through the whole channel area and the ships can navigate through it at high tide. On the other hand, the larger port has highly fluctuated tide heights at different locations for the ships' navigation through at high tide. In this study, we propose a method for the prediction of tide height which is based on the measurement of tide height combined with neural network and calculate the length of the tidal window when the ship navigates through the port at high tide.

TIDE HEIGHT MEASURING SYSTEM

STRUCTURE AND LOCATION OF OBSERVATION STATIONS

We have selected the Huanghua Port for this research project. Observation stations were located at different positions of the channel of Huanghua Port to record tidal data and calculation of forecasting the tidal window period. The tide consists of astronomical tide and water level fluctuation, caused by meteorological factors. The structure of the tide height measuring system

is shown in Figure 2. This structure consists of a database center, observation stations, and transmission system.

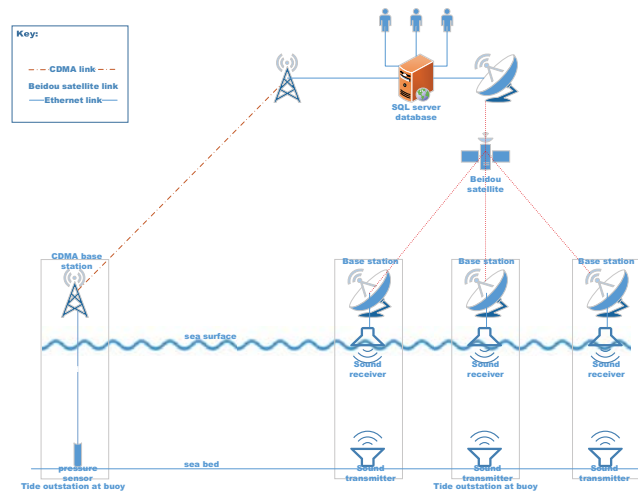


Fig. 2. Structure of the tide height measuring system

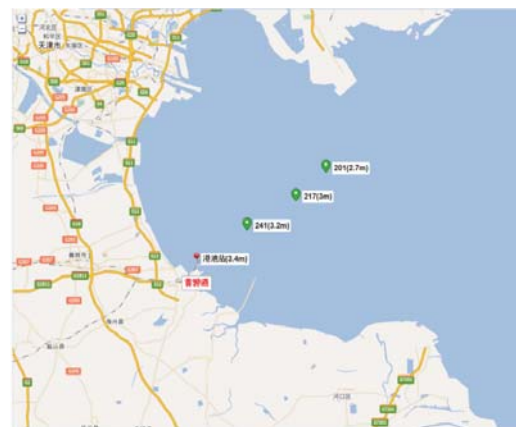


Fig. 3. Locations of observation stations

Each observation station is made up of one onshore tide height and three offshore buoy observation stations. The location of each observation station is presented in Figure 3. Shore-based tide height observation station is adapted to set up the onshore tide height observation station. Pressure-based tide gauges are used to detect the tide height, and the real-time transmission via the cellular network.

Offshore observation stations are located at channel mileage 22+000 (Buoy 241#), 44+000 (Buoy 217) and 60+000 (Buoy 201). In this work, we have employed the Beidou satellite communication technology to realize the real-time online data transmission.

The onshore tide height observation station uses a water level recorder which is equipped with a CDMA mobile data communication device and a solar power supply system. This is used to get the real-time observation and telemetry of tide height data, and uninterrupted 24 h recording and real-time telemetry of water level data.

On the other hand, the offshore buoy observation station uses an acoustic communication device which is part of a pressure-based tide gauge, mounted at the bottom of the sea and transport the monitoring data of real-time pressure to the buoy. All observation data can be collected at the buoy and subsequently transmitted to the onshore data (receiving center) via the Beidou Satellite Communication Method.

The onshore data receiving server automatically receives the transmitted data and forward to each user (client) via broadband network or mobile cellular network.

DATABASE CENTER AND USER INTERFACE

In this work, the MySQL Database is used to manage and store all the data. The data was processed by decryption, analysis, format conversion, screening, filtering, and other online processes. The results generated from these processes were then transferred to the database.

The data management program mainly triggered the instruction of looping at a time interval or by releasing the port data in a background execution mode. The environment management program of the observation station is designed to realize the browsing, management and analysis of the corresponding environment of the onshore tide height observation station. The program is constructed in B/S architecture to display the real-time in the map, station parameters configuration, graphics displaying, and tabular displaying of the station and environment data. Moreover, it is a convenient source for the users to get information from the observation stations at any time.

The online data sharing system is named as “Huanghua Port Channel Hydrology Online”. Function modules of the display system, user login at the welcome page, the observation station, and displaying a map of tide height at the homepage, tide height data, and displaying of tidal current data have been observed. The online data sharing system consists of functions or sections of the welcome page, functions of the homepage, user management, tidal data display, and tidal current data display. The user interface is presented in Figure 4.

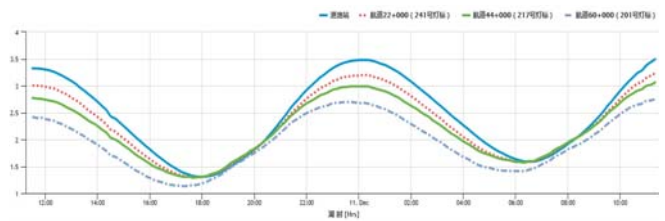


Fig. 4. Interface of database center client

A THEORETICAL MODEL FOR WINDOW PERIOD, BASED ON FEEDBACK NEURAL NETWORK

Recently, with the development of artificial intelligence, many researchers have reported the forecasting of the tide at the ports, using the artificial neural network. In Reference [11], a tide height prediction model is established from the proposed algorithm for the improved and practical genetic neural network tide height prediction. Reference [12] explains the tide height prediction model, using the artificial neural network. A neural network forecast model for storm surge elevation is established, based on high and low tide [13]. Moreover, the tide height is considered for the measuring process under abnormal weather conditions as a research object [14]. Artificial neural network BP algorithm is used as a forecasting tool due to the non-stationary time series of the tide height under these conditions. An artificial neural network model is established from the meteorological data database to predict the water level fluctuation phenomenon in the tidal process. Previously, neural networks have been used to predict the tide on a weekly basis [15]. Recently, a backward-propagation neural network application has been proposed for long-term tide prediction [16]. Moreover, artificial neural networks have also been used for the improved forecasting of ocean tide [17]. So, these studies focus on the long-term forecast of tides at a port, however, the accuracy of the forecast is limited due to the long forecast time. For the long artificial channel, the tidal change within the length of the channel is more notable. An accurate short-term tide forecasting method which involves multi-observation stations is required, to forecast tidal window period for the safe navigation of ships through ports at high tide [18].

COMPUTING ARCHITECTURE FOR TIDAL WINDOW PERIOD BASED ON ARTIFICIAL NEURAL NETWORK

In order to study the ship tidal window forecasting system, having four observation stations, it is necessary to use the tide height signals (measured by the sensors of each observation) for the establishment of a neural network. In this study, we used an artificial long channel which requires four independent observation stations. There is some minor relevance among the tide height information, collected by each observation station [19]. During the prediction process of tide height, four artificial neural network architectures

are established for the corresponding tide height prediction of four observation stations. Finally, this paper establishes a calculation system for tidal window period when the ships navigate through the port at a high time (see Figure 5). This system consists of a sensor, database, neural network prediction system, and a tidal window calculation processor.

There are four sensors which are located in Buoy 201, Buoy 217, Buoy 241, and Buoy 262, as shown in Figure 5. The recorded data of these sensors are transmitted to the data processing center, namely the database, via CDMA or Beidou Satellites Communication Method. Artificial neural networks ANN1-ANN4 were deployed in the above four observation stations to predict the tide heights [20]. Predicted results combined with the location information of four observation stations were transferred to the tidal window calculation processor for the calculation of tidal window (when the ships navigate through the ports).

for the network. This process does not terminate until the error output of the network reduced to an acceptable level, or the learning time period or the time of learning practice reached the pre-set level.

In this work, we used the forecast process and input data were collected from 00:00 to 16:00 each day, while the tide height data which is collected from 17:00 to 24:00 is used as the output data. The number of hidden layers is set to 1, the number of hidden layer nodes 25, the learning rate of 0.1, and the target value is set to 0.001. The activation function of the hidden layers is a bipolar Sigmoid type function while the transfer function of the output layer is a linear function [23]. The observed data of the Huanghua Port is collected from 1st May 2017 to 30th April 2018, so, a total of 365 groups data was processed. The first 300 groups were used as training data, and the remaining 65 groups were used as verification data. The forecast results for the verification data is shown in Figure 6.

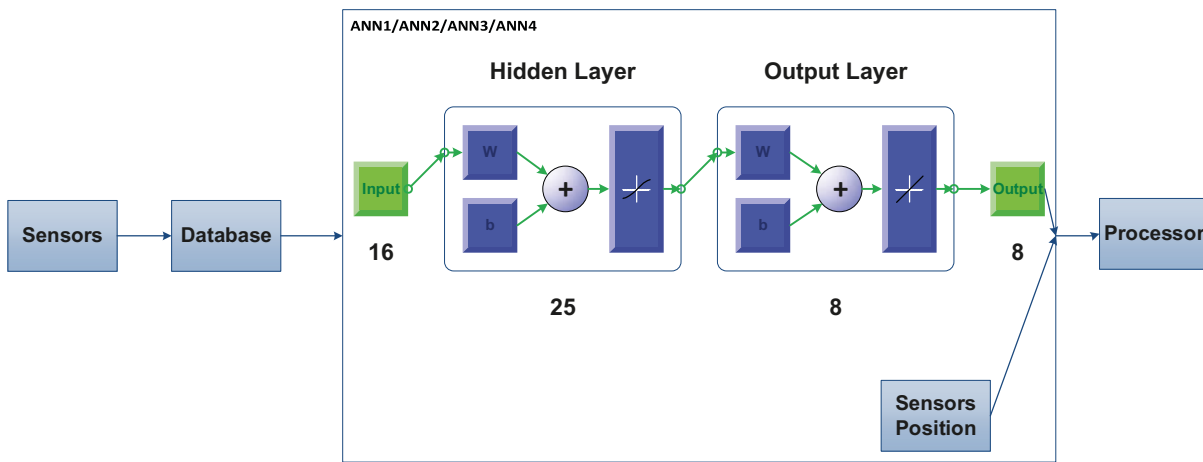


Fig. 5. Architecture for window period calculation model based on the feedback of neural network

TIDE HEIGHT FORECAST

The algorithm of feedback neural network is consisting of forwarding propagation of signal and backward propagation of error. In the forward propagation, the input samples are imported from the input layer which is processed by the hidden layers (layer-by-layer) before being exported to the output layer. If the real output of the output layer is not equal to the expected output, then the propagation process will switch to the backward propagation process [21]. In the backward propagation of error, the output error propagates backwardly through hidden layers (layer-by-layer) in a certain manner. Moreover, this error can be assigned to all the neurons of every single layer which generate the error signal of each layer. From this error signal, we can correct the weight of each neuron. This adjustment of weight in each layer occurs repeatedly, during the forward propagation of signal and backward propagation of error [22]. The continuous adjustment of weight is also a learning and training process

DATA NORMALIZATION AND CRITERIA FOR THE ANNS PERFORMANCE

All data of the input layer are normalized to a range from 0 to 1 by the function:

$$\bar{y}_i = \frac{y_i - y_{\min}}{y_{\max} - y_{\min}} \quad (4)$$

Where \bar{y}_i is the value of data after normalization, y_i is the value of data before normalization, y_{\max} is the maximum and y_{\min} is the minimum of all the hourly tide height respectively.

The ANNs performance is assessed in terms of the root mean square error (RMSE), the correlation coefficient R and mean absolute error (MAE).

$$\text{RMSE} = \sqrt{\frac{\sum_{i=1}^n (y_i - y_i^0)^2}{n}} \quad (5)$$

$$\text{MAE} = \frac{1}{n} \sum_{i=1}^n |y_i - y_i^0| \quad (6)$$

$$R = \frac{\sum_{i=1}^n (y_i^0 - \bar{y}^0)(y_i - \bar{y})}{\sqrt{\sum_{i=1}^n (y_i^0 - \bar{y}^0)^2 \sum_{i=1}^n (y_i - \bar{y})^2}} \quad (7)$$

Where y_i^0 , y_i are observed and predicted tide height. \bar{y}^0 , \bar{y} are mean values of tide height observed and predicted respectively.

Figure 6 shows the forecasted tide height and the observed tide height data of four observation stations, respectively. The forecasted tide height data measures the tide heights from 17:00 to 24:00 each day. The bigger picture in Figure 6 shows the tide heights per hour from 25th February to 30th April (1560 h in total) while the smaller picture represents the observed and forecasted tide height data per hour from 25th-28th February (72 h in total). The input and forecasted data are recorded every day from 0:00 to 16:00 and 17.00 to 24.00, respectively.

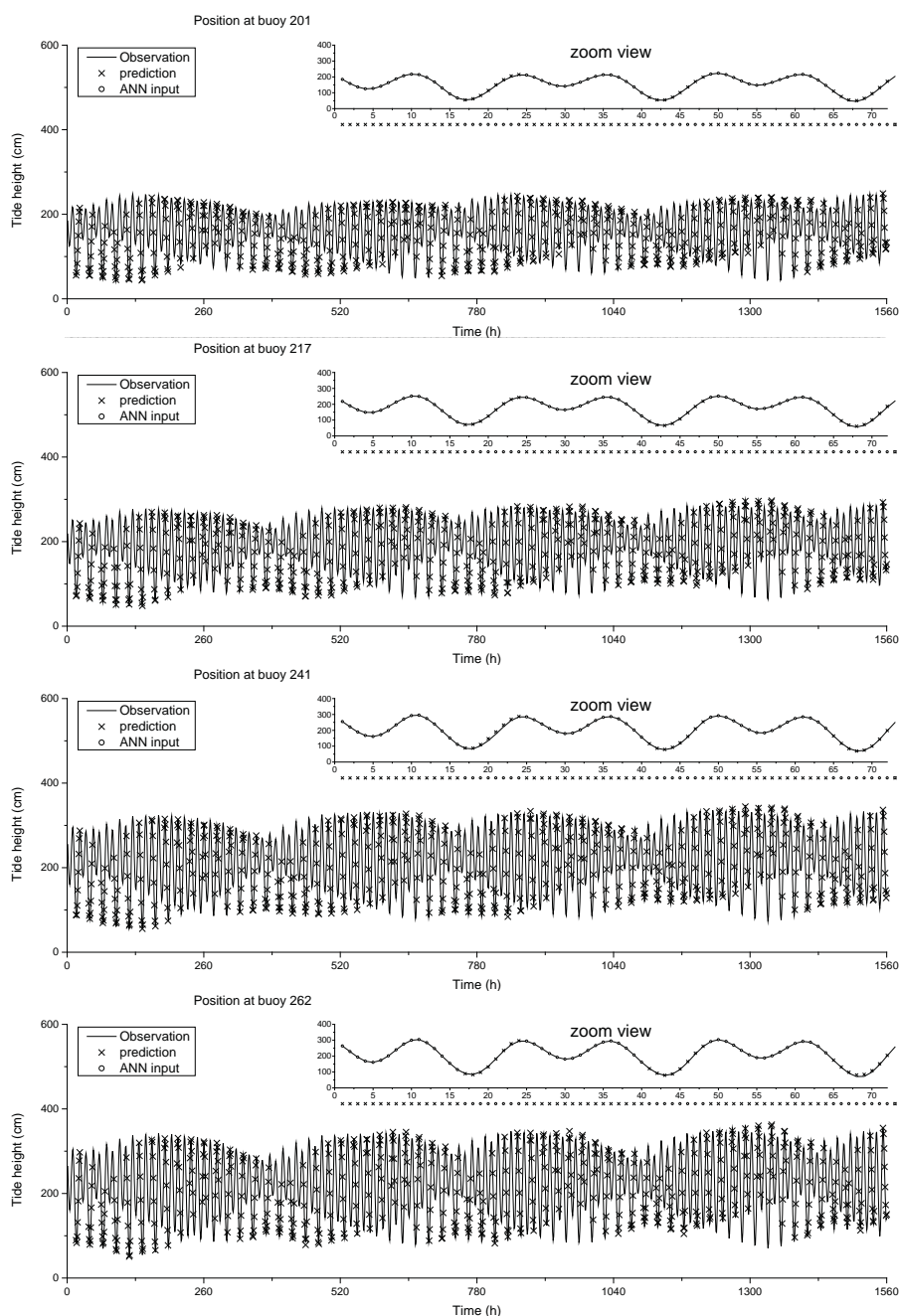


Fig. 6. Observed tide height and forecasted tide height results, obtained from the verification data in 65 days

The forecasted tide height results of four locations in Huanghua Port from 17:00 to 24:00 using four artificial neural networks with identical architecture are shown in Figure 6. Analysis of this Figure led us to conclude that all four neural networks can forecast the tide height well. However, the shorter the distance of the observation station to the port, the higher the difference between the tide heights at high tide and low tide. The scatter plots of the four neural networks are shown in Figure 7. The error of the forecasted results is listed in Table 1. In Table 1, the linear correlations of forecasted results for the next hour, based on the analysis of data recorded in the past 16 h are 0.9999, 0.9999, 0.9998, and 0.9997, respectively. This indicates that the forecast results for the next hour, generated from the four neural networks are very ideal. Moreover, the location which has the higher difference between the tide heights at high tide and low tide is also recorded, which has a lower linear correlation between the measured and the verification results. The linear correlations of the forecasted results for the next 4 h are 0.9993, 0.9993, 0.9987, and 0.9977, respectively, which are slightly lower than that of the linear correlations in the next hour. The linear correlations of the forecasted results for the next 8 h are 0.9982, 0.9984, 0.9981, and 0.9973, respectively, which are again lower than that of the linear correlations of the forecasted results for the next 4 h. This indicates that the accuracy of the forecasted results decreases with the increase of forecast time, but still maintains a satisfactory level.

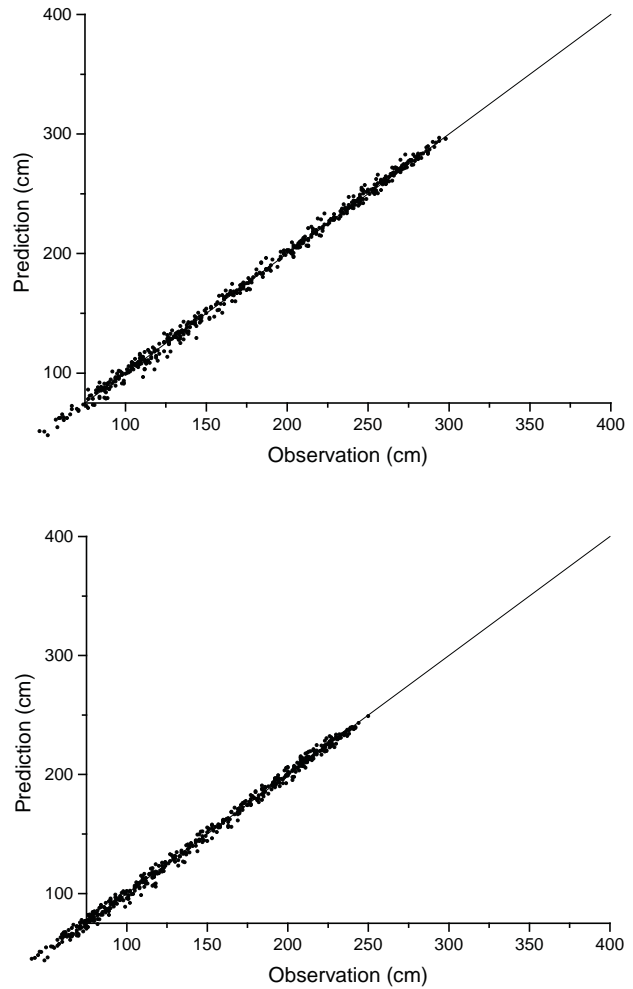
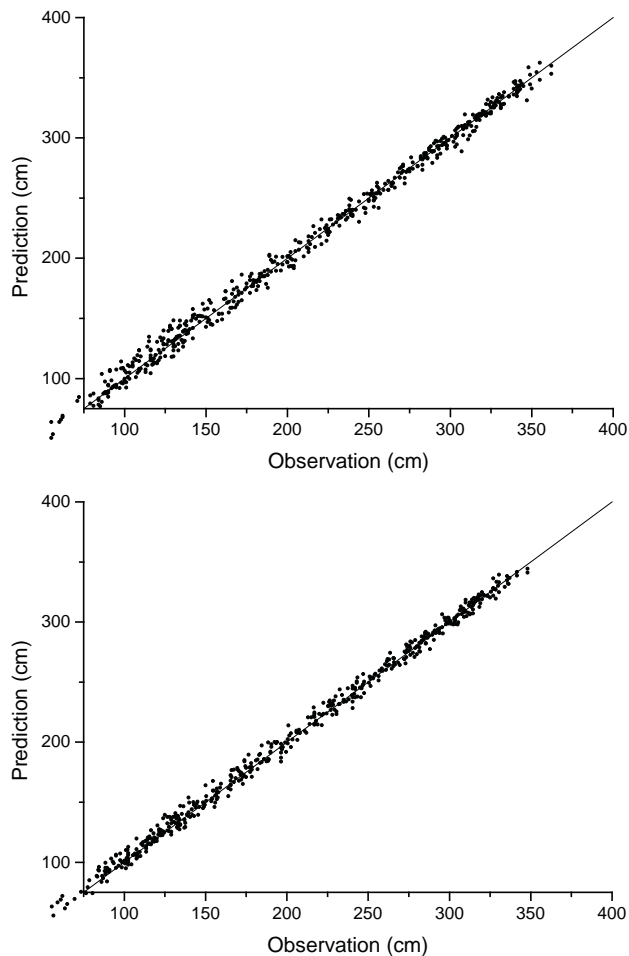


Fig. 7. Scatter plots of observed data

The root-mean-square error significantly increases with the increase of forecast time. The position error of Buoy 201 increases from 1.2 to 3.4 cm; the position error of Buoy 217 increases from 1.0 to 3.8 cm; the error for the position of Buoy 341 increases from 1.6 to 5.0 cm; and the error for the position of Buoy 262 increases from 2.2 to 6.2 cm. Similarly, mean errors for the four places change in the same manner. Our results and discussion led us to conclude that the prediction accuracy of the neural network with the channel of the port is smaller than that of the outside of the port due to the large difference between the tide heights at high tide and low tide. There may be other factors as well such as damming caused by the breakwater.

Tab. 1. RMSE, MAE and R for different position and different time using ANN

		1hr	2hr	3hr	4hr	5hr	6hr	7hr	8hr
Buoy 201	RMSE	1.2	1.8	2.3	2.6	2.8	3.1	3.3	3.4
	MAE	0.9	1.4	1.7	2.0	2.2	2.4	2.5	2.6
	R	0.9999	0.9997	0.9995	0.9993	0.9990	0.9987	0.9985	0.9982
Buoy217	RMSE	1.0	1.6	2.1	2.7	3.1	3.5	3.7	3.8
	MAE	0.8	1.2	1.6	2.0	2.3	2.6	2.8	2.8
	R	0.9999	0.9998	0.9996	0.9993	0.9990	0.9987	0.9985	0.9984
Buoy 241	RMSE	1.6	2.6	3.6	4.4	4.8	5.0	5.1	5.0
	MAE	1.4	2.1	2.8	3.4	3.7	3.9	3.9	3.9
	R	0.9998	0.9995	0.9991	0.9987	0.9985	0.9984	0.9982	0.9981
Buoy 262	RMSE	2.2	3.5	4.8	5.8	6.3	6.4	6.4	6.2
	MAE	1.7	2.6	3.5	4.3	4.8	4.9	4.9	4.8
	R	0.9997	0.9992	0.9984	0.9977	0.9973	0.9972	0.9972	0.9973

CALCULATION OF TIDAL WINDOW PERIOD

In this paper, we have verified the accuracy of the tidal window for the ships. So, the actual tidal window periods for the ships with a draught of about 18 m were observed by the observation system from 20-27th May 2017. The earliest node time and the latest tide time node of each ship, which navigates through the port at high tide were recorded. The tidal window periods were calculated with the help of neural networks. The forecasted and measured results were compared to verify the accuracy of the model.

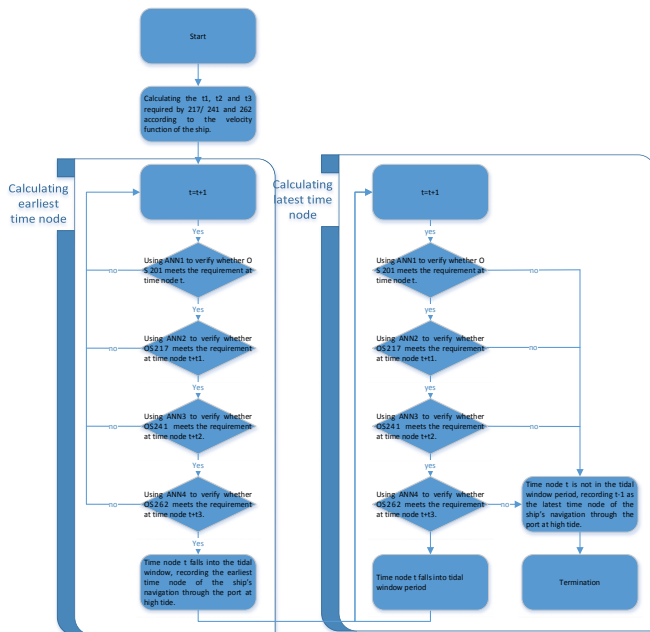


Fig. 8. Computing diagram for the tidal window period

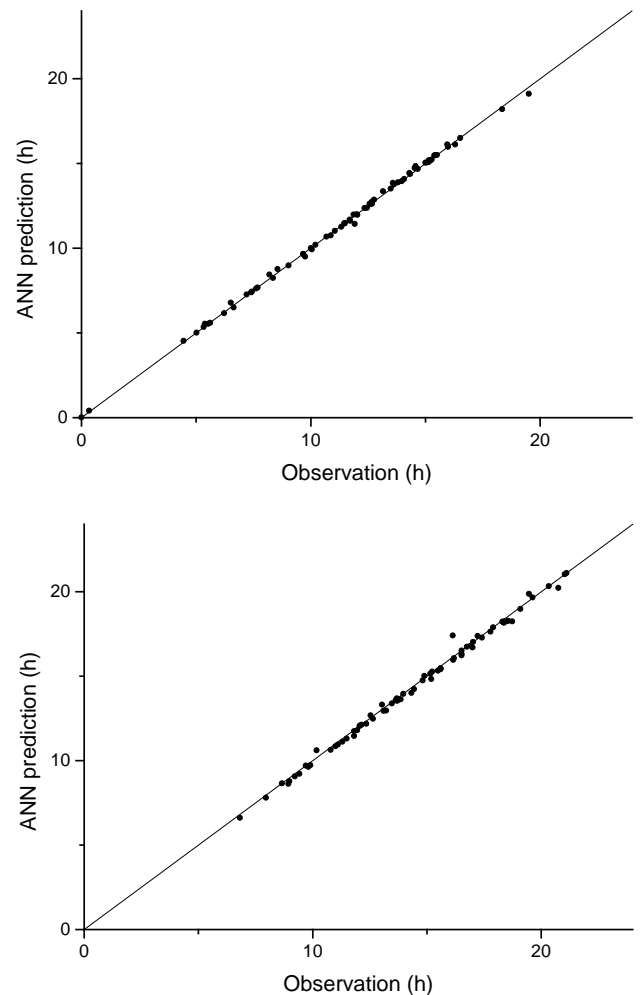


Fig. 9. Scatter plots of measured data

The calculated and observed data of the earliest and latest time nodes during 74 ships, when approaching the port at high tide was compared. The compared scatter plots are shown in Figure 9. When the ships navigate through the port, then the root-mean-square and the mean errors of the earliest time node at high tide are 0.13 and 0.08 h, respectively, while the linear correlation coefficient is 0.9995. Similarly, the root-mean-square and the mean errors of the latest time node at high tide are 0.24 and 0.17 h, respectively, with a linear correlation coefficient of 0.9980. The linear correlation coefficient of the latest time node is lower than that of the earliest time node. The reason behind this is, latest

time node is later than the former which makes longer the forecast time of the required neural network. The mean error is 0.17 h, which is approximately 10 minutes. So, it fulfills the requirements of ships for entering and exiting the port. The results and discussion of this work led us to conclude that our proposed method (based on the measured results combined with neural network forecasting method) can accurately forecast the navigation of ships through the port at high tide. In addition, our simulations satisfy the safety requirements for the ship's navigation through the port. Parameters of each ship and the forecasted and measured values of its tidal window period are listed in Table 3.

Tab. 2. RMSE, MAE and R for the earliest time node and latest time node, using ANN.

	the earliest time node	the latest time node
RMSE	0.13	0.24
MAE	0.08	0.17
R	0.9995	0.9980

Tab. 3. Parameters of each ship and the forecasted and measured values of its tidal window period

Ship' name	LOA	Draft	Date	Measured value	Calculated value using ANN
FPMC B KINGDOM	299.7	18.21	2017-5-27	15:13-17:00	15:11-16:42
HEBEI CHALLENGER	295	18.31	2017-5-30	18:21-19:05	18:12-18:59
ARIADNE	299.97	18.31	2017-5-31	19:30-19:37	19:07-19:40
LAVENDER	292	18.14	2017-6-26	15:23-18:18	15:28-18:14
MOUNT AUSTIN	292	18.04	2017-7-1	04:27-09:25	04:32-09:13
RINI	292	18.32	2017-7-4	10:12-12:03	10:12-12:03
COTSWOLD	292	18.3	2017-7-7	12:36-16:31	12:36-16:31
LOWLANDS SUNRISE	291.98	18.23	2017-7-12	15:00-19:28	15:03-19:53
LEOPOLD OLDENDORFF	299.97	18.11	2017-7-13	15:09-20:20	15:05-20:20
AM GIJON	292	18.04	2017-7-14	15:30-21:02	15:30-21:02
PERCIVAL	291.8	18.28	2017-7-20	10:00-13:41	10:00-13:41
MINERAL BELGIUM	289	18.1	2017-7-22	11:28-17:54	11:28-17:54
STAR MARISA	299.88	18.3	2017-7-22	12:00-16:45	12:00-16:45
CSK FORTUNE	289	18.1	2017-7-27	15:04-20:45	15:04-20:14
PHILIPPOS A	291.8	18.04	2017-7-29	15:59-21:06	15:59-21:07
NAVIOS FANTASTIKS	288.93	18.15	2017-8-23	13:35-18:44	13:51-18:15
NAVIOS AZIMUTH	292	18.3	2017-8-24	14:32-18:22	14:44-18:10
PACIFIC VISTA	295	18.12	2017-8-29	16:31-21:15	16:30-21:20
MINERAL EDO	299.94	18.26	2017-9-4	12:21-16:08	12:22-17:25
KSL SALVADOR	292	18.3	2017-9-6	13:29-17:01	13:31-17:02
CAPE AUSTRALIA	299.88	18.08	2017-9-24	14:20-18:28	14:23-18:15
FPMC B IMAGE	299.7	18.2	2017-9-25	15:16-18:33	15:14-18:17
CLEAR HORIZON	300	18.26	2017-9-29	07:41-09:42	07:41-09:42
ARIADNE	292	18.22	2017-10-6	13:09-16:11	13:22-16:04
FRONTIER BONANZA	291.97	18.22	2017-10-7	13:37-16:31	13:46-16:14
EDWIN	291.8	18.3	2017-10-11	16:18-18:24	16:07-18:15
ANANGEL VOYAGER	292	18.22	2017-10-12	05:32-09:13	05:32-09:04
MARLENE OLDENDORFF	299.88	18.12	2017-10-14	07:37-12:05	07:37-12:05
EHIME QUEEN	291.98	18.3	2017-10-19	12:46-15:11	12:52-14:50

Ship' name	LOA	Draft	Date	Measured value	Calculated value using ANN
OU MAY	295	18.06	2017-10-24	14:18-17:47	14:26-17:38
IMPERIUS	292	18.3	2017-10-28	07:26-08:39	07:26-08:39
PROSPER SUNWAITO	299.7	18.27	2017-10-31	10:41-12:08	10:41-12:08
RAIATEA	292.00	18.3	2017-11-1	11:28-13:06	11:28-12:57
GIANT ACE	291.97	18.3	2017-11-8	15:25-16:55	15:29-16:48
AFALES	292	18.23	2017-11-18	12:40-14:49	12:45-14:45
OCEAN COMMANDER	289	18.08	2017-11-19	12:34-15:36	12:37-15:27
ANTONIS ANGELICOUSSIS	292	18.05	2017-11-27	06:38-10:10	06:30-10:37
GUANG LI HAI	299.88	18	2017-11-28	07:24-11:18	07:24-11:07
ANDAMA	292	18.27	2017-12-1	11:03-12:38	11:01-12:29
LAKE DESPINA	291.98	18.23	2017-12-4	12:37-14:26	12:37-14:14
SEALINK	292.1	18.08	2017-12-19	12:40-15:29	12:37-15:20
STELLA CHARLENE	292	18.3	2017-12-20	14:40-15:09	14:41-15:09
SILVER ROAD	290	18	2017-12-25	05:01-08:56	05:01-08:38
BERGE ATLAS	288.93	18.16	2017-12-30	09:40-11:49	09:40-11:28
MINERAL HOKKAIDO	288.93	18.15	2018-1-2	11:43-13:58	11:37-13:57
KN AMETHYST	300	18.3	2018-1-2	12:27-13:42	12:23-13:33
CAPE INDIA	299.88	18.1	2018-1-5	13:58-16:31	13:57-16:19
FEG SUCCESS	292	18.19	2018-1-12	09:02-11:06	08:59-10:57
DAWN HORIZON	295	18.19	2018-1-15	11:42-13:28	11:41-13:23
SOUTHERN CROSS DREAM	292	18.11	2018-1-16	11:55-14:19	11:26-14:01
TAURUS	292	18.32	2018-1-18	14:34-14:53	14:51-15:01
LONDON COURAGE	299.94	18.1	2018-1-24	05:23-07:57	05:32-07:48
PAN DREAM	291.8	18.25	2018-1-27	08:21- 09:49	08:15-09:38
CAPE ISLAND	288.88	17.85	2018-1-27	06:31-10:47	06:47-10:38
MOUNT HERMON	292	18.15	2018-1-29	09:40-11:57	09:39-11:48
HEBEI TRIUMPH	295	18.27	2018-1-31	12:02-13:38	11:58-13:34
CSK GENERATION	292	17.7	2018-2-1	00:20-15:36	00:25-15:25
K VICTORY	292	18.15	2018-2-4	15:09-17:24	15:11-17:17
GOLDEN HORIZON	299.7	18.01	2018-2-8	05:37-08:59	05:36-08:47
CHINA HARMONY	295	18.09	2018-2-11	08:33-11:29	08:46-11:18
C H S SPLENDOR	289.00	17.55	2018-2-11	00:00-13:13	00:01-12:58
GREAT DYNASTY	295	18.28	2018-2-22	05:20-06:49	05:21-06:37
CAPE MARS	289.00	18	2018-2-26	07:12-11:00	07:16-10:51
SHIBUMI	292	18.25	2018-3-1	11:52-13:51	11:59-13:38
CAPE VICTORY	292	18.32	2018-3-3	13:48-15:36	13:53-15:28
LONDON COURAGE	299.94	18.04	2018-3-11	06:13-9:54	06:10-09:44
ALPHA MILLENNIUM	289	17.98	2018-3-13	08:12-12:21	08:27-12:11
TIAN LU HAI	289	18.2	2018-3-14	11:20-12:32	11:16-12:41
JABAL NAFUSA	290.49	17.82	2018-3-17	11:29-16:09	11:29-15:58
CAPTAIN PETROS H	289.98	17.68	2018-3-30	09:45-15:14	09:30-15:16
OCEAN ROAD	291.91	18.19	2018-4-26	10:03-11:49	09:56-11:45
LOWLANDS PROSPERITY	292	18.17	2018-5-1	14:04-17:13	14:05-17:23
THEODOROS P	292	18.3	2018-5-3	15:57-18:20	16:07-18:12
GREAT SUI	291.97	18.1	2018-5-12	10:52-13:02	10:45-13:19

CONCLUSIONS

An accurate calculation method for the tide height is required for the safe navigation of ships and efficiency of the port during long length channels having complicated tidal. In this work, we have proposed an accurate method from the measured results combined with neural networks for artificial long channels to forecast the tide height. An intelligent calculation model for the ship's navigation through the port at high tide is subsequently proposed. The tidal data observed for 300 days is used as the training data to train the network, and the data observed during the following 65 days is used for the verification of the proposed method. The minimum linear correlation coefficient was 0.9973, which is at an ideal level. In addition, the tidal window periods for the ships with a draught of about 18 meters, arrived at the port in one year are calculated and observed. Moreover, the linear correlation coefficient of 0.9980 indicates that our proposed method in a high tide can accurately and intelligently navigate the large deep-draft ships at the port. Finally, this research can be employed for the navigation of large ships through the port at high tide and port management.

REFERENCES

1. Bao-chun, L., Da-qi, Z.: Analysis of Safety Measures for the Entry of Large Deep Draught Ships Under the Same Tide. *China Water Transport*, 2016, 9(1), Pp. 34-35.
2. Jin-zhong, Z., Song-shan, Y.: Analysis of Design Water Level for Huanghua Port 200 000 DWT Channel. *Port Engineering Technology*, 2016, 53(6), Pp.14-16.
3. Ning, Z., Tie-zheng, S.: Analysis of Method of Calculating the Depth of Waterway by Segmented Artificial Long Channel. *China Water Transport*, 2017, 17(7), Pp.190-194.
4. Cun-bao, T., Liang, Z., Jing-xian, L.: Water Depth Investigation for Dongjiakou Port Receiving 400 000t Carrier by Tide. *Navigation of China*, 2017, 40 (2), Pp. 60-64.
5. Zhi-yang, H., Yuan, X.: Research and application of a new method for the calculation of rideable high tide level. *The Ocean Engineering*, 2017, 35(2), 2017, Pp. 83-88.
6. Yuan, X., Zhi-yang, H., Hong-feng, G.: On riding high tide level in a long waterway at a tidal estuary. *Port & Waterway Engineering*, 2011, 6(5), Pp.1-6.
7. Zhi-yang, H., Jian-feng, Z.: Research and application of rideable tide level considering the effect of tide current. *The Ocean Engineering*, 2018, 36(3), Pp.104-109.
8. Feng, M., Hong-bo, C.: An analysis for entering a port considering tide based on high-precise instantaneous depth model. *Science of Surveying and Mapping*, 2012, 37(4), Pp. 40-42.
9. Ning, M., Yan, C., Jun, W.: Design throughput capacity simulation for multi-shallow waterway. *Journal of Dalian Maritime University*, 2011, 37(1), Pp. 63-67.
10. Qing-long, H., Zu-xu, G., Peng-fei, Z.: Research on the Under-Keel Clearance and Ship Squat for VLCC Navigating within Port Area. *Marine Technology*, 2013, 17(5), Pp.2-5
11. Yi, L., Yang, Y.: A Tidal Forecasting Algorithm Based on Genetic Neural Network. *Electric Power Science and Engineering*, 2015, 31(8), Pp.1-7
12. Ze, G., Zhi-gang, L., Yan, Z.: Tide Prediction in Tidal Power Generation by Harmonic Analysis and Artificial Neural Network. *Journal of Hebei United University (Natural Science Edition)*, 2014, 36(1), Pp. 84-87.
13. Ru-yun, W., Lei, L., Fei, Z.: Neural network forecast model of storm surge elevation based on high tide and low tide. *Marine Forecasts*, 2014, 31(6), Pp. 23-27.
14. Ming-chang, L., Shu-xiu, L., Zhao-chen, S.: Research on tide supplemental prediction using ANN methods under unusual weather. *Chinese Journal of Computational Mechanics*, 2008, 25(3), Pp. 368-372.
15. Salim, A.M., Dwarakish, G.S., Liju, K.V.: Weekly Prediction of Tides Using Neural Networks. *Procedia Engineering*, 2015, 116(1), Pp.678-682.
16. Lee, T.L.: Back-propagation neural network for long-term tidal predictions. *Ocean Engineering*, 2004, 31(2), Pp. 225-238.
17. Alessandro, F., Torres, R., Kjerfve, A.: Application of Artificial Neural Network (ANN) to improve forecasting of sea level. *Ocean and Coastal Management*, 2012, 55, Pp.101-110.
18. He, Z.G., Gu, X.A., Sun, X.Y., Liu, J., Wang, B.S.: A coupled immersed boundary method for simulating multiphase flows. *Acta Electronica Malaysia*, 2017, 1(1), Pp. 05-08.
19. Ibrahim, M.S., Kasim, S., Hassan, R., Mahdin, H., Ramli, A.A., Md Fudzee, M.F., Salamat, M.A.: Information Technology Club Management System. *Acta Electronica Malaysia*, 2018, 2(2), Pp. 01-05.
20. He, Z.G., Gu, X.N., Sun, X.Y., Liu, J., Wang, B.S.: An efficient pseudo-potential multiphase lattice Boltzmann simulation model for three-dimensional multiphase flows. *Acta Mechanica Malaysia*, 2017, 1(1), Pp. 08-10.
21. Luo, X.: Research on Anti-Overturning Performance Of Multi-Span Curved Girder Bridge with Small Radius. *Acta Mechanica Malaysia*, 2(1), Pp. 04-07.

22. Halim, H., Abdullah, R., Mohd Nor, M.J., Abdul Aziz, H., Abd Rahman, N.: Comparison Between Measured Traffic Noise in Klang Valley, Malaysia And Existing Prediction Models. *Engineering Heritage Journal*, 2017, 1(2), Pp. 10–14.
23. Hassan, M.A., Mohd Ismail, M.A.: Literature Review for The Development of Dikes's Breach Channel Mechanism Caused by Erosion Processes During Overtopping Failure. *Engineering Heritage Journal*, 2017, 1(2), Pp. 23-30.

CONTACT WITH THE AUTHORS

LI Qiang, Lecturer
e-mail: manumail@dlnu.edu.cn

Navigation College
Dalian Maritime University
116026 Dalian, Liaoning
CHINA

STABILITY OF AIR NUCLEUS IN LIQUID WATER AND CAVITATION INCEPTION ON MARINE ENGINEERING

Fu Qiang
Chen Ming
Wang Xiuli
Zhu Rongsheng
Zhang Guoyu
Yu Jianen

National Research Center of Pumps, Jiangsu University, Zhenjiang, Jiangsu, China

ABSTRACT

The micro air nucleus widely distributed in the ocean is a necessary condition for the cavitation of hydraulic machinery in seawater. In order to study the stability of air nucleus in seawater and cavitation inception, the computational domain of water molecules with air nucleus was studied using the method of molecular dynamics simulation, and the transient characteristics of air nucleus in liquid water were obtained. The key factors influencing nuclei stability were analyzed. The results showed that air nucleus with a certain mass could maintain the dynamic equilibrium in liquid water. The internal density of air nuclei had a critical value that allowed the nuclei to stably exist in water. The air nuclei mass was the decisive factor in its equilibrium volume in water, and the two were positively correlated. The internal density of air nuclei was negatively correlated with the nuclei radius when the nuclei was stable in water. Liquid surface tension was an important factor affecting the stability of the air nuclei. The larger the initial radius of nuclei, the smaller the water pressure, and the more likely the cavitation occurs

Keywords: Air nuclei, Water, Molecular dynamics, Stability, Surface tension

INTRODUCTION

In the field of marine engineering, cavitation is widespread in the operation of hydraulic machinery such as propellers and underwater vehicles, which affects the safety and stability of equipment operation. However, for a long time, many scholars have focused on the macroscopic level of cavitation research, but less on the microscopic mechanism of cavitation. The cavitation phenomenon is a microscopic to macroscopic transient development process. Therefore, in-depth study of the cavitation microscopic mechanism is a necessary means to improve the understanding of the nature of cavitation. In the ocean, the micro air nucleus are widely distributed, and the micro air nuclei as a typical cavitation nucleus is a necessary condition for the cavitation of hydraulic machinery

in seawater. Micro nuclei research has profound implications for surface science, fluid dynamics, biological sciences, and some applications [1-2]. In recent decades, the nuclei in the liquid can exist stably has been the focus of academic debate [3-6]. As early as 1950, Epstein and Plesset demonstrated that free nucleus cannot be stably present in stationary fluids. They either float under buoyancy and escape from free surface or dissolve gradually under surface tension [7]. However, at present the theory and experiment of cavitation are based on the existence of air nuclei, which is called "nuclei paradox"[8]. Therefore, people have envisioned a variety of cavitation kernel models to avoid this contradiction [9-10], but all kinds of models have their own flaws and limitations. In order to study the microscopic mechanism of gas nuclei growth,

collapse and stability in liquid, people tried to observe the gas nuclei in water by experiments and microscopy [11-12]. However, nanoscale micro gas nucleus are difficult to observe directly through experiments. More recently, molecular dynamics simulation has become a powerful tool for studying microscopic nuclei. The researchers studied the gas nuclei stability in the liquid from the aspects of the density and volume of the gas nuclei and the surface tension of the liquid.

The calculation results of Zhang L et al. [14] showed that the nano nuclei with high internal density had a longer lifetime in molecular dynamics simulation.

Yoshida-Honmachi et al. [13] studied the growth and collapse of cavity in water by using molecular dynamics method under NVT ensemble. It was found that the stability of the nano cavity in the water has a certain relationship with the size of the cavity. Shin-ichi Tsuda et al. [17] studied the nucleation of L-J fluid under NVE ensemble and found that there was a critical radius of nuclei growth. The nuclei larger than the critical radius spontaneously grew, whereas the nuclei smaller than the critical radius tended to disappear. Takenori Yamamoto et al. [15] calculated that the critical radius of the helium nano-nucleus in water is 1 nm.

Yoshida-honmachi et al. [13] used the Y-L equation to estimate and found that the surface tension of water has no obvious correlation with the radius of the cavity; Takenori Yamamoto et al. [15] used NAMD software to simulate and calculate the surface tension of liquid helium relative to the gas nuclei radius is a convex function; Yan Hong [16] used molecular dynamics to study the surface tension of the argon. The results show that the surface tension of the argon decreases with the increase of the nucleus radius; Dupont V et al. [18] found the relationship between surface tension and the nuclei radii of curvature has a decisive influence on the stability of the nano nucleus.

It can be seen that although the researchers believe that the surface tension of the liquid, the volume and density of the gas nuclei are factors affecting the stability of the nuclei in the liquid, there is no final conclusion in this research field, and even some research results are mutually contradictory.

In the field of microscopic cavitation, Yijin Mao et al. [19] used molecular dynamics simulation with TIP3P water molecule model to show that the hydrodynamic model based on the Rayleigh-Plesset equation was ineffective in predicting the growth and annihilation of nano nucleus in liquid water. The conclusion of previous studies based on molecular dynamics has not yet established a reliable connection between micro-phenomena and macroscopic experiments. This paper attempts to explore the microscopic phenomena of coexistence of nano air nuclei and liquid water, and further reveals its regular characteristics connected with the macro phenomenon.

SIMULATION METHOD

The model used in this paper was to take a cubic region as the computational domain in an infinite space and apply

periodic boundary conditions around it. Considering the calculation time and accuracy and other factors, the length of the model in the x, y, z direction was taken as 5.3nm. The air nuclei was set in the center of the calculation domain, and the initial radii of the air nuclei were set as $R_0 = 0.8$ nm, 1.0 nm and 1.2 nm, respectively, and the density of water molecules outside the air nuclei was 0.997 g/cm³. The model section was shown in Figure 1. Air is a mixture of substances, of which about 78% of nitrogen, oxygen accounts for about 21%. In this simulation, the material used was 79% nitrogen and 21% oxygen molecules, ignoring other trace components. The velocity initialization satisfied the Maxwell-Boltzmann distribution.

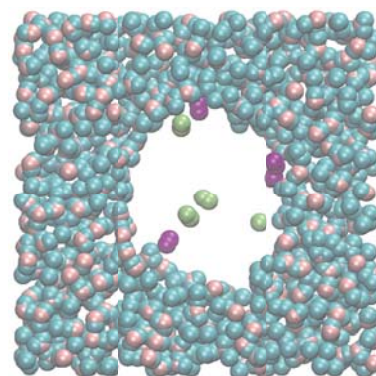


Fig.1. System initial state

In this paper, the potential energy of molecules was taken into account Coulomb force, intermolecular force and so on. The potential energy function between molecules a and b can be seen as the sum of the potential energy of Lennard-Jones and Coulomb force. The specific expression is as follows [20],

$$U_{ab} = \sum_i \sum_j^b \frac{k_c q_{a_i} q_{b_j}}{r_{a,b_j}} + \sum_i \sum_j^b 4\epsilon_{a,b_j} \left[\left(\frac{\sigma_{a,b_j}}{r_{a,b_j}} \right)^{12} - \left(\frac{\sigma_{a,b_j}}{r_{a,b_j}} \right)^6 \right] \quad (1)$$

Where a and b denote two different molecules, subscripts i and j denote two different atoms, k_c is the electrostatic constant, and the potential well depth ϵ and the characteristic length σ are potential energy parameters. The calculation software adopted the open source software Lammmps, and the water molecule adopted the TIP4P model. Newton's equations of motion were solved numerically using the leap frog algorithm. The long range force calculation used particle-particle-particle-mesh (PPPM) algorithm [21], The PPPM solver maps the water molecule's hydrogen and oxygen atoms charge in a 3D mesh then uses 3D fast Fourier transforms to solve the Poisson equation on each mesh. Finally, it interpolates from the grids to calculate the electric field and corresponding long-range Coulomb force on each charged atom [22-24].

The main parameters of the simulation were as follows: mass of nitrogen atom of 14.007 g/mol, mass of oxygen atom of

15.999 g/mol, mass of hydrogen atom of 1.008 g/mol and time step of 0.1 fs. The charge amount of an oxygen atom in the water molecules was $-1.1128e$, the charge amount of a hydrogen atom was $0.5564e$. The cut off radius of L-J potential function was 0.85nm. The length parameter σ and the energy parameter ϵ of the L-J potential function were differentiated according to the atoms that acted. $\sigma_{O_1-O_1}=0.31589\text{nm}$, $\epsilon_{O_1-O_1}=0.1852\text{Kcal/mol}$ when the oxygen atoms in the water molecules interact with each other; $\sigma_{N-N}=0.3501\text{nm}$, $\epsilon_{N-N}=0.1670\text{Kcal/mol}$ when the nitrogen atoms interact with each other; $\sigma_{O_2-O_2}=0.2860\text{nm}$, $\epsilon_{O_2-O_2}=0.2280\text{Kcal/mol}$ when the oxygen atoms in the oxygen molecules interact with each other [25]. Since the Van der Waals radius of the hydrogen atoms is much smaller than the van der Waals radius of the oxygen atoms, the Van der Waals interaction range of H-H and H-O is obscured by the range of O-O interaction, so we ignore Van der Waals interaction between H-H. The interaction parameters ϵ_{ij} and σ_{ij} for different atoms was given by the Lorentz-Berthelot formula [17]:

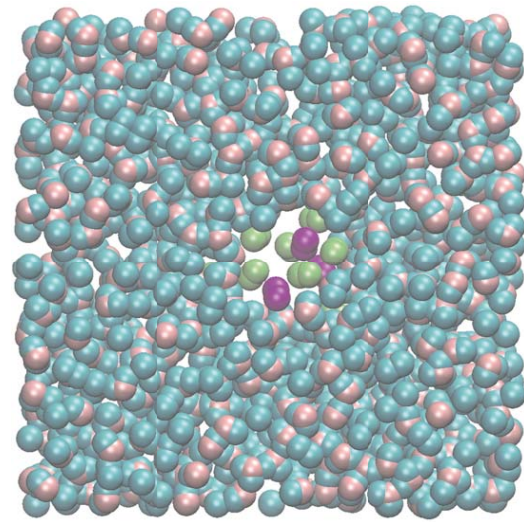
$$\sigma_{ij} = \frac{1}{2}(\sigma_i + \sigma_j) \quad (2)$$

$$\epsilon_{ij} = \sqrt{\epsilon_i \cdot \epsilon_j} \quad (3)$$

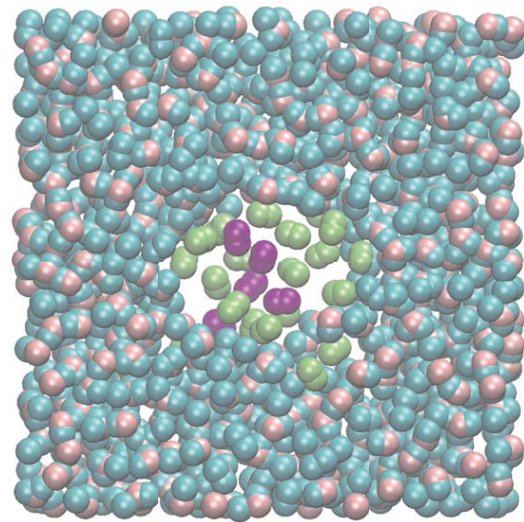
AIR NUCLEUS CHANGE IN VOLUME IN WATER

The purpose of this molecular dynamics calculation was to simulate the process of nanoscale air nuclei that was not dissolved in liquid water in nature. In the past, molecular dynamics studies used NVT ensemble (NVE) to study the gas nuclei in liquids [26]. However, the author believes that the volume-invariant system cannot reflect the real process of gas nuclei change, because the volume change rate of liquid is very small. When the total volume of liquid and gas is defined, the volume of gas also tends to remain stable, which is inconsistent with the actual situation. In the simulation process of this paper, the Nose/Hoover hot bath method was adopted to keep the temperature of the system constant [27]. At the same time, the liquid water was controlled under pressure, and the pressure was set to 1atm. In this process, the total system volume and the air nuclei volume are free to change.

a) Air nuclei contraction



b) Air nuclei stability existence



c) Air nuclei expansion

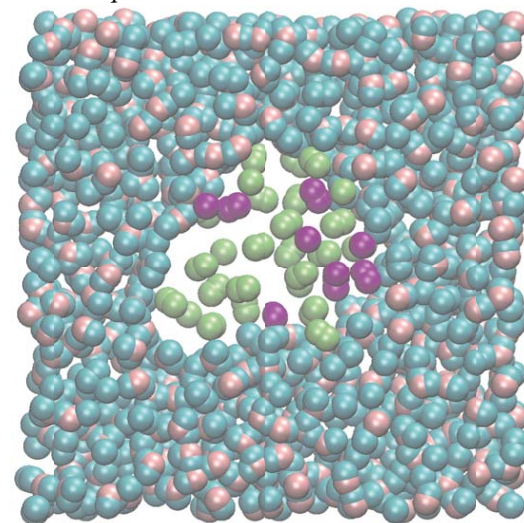


Fig. 2. Three states of air nucleus in liquid water

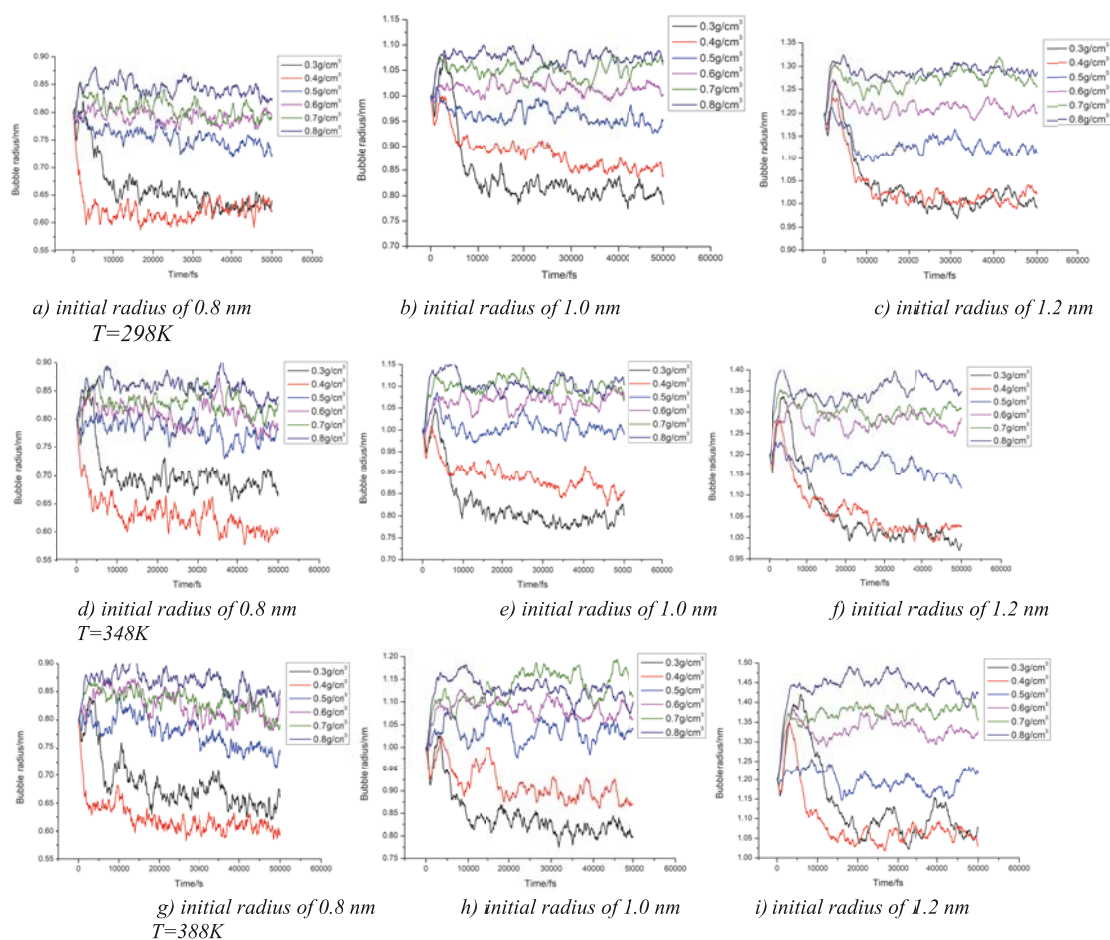


Fig.3. Variations of air nucleus with different initial radii

Voronoi tessellation method was used in this paper to estimate the size of air nuclei, that is, define a computation that calculates the volume of the Voronoi cell around each atom. Any point in an atom's Voronoi cell is closer to that atom than any other. The number of faces of the Voronoi cell is equal to the number of nearest neighbors of the central atom. In this way, the sum of volume of the Voronoi cell around nitrogen atoms and oxygen atoms in the air molecules was added to obtain a value V , and we know the radius of the nucleus R_0 at the initial moment, so that the radius of the nuclei at any moment can be deduced:

$$R = R_0 * \left(\frac{V}{V_0} \right)^{1/3} \quad (4)$$

V_0 is the initial volume of all air molecules.

Observe the change process of the air nucleus, we can find that there were three states of the air nucleus in the liquid water: contraction, stable existence and expansion, as shown in Figure 2. It has been observed that the nano air nucleus were poorly soluble in water and the molecules remained clustered even when the air nuclei contracted to a very small volume.

Comparing the changes of the air nucleus at different temperatures, it was found that the time for the air nucleus to reach equilibrium was almost constant with the increase

of temperature. Under the same initial conditions, the trends in the volume of air nuclei in the systems with different temperatures were consistent, in higher temperature systems, the equilibrium volume of the air nucleus was slightly larger, especially in the air nuclei with higher initial density. This is related to the thermal motion of the molecules and the surface tension of the liquid. This will be discussed further below.

The changes of nuclei volume with different initial radii in Fig. 3 are analyzed. The air nuclei volume varied dramatically during the first 15000fs of the calculation, and then gradually moved toward the dynamic equilibrium. That is, the air nuclei volume fluctuated within a certain range, but the average value remained stable. This dynamic balance is determined by the state characteristics of the gas: the calculation system temperature was constant, when the volume of air nuclei with a certain mass was greater than the equilibrium state, the air nuclei pressure would be reduced, the pressure of liquid water in the outside world, The air nuclei are forced to shrink and re-tend to their equilibrium values; On the contrary, when the nuclei volume was less than the equilibrium state, the pressure in the air nuclei would increase, and the air nuclei would then expand to the equilibrium value.

The volume change of the air nuclei was not only related to the initial volume of the air nuclei, but also to the internal density of the air nuclei. The air nucleus of three initial sizes showed a shrinking tendency when the initial density of

the air nucleus was less than 0.4g/cm³. The air nuclei with the initial radius of 0.8nm shrank more rapidly and the air nuclei with the initial radius of 1.0nm shrank more slowly. For the air nuclei with the initial radius of 0.8nm, when the internal initial density was about 0.5-0.6g/cm³, the nuclei slowly shrank and then balanced, and when the initial density was about 0.7g/cm³, the air nuclei could stably exist in liquid water, When the initial density was greater than 0.7g/cm³, the air nuclei began to show an expansion trend; For the air nuclei with initial radii of 1.0 nm and 1.2 nm, the nuclei slowly shrank when the initial internal density was 0.5g/cm³, when the internal initial density was 0.6g/cm³, the air nuclei could stably exist in liquid water, and when the internal initial density was more than 0.6g/cm³, the nuclei expanded. We can infer that there was a critical value for the internal density of the air nuclei. When the density was smaller than the critical value, the air nuclei shrank gradually. When the density was equal to the critical value, the air nuclei could stably exist in the liquid water. When the density was larger than the critical value, the air nuclei showed an expansion trend. The critical value was negatively correlated with the air nuclei volume, and the larger the air nuclei volume, the smaller the critical value.

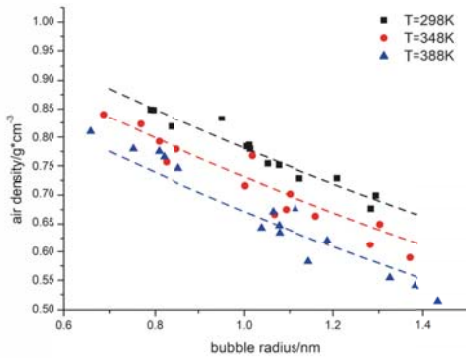


Fig. 4. Relationship Between Air Nuclei Radius and Internal Density

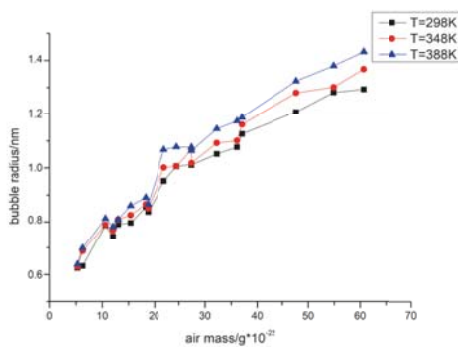


Fig.5. Relationship between Air nuclei Mass and Nuclei Radius

Figure 4 shows the relationship between nuclei density and nuclei radius when the system was in a state of dynamic equilibrium. The general trend is analyzed. It can be concluded that the density of air nuclei was negatively correlated with the nuclei radius at equilibrium, verifying the conjecture described above. At higher temperatures, the density in the

same volume of air nuclei is less. We used the function fitting map data points, and according to the obtained function speculated that the air nuclei with a radius of 3.3nm can exist stably in 298K water when its internal density is 0.00129g/cm³.

We further investigate the relationship between air nuclei mass and nuclei radius when the system was in a state of dynamic equilibrium, as shown in Figure 5. It shows that the balance volume of the air nuclei was essentially determined by the gas mass contained in the nuclei. The gas mass in the nuclei was positively correlated with the nuclei radius at equilibrium, and the same mass of air nuclei is larger in higher temperature water

INFLUENCE OF WATER SURFACE TENSION ON AIR NUCLEUS

A balanced interface with stable nuclei inside and liquid outside can be used Young-Laplace (Y-L) equation:

$$p_g = p_l + \frac{2\tau}{R} \quad (5)$$

Where p_g for the noncondensable gas pressure inside nuclei; p_l for the liquid pressure outside the nuclei; R for the nuclei radius (This article neglects the tiny differences between the nuclei equimolar surface and the surface of tension [12]); τ for the surface tension of the liquid. Studies have shown that Y-L equation (5) still holds when applied to nano nucleus [13].

In this paper, the air pressure p_g and liquid water pressure p_l were calculated under the micro-canonical ensemble (NPT) by molecular dynamics to calculate the surface tension of the liquid water through the Y-L equation (5).

The stress tensor for a single atom i is given by:

$$S_{ab} = - \left[\begin{aligned} & m v_a v_b + \frac{1}{2} \sum_{n=1}^{N_b} (r_{1a} F_{1b} + r_{2a} F_{2b}) + \frac{1}{2} \sum_{n=1}^{N_b} (r_{1a} F_{1b} + r_{2a} F_{2b}) + \\ & \frac{1}{3} \sum_{n=1}^{N_b} (r_{1a} F_{1b} + r_{2a} F_{2b} + r_{3a} F_{3b}) + Kspace(r_{ia}, F_{ib}) + \sum_{n=1}^{N_f} r_a F_{ib} \end{aligned} \right] \quad (6)$$

Where a and b take the values x, y, z to generate six components of a symmetric tensor. The first term is a kinetic energy contribution for atom i . The second term is a pairwise energy contribution where n loops over the N_p neighbors of atom i , r_1 and r_2 are the positions of the 2 atoms in the pairwise interaction, and F_1 and F_2 are the forces on the 2 atoms resulting from the pairwise interaction. The third term is a bond contribution of similar form for the N_b bonds which atom i is part of. The fourth term is the KSpace contribution from long-range Coulombic interactions. Finally, there is a term for the N_f fixes that apply internal constraint forces to atom i .

Pressure calculation formula is:

$$p = \frac{-(S_{xx} + S_{yy} + S_{zz})}{3V} \quad (7)$$

Where V is the sum of volume of the Voronoi cell around same type molecules.

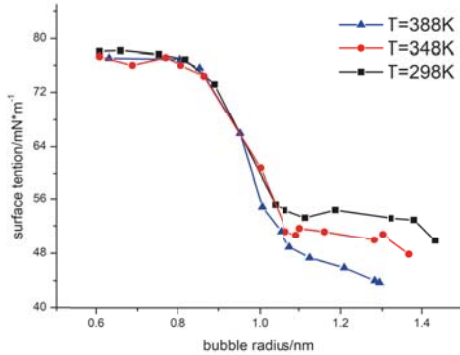


Fig.6. Relationship between surface tension of liquid water and air nuclei radius

After 30000 fs, the air nuclei volume, the liquid water pressure, and the pressure inside the air nuclei had stabilized. Therefore, the surface tension of the liquid water was calculated by averaging the air nuclei radius, the liquid water pressure, and the pressure inside the air nuclei after 30000 fs. This paper calculated and analyzed the surface tension of liquid water in 13 different size air nuclei systems. It can be seen from Figure 6 that as the air nuclei radius increased, the calculated liquid water surface tension generally decreased, which is consistent with the trend of the calculated simulation in [16], but not consistent with the trend of surface tension in [13,15]. The surface tension of liquid water in a 0.6 nm radius air nuclei system was about 77 mN/m. The surface tension of liquid water drastically decreased in systems with air nuclei radius of 0.8-1.1 nm. The surface tension of liquid water in system with 1.1 nm radius air nuclei was only 47 mN/m. The surface tension of liquid water slowly decreased in systems with air nuclei radius greater than 1.1 nm. The point data fitting function showed that when the air nuclei radius tended to infinity, the surface tension of liquid water at about 43mN/m, which was smaller than the experimental results 72mN/m, and it was close to results calculated in [13], but different from the calculated data in [15].

This tendency of the surface tension of liquid water to decrease as the air nuclei radius increases can explain the

negative correlation between the above-mentioned density critical value of the air nuclei in liquid water and the volume of the cavitated nuclei. According to the balance equation, when the pressure outside the nuclei of the air remains the same, the smaller the surface tension of the liquid water, the smaller the pressure needed to maintain balance within the air nuclei. According to the gas equation of state, when the temperature is constant, Increase, then the density decreases, the pressure value is also reduced, so that the air just reached the kinetic equilibrium nuclear.

The surface tension of liquids at different temperatures has a small difference when the nuclei radius is less than 1.0 nm, and the difference is significant when the nuclei radius is greater than 1.0 nm. Overall the higher the temperature, the smaller the surface tension of the liquid. This also explains the reason for the larger volume of air nuclei in the higher temperature system above.

This tendency of the surface tension of water to decrease as the air nuclei radius increased can explain the negative correlation between the above-mentioned density critical value of the air nuclei and the volume of the nuclei. According to the balance equation, when the pressure outside the nuclei remains unchanged, the smaller the surface tension of the liquid water, the smaller the pressure needed to maintain balance within the air nuclei. According to the gas state equation, when the temperature is constant and volume increase, then the density decreases, the pressure value is also reduced, so that the air nuclei just reaches the kinetic equilibrium.

SYSTEM STATE CHANGE DURING CAVITATION

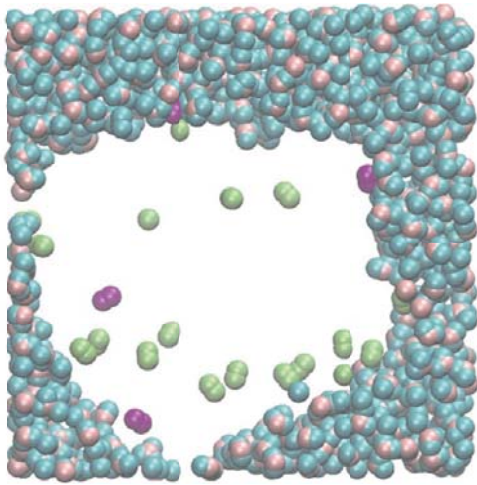
Taking the above equilibrium process as a relaxation process, we further studied the cavitation process of liquid water containing air nucleus. We chose systems in which the air nuclei was stable in water, and controlled the pressure of liquid water to promote cavitation. We observed the volume change of air nucleus during cavitation development, and monitored the potential energy change of the whole system. In this process, the system temperature remained at 298K, the system was unrestricted and could be freely changed. A visual image of the cavitation development system is shown in Figure 7. Once cavitation occurred, the air nuclei volume

Tab. 1. Cavitation Calculation Results

Initial nuclei radius (nm)	Initial PotEng (kcal/mol)	Pressure (atm)	Cavitation	End PotEng (kcal/mol)	Cavitation Timestep (fs)
0.8	-43443.054	-500	No	-42910.93	/
0.8	-43443.054	-700	Yes	-44752.241	61000
0.8	-43443.054	-1000	Yes	-45408.247	34000
1.0	-42655.704	-400	No	-42388.551	/
1.0	-42655.704	-500	Yes	-43334.101	168000
1.2	-41864.537	-300	No	-41853.478	/
1.2	-41864.537	-400	Yes	-42944.457	101500
1.2	-41864.537	-500	Yes	-42227.299	60500

increased rapidly and the entire process was irreversible until the air nuclei collapsed.

a) Initial development of cavitation



b) Full development of cavitation

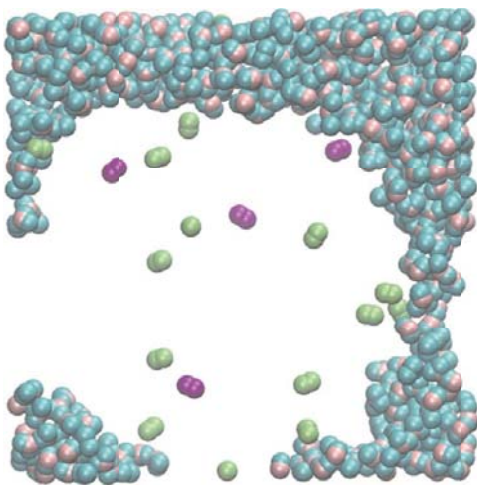


Fig.7. System state change during cavitation

After calculating the gas-liquid equilibrium above, we selected three systems in which air nucleus could exist stably and performed 8 sets of calculations. The results are shown in the table 1.

We found that the liquid negative pressure value and initial nuclei radius are the key factors affecting the occurrence of cavitation. The cavitation of system with initial nuclei radius of 0.8 nm occurs when the water pressure reaches -700 atm. The cavitation of system with initial nuclei radius of 1.0 nm occurs when the water pressure reaches -500 atm. The cavitation of system with initial nuclei radius of 1.2 nm occurs when the water pressure reaches -400 atm. The critical time for cavitation in an air nuclei system with initial radius of 1.2 nm is 101500 fs when the water pressure reaches -400 atm, and the critical time for cavitation when the water pressure reaches -500 atm is 60500 fs; The critical time for cavitation in an air nuclei system with initial radius of 1.0 nm is 168000 fs when the water pressure reaches -500 atm; It can be seen that the system can remain stable under a small negative

pressure, and cavitation occurs when the negative pressure reaches a critical value, and the larger the negative pressure, the shorter the critical time for cavitation of the system. A certain size of air nucleus corresponds to a certain cavitation critical negative pressure, and the smaller the air nucleus, the larger the cavitation critical negative pressure. Under the same negative pressure, the cavitation of the smaller air nuclei system takes a longer time. Therefore, it can be seen that the larger the initial radius of the air nuclei, the larger the liquid negative pressure, and the more likely the cavitation occurs.

The above-mentioned conclusion that the surface tension of the liquid water decreases as the nuclei radius increases can also be considered as the cause of the cavitation critical negative pressure becoming smaller. The cavitation characteristics described above can also be considered from the perspective of system potential energy. It can be seen from the table that the potential energy of the system is reduced if cavitation occurs; the initial potential energy of the system with smaller air nucleus is smaller, and the system is more stable. Cavitation has free energy barriers, and a small negative pressure does not allow the system to cross the cavitation free energy barrier, so cavitation cannot occur.

CONCLUSION

Through the molecular dynamics simulation method, the stability of air nucleus in liquid water was studied and the key factors that affect its stability were analyzed. The following conclusions are drawn:

1. Air nucleus with a certain mass could maintain the dynamic equilibrium in liquid water. In the external liquid pressure, the air nuclei pressure and liquid surface tension together, the air nucleus in the water gradually reached the dynamic equilibrium. There were three states of the air nucleus in the liquid water: contraction, stable existence and expansion. There was a critical value for the internal density of the air nuclei. When the density was smaller than the critical value, the air nuclei shrank gradually. When the density was equal to the critical value, the air nuclei could stably exist in the liquid water. When the density was larger than the critical value, the air nuclei showed an expansion trend. The critical value was negatively correlated with the air nuclei volume, and the larger the air nuclei volume, the smaller the critical value. We speculated that the air nuclei with a radius of 3.3nm can exist stably in water when its internal density is 0.00129g/cm³.
2. The balance volume of the air nuclei was essentially determined by the gas mass contained in the nuclei. The gas mass in the nuclei was positively correlated with the nuclei radius at equilibrium.
3. Liquid surface tension is an important factor affecting the stability of the air nuclei. With the increase of air nuclei radius, the interfacial tension of liquid water tends to decrease. The higher the temperature, the smaller the surface tension of the liquid.

- The larger the initial radius of the air nuclei, the smaller the water pressure, and the more likely the cavitation occurs.

ACKNOWLEDGMENTS

This work was supported by the following foundation:

- National Key R&D Program of China (SQF2018YFB060154-05);
- National Natural Science Foundation of China (51509112);
- Natural Science Foundation of Jiangsu Province of China (BK20171302);
- Key R&D Programs of Jiangsu Province of China (BE2016160, BE2017140, BE2018112).

REFERENCES

- Matsumoto, M., Tanaka, K.: Nano nuclei size dependence of surface tension and inside pressure. *Fluid Dynamics Research*, 2008, 40(7), Pp. 546-553.
- Huang, B., Qin, W.U., Wang, G.: Progress and prospects of investigation into unsteady cavitating flows. *Journal of Drainage & Irrigation Machinery Engineering*, 2018, 36(1), Pp. 1-14.
- Parker, J.L., Claesson, P.M., Attard, P.: Nucleus, cavities, and the long-ranged attraction between hydrophobic surfaces. *Journal of Physical Chemistry*, 1994, 98(34), Pp. 8468-8480.
- Borkent, B.M., Schönherr, H., Le, C.G.: Preferred sizes and ordering in surface nanonuclei populations. *Physical Review E Statistical Nonlinear & Soft Matter Physics*, 2009, 80(3), Pp. 036-315.
- Zhang, L., Zhang, X., Zhang, Y.: The length scales for stable gas nanonucleus at liquid/solid surfaces. *Soft Matter*. 2010, 6(18), Pp. 4515-4519.
- Zhang, X.H., Khan, A., Ducker, W.A.: A nanoscale gas state. *Physical Review Letters*, 2007, 98(13), Pp. 136101.
- Epstein, P.S., Plesset, M.S.: On the Stability of Gas Nucleus in Liquid-Gas Solutions. *Applied Scientific Research*, 1951, 19(2), Pp. 256-256.
- Pan, S.S., Peng, X.X.: Physical mechanism of cavitation. *National Defense Industry Press, Beijing*, 2014.
- Cha, Y.S.: On the Equilibrium of Cavitation Nuclei in Liquid-Gas Solutions. *Journal of Fluids Engineering*, 1981, 103(3), Pp. 1335-1349.
- Mori, Y., Hijikata, K., Nagatani, T.: Fundamental study of nuclei dissolution in liquid. *International Journal of Heat & Mass Transfer*, 1977, 20(1), Pp. 41-50.
- Lou, S.T., Ouyang, Z.Q., Zhang, Y.: Nanonucleus on solid surface imaged by atomic force microscopy. *Journal of Vacuum Science & Technology B Microelectronics & Nanometer Structures*, 2000, 18(5), Pp. 2573-2575.
- Yang, J., Duan, J., Daniel Fornasiero, A.: Very Small Nuclei Formation at the Solid-Water Interface. *Journal of Physical Chemistry B*, 2003, 107(107), Pp. 6139-6147.
- Matsumoto, M.: Surface Tension and Stability of a Nanonuclei in Water: Molecular Simulation. *Journal of Fluid Science & Technology*, 2008, 3(8), Pp. 922-929.
- Zhang, L., Zhang, X., Zhang, Y.: The length scales for stable gas nanonucleus at liquid/solid surfaces. *Soft Matter*, 2010, 6(18), Pp. 4515-4519.
- Yamamoto, T., Ohnishi, S.: Molecular dynamics study on helium nanonucleus in water. *Physical Chemistry Chemical Physics*, 2011, 13(36), Pp. 16142-16145.
- Hong, Y., Ru-Zeng, Z., Jiu-An, W.: Size-dependent surface tension of a cylindrical nanonuclei in liquid Ar. *Chinese Physics B*, 2012, 21(8), Pp.146-151.
- Tsuda, S.I., Shu, T., Matsumoto, Y.: A study on the growth of cavitation nuclei nuclei using large-scale molecular dynamics simulations. *Fluid Dynamics Research*, 2008, 40(7), Pp. 606-615.
- Dupont, V., Miscevic, M., Joly, J.L.: Boiling incipience of highly wetting liquids in horizontal confined space. *International Journal of Heat & Mass Transfer*, 2003, 46(22), Pp. 4245-4256.
- Mao, Y., Zhang, Y.: Nonequilibrium Molecular Dynamics Simulation of Nanonuclei Growth and Annihilation in Liquid Water. *Nanoscale & Microscale Thermophysical Engineering*, 2013, 17(2), Pp. 79-91.
- Knapp, R., Daily, J.W., Hammit, F.G.: Cavitation. *McGraw-Hill Book Company, New York*, 1970.
- Mao, Y., Zhang, Y.: Molecular dynamics simulation on rapid boiling of water on a hot copper plate. *Applied Thermal Engineering*, 2014, 62(2), Pp. 607-612.
- Kasim, S., Karunakaran, E., Omar, N.A., Wahid, N., Hafit, H., Alyani, A.: Pdk Fire Fighting Management System. *Acta Electronica Malaysia*, 2017, 1(2), Pp. 23-25.

27. Adrian, C., Abdullah, R., Atan, R., Jusoh, Y.Y.: Theoretical Retical Aspect In Formulating Assessment Model Of Big Data Analytics Environment. *Acta Mechanica Malaysia*, 2018, 2(1), Pp. 16-17.
28. Farrajia, H., Qamaruzaman, N., Md Sa'ata, S.K., Dashtia, A.F.: Phytoremediation of suspended solids and turbidity of palm oil mill effluent (POME) by Ipomea aquatic. *Engineering Heritage Journal*, 2017, 1(1), Pp. 36-40.
29. Ismail, N.S., Kasim, S., Jusoh, Y.Y., Hassan, R., Alyani, A.: Medical Appointment Application. *Acta Electronica Malaysia*, 2017, 1(2), Pp. 5-9.
30. Abugalia, A., Shaglouf, M.: Analysis Of Different Models Of Moa Surge Arrester For The Transformer Protection. *Acta Mechanica Malaysia*, 2018, 2(2), Pp. 19-21.
31. Halim, H., Abdullah, R., Mohd Nor, M.J., Abdul Aziz, H., Abd Rahman, N.: Comparison Between Measured Traffic Noise in Klang Valley, Malaysia And Existing Prediction Models. *Engineering Heritage Journal*, 2017, 1(2), Pp. 10-14.

CONTACT WITH THE AUTHORS

Wang Xiuli, Ph.D.

e-mail: ujsfq@sina.com

National Research Center of Pumps
Jiangsu University
Zhenjiang Jiangsu
212013
CHINA

EFFECT OF REINFORCEMENT RATIO AND VERTICAL LOAD LEVEL ON LATERAL CAPACITY OF BRIDGE PILE FOUNDATIONS

Fan Qinglai¹⁾

Gao Yufeng²⁾

¹⁾ School of Civil Engineering, Ludong University, China

²⁾ College of Civil and Transportation Engineering, Hohai University, China

ABSTRACT

The bearing response of pile foundations for cross-sea bridge subjected to lateral loading is investigated through three-dimensional finite element numerical analyses. In the analyses, non-linear behavior of concrete is simulated using smeared cracking model, and the strain-stress relationship of rebar is modeled through perfectly elasto-plastic model obeying Mises yield criterion. The finite element model is validated against published lateral static loading test in situ. The effect of reinforcement ratio of reinforced concrete and vertical load level is explored on the displacement of pile head and lateral capacity of pile. The results show that for the pile with low reinforcement ratio, the allowable lateral capacity is controlled by concrete cracking, however the allowable lateral capacity is controlled by the displacement of pile head with high reinforcement ratio. The vertical load applied on the pile head may reduce its displacement but increase simultaneously the maximum moment in the pile body. Therefore, the optimum vertical load level is 0.4~0.6 times of the vertical ultimate load of a single pile.

Keywords: cross-sea bridge, pile foundations, lateral capacity, concrete damage, numerical analysis

INTRODUCTION

In the last few decades, the bored pile foundation has been widely utilized in cross-sea bridges. In the marine environment, the pile foundation not only bears the vertical load caused by self weight of upper structure and pile body, but also bears lateral load induced by wave, wind and vehicle braking, etc. Under the extreme sea conditions, pile foundations are always subjected to large horizontal load, therefore two kinds of failure modes may occur, including plastic failure of soil around pile and concrete damage and rebar yielding of pile body. Most of the available numerical analyses have assumed that the pile is linear elastic [1-6]. In fact, in these studies, only the influence of plastic flow of soil around the pile on the lateral capacity is actually analyzed, but

the effect of concrete damage and rebar yielding of pile body is not considered. Using finite element method, Zheng and Wang [7] analyzed the effect of level as well as sequence of vertical and lateral load on the capacity of single pile. The concrete and rebar were simulated through plastic damage model and linear elastic model respectively in their finite element method. The computation results showed that the long pile and short pile exhibit different deformation characteristic. Through similar method, the influence of reinforcement ratio, pile head constraint and vertical load level was investigated on response of small diameter cast-in-place pile by Cai et al [8]. Through comparison of results of in-situ test and numerical analysis, Conte et al. [9] concluded that under large horizontal load, the displacement of pile head may be underestimated considerably without considering the damage of concrete and

reinforcement yielding. However, the determination method of ultimate capacity of single pile is not proposed in their work. Therefore, the lateral bearing response of single pile is studied considering concrete damage and rebar yield in the paper. The effect of reinforcement ratio of reinforced concrete and vertical load level is explored on the displacement of pile head and lateral capacity of pile. The determination method of ultimate lateral capacity is proposed.

FINITE ELEMENT MODEL

The in-situ horizontal load test for large diameter reinforced concrete pile was carried out by Huang etc [10]. In this present study, the results from the horizontal loading test conducted on a single pile with diameter $D=1.5\text{m}$ and embedment depth $L=34\text{m}$ are considered. The reinforcement consisted of $52\phi 32$ bars arranged in two rings. The properties of the concrete and rebar are showed in Table 1. A hydraulic jack was utilized to apply the lateral load at the pile head which is off the ground surface by about 0.9m . The stratification of the subsoil and the corresponding parameters are indicated in Table 2. In particular, the dilatancy angle ψ , is evaluated using the following empirical relationship [11]: for the soil layer with internal friction angle φ less than 30° , a value of $\psi = 0$ is assumed, however for the layer with $\varphi > 30^\circ$, the value of dilatancy angle is calculated using the expression with $\psi = \varphi - 30^\circ$.

In order to identify the applicability of finite element method, the in situ test is simulated numerically in this paper. A linear elastic perfectly plastic model with Mohr-Coulomb failure criterion is used for modelling the soil behaviour. The stress-strain relationship of steel rebar is elastic perfectly plastic with Mises failure criterion. The reinforcement is assumed to be smeared in concrete and is fully bonded to it. The concrete is modelled with smeared cracking model proposed by Hillerborg etc [12, 13]. In the model, it is assumed that the concrete material follows the plasticity theory under compression condition, and obeys fracture mechanics under tension state. The model is relatively simple and requires few material parameters. In addition, these parameters can be obtained from conventional experiments. The constitutive model is suitable for reinforced concrete pile subjected to monotonic loading [13].

Tab. 1. Material parameters of soil

Layer No	Thickness/m	Soil category	Shear modulus G/MPa	Poisson's ratio ν	Cohesion c/kPa	Internal friction angle $\varphi/^\circ$	Dilatancy angle $\psi/^\circ$
1	1.5	silt	30.8	0.3	2	33	3
2	5	Silty sand	57.7	0.3	0	34	4
3	4.5	Sandy silt	57.8	0.3	2	28	0
4	11	Silt sand	87.7	0.3	0	33	3
5	7	Sandy silt	87.7	0.3	2	28	0
6	-	Silty sand	87.7	0.3	0	30	0

Tab. 2. Material parameters of concrete and rebar

Material	Young's modulus E/Mpa	Poisson's ratio ν	Compressive strength f_c/MPa	Tensile strength f_{ct}/MPa
Concrete	32173	0.2	27.5	2.7
Steel	210000	0.3	-	471

In the finite element model, the mesh adopted for discretizing the soil and pile consists of 8 node reduced integration solid elements. Rebar is discretized by truss elements. To avoid the boundary effect, the diameter of the soil domain is $D_s=32D$, and the depth of that is $L_s=41\text{m}$. The lateral sides of the domain are constrained by vertical rollers, and the base is fully fixed. Mesh refinement, as shown is Figure 1, is conducted in the soil near the pile where high levels of plastic strain are expected to develop.

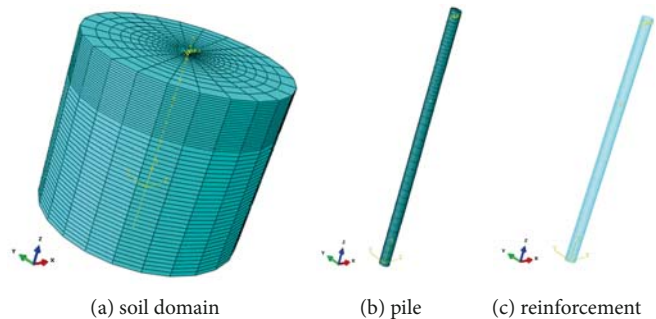


Fig. 1. Finite element mesh for the soil, pile and reinforcement

The frictional contact pairs algorithm with Mohr-Coulomb criterion is used to simulate the contact response at the soil-pile interface [14]. When the normal tensile stress develops at the soil-pile interface, separation between soil and pile occurs. When the normal stress is compressive, the Coulomb friction law, as shown in Eq. (1), is used to describe the tangential friction stress,

$$\tau_{\text{crit}} = \mu p_{\text{int}} \quad (1)$$

where τ_{crit} is the critical shear stress, p_{int} is the normal stress at the interface and μ is the friction coefficient. When the tangential stress at the interface is less than τ_{crit} , the pile-soil interface keeps the bonding state. Once the tangential stress reaches the critical value, slip can occur at the soil-pile interface. In the paper, a value of $\mu = 0.6$ is selected for any soil layer.

The initial stress field within the soil domain is calculated under K_0 -conditions before loading, which can eliminate the additional deformation caused by applying gravity. On the basis of the available data from Huang etc [10], it is found that the soil is submerged with buoyant unit weight $\gamma' = 9\text{kN/m}^3$ and the coefficient of earth pressure at rest is $K_0 = 0.72$. After this stage, a lateral load is applied at the pile head. The magnitude of the load is progressively increased to the maximum value for which a solution is obtained successfully.

A comparison in terms of the horizontal displacement-load curve, i.e. Q-s curve, at the pile head is shown in Figure 2. The displacement-load curve calculated under the assumption that the pile behaves as an elastic solid is also shown in the same figure. As can be seen, the assumption of ignoring concrete damage and rebar yielding leads to a considerable underestimation of the pile deflection, however there is significantly good agreement between numerical simulation and field measurement when concrete damage and rebar yielding is considered. When the lateral load applied at the pile head is less than 480kN, the concrete stays in elastic stage, as illustrated in Figure 3(a), therefore the calculated result without considering concrete damage and rebar yielding is also consistent with the measured result. However, when the horizontal load is higher than 480kN, concrete damage begins to occur on the tension side of pile body, as indicated in gray color in Figure 3(b). With increasing the applied load, the cracking domain is expanding in the concrete, as shown in gray area of Figure 3(c) and 3(d). At the same time, the tensile stress in the steel rebar on the tension side of pile body increases gradually until the yield state is reached.

Figure 4 and 5 show the longitudinal strain-normal stress curves calculated in the elements of concrete and rebar which are affected by the highest stress level. As shown in Figure 4(b), the maximum compressive stress in the concrete is about 24.2MPa which is lower than the strength of concrete, i.e. 27.5MPa, so failure at compression does not take place in concrete during the whole loading process. However the tensile stress of concrete and rebar does attain the respective strength which is shown in Table 2. In view of the above results, it can be concluded that a plastic hinge may form in the upper portion of the pile at the end of loading event. This failure mechanism is expected to occur in the flexible or long pile [9, 10].

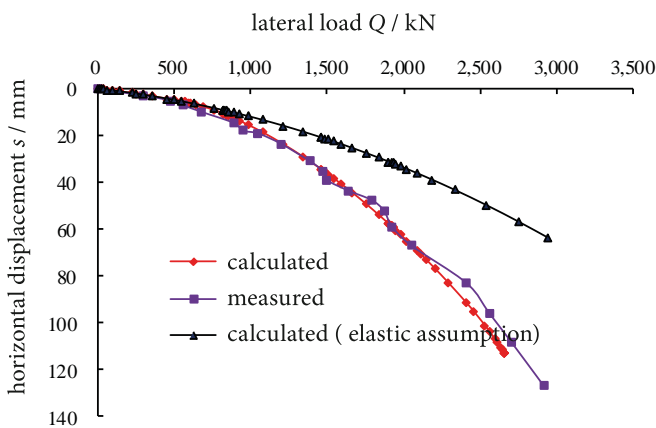


Fig. 2. Displacement curve at the pile head under lateral loading

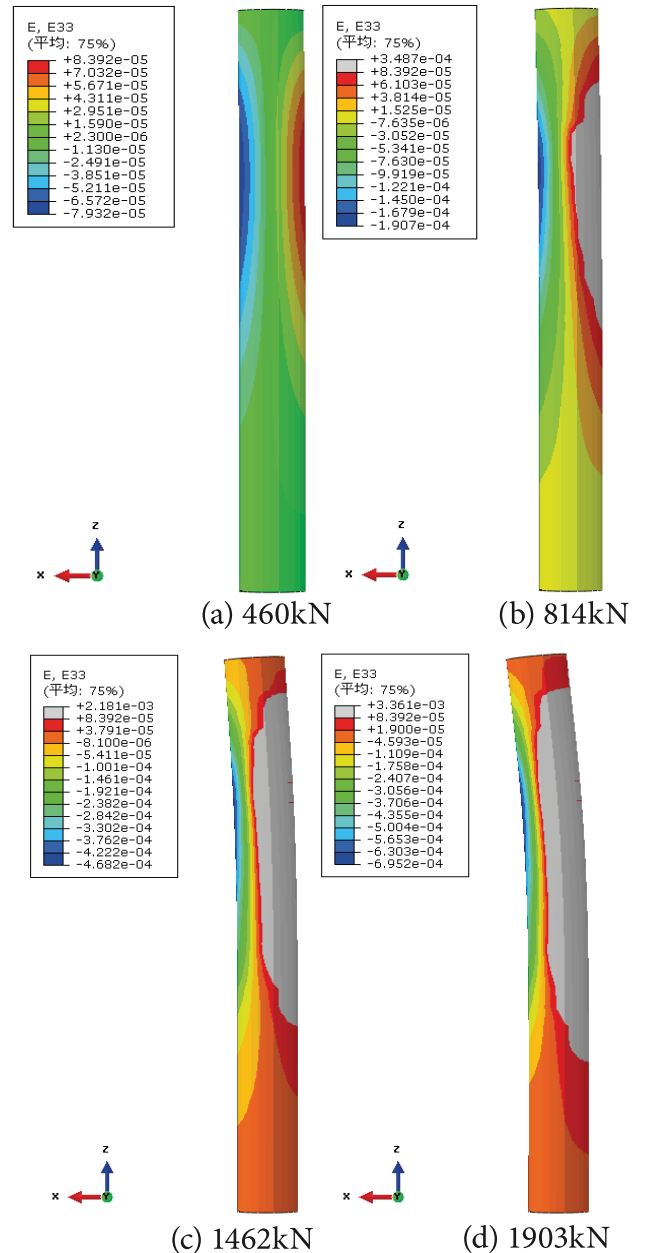
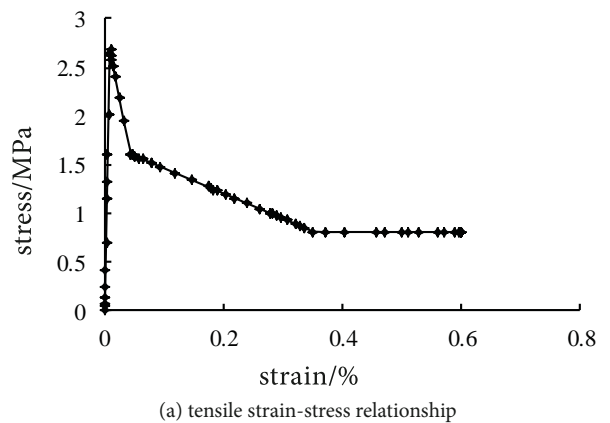
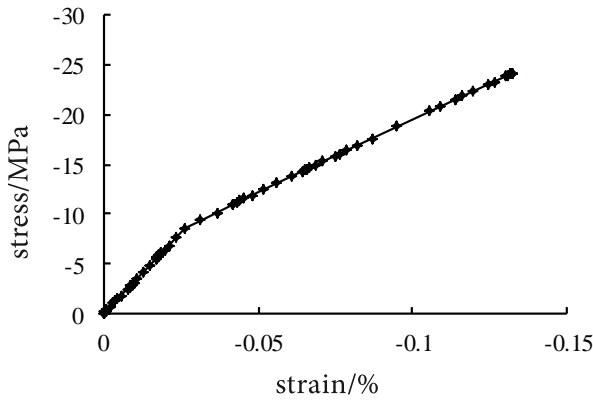


Fig. 3. Evolution of normal strain and cracking at the pile



(a) tensile strain-stress relationship



(b) compressive strain-stress relationship

Fig. 4. Curves of strain-stress relationship for concrete

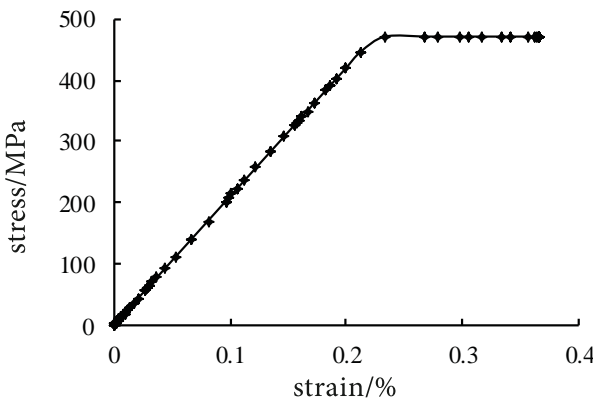
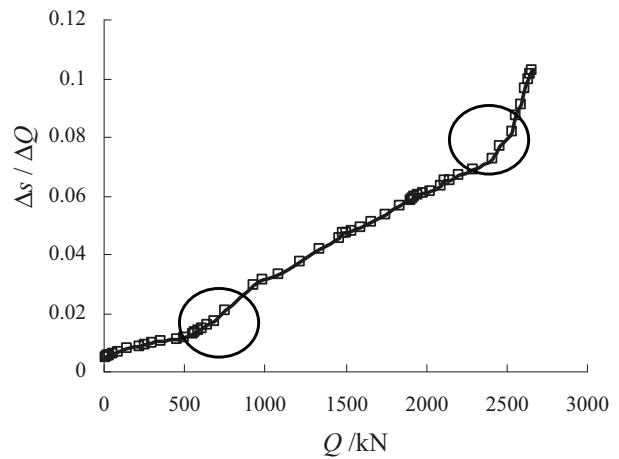


Fig. 5. Curves of strain-stress relationship for rebar

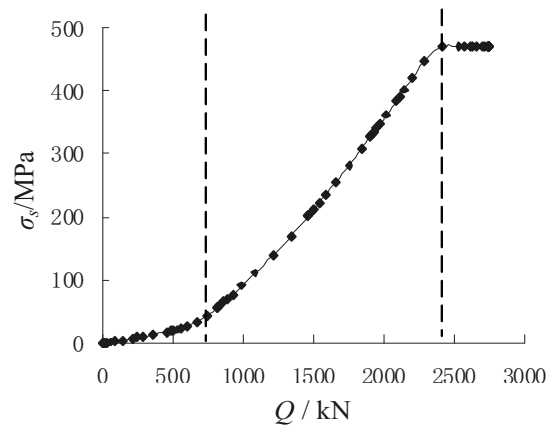
DETERMINATION METHOD OF ALLOWABLE LATERAL CAPACITY

The critical capacity and ultimate capacity are usually determined according to the strength conditions in the design of the horizontally loaded pile. Based on ‘Technical code for testing of building foundations piles’ of China [15], the critical capacity of single pile can be determined according to the value of lateral load corresponding to the first inflection point on the $Q - \Delta s / \Delta Q$ curve or the $Q - \sigma_s$ curve, in which σ_s is the tensile stress in the rebar located at the pile section with maximum bending moment. The ultimate capacity can be determined according to the value of lateral load corresponding to the second inflection point on the $Q - \Delta s / \Delta Q$ curve or the load that causes the steel rebar to begin to yield. For the pile with strong bending capacity, although obvious damage does not occur in the pile body, it is considered that the horizontal capacity of the pile reaches the limit state when the displacement of pile head exceeds the allowable value due to the plastic flow of soil around the pile.

According to Technical code for building pile foundations of China [15], the maximum displacement at the ground of bridge structure is not allowed to exceed 6mm. In view of the above numerical computation results, these methods are compared of selecting the allowable value of the horizontal capacity, as illustrated in Figure 2 and 6. It can be seen that the allowable capacity is $Q_{6\text{mm}} = 600\text{kN}$ from Figure 2, and the value of critical load and ultimate load are respectively 690kN and 2410kN from Figure 6(b). The inflection point on the $Q - \Delta s / \Delta Q$ curve is not very significant, therefore it is suggested that determination of the critical value and limit value of single pile under lateral loading is more reliable in the light of $Q - \sigma_s$ curve. During in situ test of pile foundations in transportation infrastructure construction, the stress of the steel rebar can be monitored by embedding rebar stress gauges into the pile body, and then the $Q - \sigma_s$ curve can be obtained.



(a) $Q - \Delta s / \Delta Q$ relation



(b) $Q - \sigma_s$ relation

Fig. 6. Two curves utilized in determining lateral capacity of single pile

EFFECT OF REINFORCEMENT RATIO

With the increase of the horizontal load applied at the pile head, concrete cracks occur on the tension side of pile body, then the stress is mainly carried by the steel rebar. Therefore, it is important of reinforcement ratio to the lateral bearing capacity of pile foundations. In order to investigate influence of reinforcement ratio on the capacity of single pile, the various reinforcement ratio of the pile is shown in Table 3. In this section, the soil is uniform with the elastic modulus $E = 140\text{MPa}$, and internal friction angle $\varphi = 35^\circ$.

Tab. 3. Reinforcement of piles

arrangement	Reinforcement ratio
52 ϕ 22	1.12%
52 ϕ 28	1.81%
52 ϕ 32	2.37%
52 ϕ 36	2.99%

The Q-s curve obtained at the pile head under the different reinforcement ratios is given in Figure 7. It can be seen from Figure 7 that when the horizontal load is smaller, concrete cracking does not take place on the tensile side of pile body, therefore the reinforcement ratio has little effect on the Q-s curve. However, with the increasing lateral load, the damage area of concrete is expanding gradually, and the steel rebar becomes the main tensile member, so it can be concluded that increasing the reinforcement ratio can reduce effectively the lateral deflection of pile head. In Figure 7, under the case of lateral load level $Q=1500\text{kN}$, when the reinforcement ratio increases from 1.12% to 2.99%, the horizontal displacement of the pile head is reduced by 40.16%.

In order to determine the allowable capacity of the pile, the curve of the rebar under the condition of different reinforcement ratio is shown in Figure 8. From Figure 8, it can be seen that the horizontal bearing capacity of the pile increases with the increase of reinforcement ratio. For the case of reinforcement ratio 1.12%, $Q_{6mm}=593\text{kN}$, and the critical load is 567kN, therefore the allowable value of the horizontal capacity is controlled by the cracking of the pile in such situation of low reinforcement ratio. For other cases of high reinforcement ratios, the critical load is always higher than Q_{6mm} , so the allowable value of the horizontal capacity is controlled by the horizontal displacement of pile head in such situation [16]. For example, for the case of reinforcement ratio 2.99%, $Q_{6mm}=640\text{kN}$, and the critical load is 760kN. When the reinforcement ratio increases from 1.81% to 2.99%, the allowable value of lateral capacity is only increased by 8%, therefore for the case of higher reinforcement ratio, the allowable value of the horizontal capacity is controlled by the displacement of pile head, and the increase of reinforcement ratio has little influence on the increase of the allowable capacity.

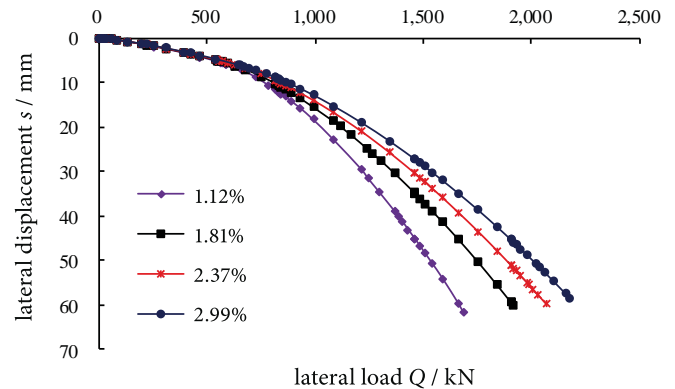


Fig. 7. Effect of reinforcement ratios on displacement of pile head

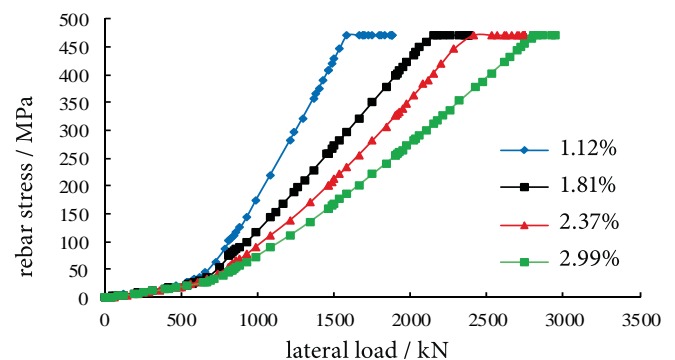


Fig. 8. Effect of reinforcement ratios on the stress of rebar

EFFECT OF VERTICAL LOAD LEVEL

In transportation engineering practice, the pile simultaneously bears the interaction of horizontal and vertical loads, and the vertical load level may have significant influence on the lateral bearing capacity of pile foundations. However, the effect of vertical load level on the lateral capacity is generally ignored during in situ loading test. In numerical computation, the vertical load is applied first at the pile head, then the vertical load is kept unchanged, before the lateral load is applied until the ultimate state is reached.

Assuming that the vertical load level is 0, 0.2, 0.4, 0.6 and 0.8 times of the vertical ultimate capacity of single pile, the horizontal displacement-load curve at the pile head is obtained. It can be seen that in the linear stage of Q-s curve, the vertical load has little effect on the lateral displacement of pile head, but with increasing vertical load level there is a significant difference between the curves with various vertical load levels. With the increase of vertical load applied at the pile head, the deflection of pile head caused by the same lateral load level is reduced, which is consistent with the conclusions of Karthigeyan et al [4, 5]. This is mainly because that the vertical load causes the compaction effect of the soil around the pile, which leads to the increase of horizontal reaction stress and friction resistance distributed

on the sides of pile [17]. Under the case of the same level of lateral load, the friction resistance on the front side of pile body increases with the increase of the vertical load. The friction resistance increases gradually from the seabed level, reaching the maximum value at the depth of $1.5D$, then decreases until the minimum value is attained at the depth of $6D$, and increases soon afterwards [18-20]. This scenery does also occur on the front side of the pile, except for the separation zone between pile and soil.

The profile of bending moment of pile body on the case of the lateral load $Q=1400\text{kN}$ under different vertical load levels is also obtained. The bending moment of the pile increases with the increase of vertical load until the vertical load level $V = 0.6V_{ult}$ is reached [21-23]. This is mainly because that when the displacement of pile head is induced by lateral load, the vertical load leads to an additional moment in the pile body, i.e. $P - \Delta$ effect, resulting in the increase of bending moment on the tensile side of pile. Considering the existence of vertical load can alleviate the deflection of pile head, and to prevent the failure of pile under vertical load, it is concluded that the optimum vertical load level is 0.4~0.6 times of the vertical ultimate load of a single pile.

CONCLUSIONS

(1) In numerical analyses of the response of reinforced pile foundations subjected to large lateral load in transportation engineering, the influence of concrete damage and rebar yielding must be taken into account on the capacity of pile foundations.

(2) For the pile with low reinforcement ratio, the allowable lateral capacity is controlled by cracking of the concrete, however the allowable lateral capacity is determined by the displacement of pile head with high reinforcement ratio.

(3) The vertical load transferred from the superstructure can reduce the deflection of pile head subjected to lateral loading, however at the same time will increase the maximum bending moment of pile body.

ACKNOWLEDGEMENT

This work was supported by the China Postdoctoral Science Foundation (2015M581713) and Shandong Provincial Natural Science Foundation (ZR2015EM047).

REFERENCES

- Jin, L., Junqiang, L., Xu, J.: Research of Bearing Behaviour on Bridge Piles Under Complex Geological Condition. *Beijing: China Water & Power Press*, 2015, Pp. 85-92.
- Zheng, C., Ling, M., Guoxiong, M.: Numerical Simulation of Lateral Bearing Capacity of Flexible Micropile. *Rock and Soil Mechanics*, 2011, 32(7), Pp. 2220-2224.
- Fan, C., Long, J.H.: Assessment of Existing Methods for Predicting Soil Response of Laterally Loaded Piles in Sand. *Computers and Geotechnics*, 2005, 32(9), Pp. 274-289.
- Karthigeyan, S., Ramakrishna, V. V. G. S. T., Rajagopai, K.: Influence of Vertical Load on the Lateral Response of Piles in Sand. *Computers and Geotechnics*, 2008, 33(2), Pp. 121-131.
- Karthigeyan, S., Ramakrishna, V.V.G.S.T., Rajagopai, K.: Numerical Investigation of the Effect of Vertical Load on the Lateral Response of Piles. *Journal of Geotechnical and Geoenvironmental Engineering*, 2007, 133(5), Pp. 513-521.
- Liuyong, C., Xichang, X., Shanxiong, C.: Model Test and Numerical Simulation of Horizontal Bearing Capacity and Impact Factors for Foundation Piles in Slope. *Rock and Soil Mechanics*, 2014, 35(9), Pp. 2685-2691.
- Gang, Z., Li, W.: Load Transfer and Bearing Capacity of Inclined Pile Under Vertical Load. *Chinese Journal of Geotechnical Engineering*, 2008, 30(12), Pp. 1796-1804.
- Zhongxiang, C., Shannan, L., Chengyong, G.: Analysis of Lateral Response of Bored Piles Based on Concrete Damaged Plasticity Model. *Chinese Journal of Rock Mechanics and Engineering*, 2014, 33(s2), Pp. 4033-4040.
- Conte, E., Troncone, A., Vena, M.: Nonlinear. Three-dimensional Analysis of Reinforced Concrete Piles Subjected to Horizontal Loading. *Computers and Geotechnics*, 2013, 49, Pp. 123-133.
- Huang, A.B., Hsueh, C.K., O'Neill, M.W.: Effects of Construction on Laterally Loaded Pile Groups. *Journal of Geotechnical and Geoenvironmental Engineering*, 2001, 127(5), Pp. 385-397.
- Qiu, G., Henke, S.: Controlled Installation of Spudcan Foundations on Loose Sand Overlying Weak Clay. *Marine Structures*, 2011, 24(4), Pp. 528-550.
- Hillerborg, A., Modeer, M., Petersson, P.E.: Analysis of Crack Formation and Crack Growth in Concrete by Means of Fracture Mechanics and Finite Elements. *Cement and Concrete Research*, 1976, 6, Pp. 773-782.
- Li, C., Qin, F., Yi, H.: Analysis on Static Performances of Smearred Cracking Model for Concrete in ABAQUS. *Journal of PLA University of Science and Technology*, 2007, 8(5), Pp. 478-485.
- Maotian, L., Xiyuan, S., Xiaowei, T., Qinglai, F.: Lateral Bearing Capacity of Multi-Bucket Foundation in Soft Ground. *China Ocean Engineering*, 2010, 24(2), Pp. 333-342.

15. BCABP.: Ministry of Housing and Urban-Rural Development of the People's Republic of China, JGJ 106-2014. *Technical Code for Testing of Building Foundations Piles*. Beijing: China Architecture & Building Press, 2014.
16. Shengnan, H., Shannan, L., Zhongxiang, C.: Test Standards for Lateral Capacity of Single PHC Pile. *Chinese Journal of Geotechnical Engineering*, 2013, 35(s1), Pp. 378-382.
17. Wu, K., Fan, Q., Hao, D., Chen, R., Liu, J.: Construction Mechanics Effect of Submarine Immersed Tube Tunnel Subjected to Different Pore Pressures Based on Numerical Analysis. *Journal of the Balkan Tribological Association*, 2016, 22(3), Pp. 2447-2453.
18. Abdullah, N.A., Rashid, N.M.: Acquiring Cybercrime Evidence on Mobile Global Positioning System (Gps): Review. *Acta Electronica Malaysia*, 2017, 1(2), Pp. 17-19.
19. Basir, N.F., Kasim, S., Hassan, R., Mahdin, H., Ramli, A., Md Fudzee, M.F., Salamat, M.A.: Sweet8bakery Booking System. *Acta Electronica Malaysia*, 2018, 2(2), Pp. 14-19.
20. Abugalia, A., Shaglouf, M.: Analysis Of Different Models Of Moa Surge Arrester For The Transformer Protection. *Acta Mechanica Malaysia*, 2018, 2(2), Pp. 19-21.
21. Adrian, C., Abdullah, R., Atan, R., Jusoh, Y.Y.: Theoretical Retical Aspect In Formulating Assessment Model Of Big Data Analytics Environment. *Acta Mechanica Malaysia*, 2018, 2(1), Pp. 16-17.
22. Abdul Sukor, N.S., Jarani, N., Muhammad Fisal, S.F.: Analysis of Passengers' Access and Egress Characteristics to The Train Station. *Engineering Heritage Journal*, 2017, 1(2), Pp. 01-04.
23. Abdul Sukor, N.S., Mohd Sadullah, A.F.: Addressing the road safety results impasse through an outcome-based approach in the state of Penang, Malaysia. *Engineering Heritage Journal*, 2017, 1(1), Pp. 21-24.

CONTACT WITH THE AUTHORS

Fan Qinglai

e-mail: fanqinglai@foxmail.com

School of Civil Engineering
Ludong University
Yantai
CHINA

Gao Yufeng

e-mail: yfgao@163.com

College of Civil and Transportation Engineering
Hohai University
Nanjing
CHINA

MODEL TESTS ON CHARACTERISTIC OF SUCTION CAISSONS IN SATURATED FINE SAND UNDER INTERMITTENT LOADING

Ping Shi ^{1,2}

¹ Key Laboratory of Civil Engineering Disaster Prevention and Mitigation, Shandong University of Science and Technology, Qingdao, China

² School of Architecture Engineering, Shandong University of Technology, Zibo, China

ABSTRACT

Suction caissons are often used for the caissons of both offshore oil platforms and offshore wind power projects because of their advantages of simple construction, economical cost, and reusability. In this study, model tests were conducted in sand in order to investigate the effects of the caisson installation method on the penetration depth and the critical suction. Results of the test program showed that the method of changing the frequency of suction during different stages of the process can increase the penetration depth of the caisson. Combining with the deformation of the soil body inside and outside the caisson, the existing method for calculating the critical suction is modified, and the critical suction calculation equation of the discontinuous penetration test is proposed. Based on the test results, the calculation equation of the soil heave height can be more accurately predicted. The analysis results verify that the calculation method and the actual results are in good agreement.

Keywords: intermittent suction installation, model test, sand, suction caisson

INTRODUCTION

Suction bucket caisson is a foundation form applied to both offshore oil platforms and offshore wind power projects. It is also called a suction caisson or a suction caisson. Due to its advantages of simple construction, economical cost, and reusability, it has been widely used in recent years and has attracted attention at home and abroad.

Suction control is a major problem in the process of the penetration of suction caissons in sand. The seepage in the caisson caused by suction affects the effective stress of the soil and reduces the installation resistance of the suction caisson [1-4]. The large suction will cause large inflow of the soil near the end of the suction caisson side wall to the inside, and the internal mud surface will swell, that is, “the

phenomenon of the soil heave plug”. When the seepage is too large, it will also cause caisson piping [5, 6].

Therefore, important design aspects in connection with the installation of suction caissons are to determine the critical under pressure and the amount of “soil heave plug” inside the cylinder during penetration.

The phenomenon of “soil heave plug” was first discovered in 1980 at the site of the installation of suction caissons at the Gorm site, and its impact cannot be ignored [7]. On the one hand, the internal mud surface of the suction caisson because of the soil heave plug is brought into contact with the caisson roof in advance so that the suction caisson cannot penetrate to the designed depth [8, 9]. It will lead to a decrease in the bearing capacity of caisson. A scholar [10] pointed out that

the response of the suction caisson was mainly depended on the degree of development of the internal soil heave. On the other hand, it will cause changes in the seepage field around the caisson and increase the degree of erosion of the surrounding soil (for shallow sea areas, this effect is particularly significant).

Given that the emergence of “soil heave plug” has an ad-verse effect on the safety and stability of the caisson itself and the superstructure, many scholars have done research on the soil heave plug characteristics in the caisson installation process, such as a scholar [11]. The influence of suction and installation depth on the development of soil heave was discussed, and the soil heave height was calculated numerically. Other scholar [12] derived the theoretical calculation equation of the soil heave height based on the assumption that the volume of the soil inside the caisson is m times of the volume of the soil displaced by the skirt moved into the caisson. He point-ed out that the coefficient m is not affected by the model size, which is mainly related to soil strength. A study of excessive internal soil uplift was carried out through the model tests, for example [13].

In order to improve the quality of caisson installation, a scholar [14] added permeable stones to the upper part of the inner soil and other scholar [15] introduced a filter layer consisting of geotextile and gravel. These measures delayed the time for the sand to contact the inner roof, but so far there are no measures that can effectively suppress the development of soil heave plug. In view of the development process of soil heave plug, many tests and theoretical studies have found that they are related to the suction and the real-time penetration depth of the suction caisson. Based on the internal soil stability, a previous researcher [16, 17], API specification [18] and DNV specification [19] gave equations for calculating suction critical penetration values. Whittle, Rauch, and Chen all agreed that the base sidewall penetration. The displaced soil volume is equivalent to the internal soil heave volume [20].

In order to achieve the desired penetration effect of the suction caisson, some scholars consider using a non-continuous suction penetration method. A scholar [21-22] proposed the concept of intermittent suction penetration and obtained a result that its final penetration depth is greater than the continuous suction penetration; a scholar [23] took an intermittent penetration scheme for indoor model tests, different durations of suction pulses were used in 4 tests and it was found that proper selection of the time of impact suction and the peak value of suction force can effectively reduce the up-lift height of soil heave. A scholar [24] first made the model sink by a certain depth under the action of its own weight and counterweight during the test and applied five levels of stable suction in the second stage. The test results showed that the seepage flow drag reduction effect of this test scheme is obvious, and an ideal final penetration depth could be obtained.

As mentioned above, in the existing studies on the characteristics of discontinuous suction penetration, the same suction was applied with the same frequency along the tests and the influence of the frequency of the suction didn't

be considered. However, the frequency of the suction directly affects the suction and the development process of the soil heave. The project described in this paper aimed at addressing the influence of the frequency of the suction changing on the mechanism of suction installation tests.

TEST DEVICE AND SOIL PREPARATION

SAND TANK

The sand tank (1 m long, 1 m wide, and 0.8 m high) is used to carry out model tests in saturated fine sand. Its dimension is large enough to eliminate the effect of the boundary on the result. The sand tank is welded with galvanized steel which reduces the friction between the soil and the inner wall and prevents the corrosion of the tank. A drainage channel is provided at the bottom side wall of the tank to adjust the height of the water level. Through the bottom drainage it can also accelerate the consolidation of the sand in the tank.

INSTRUMENTATION

A schematic diagram of a test device is shown in Fig. 1. The system includes model tank, suction caisson, displacement sensor, negative pressure sensor, and suction piping. The model penetrates into the soil (sand) through suction which is provided by an intelligent vacuum pump and is sent to the top of the model through the suction pipeline. A ball valve is provided in the middle of the suction pipeline to control the rate of suction. The vacuum pump used in the test was a water and air vacuum pump WKA1300-24A. A vertical displacement sensor (LVDT) and a negative pressure sensor are arranged on the top of the model caisson. Two sensors connected through a data acquisition instrument (Data Taker DT-80G) for data acquisition. The ranges of the LVDT and negative pressure sensor are 300mm and ± 0.1 MPa. The accuracy is 0.1mm and 0.15 kPa, respectively.

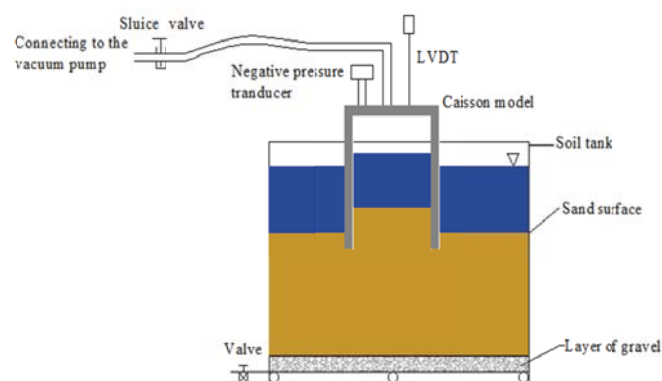


Fig. 1. Test tank and model

MODEL DETAILS

The structure of the model is barrel-shaped and machined from steel with a diameter of 120mm, a skirt wall thickness of 2mm, a roof thickness of 10mm, and a length of 240 mm. The caisson model had no internal stiffeners. A suction hole is provided for connecting the suction pipe, and a negative pressure sensor connection hole is provided on the other side.

To observe the phenomenon of soil heave inside the caisson during the penetration process, the model of organic glass was processed follow the same dimension as the steel caisson.

FORMATION OF SAND SAMPLE

Since the suction caisson is applied in the field of ocean engineering, soils with marine characteristics should be se-lected for the test soil. The test sand was taken from Qingdao Golden Beach.

The basic physical parameters were as follows: average particle size $D_{50}=0.097$ mm, non-uniform coefficient $C_u=1.78$, curvature coefficient $C_c=0.997$, natural porosity ratio $e=0.62$, and maximum pore ratio $e_{max}=0.903$, mini-mum void ratio $e_{min}=0.61$, specific gravity $G_s=2.69$; mechanical parameters: internal friction angle $\varphi=34^\circ$, dilatancy angle $\psi=10^\circ$, internal cohesive force $c=0.8$ kN/m², compression modulus $E_s=686$ kN/m².

SOIL PREPARATION

First, gravel with a thickness of 10 cm is laid at the bottom of the model tank as a drainage layer, and two layers of geotextiles are laid on the gravel cushion as an inversion filter to prevent the loss of fine sand and clay particles as the model tank drains. The "sand rain method" is used to layer the sand, and at the same time, the water is slowly poured into the model tank and the water level is higher than the sand surface. Then, the sand was consolidated by circulating drainage, and each test cycle was repeated twice. After consolidation of the sand, ensure that the water level in the model tank exceeds about 10 mm from the surface of the sand, ensuring that the sand in the model tank is always saturated. To ensure the reliability and repeatability of the test results, each test condition was strictly controlled.

Sand density and permeability coefficient are two influencing factors of its mechanical properties. At the same time, it has a great influence on the sink penetration characteristics of the suction caisson. Sand consolidation is achieved by circulating drainage, and the relative compactness of the sand after consolidation is determined. The degree is 0.997 and the permeability coefficient is 0.002 cm/s.

TESTING PROCEDURE

TESTING PROGRAMS

The test includes Continuous Suction Penetration(CSP)and Intermittent Suction Penetration According to Frequencies of Suction(IPT), as shown in Table I.

Tab 1. Test arrangements

Model diameter/mm	Model height/mm	Code	Test method
120	240	CSP	Apply suction continuously.
		IPT-1	Apply suction at an interval of 2s.
		IPT-2	Phase I (before 2 min): apply suction continuously. Phase II (after 2 min): apply suction at intervals of 2s.
		IPT-3	Phase I (before 2 min): apply suction continuously. Phase II (after 2 min): apply suction at intervals of 4s.
		IPT-4	Phase I (before 2 min): apply suction at intervals of 1s. Phase II (after 2 min): apply suction at intervals of 4s.

The traditional penetration method is to first make the caisson penetrate into a certain depth under the action of its own weight. Then apply continuous suction to make it penetrate to a predetermined depth. In the intermittent suction installation test, the frequency of suction is mutative, and the intermittent penetration time is longer.

Existing research results indicate that as the penetration depth increases, the height of soil heave increases gradually, and the rate of increase gradually slows during the later period of the experiment. Simultaneously, the seepage flow gradually weakens. According to this rule, different suction frequencies are adopted in different stages of the IPT-II, IPT-III, and IPT-IV tests. Considering the dimensions of the caisson and the test time, after many trials, 2 min time node is considered as a time separator.

TESTING PROCEDURE

To make the test results reproducible, it is vital to keep each testing condition unchanged, especially the relative densities of sand.

First, placing the caisson vertically on the sand surface so that it will plunge under its own weight. When the caisson is in a stable state, the drainage outlet of the roof to form a sealed environment inside the caisson. After end of self weight penetration, the caissons are penetrated by means of under pressure inside the caissons corresponding to a prototype rate

of about 1–2 *m/h*. A relatively high under pressure is needed to initiate further penetration. This ‘set-up’ is probably due to some pore pressure redistribution and consolidation of the remolded zone near the caisson wall during the rest period. The penetration resistance decreases after some penetration, indicating that the sand become remolded again. The caisson continues to penetrate into the sand until the inner roof contacts the sand surface.

The above is the conventional penetration testing process. In this process, the suction is applied continuously. However, intermittent penetration tests (IPT) are used in this paper which the suction is applied discontinuously (Table. 1)

Now, take the intermittent suction (IPT-I) as an example. The caisson first penetrated under the action of its own weight. Then, by controlling the intelligent vacuum pumping, the suction pump was turned off after 2s. Pause for 2s and then exhaust for 2s to form a “cyclical” loading way until the inner roof contact with the sand surface. In the same way, test conditions IPT-II, IPT-III, and IPT-IV were performed, and each set of test conditions was repeated at least three times.

The purpose of this paper is to study the penetrating characteristics and suction dissipation mechanism of the suction caisson during the intermittent installation. The characteristics of the caisson itself and the deformation of the surrounding soil are not considered.

TESTS RESULTS

COMPARISON OF TESTS CONSULTS

The test time and suction penetration depth of various working conditions are shown in Table 2. From the consideration of the penetration depth and the time-consuming of the test, a test plan that is more suitable for suction penetration is tried to be determined.

Tab. 2. Test time and final penetration depth

	CSP	IPT-I	IPT- II	IPT- III	IPT- IV
Test time / s	98	372	251	196	471
Final penetration depth / mm	104.9	158.1	156.9	149.2	163
Peak of suction /kPa	-1.29	-3.53	-4.42	-2.66	-4.99

Considering the penetration depth of suction, the depths of the caissons obtained by conventional suction penetration tests CSP and four intermittent penetration tests IPT-I, IPT-II, IPT-III, IPT-IV are 104.9mm and 158.1mm, respectively. The penetration depths of mm, 156.9mm, 149.2mm, and

163mm obtained by different penetration frequency methods are less than 9.3%. However, compared to the conventional penetration tests, the final penetration depth obtained by the intermittent penetration method is significant. The maximum difference reached 55.4%.

From the time-consuming aspect of the test, for the intermittent penetration tests that can obtain a large penetration depth, the longest time-consuming (IPT-IV) is 471s, and the shortest time-consuming (IPT-III) is 148s. The test time-consuming difference exceeds 218 %. It can be seen that due to the use of different suction frequency, the intermittent penetration test takes a lot of time.

In summary, in the two time-consuming tests (IPT-II and IPT-III), the base final penetration depth (with a self-invasive depth of 70 mm) reached 226.9 mm and 219.2 mm, respectively, which is the base length. 94.5% and 91.3% of the total penetration depth exceeds the conventional penetration test depth of 52mm and 44.3mm. It can be seen that the IPT-II and IPT-III intermittent pendulum penetration method is a better solution. The continuous application of suction during the early penetration process, and the intermittent application of suction during the later period can achieve a greater penetration depth in a shorter period of time. It is more suitable for suction caisson penetration.

COMPARISON OF MAXIMUM SUCTION AND CRITICAL SUCTION

Under intermittent suction, pore water pressure is generated inside the soil heave. The pore water pressure continuously diffuses and dissipates due to the presence of dynamic seepage. This effect may even cause sand liquefaction. Based on the analysis of soil stability, the internal soil of the caisson will undergo infiltration and destruction if suction exceeding the critical is applied. So, it is necessary to predict the critical suction.

Several authors have used numerical methods to study the critical suction’s calculation method on the conventional suction penetration methods. For example, Feld used the numerical model to analyze the conditions that caused the osmotic failure, and the outlet hydraulic gradient was used as the controlled condition to obtain the critical suction calculation equation of the undivided plate cylinder type:

$$\frac{P_{crit}}{\gamma' D} = 1.32 \left(\frac{L}{D} \right)^{0.75} \quad (1)$$

Senders used a finite element numerical model to suggest a critical suction calculation method:

$$\frac{P_{crit}}{\gamma' D} = \left\{ \pi - \arctan \left[5 \left(\frac{L}{D} \right)^{0.85} \right] \left(2 - \frac{2}{\pi} \right) \right\} \frac{L}{D} \quad (2)$$

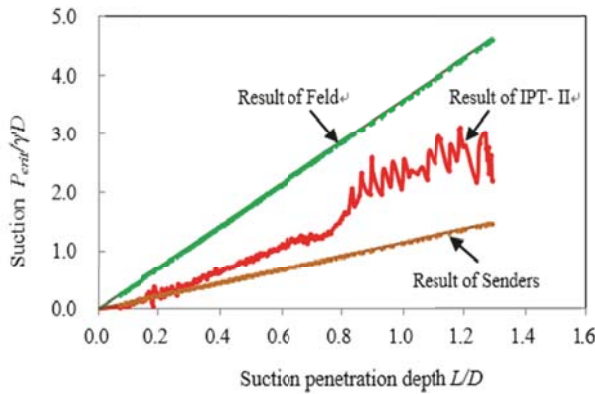
However, there is no critical suction calculation method for the intermittent penetration method.

Fig. 2 (a) and Fig. 2 (b) are the result of the comparison between the maximum suction applied in IPT-II and IPT-III and the critical suction calculated using the Feld equation

and the Senders equation. (The actual suction in the process of intermittently applying suction has a large fluctuation range, so take the maximum suction value for comparison).

It can be seen that the suction applied during the IPT-II and IPT-III tests are greater than the critical suction calculated by the Senders equation. In the test, the inside of the cylinder was found through the entire top of the plexiglass cover. It is stable and there is no infiltration damage such as piping. It shows that the critical suction calculated according to the Senders equation is conservative, which is caused by the assumption that the permeability coefficient of the soil is constant in the process of sinking. It is consistent with the conclusion of Chen Fei. The IPT-III test was anastomosis better than the IPT-II test. The reason was that the IPT-III test had a longer pause between suction in the later period of the experiment, which made the dissipation of suction relatively thorough, made the soil density relatively larger, and made the soil permeability coefficient relatively higher.

(a) Experiment IPT- II



(b) Experiment IPT- III

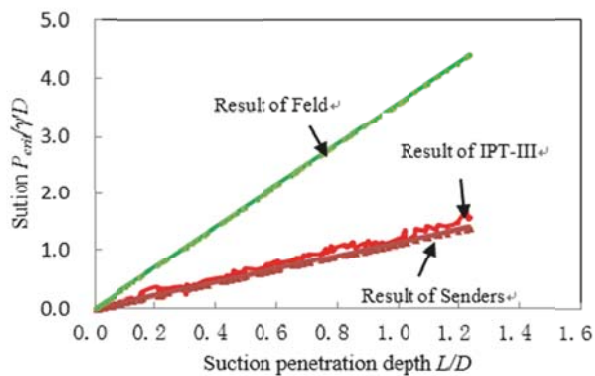


Fig. 2. Comparison between applied suction and existing critical suction

This is consistent with the view that the permeability coefficient of sand permeability test data and theoretical results in Dr. Senders's thesis are in good agreement, but the consistency of the permeability coefficient is not good.

The actual applied suction is less than the critical suction calculated with the Feld equation. This is because Feld's

equation assumes that sand is an undrained material, and Feld does not clearly determine the variation law of shear strength of sand. The Feld equation is rarely used.

In summary, the above two calculation methods are not suitable for the critical suction calculation of the intermittent suction penetration test. A new calculation method needs to be introduced and the influence of the sand permeability coefficient with the depth and the seepage flow should be considered.

A scholar considered the change of the permeability coefficient k_{fac} of the soil inside and outside the suction caisson during the test, and used the finite element method to calculate the critical suction force equation:

$$\frac{P_{crit}}{\gamma D} = \left(\frac{L}{D}\right) \left(1 + \frac{\alpha_1 K_{fac}}{1 - \alpha_1}\right) \quad (3)$$

where:

$$\alpha_1 = 0.45 - 0.36(1 - e^{-2.08L/D})$$

$$k_{fac} = \frac{k_i}{k_o}$$

For the calculation of k_{fac} in (3), there are many methods in the existing research results. For example, Houlsby and Byrne assumed that k_{fac} is a constant value. Senders thought that in the process of continuously applying suction, the soil heaves inside the suction base was on the soft state. The coefficient k_{fac} is a factor of not less than 1.

In fact, during the penetration process, the suction induces seepage in the soil around the caisson. The permeability coefficient ratio k_{fac} of the soil inside and outside is constantly changing. In the penetration test of intermittently applied suction, the permeability coefficient of the soil heave in the caisson is relatively small and has good permeability due to the presence of seepage at the beginning of the test. After intermittent suction is applied, it is equivalent to the intermittent period when suction is stopped. When the earth plug is unloaded, and the suction is dissipated, the permeability coefficient of the soil heave decreases at this stage. When suction is applied again, the seepage occurs again within the soil heave, and the permeability coefficient increases. This cycle occurs. Therefore, the value of the permeability coefficient k_{fac} is related to the size of the suction.

Some scholars have obtained that ABAQUS finite element software considering the stress-seepage coupling was employed to figure out the influence of variation of water level on the stability of cement shear wall reinforced approach channel side slope, in combination with the strength reduction technique [25]. And Some scholars have obtained a certain relationship between permeability coefficient and stress through laboratory tests and engineering practice, such as negative exponential equations, negative power exponential equations, hyperbolic equations and exponential equations, among which the most widely used one is the negative exponential equation which is studied in the pumping test [26].

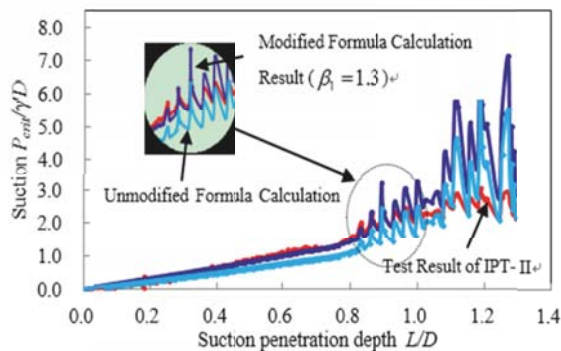
With Louis' empirical relationship, the permeability coefficient ratio $k_{fac} = 4k_o \exp(-\alpha_1 P)$ is defined here, and the

permeability coefficient $k_0=0.006\text{cm/s}$ of sand under the effect of initial effective stress, and P is the actually applied suction force [27]. Substituting k_{fac} into (3) yields the following equation:

$$P_{crit} = \beta \gamma' L \left(1 + \frac{4\alpha_1 k_0 \exp(-\alpha P_1)}{1 - \alpha_1} \right) \quad (4)$$

Fig. 3(a) and (b) are the comparison of the maximum suction applied in the two intermittent penetration methods of IPT-II and IPT-III and the critical suction calculated by (4). It can be seen that the IPT-III test result is very close to the equation calculation result. And the initial segment of the IPT-II test result is close to the equation calculation result. However, the later deviation is relatively large because of the intermittent action of the suction at the later stage of the IPT-II test is relatively short and the suction is not fully dissipated, the actually applied suction value is relatively large [28]. Here, the correction coefficient β is added to 1.3. Fig. 3 (a) proves that the experimental data is in good agreement with the theoretical calculation results. Therefore, equation (4) can be used as the critical suction calculation equation for the intermittent penetration of the suction caisson in saturated fine sand. The value of β in the equation is: in IPT-II with continuous suction for early stage and intermittent suction for 2s at late interval, $\beta_1=1.3$; for the IPT-III duration of the continuous application of suction at the early stage and the intermittent application of the suction at the late interval 4s, $\beta_2=1.0$.

(a) Experiment IPT-II



(b) Experiment IPT-III

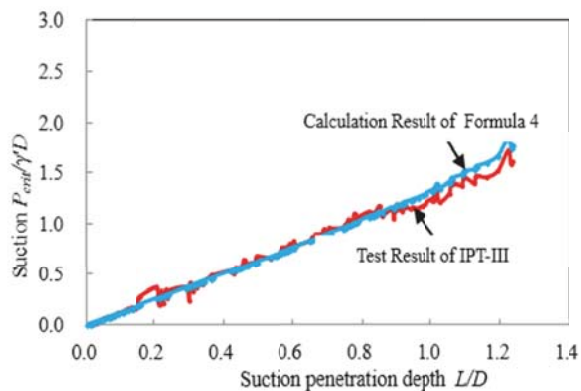


Fig. 3. Comparison between applied suction and existing critical suction

THE DEVELOPMENT LAW OF SOIL HEAVE IN THE PROCESS OF INTERMITTENT PENETRATION

In order to better study the development law of the internal soil heave under intermittent suction, the IPT-III test was conducted with the organic glass caisson [29]. The development of soil heave during the test is shown in Fig. 4.

As shown in Fig. 4, the suction is continuously applied during the initial stage of IPT-III test, the soil heave develops a certain lag and the caisson sinks slowly. The penetration depth increases significantly as the suction increases [30]. The rise of the plug is faster, and at the same time the speed of the caisson sinks faster, and the rate of growth of the soil heave slows down [31]. At the later stage, the suction is applied intermittently, and the height of the soil heave changes significantly. Otherwise under the effect of the fluctuation suction, the height of the plug decreases.

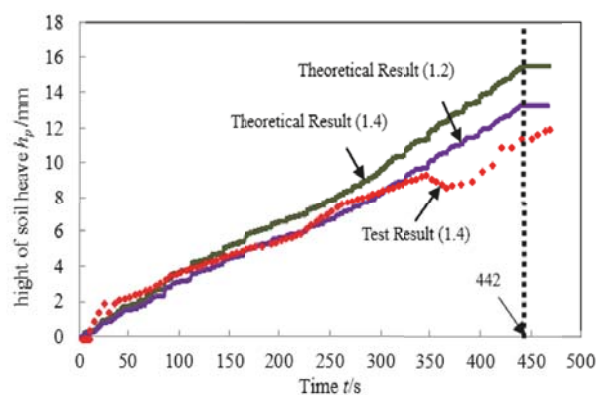


Fig. 4. Curves of soil heave during intermittent suction insertion

The internal soil heave touches the inner cap at 442s. Because the water inside the soil heave is still being pumped out, the caisson sinks a bit, while the soil heave has a slight increase.

If the suction increases to a larger value at the later stage of the test, the height of soil heave will develop rapidly. The caisson used in this experiment is a small-scale model, and the suction rate is small. Hence, the soil heave is almost linearly developed. The height of soil heave measured in the experiment is compared with the theoretical calculation result [32], as shown in Fig. 4.

In order to obtain the calculation equation of soil heave height, it is assumed that the volume of the internal soil of the caisson is m times the penetration volume, that is, the equation for the soil heave height is:

$$P_{crit} = \beta \gamma' L \left(1 + \frac{4\alpha_1 k_0 \exp(-\alpha P_1)}{1 - \alpha_1} \right) \quad (5)$$

In the above equation:

- m is the coefficient of soil heave height calculation;
- h is the penetration depth;
- D_0 is the diameter;
- D_i is the diameter.

If the cyclic loading time is short and the permeability coefficient of soil heave is small, it is assumed that the pore water confined in the soil heave does not seep during the cyclic loading, and the diffusion and dissipation of the pore water pressure can be neglected. But If the cyclic loading time is long and a large soil permeability coefficient, this assumption will inevitably cause some errors. Therefore, it is necessary to study the influence of the intermittent suction on the soil heave inside the caisson. The pore water pressure generation, diffusion and dissipation were taken into account together. Try to take m was 1.2 and 1.4 and after trial calculations, it is better that the initial suction e is applied when m is 1.2. Therefore, the calculation equation of the soil heave height during the intermittent penetration process of the suction caisson in saturated fine sand can be expressed as:

$$h_p = 1.2h \left(\frac{D_0^2}{D_i^2} - 1 \right) \quad (6)$$

From Fig. 4, the actual soil heave obtained in the later stage of the experiment is less than the theoretical value calculated by (6). It indicates that the dissipation of suction during the intermittent penetration test makes the soil heave effectively controlled. This measure delays the time that it touches the inner lid and leads to a larger final suction penetration depth. As the suction is dissipated and the rule of the soil heave changes, the soil heave rise rate and the caisson sink rate no longer have a linear relationship.

CONCLUSION

This paper proposes a new type of intermittent suction penetration test program, which changes the frequency of suction on the basis of the traditional suction penetration test scheme and introduces the permeability coefficient ratio k_{fac} of the soil inside and outside the suction caisson. Considering the influence of variation of permeability coefficient of sand with depth and seepage, the calculation method of critical suction in intermittent suction test is analyzed and discussed.

By observing the development process of the internal soil heave during the test and embedding the relationship between the volume of the soil inside the caisson and the volume of soil that penetrates the caisson, the calculation equation of the soil heave height in the intermittent suction test is studied.

The results showed that during the penetration testing process, the suction is continuously applied to the suction caisson, and the method of intermittently applying the suction at the later stage is more suitable for the suction caisson.

The actual soil heave value obtained in the later stage of the intermittent penetration test is less than the theoretical value, which indicates that the dissipation of suction in the experiment makes the soil heave development effectively controlled and delays the time for the plug to contact the inner top cover. At the same time, because the suction has dissipated and the soil heave development law changes, the rise rate of the soil heave and the caisson's sink rate has no longer

been linearly related. Based on the results of the soil heave measurement, the calculation equation of the soil heave height is deduced, and the results confirm this calculation method is suitable for intermittent frequency suction penetration test.

Through the comprehensive comparison between the theoretical settlement results and the experimental data, the calculation method of the existing critical suction is not suitable for the intermittent suction penetration test. The calculation of the critical suction by Senders tends to be safer, and the Feld calculation is more conservative. Considering the change of the permeability coefficient of the soil inside and outside the caisson, the prediction method of the suction is improved, and it is proved that this method is more suitable for the intermittent penetration test.

Even in the same experimental phase, the suction's rate directly affects the penetration depth. Therefore, the determination of the suction's rate in each test phase is the focus of the next step.

REFERENCES

1. T. Tjelta, "Geotechnical experience from the installation of the Europepipe Jacket with bucket caissons," in Proc. 27th AOTC, Houston, America, pp. 897–908, 1995.
2. M. N. Tran, and M. F. Randolph, "Variation of suction pressure during caisson installation in sand," *Geotechnique*, vol.58, no.1, pp. 1–11, 2008.
3. R. D. Zhu, H. Q. Gao, and X. B. Ma, "The model experiment studies of model's press installation and suction installation of bucket caisson on the platform in the sea," *Coastal Engineering*, vol. 18, pp. 60–66, 1999.
4. J. J. Lian, F. Chen, and H. Wang, "Laboratory tests on soil-skirt interaction and installation resistance of suction caissons during installation in sand," *Ocean Engineering*, vol.1, no.13, pp.1–13, 2014.
5. M. Senders, and M. F. Randolph, "CPT-based method for the installation of suction caissons in sand," *Journal of Geotechnical and Geo environmental Engineering*, vol.135, no.1, pp. 14–25, 2009.
6. T. Feld, "Suction buckets, a new innovative caisson concept, applied to offshore wind turbines," Ph.D. thesis, Aalborg University, Aalborg, Denmark, 2001.
7. D. Senpere, and G.A. Auvergne, "Suction caisson piles approve alternative to driving or drilling," in Proc. 14th AOTC, Houston, USA, pp. 483–493, 1982.
8. S. E. Gharbawy, and R. E. Olson, "Suction Caissons Installations for Deep Gulf of Mexico Applications," pp. 747-754, 1999.

9. N. Manh Tran, and F. Mark, "Randolph. Experimental study of suction installation of caissons in dense sand," in Proc. 23rd ICOM-AE, Canada, pp.1-8, 2004.
10. P. Kyuho, and S. Rodrigo, "Effect of Pile Installation Method on Pipe Pile Behavior in Sands," *Geotechnical Testing Journal*, vol. 27, no. 1, pp. 1–11, 2004.
11. H.Y. Ding, Z. Y. Liu, and X. Chen, "Model tests on soil plug formation in suction caisson for silty clay," *Chinese Journal of Geotechnical Engineering*, vol. 23, no. 4, pp. 441–444, 2001.
12. W. Guo, and J. Chu, "Suction caisson installation in shallow water: model tests and prediction," in Proc. 18th ICSMGE, Paris, France, pp. 1999–2002.
13. S. L. Yang, A.L. Li, and J. F. Qi, "Experimental study of bucket caisson during installation by suction," *Chinese Journal of Geotechnical Engineering*, vol. 25, no. 2, pp. 236–238, 2003.
14. D. Y. Li, Y. K. Zhang, and Y. F. Gao, "Model tests on installation of suction caissons in medium-coarse sand," *Chinese Journal of Geotechnical Engineering*, vol. 34, no. 12, pp. 2277–2283, 2012.
15. L. Q. Yu, Study on the installation behavior of suction caisson and the dynamic properties of offshore wind turbine structure," Ph.D. thesis, Zhe Jiang University, Zhejiang, China, 2014.
16. G. T. Houlsby, and B. W. Byrne, "Design procedures for installation of suction caissons in clay and other materials," *Geotechnical Engineering*, vol. 158, no. 2, pp. 75–82, 2005.
17. S. M. Junaideen, L. G. Then, K. T. Law, C. F. Lee, and Z. Q. Yue, "Laboratory study of soil-nail interaction in loose, completely decomposed granite," *Canadian Geotechnical Journal*, vol. 41, no. 2, pp. 274–286, 2004.
18. Design and analysis of station keeping systems for floating structures, API RP-2SK, 2005.
19. Geotechnical design and installation of suction caissons in clay, DNV RP-E303, 2005.
20. A. Muller, and M. Debbah, "Random matrix theory tutorial. Introduction to deterministic equivalents," *TRAITEMENT DU SIGNAL*, vol. 33, no. 2-3, pp. 223-248, 2016.
21. H. G. B. Allersma, J. R. Hogervorst, and M. Pimouille, "Centrifuge modeling of suction pile installation using a percussion technique," in Proc. 11th IOPE, Norway, pp. 620-625, 2001.
22. H. G. B. Allersma, J. R. Hogervorst, and M. Pimouille, "Centrifuge and numerical modelling of horizontally loaded suction piles," in Proc. 9th. Int. Offshore and Polar Eng. Conference, ISOPE99, pp. 711-717.
23. Z. Guo, L. Z. Wang, and F. Yuan, "An experimental investigation of insertion resistance and soil heave during caisson installation in soft clay," *Ocean Engineering*, vol. 29, no.1, pp. 9–17, 2011.
24. F. Chen, and J. J. Lian, "Model tests on bucket-soil interaction during installation of bucket caisson in silt sand." *Chinese Journal of Geotechnical Engineering*, vol. 37, no. 4, pp. 683–691, 2015.
25. Y. Li, N. P. Yi, X. G. Zhang, and S. C. Xu, "Numerical investigation on the effect of variation of water level on the stability of soil-cement column reinforced waterway side slope." *International Journal of Heat and Technology*, vol. 36, no. 1, pp. 344-352, 2018.
26. C. A. Louis, "A study of groundwater flow in jointed rock and its influence on the stability of rock masses," Imperial College of Science and Technology, London, 1969.
27. P. Zamanian, and M. Kasiri, "Investigation of Stage Photography in Jee Lee's Works and Comparing them With The Works Of Sandy Skoglund," *Acta Electronica Malaysia*, vol. 2, no. 1, pp. 01-06, 2018.
28. K. S. N. H. Ku Mohd Razali, S. Kasim, R. Hassan, H. Mahdin, A. A. Ramli, M. F. Md Fudzee, and M. A. Salamat, "Lensalyza Photography Studio Reservation System," *Acta Electronica Malaysia*, vol. 2, no. 2, pp. 06-09, 2018.
29. Z. G. He, X. N. Gu, X. Y. Sun, J. Liu, and B. S. Wang, "An efficient pseudo-potential multiphase lattice Boltzmann simulation model for three-dimensional multiphase flows," *Acta Mechanica Malaysia*, vol. 1, no. 1, pp. 08-10, 2017.
30. R. Vasanthakumari, and P. Pondy, "Mixed convection of silver and titanium dioxide nanofluids along inclined stretching sheet in presence of MHD with heat generation and suction effect," *Mathematical Modelling of Engineering Problems*, Vol. 5, No. 2, pp. 123-129, 2018.
31. M. R. Rozainy, M. A. Z. Khairi, A.W. I. Abustan, S. S. Rahim, and M. N. Nasehir Khan, "A study on the selection of suitable sites for integrated smart trapper system installation (InSmarts)," *Engineering Heritage Journal*, vol. 1, no. 1, pp. 06-10, 2017.
32. H. Halim, R. Abdullah, M. J. Mohd Nor, H. Abdul Aziz, and N. Abd Rahman, "Comparison Between Measured Traffic Noise in Klang Valley, Malaysia And Existing Prediction Models," *Engineering Heritage Journal*, vol. 1, no. 2, pp. 10–14, 2017.

CONTACT WITH THE AUTHOR

Ping Shi

e-mail: pshi66@sdut.edu.cn

Key Laboratory of Civil Engineering Disaster Prevention
and Mitigation
Shandong University of Science and Technology,
Qingdao 266590

School of Architecture Engineering
Shandong University of Technology
Zibo, CO 255000
CHINA

RESEARCH AND APPLICATION OF RULE UPDATING MINING ALGORITHM FOR MARINE WATER QUALITY MONITORING DATA

Qihong Sun^{1,2}

Junhai Zhang¹

Xinhang Xu³

¹ Postdoctoral research station of Geography, Hebei Normal University, Shijiazhuang, China

² Hebei University of Science and Technology, Shijiazhuang, China

³ State Grid Hebei Electric Power Research Institute, Shijiazhuang, China

ABSTRACT

This paper studies the characteristics of marine water quality monitoring data monitored by photoelectric sensor network, mines the potential information from the massive data. on account of the continuous accumulation of monitoring data, this paper focuses on the study of database with numerical attribute and proposes a rule updating algorithm for solving the rule maintenance issues caused by changes in the database. according to the rule, the algorithm forms a new database from part of the original data and the new data, and searches the new database by random search, thus can avoid creating a large number of redundant rules and can quickly mine effective rules at the same time. experimental results show that this method not only can avoid mining in the whole original massive data, but also can improve work efficiency, and can quickly and effectively find new data and find useful rules in the data with high practicability.

Keywords: Marine water quality monitoring, database updating, data mining, rule updating

INTRODUCTION

At present, the monitoring data of marine water quality are mainly based on the static database for rule mining and output. In the actual water quality monitoring process, the server side will accumulate a large amount of data over time, and these data on the monitoring of water quality are constantly updating and changing. Therefore, in this case, it is a very important issue to update the association rules in the process of dynamic database changes, and that is a mining problem of incremental association rules. The traditional update algorithm uses Apriori algorithm, but this algorithm is inefficient due to frequent I/O access and it's hard to measure the support settings. If the setting is too low, a lot of redundant rules will be generated. If the setting is too high, some useful but low-supportive information will be filtered out [1–3]. Therefore, this paper studies a rule updating mining algorithm and applies this method to update the rules of ocean water quality monitoring data mining.

RULE UPDATING

The traditional work of association rules data mining is based on the static database and according to the pre-set minimum support degree and minimum credibility [4–6], while the update issue of the dynamic database mainly studies the data changes in the database, the changes in the pre-set minimum support degree or the minimum credibility, and how to update the association rules without overall re-mining on the basis of existing rules.

The current rule updating algorithm mainly aims at Boolean database mining, which can effectively solve the data update mining problems, such as D. W. Cheung et al.'s FUP and FUP2 algorithms, and Feng Yu et al.'s IUA algorithm [7–9]. All of these algorithms can make full use of the rules and information of the previous mining and conduct rule updating, which can avoid duplication work and improve work efficiency. However, in most actual production processes, the attribute values of various fields to be mined are not only Boolean type, and the

numerical databases are more widely used [10–12]. In such a database, it is also necessary to update the rules, previous scholars have proposed to transform the numerical attribute database into Boolean, and conduct association rules mining. Since the water quality monitoring database belongs to the numerical database type, this paper mainly studies the rule updating problem of the numerical attribute database.

Rule updating refers to that, when the setting of the minimum support degree and the minimum confidence is unchanged, there are new data adding to the original database. Here marks the original database as DB, the new dataset is db, and we mainly studies how to put the original data and the new data set into a new database.

For the update of association rules, we start mainly from the following two situations [13–15]:

- (1) When the minimum support degree and the minimum confidence are set, the database changes. How to generate new association rules when new data is added to the original database, how to delete some data from the original database and how to generate new association rules [16].
- (2) How to generate new association rules when the data in the database is not changed, and the minimum support degree and the minimum confidence are changed [17].

As the water quality data monitored by the photoelectric sensor network continuously accumulates over time, the data in the database is getting more and more, and we mainly study the first updating situation above [18].

Add db into DB, for any set of items X, there are the following possibilities.

- (1) X are frequent itemsets both in DB and db;
- (2) X is a frequent itemset only in DB, but is not in db;
- (3) X is a non-frequent itemset only in DB, and also is in db;
- (4) X is not a frequent itemset either in DB or db.

RESEARCH ON THE RULE UPDATING ALGORITHM

RULES UPDATING ALGORITHM PRINCIPLE

During the monitoring process of the photoelectric sensor network, the water quality data is affected by factors such as climate, ocean currents and emergencies, the water quality monitoring data will change, the monitoring data will accumulate more and more over time, and the initial database will change constantly. The changing data will cause corresponding changes in the association rules, and we use the difference to reflect these changes. When the difference becomes larger, namely there are more and more data, new data may imply some new potential information [19]. Therefore, the algorithm in this paper first calculates the difference between DB and db, and then draws part of the data from the DB according to the degree of difference, forms a new database with db, and then carries out the mining operation based on adaptive immune genetic association rules. Such mining results can both retain some rules of high support degree in DB, and

reflect the potential rules of new database, meanwhile shorten the mining time and improve the mining efficiency.

RULE UPDATING ALGORITHM DEFINITION

The proposed algorithm in the initial stage needs to be calculated by the following two formulas to form a new database.

- (1) Attribute abnormality: The importance of an attribute does not depend on the occurrence frequency of the attribute. Attribute importance is a specific value. The value is not more important when the value is greater, but if the value is quite different from the original value of the attribute, it indicates that there is a new rule contained in the new data, and this information is very important. Water quality monitoring network has detected the new situation; thus, it is more valuable for mining [20].

For numerical databases, we set the data elements in database D have m attributes that make up the set of attributes. The dependencies between these attributes are different, and the degree of importance is different as well. For the k -th attribute of an element, its importance is marked as E_k according to its importance [21]. This paper simplifies the calculation of the importance of attributes, attribute importance E_k can be calculated as follows:

$$E_k = \frac{\sum_{i=1}^{|\mathcal{D}|} T_{ik}}{|\mathcal{D}|} \quad (1)$$

Where T_{ik} is the k -th attribute in the i -th record. $T_{ik} \in \{0,1\}$; $|\mathcal{D}|$ is the number of samples in database D.

- (2) Difference of data set: the degree of difference $dif(D_1, D_2)$ between the original data set D_1 and the new data set D_2 is calculated via following formula:

$$dif(D_1, D_2) = \sqrt{\frac{\sum_{i=1}^m (E_{1i} - E_{2i})^2}{m}} \quad (2)$$

Where E_{1i} is the importance of the i -th attribute in D_1 ; E_{2i} is the importance of the i -th attribute in D_2 ; m is the total number of attributes in the entire data set.

Therefore, greater $dif(D_1, D_2)$ indicates greater difference between D_1 and the newly added data D_2 , which means greater difference between the original data and the new data.

The main goal of this algorithm in the initial stage is to form a new database.

RULE UPDATING ALGORITHM PROCESS STEPS

The main steps of the rule updating algorithm are as follows.

- (1) Obtain the degree of importance of each attribute E_1, E_2, \dots, E_m in D by (Formula 1);
- (2) Obtain the degree of importance of each attribute e_1, e_2, \dots, e_m in d by (Formula 1);

- (3) Calculate the degree of difference $dis1 = dif(D, d)$ between D and d by (Formula 2);
- (4) Via $dis1$ from Formula (3), obtain the data randomly according to $dis1$;
When $0 < dis1 < 0.5$, choose $(1 - dis1) \times |D|$ records from D to form D' ;
When $0.5 < dis1 < 1$, choose $dis1 \times |D|$ records from D to form D' ;
- (5) Calculate the difference $dis2$ between D and D' ;
When $dis2 < 0.2$, a new dataset Dd was formed with D and D' ;
When $dis2 \geq 0.2$, return to the previous step and randomly choose new data again.
- (6) Set evolutionary algebra T , with a group size of M ;
- (7) Initialize $t = 0$, select initial population G randomly from Dd ;
- (8) Calculate the fitness of individuals, and also calculate the concentration, crossover probability and mutation probability. Add rules that are greater than the minimum threshold to the association rules table.
- (9) Through the selection, crossover and mutation operation, get the next generation of population;
- (10) If $t < T$, then $t \leftarrow t + 1$, return to the previous step; Otherwise, proceed the next step;
- (11) Output the current mining result from the association rules table.

APPLICATION OF THE RULE UPDATING ALGORITHM IN THE WATER QUALITY MONITORING DATA MINING

In the actual rule updating algorithm application, the original database is generally large, and the incremental database is relatively small, if we do not use the rule updating method, each time the database changes after the mining, it will mine

the mined original database once again, and it is a big waste of time. If we do adopt the rule updating method, and fully use the mining results of the original database, then when re-mining new data and part of the original data, the mining time will be much shorter, thus improve the mining efficiency. In the water quality monitoring database, under a relatively stable environment, the new data will not change greatly compared with the data in the original database. The values of each parameter are approximate and the results of incremental mining are also similar to the original results. However, when there is a big change in the marine ecological conditions, except for seasonal reasons, such as aviation fuel leaks and the sudden emission of pollutants and other emergencies, data with large differences would suddenly appear in the smooth monitoring data, thus will lead to big difference between the new data and the original data, in which case the algorithm needs to be re-standardized and re-mined, and it cannot reflect the advantages of the incremental mining algorithm. As the season changes, the performance of the photoelectric sensor for water quality monitoring may change in a stable working environment. The data in the database should be checked at regular intervals to ensure the accuracy of data mining.

The monitoring value of each field is divided into 1 ~ n according to different value intervals. Here, each field can be added 0 encoding, which represents that there is no relation between this attribute and other attributes. Randomly generate the rules under constraints. According to the coding of the specific data of the detected parameters, the parameters are mined to obtain the mapping table shown in Table 1.

CONCLUSION

When the original database obtains new data, the rules mining of the original database will have some failures, the new data brings new rules at the same time, and the overall

	A	B	C	D	E	F	G	H	I	J	K	L
1	Time	Latitude value	Longitude values	Salinity	Temperature	Turb	ST	Fluorescent algae	COD	The reserved inspection	Hi	Buoy ID
2	150909	3954.4474	11931.8872	0	0	0	0	0	10	7	3	8110004122
3	150915	3954.4474	11931.8872	0	4	1	1	3	12	10	25	8110004122
4	150921	3954.4474	11931.8872	0	3	0	3	2	13	11	7	8110004122
5	150927	3954.4474	11931.8872	0	2	0	1	2	14	11	7	8110004122
6	150933	3954.4474	11931.8872	0	0	0	0	2	10	7	6	8110004122
7	150939	3954.4474	11931.8872	0	3	1	2	3	13	0	0	8110004122
8	150945	3954.4474	11931.8872	1	1	7	4	2	13	11	6	8110004122
9	150951	3954.4474	11931.8872	0	0	6	3	0	10	10	6	8110004122
10	150957	3954.4474	11931.8872	0	3	2	2	0	11	11	6	8110004122
11	151003	3954.4474	11931.8872	0	1	0	7	1	11	10	4	8110004122
12	151009	3954.4474	11931.8872	0	0	0	0	0	4	2	2	8110004122
13	151015	3954.4474	11931.8872	0	0	4	0	0	7	4	1	8110004122
14	151021	3954.4474	11931.8872	0	2	8	1	0	11	10	6	8110004122
15	151027	3954.4474	11931.8872	0	0	0	0	0	9	7	3	8110004122

Fig. 1. Some monitoring data from the optical sensor network

Tab. 1. Field mapping table

ID	SI	TEMP	SAL	FA	COD	pH	TURB
150908	1	1	1	1	1	2	1
150909	2	5	1	3	3	2	2
150910	2	4	1	2	4	1	1
150911	1	3	1	2	5	1	1
150912	1	1	1	2	1	2	1
150913	2	4	1	3	4	1	2
150914	1	2	2	2	4	3	8
150915	2	2	1	2	2	1	3
150916	1	3	1	3	5	2	3
150917	5	1	1	2	2	1	2
150918	2	2	2	3	4	3	3
150919	1	1	2	2	2	3	2
150920	1	1	2	3	5	3	3
150921	2	1	1	2	3	2	2
150922	4	1	1	1	2	1	1
150923	1	4	1	1	2	3	2

remining of the new database is low in efficiency, so the rule updating mining algorithm is quite important. According to the characteristics of the water quality monitoring database studied in this paper, we focus on the numerical attribute database and propose a rule updating algorithm to solve the problem of rule maintenance caused by the dynamic changes of the database. According to the rule, this algorithm forms a new database from part of the original data and the new data, and searches the new database by random search and mining, which can quickly mine the effective rules without generating a large number of redundant rules. The experimental results show that the algorithm can quickly and effectively update the rules mining in the water quality monitoring database and can rapidly excavate potential information of the new data, which is of high practicability.

Tab. 2. Water quality monitoring data mining comparative result

Static database mining results	Rule updating mining results
0200010	0200010
0030003	0031013
0100110	0100110
0303000	0303000
0020300	0030300
3000010	3100010
4010000	4010000
0301000	0301000
0303000	0303000
0021000	0021001
1200000	1200001
0003003	0003013
1000110	1000110

ACKNOWLEDGMENT

Hebei Province Postdoctoral Research Project Funding No: B2018003012

REFERENCES

1. J. Wang, F. Zhang, and F. Liu, *Hybrid Forecasting Model-based Data Mining and Genetic Algorithm-adaptive Particle Swarm Optimisation: A Case Study of Wind Speed Time Series*, IET Renewable Power Generation, Vol. 10, No. 3, pp. 287–298, 2016.
2. C. K. Huynh, and W. C. Lee, *An Interference Avoidance Method using Two-Dimensional Genetic Algorithm for Multicarrier Communication Systems*, Journal of Communications and Networks, Vol. 15, No. 5, pp. 486–495, 2013.
3. H. Ghorbaninejad, and R. Heydarian, *New Design of Waveguide Directional Coupler using Genetic Algorithm*, IEEE Microwave and Wireless Components Letters, Vol. 26, No. 2, pp. 86–88, 2016.
4. M. M. Abouelsaad, M. A. Abouelatta, and A. R. Salama, *Genetic Algorithm-optimised Charge Simulation Method for Electric Field Modelling of Plate-Type Electrostatic Separators*, IET Science, Measurement & Technology, Vol. 7, No. 1, pp. 16–22, 2013.
5. B. Mohammadi-Ivatloo, A. Rabiee, and A. Soroudi, *Nonconvex Dynamic Economic Power Dispatch Problems Solution using Hybrid Immune-Genetic Algorithm*, IEEE Systems Journal, Vol. 7, No. 4, pp. 777–785, 2013.

6. W. H. Ip, D. Wang, and V. Cho, *Aircraft Ground Service Scheduling Problems and Their Genetic Algorithm with Hybrid Assignment and Sequence Encoding Scheme*, IEEE Systems Journal, Vol. 7, No. 4, 649–657, 2013.
7. S. H. Chung, and H. K. Chan, *A Two-Level Genetic Algorithm to Determine Production Frequencies for Economic Lot Scheduling Problem*, IEEE Transactions on Industrial Electronics, Vol. 59, No. 1, pp. 611–619, 2011.
8. W. Verly, L. R. Araujo, and D. R. R. Penido, *A Method for Sizing of Industrial Electrical Systems using Genetic Algorithm*, IEEE Latin America Transactions, Vol. 14, No. 2, pp. 681–686, 2016.
9. Y. Tominaga, Y. Okamoto, and S. Wakao, *Binary-based Topology Optimization of Magnetostatic Shielding by a Hybrid Evolutionary Algorithm Combining Genetic Algorithm and Extended Compact Genetic Algorithm*, IEEE Transactions on Magnetics, No. 49, No. 5, pp. 2093–2096, 2013.
10. T. Lu, and J. Zhu, *Genetic Algorithm for Energy-Efficient QoS Multicast Routing*, IEEE Communications Letters, Vol. 17, No. 1, 31–34, 2012.
11. L. Shi, Y. K. Deng, and H. F. Sun, *An Improved Real-Coded Genetic Algorithm for the Beam Forming of Spaceborne SAR*, IEEE Transactions on Antennas and Propagation, Vol. 60, No. 6, pp. 3034–3040, 2012.
12. K. Boudjelaba, F. Ros, and D. Chikouche, *Adaptive Genetic Algorithm-based Approach to Improve the Synthesis of Two-Dimensional Finite Impulse Response Filters*, IET Signal Processing, Vol. 8, No. 5, pp. 429–446, 2014.
13. T. A. Mota, J. F. Leal, and A. C. Lima, *Neural Equalizer Performance Evaluation using Genetic Algorithm*, IEEE Latin America Transactions, Vol. 13, No. 10, pp. 3439–3446, 2015.
14. K. Thirugnanam, M. Singh, and P. Kumar, *Mathematical Modeling of Li-Ion Battery using Genetic Algorithm Approach for V2G Applications*, IEEE Transactions on Energy Conversion, Vol. 29, No. 2, pp. 332–343, 2014.
15. X. K. Wei, W. Shao, and C. Zhang, *Improved Self-Adaptive Genetic Algorithm with Quantum Scheme for Electromagnetic Optimisation*, IET Microwaves, Antennas and Propagation, Vol. 8, No. 12, pp. 965–972, 2014.
16. S. C. Sen, S. Kasim, M. F. Md Fudzee, R. Abdullah, and R. Atan, *Random Walk from Different Perspective*, Acta Electronica Malaysia, Vol. 1, No. 2, pp. 26–27, 2017.
17. B. Q. Li, and Z. Li (). *Design of Automatic Monitoring System for Transfusion*, Acta Electronica Malaysia, Vol. 2, No. 1, pp. 07–10, 2018.
18. X. N. Gu, Z. G. He, X. Y. Sun, J. Liu, and B. S. Wang, *Algebraic dynamic multilevel (ADM) method for compositional multi-phase flow simulation*, Acta Mechanica Malaysia, Vol. 1, No. 1, pp. 01–03, 2017.
19. X. Luo, *Research on Anti-Overturning Performance of Multi-Span Curved Girder Bridge with Small Radius*, Acta Mechanica Malaysia, Vol. 1, No. 1, pp. 11–15.
20. S. K. Md Sa'at, and N. Qamaruzaman, *Phytoremediation potential of palm oil mill effluent by constructed wetland treatment*, Engineering Heritage Journal, Vol. 1, No. 1, pp. 49–54, 2017.
21. S. R. Hassan, N. Qamaruz Zaman, I. Dahlan, *Influence of Seed Loads on Start Up of Modified Anaerobic Hybrid Baffled (MAHB) Reactor Treating Recycled Paper Wastewater*, Engineering Heritage Journal, Vol. 1, No. 2, pp. 05–09, 2017.

CONTACT WITH THE AUTHORS

Junhai Zhang

e-mail: zhangresc@163.com

Postdoctoral research station of Geography
Hebei Normal University
Shijiazhuang 050024
CHINA

IMPACT OF GREEN TOTAL FACTOR PRODUCTIVITY IN MARINE ECONOMY BASED ON ENTROPY METHOD

Danje Wu^{1,2}

¹ School of Economics & Management, Northwest University

² Fujian Jiangxia University

ABSTRACT

In order to improve the efficiency of marine economic production and realize the sustainable and healthy development of marine economy, the spatial-temporal and dynamic evolution trend of marine economic green production efficiency in coastal areas of China is analysed by means of SFA basic model, coefficient of variation, coefficient of Gini and entropy method. It mainly includes three aspects: the result analysis of marine economy green production efficiency; the dynamic trend analysis of marine economy green production efficiency; the analysis of factors affecting marine economy green production efficiency. The results show that the factors affecting the total factor productivity of the marine economy are: development level of marine economy, marine material capital, level of opening to the outside world, marine industrial structure, marine human capital and marine environmental governance.

Keywords: marine economy, green production efficiency, entropy method

INTRODUCTION

Based on the current situation of unbalanced marine economic development and environmental pollution in China, in the 12th Five-Year Plan, the state clearly put forward the idea of “adhering to the overall planning of land and sea, formulating and implementing marine development strategies, and improving the capacity of marine development, control and comprehensive management”. The report of the Eighteenth National Congress of the Communist Party of China put forward “improve the capacity of marine resources development, develop marine economy, protect marine ecological environment, resolutely safeguard national marine rights and interests, and build a strong marine country.” In promoting the green development of China’s marine economy, the State Oceanic Administration will make great efforts to improve the policy system, enhance the innovation capacity, strengthen the protection of the ecological environment,

and carry out international cooperation and exchanges. It is an urgent problem to be solved how to give consideration to the development of marine economy and environmental protection, improve the production efficiency of marine economy, make the marine economy and environment harmoniously and rapidly develop, achieve the maximum benefits, and ultimately achieve the goal of healthy and sustainable development of marine economy.

In the traditional evaluation of marine economy, most of them only take the gross marine product as the evaluation criterion, but neglect the marine environmental pollution caused by the development of marine economy. This kind of economic growth at the cost of environmental pollution cannot reflect the objective situation of marine economic development. Even some areas in the development of the marine economy pay much more environmental costs than the economic benefits of the marine economy. Based on this, when carrying out marine economic evaluation,

the environmental cost is considered comprehensively, and the marine environmental evaluation index is incorporated into the quantitative system of the whole marine economic evaluation, so as to establish a more reasonable marine economic evaluation index system, which can be used to guide the marine economy of China develop towards a healthy and sustainable direction.

Based on the urgency of real environment and marine economic growth and the limitations of similar studies, the marine total factor rate is calculated and a comprehensive and systematic analysis is made. By means of entropy method, nuclear density estimation, Gini coefficient, coefficient of variation, α convergence and β convergence, the spatial-temporal analysis and dynamic evolution trend analysis of green production efficiency of marine economy in coastal areas of China are carried out. Quantitative analysis is made on the effect degree and role direction of various possible influencing factors on green production efficiency of marine economy. It has an important influence on the development of China's marine economy.

STATE OF THE ART

Some scholars put the marine environment and marine economy into a whole equilibrium model to study. And they concluded that the problem of marine environment is related to the huge population growth and that improving the marine environment must be based on the premise of controlling population growth [1,2]. On the basis of selecting the index system, the scholar Morrissey used the theory of marine ecology to divide the marine economic system, the marine environmental system and the social cultural system. The result shows that the transformation of the mode of marine economic development and the improvement of the marine environment are mutually reinforcing [3]. Some scholars also calculated the damping effect of the marine resources and environment on the marine economy in the Bohai Rim by Romer model, and put forward the countermeasures to improve the damping effect of the marine resources and environment on the marine economic development [4,5]. Relevant scholars decomposed the total factor productivity of the marine economy and found that there is a strong spatial spill-over effect between TFP index and technological progress index, and the degree of regional openness has a positive impact on TFP index and technological progress index [6,7]. Some scholars used the panel data of marine GDP of coastal provinces and cities and used SFA method to analyze the regional marine economic and technological efficiency. The results show that the regional marine economic and technological efficiency is high and there is an upward trend in the study period [8]. Some scholars used GRA-DEA to evaluate marine economic efficiency and put forward countermeasures and suggestions [9]. Relevant scholars used DEA to analyze the marine economic efficiency in coastal areas and found that the level of marine economic efficiency of 73% of the areas has not been fully developed [10].

METHODOLOGY

PRINCIPLES AND STEPS OF ENTROPY METHOD

In the selection of leading industries, it is usually necessary to consider the relative importance of each evaluation index. The most direct and simple method to indicate the importance is to give each index weight coefficient [11]. According to entropy theory, the amount and quality of information people obtain in decision-making is one of the decisive factors of decision accuracy and reliability. Entropy can measure the amount of useful information provided by the acquired data, and it is an ideal scale when applied to the evaluation of different decision-making processes or the evaluation of the effect of cases [12]. In information theory, entropy is a measure of uncertainty in information. The less the information is, the greater the information entropy is, and the greater the uncertainty of information is; otherwise, the smaller the information entropy is, the smaller the uncertainty of information is. According to the characteristics of entropy, the discrete degree of an index can be judged by calculating the entropy value [13]. The greater the discrete degree of the index is, the greater the impact of the index on the comprehensive evaluation is.

Basic steps: First, quantify the values of each index, and calculate the proportion of the j -th index on the i -th production index value.

$$P_{ij} = X_{ij} / \sum_{i=1}^m X_{ij} \quad (1)$$

Second, calculate the entropy e_j of the j -th index:

$$e_j = -k \sum_{i=1}^m p_{ij} \ln p_{ij} \quad (2)$$

In the above formulas, $k > 0$ is related to m , and in general, $k = 1/\ln m$.

If the value of X_{ij} is all equal for all the given index j , then:

$$e_j = -k \sum_{i=1}^m \frac{1}{m} \ln \frac{1}{m} = k \ln m \quad (3)$$

Then, e_j is the maximum value. If $k = 1/\ln m$, $0 \leq e_j \leq 1$ can be obtained.

Third, calculate the differential coefficient g_j of the j -th index:

Define the differential coefficient $g_j = 1 - e_j$, then the smaller the entropy of the i -th index is, the greater the corresponding entropy is, and the more important the index is.

Fourth, determine the weight of evaluation index: The essence of using entropy method to estimate the weight of each index is to use the value coefficient of index information to calculate. The higher the value coefficient

is, the greater the importance of evaluation is. After the differential coefficient g_j of the j -th index is determined, then the corresponding weight coefficient d_j can be obtained.

$$d_j = g_j / \sum_{j=1}^n g_j \quad (4)$$

Fifth, calculate the evaluation values of each production.

$$T_i = \sum_{j=1}^n p_{ij} d_j \quad (5)$$

ANALYSIS OF CALCULATION RESULTS OF GREEN PRODUCTION EFFICIENCY OF MARINE ECONOMY

Using the stochastic frontier analysis model and Frontier 4.1 program, the green production efficiency of marine economy in 11 coastal provinces and cities in China from 2001 to 2012 is calculated [14]. The results show that, $\gamma=0.810$ and it is obvious at the level of 1%. It indicates that the difference between the actual output and the frontier production is caused by the inefficiency of technology. It is larger than 0 and close to 1, which suggests that it is reasonable and necessary to use SFA to calculate the green production efficiency of marine economy.

Tab. 1. Parameter estimation results for stochastic frontier analysis

predictor	coefficient	standard deviation	T Statistical value
β_0	-130.44	97.926	-1.3320
β_1	2.6361	0.5988	4.4026***
β_2	0.9154	0.1032	8.8664***
β_3	0.0005	0.0003	1.9118**
β_4	0.5619	0.1854	3.0308***
β_5	0.0062	0.0040	1.5486*
β_6	0.0074	0.0089	1.8359**
σ^2	94799.5	1.4424	65724.7***
γ	0.8100	0.0254	31.948***
η	0.0366	0.0112	3.2727***
Log likelihood function			-860.22
Unilateral likelihood ratio test			118.68**

Note: LR conforms to Chi square distribution; ***, ** and * represent the test at the obvious level of 1%, 5% and 10%.

Tab. 2. The results of green production efficiency of marine economy

	Tianjin	Hebei	Liaoning	Shanghai	Jiangsu	Zhejiang	Fujian	Shandong	Guangdong	Guangxi	Hainan
2001	0.6306	0.6905	0.4970	0.5759	0.6118	0.5968	0.6293	0.4983	0.6838	0.6572	0.3697
2002	0.6438	0.7016	0.5151	0.5911	0.6257	0.6113	0.6426	0.5163	0.6952	0.6695	0.3924
2003	0.6566	0.7123	0.5325	0.6058	0.6392	0.6253	0.6555	0.5336	0.7061	0.6814	0.4142
2004	0.6689	0.7227	0.5492	0.6200	0.6521	0.6387	0.6678	0.5504	0.7167	0.6928	0.4352
2005	0.6808	0.7326	0.5654	0.6336	0.6646	0.6517	0.6798	0.5665	0.7268	0.7039	0.4555
2006	0.6923	0.7422	0.5810	0.6468	0.6767	0.6642	0.6913	0.5821	0.7366	0.7145	0.4750
2007	0.7033	0.7515	0.5961	0.6595	0.6883	0.6763	0.7024	0.5971	0.7461	0.7248	0.4939
2008	0.7140	0.7604	0.6106	0.6717	0.6995	0.6879	0.7130	0.6116	0.7552	0.7346	0.5121
2009	0.7243	0.7690	0.6246	0.6835	0.7103	0.6691	0.7233	0.6255	0.7640	0.7442	0.5296
2010	0.7342	0.7773	0.6380	0.6948	0.7207	0.7099	0.7333	0.6390	0.7725	0.7534	0.5465
2011	0.7437	0.7853	0.6510	0.7058	0.7307	0.7203	0.7429	0.6519	0.7806	0.7622	0.5628
2012	0.7529	0.7930	0.6636	0.7164	0.7404	0.7304	0.7521	0.6644	0.7885	0.7707	0.5785

According to the output elasticity of the two traditional input factors of employment and marine capital stock, $\beta_1=2.6361$, that is, the employment (10,000 people) in China's marine areas is increased by 1%, which can make GOP increase by 2.6361 percentage points; $\beta_2=0.9154$, that is, the stock of marine capital (100 million yuan) is increased by 1%, which can make GOP increase by 0.9154 percentage points [15]. Labour and capital play a great role in pulling the marine economy, in which labour input plays a dominant role, and marine economic growth is mainly driven by labour force, belonging to the extensive mode of economic growth. Under the existing technological level, the development of China's marine economy is based on increasing the number of employees and transforming as much capital stock as possible. The sustainable development of marine economy needs to change the mode of economic growth, improve the technological level and enhance the ability to develop the ocean. The independent variable of $\beta_3=0.0005$ is the discharge of industrial wastewater, the independent variable of $\beta_4=0.5619$ is the ratio of polluted sea area, the independent variable of $\beta_5=0.0062$ is the amount of pollutants carried into the sea by rivers, and the independent variable of $\beta_6=0.0074$ is the area of red tide (km²) [16]. According to the estimation result of environmental input factors, the growth of marine economic output is accompanied by the aggravation of marine environmental pollution. Comparing these marine environmental input factors, the proportion of industrial wastewater discharge is the largest when the marine economy increases the same proportion. Generally speaking, the contribution of marine traditional economic input to marine economic output value is greater than the dependence of marine output value on environmental input.

The results calculated by SFA can reflect the inter-annual variation trend of marine economic green productivity in coastal areas (table 2).

According to previous studies, the green production efficiency of marine economy in China is divided into six grades: low efficiency (0-0.400), medium and low efficiency (0.401-0.500), general efficiency (0.501-0.600), medium and high efficiency (0.601-0.700), relatively high efficiency (0.701-0.800), and high efficiency (0.801-1). Generally speaking, according to the above-mentioned classification principle, China's marine economic green production efficiency level

from 2001 to 2012 can be divided into four categories: the first category of Hainan, the average of its marine economic green production efficiency is 0.4804, belonging to the medium and low efficiency level; the second category of Liaoning and Shandong, the average of the marine economic green production efficiency is 0.5853 and 0.5864, belonging to the general efficiency level; The third category of Tianjin, Shanghai, Jiangsu, Zhejiang and Fujian, the average green production efficiency of marine economy in these areas ranges from 0.601 to 0.700, belonging to the medium and high efficiency level; the fourth category is the higher efficiency level, including Hebei, Guangdong and Guangxi, and the average green production efficiency of marine economy is between 0.701 and 0.800. The spatial difference is more obvious, forming a pattern of “three regions are higher efficiency points, two regions are general efficiency points, most of the medium and high efficiency areas are clustered and distributed, and the medium and low efficiency is on the side”.

DYNAMIC TREND ANALYSIS OF GREEN PRODUCTION EFFICIENCY OF MARINE ECONOMY

The calculation results of green production efficiency of marine economy in each region are input into Eviews6.0 software to calculate the nuclear density distribution of green production efficiency of marine economy in each year. The nuclear density distribution map of green production efficiency in China's marine economy is drawn from the calculation results in 2001, 2005, 2009 and 2012, which can reflect the annual changes of green production efficiency of marine economy.

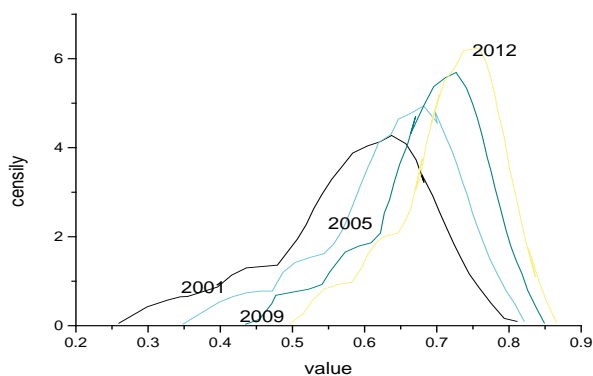


Fig. 1. The nuclear density distribution of green production efficiency of marine economy in China

The Gini coefficient is gradually decreased from 0.0922 in 2001 to 0.0500 in 2012, which proves that the difference of green production efficiency of marine economy in various regions of China is decreasing year by year. The coefficient of variation is decreased from 0.1644 to 0.0891 year by year, and the value of coefficient of variation becomes smaller and smaller, indicating that the gap between the green production efficiency of marine economy in various regions of China is narrowing with time.

Tab. 3. The convergence regression analysis

	A convergence		B convergence	
	Coefficient	T Test value	Coefficient	T Test value
α_1	13.703	27.986***		
α_2	-0.007	-27.737***		
β_1			-0.004	-10.535***
β_2			-0.041	-61.217***
R ²	0.986	0.997		
F value	769.333***	3747.479***		
Sig value	0	0		
μ value		0.0564		

Note: *** represents obvious at 1% level, t test and F test both obvious at 1% level, and equation acceptable for Sig value less than 0.5.

FACTORS AFFECTING GREEN PRODUCTION EFFICIENCY OF MARINE ECONOMY

The level of marine economic development (X1) is represented by the statistical data of per capita marine output value (10,000 yuan / person). The per capita marine output of each coastal area is increasing year by year. Generally speaking, from 2001 to 2012, the per capita marine output value of 10,000 yuan is the highest in Shanghai, 1.5819, followed by Tianjin, with 0.0707 in Guangxi Province as the lowest level.

The marine industrial structure (X2) is represented by the statistical data of the proportion of the third marine industries (%). The change trend of the marine tertiary industry in coastal areas is not consistent. The proportion of the marine tertiary industry in Tianjin and Shanghai shows a downward trend in the fluctuation. The marine tertiary industry in the other nine provinces is rising in the fluctuation. The marine tertiary industry occupies an important position in the marine economy, and the marine industrial structure tends to be reasonable.

Marine human capital (X3) is expressed by the proportion of marine professionals in marine employment. There are frequent fluctuations in marine human capital in coastal areas. Among them, the marine human capital in Tianjin, Shandong and Fujian declines in fluctuations, while the other areas have risen to varying degrees. Generally speaking, more and more attention has been paid to the training of high-quality marine personnel in various regions, and marine professional and technical personnel play an important role in the development of marine economy.

Marine material capital (X4) is expressed in terms of the ratio of the total formation of marine fixed capital to the number of employees involved in the marine area. In addition to the slight fluctuation in individual years, the marine material capital in coastal areas shows a rising trend as a whole. With the further development of marine economy in various regions, the amount of marine capital investment in each region will also increase.

The intensity of marine environmental management (X5) is expressed by the number of wastewater and solid waste treatment items. On the one hand, it is related to the demand of marine economic development. In some areas, the degree

of marine environmental pollution needs a greater degree of control, while others do not. The main aspect is related to the degree of attention paid to the control of the marine environment. Some areas pay more attention to the control of the marine environment and will provide greater financial support to deal with the marine environment.

The level of opening to the outside world (X6) is expressed by the statistical data of international tourism foreign exchange receipts (million US dollars). Among the statistical indicators of international tourism foreign exchange income, most of the regions show a regular trend of development and change. After 2003, the international tourism foreign exchange income is lower than that after 2002, and the international tourism foreign exchange income after 2004 shows a trend of increasing year by year.

RESULTS

Tab. 4. Regression result of the green production efficiency of marine economy in China

	Coefficient	Standard error	Z statistics	P value
X1	-0.044749	0.016565	-2.701469	0.0069***
X2	0.00036	0.00043	0.837932	0.4021
X3	-0.069216	0.138095	-0.501216	0.6162
X4	0.16343	0.002928	5.582459	0***
X5	4.47E-05	4.17E-05	1.073592	0.283
X6	0.001075	0.00027	3.97943	0.0001***
C0	0.577029	0.01923	30.00706	0***

Development level of marine economy: Regression results show that the green production efficiency of marine economy decreases by 0.045 units per capita per unit of marine output value. From 2001 to 2012, China's per capita marine output value rose from 0.14 million yuan to 108,000 yuan. The level of marine economic development has been constantly improving, which has a negative effect on the green production efficiency of China's marine economy. The relationship between marine economic development and marine environment is a unity of opposites.

Marine material capital: Regression results show that marine material capital has a positive role in promoting the green production efficiency of marine economy. Every unit of labour density of marine capital increases, the green production efficiency of marine economy rises by 0.016. The higher the marine material capital is, the higher the marine technological progress occurs with capital input, which promotes the development of marine industry, reduces the pollution and promotes the green production efficiency of marine economy.

The level of opening to the outside world: it has a positive effect on promoting the green production efficiency of marine economy. The results show that the green production efficiency of China's marine economy increases by 0.001 per unit of international tourism foreign exchange income. On the one hand, the increase of international tourism income in coastal areas improves economic output and economic benefits, so

environmental protection has become an inevitable choice and trend.

Marine industrial structure: The change of marine industrial structure also has an impact on the green efficiency of marine economy. Compared with the first and second industries, the regression results show that the proportion of marine tertiary industry has no obvious effect on the green efficiency of marine economy.

Marine human capital: Marine professional and technical personnel have higher labour productivity and creativity, which is conducive to improving the efficiency of marine economic decision-making and promoting the scientific and rational development of marine economic. The regression results show that the impact of marine human capital on marine economic green production efficiency is not obvious.

Marine environment governance: The regression results show that the impact of environmental governance on the green production efficiency of marine economy is not obvious. Overall, China's marine environment governance has not played an effective role in the green production efficiency of marine economy.

CONCLUSION

The constant decrease of coefficient of variation and Gini coefficient shows that the difference of green production efficiency of marine economy in China is gradually becoming smaller. From the perspective of influencing factors, the development level of marine economy plays a negative role in promoting the green production efficiency of marine economy. The main reason is that the economic benefit of marine development is less than the cost of resource destruction and environmental pollution. Marine material capital and the level of opening to the outside world play a positive role in promoting the green production efficiency of marine economy. Marine industrial structure, marine human capital and environmental governance have not passed the model test and have no obvious impact on the green production efficiency of marine economy. Adopting the means of changing the economic growth mode, adjusting the industrial structure and improving the utilization rate of technology are all effective measures to save energy and reduce emissions from the source of production while pursuing the maximum economic benefits. The follow-up environmental governance work is also essential to the promotion of economic production efficiency.

REFERENCES

1. Jiang, Y.: Total Factor Productivity. *Pollution And 'Green' Economic Growth in China*, 2013, 27(4), Pp. 504-515.
2. Lenton, T.M., Pichler, P.P., Weisz, H.: Revolutions in energy input and material cycling in Earth history and human history, 2016, 7(2), Pp. 1-30.

3. Morrissey, K.: Using secondary data to examine economic trends in a subset of sectors in the English marine economy, 2014, 50(3), Pp. 135-141.
4. Zhang, J., Qu, X., Sangaiah, A.K.: A Study of Green Development Mode and Total Factor Productivity of the Food Industry Based on the Industrial Internet of Things, 2018, 56(5), Pp. 72-78.
5. Apokin, A.Y., Ipatova, I.B.: Components of total factor productivity of the Russian economy with respect to other countries of the world: The role of technical efficiency, 2017, 28(1), Pp. 15-21.
6. Ashraf, A., Herzer, D., Nunnenkamp, P.: The Effects of Greenfield FDI and Cross-border M&As on Total Factor Productivity, 2016, 39(11), Pp. 1728-1755.
7. Zhang, K., Yi, Y., Zhang, W.: Environmental total factor productivity and regional disparity in China, 2014, 7(1), Pp. 9-21.
8. Han, Z., Li, B., Zhang, K.: Knowledge Structure of China's Marine Economy Research: An Analysis Based on Cite Space Map, 2016, 36(5), Pp. 643-652.
9. Børsheim, K.Y., Drinkwater, K.F.: Different temperature adaptation in Arctic and Atlantic heterotrophic bacteria in the Barents Sea Polar Front region, 2014, 130(1), Pp. 160-166.
10. Zhao, L., Sun, C.: Water Resource Total Factor Productivity Efficiency in China Using the Global-Malmquist-Luenberger Index, 2013, 35(6), Pp. 1229-1237.
11. Li, B.Q., Li, Z.: The Design of Wireless Responder System Based on Radio Frequency Technology. *Acta Electronica Malaysia*, 2018, 2(1), Pp. 11-14.
12. Zamanian, P., Kasiri, M.: Investigation of Stage Photography In Jee Lee's Works And Comparing them With The Works Of Sandy Skoglund. *Acta Electronica Malaysia*, 2018, 2(1), Pp. 01-06.
13. Elmnifi, M., Amhamed, M., Abdelwanis, N., Imrayed, O.: Solar Supported Steam Production for Power Generation In Libya. *Acta Mechanica Malaysia*, 2018, 2(2), Pp. 05-09.
14. Tian, X.C., Li, Q.H., He, C.S., Cai, Y.G., Zhang, Y., Yang, Z.G.: Design and experiment of reciprocating double Track Straight Line Conveyor. *Acta Mechanica Malaysia*, 2018, 2(2), Pp. 01-04.
15. Md Sa'at, S.K., Qamaruzaman, N.: Phytoremediation potential of palm oil mill effluent by constructed wetland treatment. *Engineering Heritage Journal*, 2017, 1(1), Pp. 49-54.
16. Qiao, F.: The Study On The Integration Of Green Architecture And Appropriate Technology. *Engineering Heritage Journal*, 2018, 2(2), Pp. 01-03.

CONTACT WITH THE AUTHOR

Danje Wu

School of Economics & Management
Northwest University
Shaanxi, 71027

CHINA

Fujian Jiangxia University
Fujian, 350108

CHINA

THE INFLUENCE OF FINITE ELEMENT MESHING ACCURACY ON A WELDING MACHINE FOR OFFSHORE PLATFORM'S MODAL ANALYSIS

Jiuming Xie¹
Dengyue Sun²
Chengying Xu¹
Jin Wu¹

¹ School of Mechanical Engineering, Tianjin Sino-German University of Applied Sciences, Tianjin, China

² National Engineering Research Center for Equipment and Technology of Cold Strip Rolling, Yanshan University, Qinhuangdao, China

ABSTRACT

The purpose objective of this study was to investigate the influence of finite element meshing accuracy on modal analysis which is one of the basic factors affecting the accuracy of finite element analysis and mostly preoccupies the working staff in pre-processing finite element simulation models. In this paper, we established several finite element models of a welding machine for offshore platform, with the meshing accuracy as the variable and workbench software as the platform for modal analysis, as the same time, comparing the analysis results. The results indicated that for some specific structures and simulation types, mesh refinement alone does not achieve desired results, and the authors indicate that mesh refinement is rarely related to the equipment's low-frequency modal analysis but it's great related to the equipment's high-frequency modal analysis. The findings of this study may serve as breaking the opinion that smaller mesh size means higher calculation precision and provides references for mesh division practices in low frequency modal analysis.

Keywords: Finite element analysis, Meshing, Meshing accuracy, Modal analysis

INTRODUCTION

With the rapid development of the finite element software and simulation technology, finite element analysis has been widely used in engineering, gaining momentum in analyzing the static and dynamic characteristics of structures, equipment, etc. [1]. Modal analysis is the fundamental dynamic finite element analysis, and a numerical technique to calculate the vibration characteristics (i.e. natural frequencies and formation) of structures and equipment [2].

As a theoretical mathematical modeling process, modal analysis is the field of discretizing vibration structures and seeking the solutions to system eigenvalues and eigenvectors with approximation approaches and finite element analysis [3]. In finite element software, the result of model analysis is used to determine the natural frequencies and modes of a structure,

and modal analysis is the basis of other kinetic analyses such as response dynamics analysis, harmonic response analysis and transient analysis [4].

In the finite element analysis of the equipment, the finite element mesh exerts measurable influence on calculation accuracy. Theoretically, smaller mesh size means higher calculation precision, but with the increase in finite element meshes, the computational efficiency is reduced, and in some cases, mesh refinement alone does not achieve desired results. In this paper, we studied on the influence of finite element mesh division precision on the modal analysis result of the welding machine for offshore platform which is designed according to the Tianjin Marine Economic Science and Technology Development Program—Research on double-sided steel structure welding technology and the welding equipment of structure reinforcement in Marine Engineering (KJXH2013-14).

THE BASIC PRINCIPLES OF MODAL ANALYSIS

Modal analysis is an approach to study the dynamic characteristics of a structure, and modality is the inherent vibration characteristics of mechanical structures. The latter one determines the structure's response to dynamic loads, each of which has a specific natural frequency, damping ratio and mode shape. Therefore, modal analysis must be carried out before other dynamic analyses.

In engineering practice, vibration systems are continuous elastic bodies, which theoretically belong to a system of infinite degree of freedom and need to be described by a continuous model. But the vibration system is always simplified as a model of finite degrees of freedom. In doing so, the system is abstracted as a model of lumped blocks and elastic elements [5–7]. Thus, the dynamic properties of a structure can be described by N-order matrix differential equations, i.e., the general dynamic equation is as follow:

$$[M]\{\ddot{u}\} + [C]\{\dot{u}\} + [K]\{u\} = \{F(t)\} \quad (1)$$

In the formula, $[M]$, $[C]$ and $[K]$ are the respective mass matrix, damping matrix and individual matrix, $\{\ddot{u}\}$, $\{\dot{u}\}$, $\{u\}$ are the structure's respective acceleration vector, velocity vector and displacement vector, and $\{F(t)\}$ is the excitation vector of the structure.

In conducting modal analysis, we assume $F(t) = 0$ and ignore $[C]$. The natural frequency of the structure is determined by the properties of the structure itself, independent of the external load; the damping has little effect on the natural frequency and mode of the structure [8].

The general dynamic equation under free vibration (free of external load and neglecting damping effect) is as follow:

$$[M]\{\ddot{u}\} + [K]\{u\} = 0 \quad (2)$$

When resonance occurs, $u = U\sin(\omega t)$, and the equation becomes:

$$([K] - \omega_i^2 [M]) = \{\varphi_i\} = 0 \quad (3)$$

For the modal analysis of a structure, its natural circular frequency ω_i and formation φ_i are derivable from the matrix equation above, and the equation root or eigenvalue is ω_i^2 , i ranging from 1 to the numerical number of degrees of freedom. The corresponding vector is the eigenvector $\{u\}_i$. The square root of the eigenvalue is ω_i , which expresses the natural circular frequency structure (rad/s) and thus we calculate the natural frequency $f_i = \omega_i/2\pi$. $\{u\}_i$ represents vector formation or structure mode in the engineering sense, which is the structure shape when vibrating at the frequency of f_i . Thus, the natural frequencies of the system and their corresponding modes of vibration can be solved. Modal extraction is only used to describe eigenvalues and eigenvectors.

ESTABLISHMENT OF THE SOLID MODEL

In establishing a finite element analysis model, we combine parametric modeling and feature-based solid modeling to effectively realize the output requirements of the full-scale simulation model [9]. The UG-based parametric modeling method allows the size and parameters of various part in the welding machine for offshore platform be modified at any time according to the design results; With feature modeling, the equipment model can be finished by operations of superimposing, intersecting, cutting, etc. In the process of modeling, in order to reduce the number of model features and mesh elements and shorten the computation time, some insignificant features such as small round corners and small holes are excluded. After the solid model is established, the UG modeling module interface can be directly switched to the UG / CAE pre-processing module to further complete the work of finite element meshing, which avoids the model distortion in the data transfer process between software [10].

The main structure and characteristics of the welding machine are constructed as follows to meet the design requirements (Du et al., 2014). Based on the working conditions and technical requirements of welding machine for offshore platform, the main structure and characteristics are designed, and the final design model structure is shown in Figure 1.

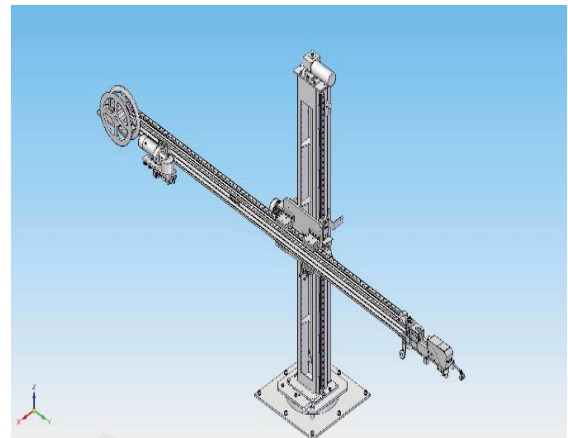


Fig. 1. The modal of welding machine for offshore platform

As can be seen from Figure 1, the welding machine for offshore platform has a very complex structure with a variety of chains, bearing holes, connecting holes, etc. In the finite element analysis, the model must be simplified appropriately lest the model complexity will cause extra troubles to our follow-up work.

In order to reflect the structural and mechanical characteristics, the simplification must follow the following principles:

- 1) Represent the structural geometry and force transmission route of the model in an accurate manner.
- 2) Apply the quality equivalent method by removing small bearing bores/bodies and chamfering secondary parts.

- 3) Simplify thin-walled structure (irregular and complex components like bearings or sensors do not affect the analytical accuracy).
- 4) Conduct the finite element equivalent treatment on loads under various working conditions. The simplified model is shown in Figure 2.

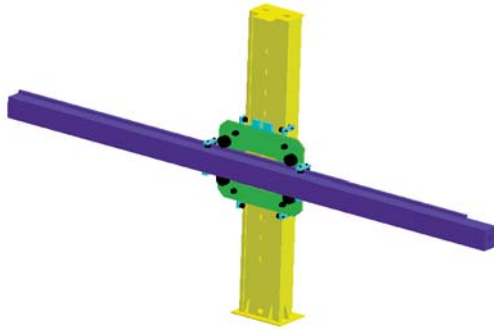


Fig. 2. The simplified model of welding machine for offshore platform

FINITE MODEL MESH DIVISION

In the finite element simulation analysis, the meshing of the finite element is particularly important as the main pre-processing part. The quality of division is directly related to the simulation scale, speed, the subsequent finite element calculation, the accuracy of analysis results and the success of computing. Meanwhile, mesh division involves element shape and type, topology type, the choice of mesh generator, grid density, geometric speed, etc. [11, 12].

In dividing finite element meshes, the element type must be determined first, and the results obtained by different element types are different. If all the structural elements are ideally composed of equilateral triangle, square, tetrahedron or cube hexahedron, the simulation accuracy should be close to the actual value. However, as this situation is rarely seen in practical engineering structures, it is necessary to select those mesh types and shapes that can fit for model characteristics, to improve mesh quality and the precision of solutions [13]. Mesh quality is generally considered from the aspects of distortion and aspect ratio. The ideal side ratio of meshes is 1:1. On the premise of uniform mesh size, the calculation result will be less accurate if the side ratio becomes larger. However, when the meshes are intensified in parallel in a certain direction, the mesh size will decrease, which contributes to precise calculation, while the aspect ratio will increase, which reduces calculation precision [14].

Based on the above analysis, in the finite element mesh, in order to truly reflect the structure and the actual situation of welding machine for offshore platform, the high-order 3D 20-node Solid186 is chosen to simulate the structure of different parts. The solid structure unit has a quadratic displacement mode to simulate irregular grids. It also supports the simulation

of the parts with high plasticity, super elasticity, creep, stress, toughness, deformation, strain and spatial anisotropy. Once some nodes overlap, hexahedron units will degrade into tetrahedrons, wedges, pyramids or prisms [15], as shown in Figure 3.

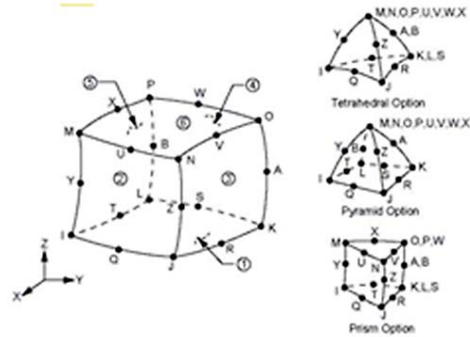


Fig. 3. The mesh of Solid186

The density of mesh directly affects the accuracy of calculation results and the size of the calculation scale. Generally, if the mesh number increases, the calculation precision can be improved, which is equal to the enhanced finite element convergence. However, the computation scale will increase greatly at the same time. And the calculation accuracy is increase very rarely once the mesh number increase to a certain extent, while the calculation scale is much larger. Therefore, the grid number should be decided taking the account of both computation scale and calculation precision. Generally, in calculating the structural dynamic characteristics, fewer grids can be used in calculating low-order modes; but more grids are required for high-order modes. Grids should be divided finer in the structure where mutation happens.

Finite element meshing is done by using adaptive partition strategy, so that the meshes can be refined or coarsened continuously in the iteration process in areas with abrupt changes. In this way, mesh points distribution is coupled with physical solution to improve the precision and resolution ratio of solutions. When the relevance in meshing are 80 and 40 respectively, mesh quality is inspected in terms of aspect ratio, area ratio or volume ratio, twist degree and density transition.

The mesh is divided by different relevance, and the number of elements and nodes are obtained, as shown in table 1:

Tab. 1. The compare of the mesh in different relevance

relevance	number of elements	number of node
40	50286	180058
80	71464	250567

The mesh results at the relevance of 80 is shown in Figure 3:

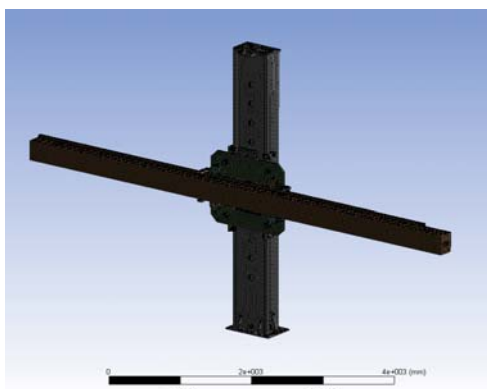


Fig. 3. The result of the mesh

The mesh quality inspection result at the relevance of 80 is shown as Figure 4:

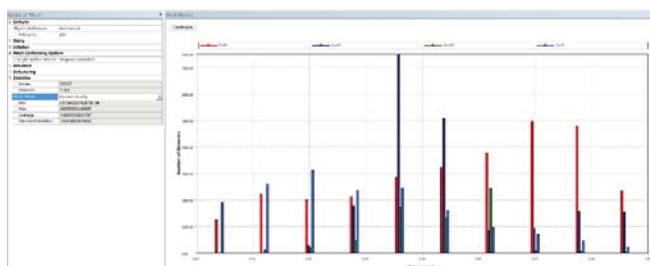


Fig. 4. The result of the mesh quality checking

MODAL ANALYSIS

The welding machine for offshore platform must meet the requirement of NVH (Noise, Vibration, Harshness), and the natural frequency is the main factor to evaluate the NVH characteristics of the structure and to determine the accuracy of the vibration response. Natural frequency is an important means to avoid the resonance between mechanical parts and the structure [16]. Therefore, it is a must to conduct modal analysis on the welding machine for offshore platform, lest there are unnecessary noises or resonance in the structure. At the same time, modal analysis is the basis of seismic response spectrum analysis. The modal analysis method can determine the natural frequency and vibration mode at any order, through which the structure's modal characteristics can be determined in a frequency range vulnerable to changes to achieve the goal of predicting the possible actual vibration responses in this frequency range under the action of various seismic focuses [17]. In order to carry out the seismic response spectrum analysis, the structure's natural frequencies and vibration modes must be calculated out through modal analysis.

Generally, all modes do not play a role in the seismic response of welding machine for offshore platform. In order to ensure the precision and accuracy of seismic calculation results, additional modes of modal mass participation coefficients should be used [18]. In this calculation, if the modal mass reached the request of 90% of the total mass, the participation coefficient of vibration modes must be evaluated to identify which vibration

modes play a major role in the subsequent earthquake load. In this way, we can select adequate vibration modes.

Modal analysis mainly uses the methods of subspace iteration and Block Lanczos. The method of subspace iteration is mainly suitable for solving the problem of extracting a few order modes in the large-scale eigenvalue problem, and the complete mass and stiffness matrix used in the method has high precision. However, demands for mesh quality are high and the calculation time is long [19]. The method of Block Lanczos uses a sparse matrix solver with similar precisions, responds well to ill-conditioned matrixes, and is quite time-saving. However, demands for memory are high and the method is limited to the case of extracting multi-order modes with large degrees of freedom [20]. In this paper, to improve the speed of calculation, Block Lanczos is used in modal analysis.

Before the modal analysis, it is necessary to set the boundary conditions of the welding machine for offshore platform [21]. The boundary conditions of welding machine in the actual operation process are very complex, which not only renders loading difficult to achieve, but increases the calculation load of finite element analysis [22]. To facilitate loading and simplify the calculation, the boundary conditions and loading should be equivalent. The welding machine for offshore platform model is an assembly in which all parts are connected with sliding pairs and revolute pairs [23]. Surface constraints are applied between the two parts, and the corresponding units are formatted automatically on the constrained surfaces. Then, the corresponding units are connected to form a complete and continuous [24]. The entire welding machine for offshore platform is connected with the base through the bottom connecting hole. Fixed support is applied to the surface of the bottom connecting rod. The welding machine for offshore platform is mainly subjected to the following long-term, stable loads:

- 1) The gravity of the welding machine itself, which is simulated by applying the standard gravity along the Z-direction, $g=9806.6\text{mm/s}^2$;
- 2) The gravity of the welding flux and the motor on the left, which is properly magnified into the gravity loads.
- 3) The gravity of the submerged arc welding machine on the right, which is properly magnified into the gravity loads.

According to the actual working conditions of the welding machine for offshore platform, the boundary conditions and load models of the equivalent welding machine are shown in Figure 5.

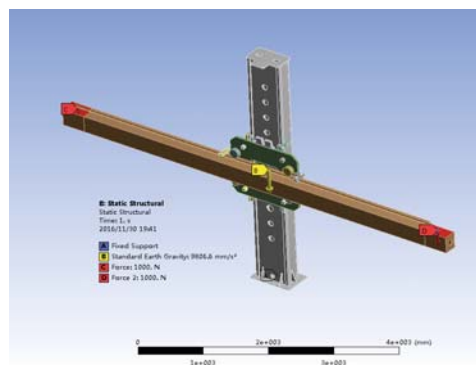


Fig. 5. The load model of the welding machine

In order to compare the influence of different grid numbers on the modal analysis, the frequency and formation of modal analysis at respective low and high orders (first-order, second-order, fourth-order and fiftieth-order) are extracted in the process of morphological analysis. The modal frequencies at each order under different relevance are shown in the Table 2.

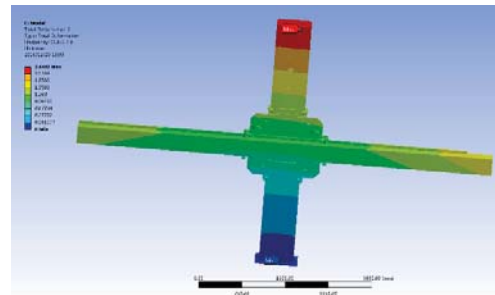
Tab. 2. The modal frequency at each order under different relevance

order	modal frequency in different relevance		Error
	relevance 80	relevance 40	
1	6.669	6.537	2.0%
2	11.633	11.208	3.7%
4	24.770	23.986	3.2%
50	356.17	308.49	13.4%

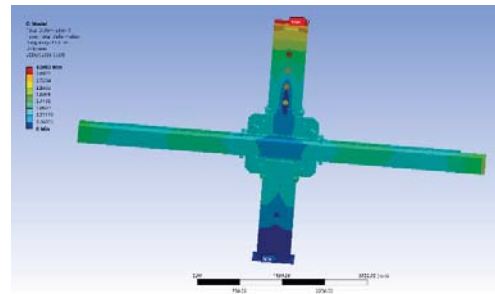
In fact, for the pre-stressed non-free modal analysis which only responds greatly to low-order frequencies, we can simplify the analysis by analyzing the first ten frequencies and the corresponding vibration modes.

It can be seen from Table 2 that the natural frequency of the model increases with the increase of the order. The rated speed of the welding machine motor is 1500r / min and the excitation frequency is 25Hz. It can be seen from the modal analysis that the frequency of the model and the fundamental frequency of the welding operator differ little at the fourth order, meaning the easiness to resonate [25]. But after analysis, the equivalent participation quality of the welding machine is 18.6 %, so there are no security risks in welding machine for offshore platform.

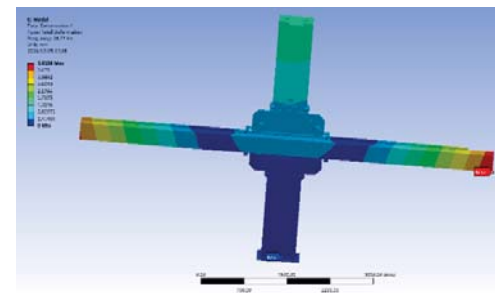
The various modes of vibration distribution in different conditions of grid division are shown in Figure 6:



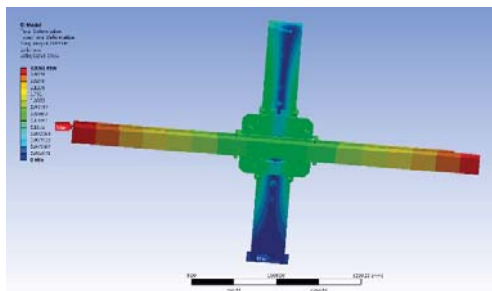
(c) The second-order vibration mode at the relevance of 80



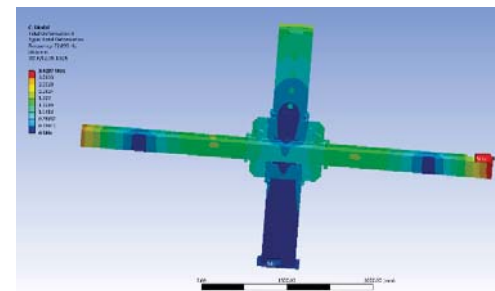
(d) The second-order vibration mode at the relevance of 40



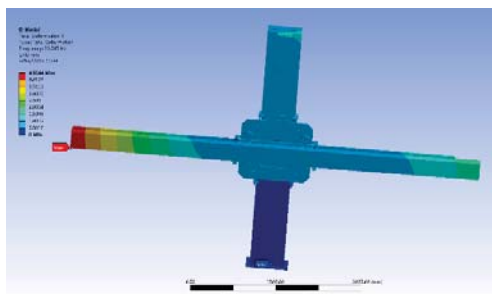
(e) The fourth-order vibration mode at the relevance of 80



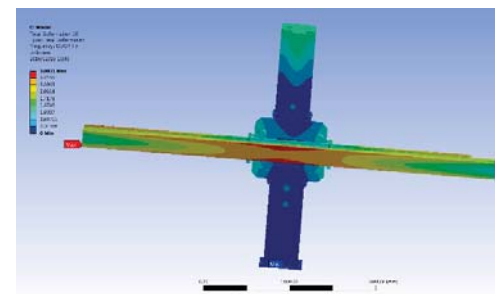
(a) The first-order vibration mode at the relevance of 80



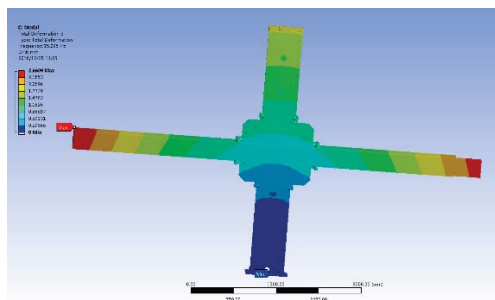
(f) The fourth-order vibration mode at the relevance of 40



(b) The first-order vibration mode at the relevance of 40



(g) The fiftieth-order vibration mode at the relevance of 80



(h) The fiftieth-order vibration mode at the relevance of 40

Fig. 6. The various modes of vibration distribution in different conditions of mesh division

It can be seen from the modal analysis results that the difference between frequencies and between amplitudes under different meshing precisions are less than 10% at the first/second/fourth order but more than 10% at the fiftieth order. Therefore, for the low-order modal analysis, the partitioning accuracy of the mesh has little effect on the modal analysis results [26]. For the high-order modal analysis, the meshing accuracy of the mesh has a great influence on the modal analysis results. In the low-order modal analysis, the accuracy of meshing can be slightly lower to increase the speed of the calculation; while in the high-order modal analysis, we should try to improve the accuracy of meshing to obtain more accurate results.

CONCLUSIONS

In this paper, mesh division is carried out under different precisions in a welding machine for offshore platform, on whose basis the modal analysis is conducted. The main conclusions are as follows:

In the case that the solution accuracy meets the requirements, the difference between modal frequencies obtained by finite element modal analysis in different precision levels is small, and the modal formation is basically the same.

When the finite element method is used in low frequency modal analysis, the number of meshes can be appropriately reduced to improve the computational efficiency in the conditions to meet the accuracy requirements.

When the finite element method is used in high frequency modal analysis, it is necessary to increase the number of meshes to improve the precision of solutions without failing the accuracy requirements.

ACKNOWLEDGMENT

The research of this paper is made possible by the generous support from the project team of KJXH2013-14 and E2016203182.

REFERENCES

1. N. Larbi, and J. Lardies, *Experimental modal analysis of a structure excited by a random force*, Mechanical Systems & Signal Processing, Vol. 14, No. 2, pp. 181–192, 2000.
2. K. Yang, and T. Han, *The application of Ansys in modal analysis*, Journal of Jiamusi University (Natural Science Edition), Vol. 23, No. 1, pp. 81–84, 2005.
3. Y. N. Lv, Z. H. Lv, B. Zhao, and C. Wang, *A finite element analysis and topology optimization method for structures with free damping*, Chinese Journal of Computational Mechanics, Vol. 29, No. 2, pp. 178–183, 2012.
4. L. G. Cai, S. M. Ma, Y. S. Zhao, Z. F. Liu, and W.T. Yang, *Finite element modeling and modal analysis of heavy-duty mechanical spindle under multiple constraints*, Journal of Mechanical engineering, Vol. 48, No. 3, pp. 165–167, 2012.
5. X. Cui, L. Gao, and J. X. Liu, *Wind tunnel test study on the influence of railing ventilation rate on the vortex vibration characteristics of the main beam*, International Journal of Heat and Technology, Vol. 36, No. 1, pp. 65–71, 2018.
6. J. Huang, Z. Ji, H. M. Duan, and S. R. Qin, *Experimental modal analysis of mechanical structure and typical applications*, China Measurement & Test, Vol. 36, No. 2, pp. 4–8, 2010.
7. Y. Dai, S. M. Cui, and L.W. Song, *Finite element method modal analysis of driving motor for electric vehicle*, Proceedings of the Chinese Society for Electrical Engineering, Vol. 31, No. 9, pp. 100–104, 2011.
8. Y. Y. Cao, and D. F. Zhao, *Finite element modal analysis theory and application*, Mechanical Engineering & Automation, Vol. 140, No. 1, pp. 73–74, 2007.
9. W. G. Zheng, Z. J. Liu, and N. Yang, *Analysis on modal and static of steering pump bracket*, Machinery Design & Manufacture, No. 6, pp. 182–184, 2014.
10. E. W. Zhang, Y. S. Sun, and X. H. Zhou, *Example analysis in date conversion between UG and Ansys*, Mechanical Manufacturing & Automation, Vol. 36, No. 2, pp. 90–91, 2007.
11. I. G. Jang, and B. M. Kawk, *Evolutionary topology optimization using design space adjustment base on fixed grid*, International Journal for Numerical Methods in Engineering, Vol. 66, No. 11, pp. 1817–1840, 2006.
12. A. O. Cifuentes, and A. Kalbag, *A performance study of tetrahedral and hexahedral elements in 3-D finite element structural analysis*, Finite Element in Analysis and Design, Vol. 12, No. 3, pp. 313–318, 1992.

13. B. Y. Shih, and H. Sakurai, *Automated hexahedral mesh generation by swept volume decomposition and recomposition*, "International Meshing Roundtable, pp. 273–280, 1996.
14. H. C. Lu, I. Song, W. R. Quadros, and K. Shinmada, *Geometric reasoning in sketch-based volumetric decomposition framework for hexahedral meshing*, *Engineering with Computers*, Vol. 30, No. 2, pp. 237–252, 2013.
15. C. F. Ning, Z. D. Fang, F. Wang, and X. Wang, *Several Entity Element in the Comparison of Aviation Gear Box Calculation*, *Journal of Mechanical Strength*, Vol. 4, No. 37, pp. 742–747, 2015.
16. V. N. Nikishin, A. P. Pavlenko, K. N. Svetlichnyi, and V. S. Makov, *Analysis of torsional crankshaft oscillations in a diesel engine on the basis of cylinder-block vibration*, *Russian Engineering Research*, Vol. 33, No. 12, pp. 687–691, 2010.
17. P. Han, J. J. Wang, and Z. R. Wang, *Elasto-plastic response spectrum analysis in the seismic design of viaducts*, *Journal of Harbin Engineering University*, Vol. 34, No. 4, pp. 461–470, 2013.
18. M. L. Aenlle, P. F. Fernandez, R. Brincker, and A. F. Cantel, *Scaling-factor estimation using an optimized mass-change strategy*, *Mechanical Systems & Signal Processing*, Vol. 24, No. 5, pp. 1260–1273, 2010.
19. Y. Saad, *Analysis of subspace iteration for eigenvalue problems with evolving matrices*, *Siam Journal on Matrix Analysis & Application*, Vol. 37, No. 1, pp. 103–122, 2016.
20. A. H. Bentbib, M. E. Guide, and K. Kbilon. *The block Lanczos algorithm for linear ill-posed problem*, *scalclo*, pp. 1–22, 2016.
21. S. Kasim, N. A. Omar, N. S. Mohammad Akbar, R. Hassan, and M. A. Jabar, *Comparison Semantic Similarity Approach Using Biomedical Domain Dataset*, *Acta Electronica Malaysia*, Vol. 1, No. 2, pp. 1–4, 2017.
22. S. C. Sen, S. Kasim, M. F. Md Fudzee, R. Abdullah, and R. Atan, *Random Walk from Different Perspective*, *Acta Electronica Malaysia*, Vol. 1, No. 2, pp. 26–27, 2017.
23. S. Sathishkumar, and M. Kannan, *Design and Fatigue Analysis of Multi Cylinder Engine and Its Structural Components*, *Acta Mechanica Malaysia*, Vol. 2, No. 2, pp. 10–14, 2018.
24. A. Abugalia, M. Shaglouf, *Analysis of Different Models of Moa Surge Arrester for The Transformer Protection*, *Acta Mechanica Malaysia*, Vol. 2, No. 2, pp. 19–21, 2018.
25. X. G. Yue, and M. A. Ashraf, *Opposite Degree Computation and Its Application*, *Engineering Heritage Journal*, Vol. 2, No. 1, pp. 05–13, 2018.
26. M. Elmnifi, M. Alshelmany, M. Alhammaly, and O. Imrayed, *Energy Recovery from Municipal Solid Waste Incineration on Benghazi – Case Study*, *Engineering Heritage Journal*, Vol. 2, No. 1, pp. 19–23, 2018.

CONTACT WITH THE AUTHORS

Dengyue Sun

e-mail: sdy@ysu.edu.cn

National Engineering Research Center
for Equipment and Technology of Cold Strip Rolling
Yanshan University
Qinhuangdao – 066004
CHINA

HYDRODYNAMIC LOAD AND PARAMETRIC DESIGN OF GROUTED CLAMP USED ON OFFSHORE JACKET

Bo Zhang¹

Zhuo Wang¹

Tao Wang²

¹ College of Mechanical and Electrical Engineering, Harbin Engineering University, Harbin, Heilongjiang, China

² School of Mechanical Engineering, Hebei University of Technology, Tianjin, China

ABSTRACT

The reliability and safety of offshore platform are an important research aspect in marine engineering. The jacket platform is mainly used for oil development and submarine drilling, and the long-term work in the marine environment will be subjected to different loads, which will lead to the damage of the structure part of the offshore platform. It affects the structural strength of the platform. For the repair of jacket damage, grouted reinforcement technology is adopted, which has the advantages of simple underwater installation and low cost. The reinforcement technology of the grout hoop has been applied to the engineering projects abroad, but the stress and serialization design of the hoop in the marine environment need further study. This paper will combine the ocean current and wave force to carry out the research of underwater work and prevent loosening, and put forward the parametric design method for the specific size of the hoop. Two types of experimental models are designed: short bolt form clamp and long bolt form clamp. The mechanical experiment of the long bolt clamp is carried out, and the relationship between the slipping force and the bolt preload is analyzed, so as to verify the theoretical analysis.

Keywords: Offshore Jacket, Grouted Clamp, Parameterized Design, Mechanics Experiment

INTRODUCTION

Nowadays, people turn their eyes to the ocean and have entered a new era of comprehensive exploitation and utilization of the ocean. In recent years, in the new discovery of global oil and gas resources, most of them are concentrated on the sea, and the share of marine oil reserves and production in the global oil production is increasing [1]. According to statistics, there are more than 6000 platforms in the world continental shelf. Since 1930s, the world ocean platform has flourished and developed from small to large, from wooden structure to steel structure, from shallow sea to deep sea[2], and the deepest platform has been working in the deep sea of thousands of meters[3]. The jacket offshore platform is the most widely used in the steel pile foundation platform. The

jacket offshore platform has the outstanding characteristics such as large volume, expensive cost, complex structure, complex marine environment and so on [4]. At the same time, the jacket offshore platform is in the marine environment, which will be subjected to severe and harsh sea wind, sea current and so on[5]. Once the accident happens, it will cause serious marine environment pollution, influence the marine environment, bring inestimable economic losses and casualties, and cause unimaginable consequences and cause bad social impact [6, 7]. Therefore, higher engineering requirements and security challenges are put forward to the offshore platform of the jacket.

In recent years, the repair and reinforcement of offshore platform partial damage structure has become a hot research

topic at home and abroad, and is still a challenging research topic. On the basis of considering the safety and reliability of the jacket offshore platform, this paper studies the maintenance and reinforcement technology of the partially damaged components of the underwater jacket offshore platform, and designs a set of devices which are simple and feasible, and the cost of maintenance and reinforcement is low. The grouting clamp reinforcement technology is widely used in the maintenance and reinforcement engineering of the offshore platform because of its advantages of convenient operation, low cost and good strengthening effect. Therefore, this paper focuses on the design and analysis of the local damaged structure grouting clamp reinforcement device for the offshore platform.

In 1989, Shuttleworth and others summarized and summarized the maintenance and reinforcement methods for the local damaged components of more than 60 offshore platforms in the world. The static test and fatigue life test were carried out for the T type joint grouting clamp with the grouting clamp reinforcement method and the mechanical clamp reinforcement method [8].

In 2007, the British Found Ocean Company designed a variety of grouting clamp [9], the grouting clamp used to repair and strengthen the offshore platform, such as pretension pinch clip and tighten tight clamp. This is similar to a grout clip. Grouting is injected into the annular space between the clamp and the existing joint. The grouting reaches the predetermined strength before exerting external force.

In 2008, the Advantech agency and Subsea developed a grouting three pipe, and used the grouting three pipe for the field operation of the submarine pipeline in the United States. The device was applied to the submersible area and the ultimate goal was used in ultra-deep waters [10].

In 2015, Australia advanced composite structure Co., Ltd. combined with Malaysia national oil company to develop polymer composite clamp [11]. The use of composite clamp instead of metal clamp has important advantages in small relative density, light quality, corrosion resistance and so on. The design method of these composite hoops is successfully demonstrated.

In 2015, Shi Xiang and others of Ocean University of China carried out a test on the short bolt type expansion self-stress grouting clamp [12], and found that the performance of the short bolt type expansion self-stress grouting clamp is better than the long bolt traditional structure.

In 2016, Sum W S and Leong K H, a researcher at the National Petroleum Corporation of Malaysia, proposed a new method [13], which uses a composite clamp to repair leakage or other damaged metal pipes, which uses a uniquely designed resin into the compound clamp. In 2016, CNOOC Zhang Yong engineer and others repaired the cracks at the cross strut of the cross - strut of the deep HZ21-1A jacket platform on the seabed [14].

In 2018, Shi Xiang and others of Ocean University of China tested the bearing capacity of the actual size of the marine application of self-stress grouting clamp, and carried out

laboratory and marine experimental studies on two hoop models respectively [15].

The reinforcement and repair technology of the grout hoop has been applied to the engineering projects abroad, but the stress and serialization design of the hoop in the marine environment need further study. This paper will combine the ocean current and wave force to carry out the research of underwater work and prevent loosening, and put forward the parametric design method for the specific size of the hoop. Two types of experimental models are designed: short bolt form clamp and long bolt form clamp.

ANALYSIS OF HYDRODYNAMIC LOAD OF GROUTING CLAMP ON WAVE AND CURRENT

DETERMINATION OF WAVE FORCE ON GROUT HOOP

In view of small scale structures, such as isolated pile columns, various pipelines, and seabed risers, the method proposed by Professor Morrison and others at the American University of Berkeley, 1950, is called the Morison method [16].

The Morison equation assumes that the existence of the small structure column does not affect the wave propagation. Because the grouting clamp on the jacket belongs to the small size component (the diameter of D is 3.45 m), the Morison equation is used to calculate the hydrodynamic force, which is mainly composed of two parts: the inertia force and the drag force.

On the seabed with a depth of d , a grouting clamp with a diameter of D is set on the jacket, and the wave height of H propagates along the sea surface, f_H is the horizontal force of the grout hoop at the height of Z , as shown in Fig. 1.

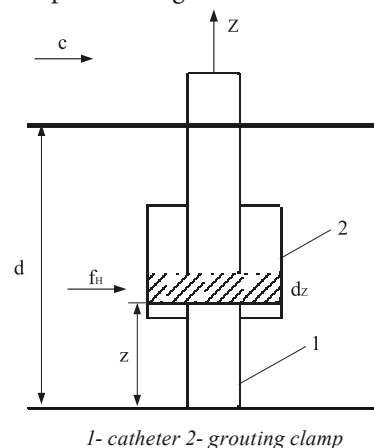


Fig. 1. Diagram of wave action of jacket hoop

The Morison equation divides the horizontal a force f_H acting on the Z height of the grouting clamp into two parts [17].

- 1) Horizontal drag force is: $f_D = \frac{1}{2} C_D \rho A u_x |u_x|$

2) Horizontal inertia force is: $f_I = C_M \rho V_0 \frac{du_x}{dt}$.

Combined with the above two formulae, the horizontal wave force of the grout clamp can be obtained. When the height is z , the wave force of the length dz is shown below:

$$f_H = f_D + f_I = \frac{1}{2} C_D \rho A u_x |u_x| + C_M \rho V_0 \frac{du_x}{dt} \quad (1)$$

Select a unit, assuming that its height is one, $A = 1 \times D$, $V_0 = \pi D^2 / 4$. When $D/L < 0.2$, the horizontal acceleration of wave water quality point can be replaced by $\frac{\partial u_x}{\partial t}$. For the clamps on the seabed, the wave forces received are different from those of other locations, and the wave forces they are subjected to can be written as:

$$f_H = \frac{1}{2} C_D \rho D u_x |u_x| + C_M \rho \frac{\pi D^2}{4} \frac{\partial u_x}{\partial t} \quad (2)$$

The Morison equation is a semi empirical and semi theoretical formula. The most important parameters are C_D and C_M when solving the wave forces acting on the grouting clamp. They will vary with the Reynolds number, without a fixed value. In addition, due to the complexity of the velocity and acceleration of the wave, it is difficult to get directly from the existing technology. So, when calculating the value, the wave theory should be used to simplify the treatment of C_D and C_M . In this paper, C_D was selected as 1.2 and C_M was 2.

The magnitude of horizontal wave force will be affected by many factors, including water depth d , wave height h , cycle t and so on. u_x and $\frac{du_x}{dt}$ are the main parameters of wave force. Analysis of wave loads by linear wave theory

According to the velocity potential correlation theory, the velocity of the wave water point can be obtained (the next $kx - \omega t$ is replaced by the $k(x - ct)$), in which the velocity of the horizontal and vertical directions is shown as Eq. (3) and Eq. (4), respectively.

$$v_x = \frac{\partial \Phi}{\partial x} = \frac{\pi H}{T} \frac{\text{ch}[k(z+d)]}{\text{sh}(kd)} \cos(kx - \omega t) \quad (3)$$

$$v_z = \frac{\partial \Phi}{\partial z} = \frac{\pi H}{T} \frac{\text{sh}[k(z+d)]}{\text{sh}(kd)} \sin(kx - \omega t) \quad (4)$$

At the same time, the acceleration of wave water points can be calculated. The horizontal and vertical accelerations are shown in Eq. (5) and Eq. (6) respectively.

$$\dot{v}_x = \frac{2\pi^2 H}{T^2} \frac{\text{ch}[k(z+d)]}{\text{sh}(kd)} \sin(kx - \omega t) \quad (5)$$

$$\dot{v}_z = \frac{2\pi^2 H}{T^2} \frac{\text{sh}[k(z+d)]}{\text{sh}(kd)} \cos(kx - \omega t) \quad (6)$$

In order to facilitate calculation, the wave is simplified and calculated by regular wave. The regular wave height is 1.5 m, the wave period is 10 s and the wavelength is 150 m.

From Eq. (3), (4), (5), (6), the velocity and acceleration of water points under different depths can be obtained, as shown in the following Fig. 2 and 3.

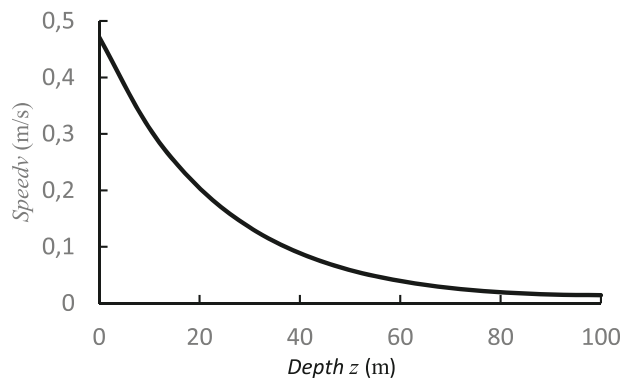


Fig. 2. Maximum horizontal velocity of water point in different water depths

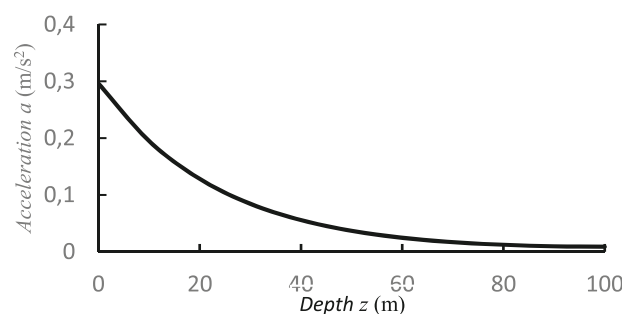


Fig. 3. Maximum horizontal acceleration of water point in different water depths

Under wave conditions, the maximum horizontal velocity of water quality decreases with the increase of water depth. Get the maximum at the sea level. When the water depth exceeds a wavelength of two, the maximum horizontal velocity of water quality is almost zero. It can be seen from Fig. 2 and 3 that the maximum horizontal acceleration of water quality is consistent with the horizontal velocity in the vertical direction, and decreases with the increase of water depth. Thus, it is possible to obtain the maximum wave force on the surface of the clamp.

The horizontal wave force at the height of z and the length dz of the grate hoop are shown in Fig. 1, and the force is obtained as follows:

$$dF_H = f_H dz = \frac{1}{2} C_D \rho D \left(\frac{\pi H}{T} \frac{\text{ch}(kz)}{\text{sh}(kd)} \right)^2 \cos \theta |\cos \theta| dz + C_M \rho \frac{\pi D^2}{4} \frac{2\pi^2 H}{T^2} \frac{\text{ch}(kz)}{\text{sh}(kd)} \sin \theta dz \quad (7)$$

Since the origin of the coordinate changed, and the previous still water surface changed to the bottom of the sea, z instead of $z+d$ was needed. $\theta = kx - \omega t$ in the form.

By integrating the Eq. (7), the horizontal wave force on the grit clamp can be obtained as follows:

$$F_H = \int_0^d f_H dz = C_D \frac{\rho g D H^2}{2} K_1 \cos \theta |\cos \theta| + C_M \frac{\rho g \pi D^2 H}{8} K_2 \sin \theta \quad (8)$$

In the Eq. (7)

$$K_1 = \frac{2kd + \text{sh}(2kd)}{8 \text{sh} 2(kd)} \quad (9)$$

$$K_2 = \tanh(kd) \quad (10)$$

Therefore, the maximum horizontal drag force and the maximum total horizontal force acting on the grouting clamp can be obtained by the Eq. (8).

$$F_{HD_{\max}} = C_D \frac{\rho g D H^2}{2} K_1 \quad (11)$$

$$F_{H_{\max}} = C_M \frac{\rho g \pi D^2 H}{8} K_2 \quad (12)$$

DETERMINATION OF FLOW FORCE IN SHANGHAI WITH GROUDED CLAMP

The situation inside the sea is very complicated. There are not only waves but also ocean currents. Generally, we think that the large-scale non periodic motion of sea water in the horizontal direction is called the ocean current, which is mainly divided into periodic and short-term flow, cold current and warm current, compensation flow and wave flow [18]. The grouting clamp is also affected by the sea flow force in the sea water.

Because the ocean wave usually takes several months, it can be considered that for a given sea condition, the current does not change with time. At the time of calculation, the current force is considered to be a constant value. Ocean currents and waves will be affected. It is generally considered that ocean currents only change the wave velocity, while the effect on wave amplitude can be ignored. The Morison equation can be used to calculate the wave forces acting on the grouting clamp. It is generally considered that the force acting on the cylinder is limited to the drag force [19].

According to the method of calculating the force of pure sea current in the API standard (American Petroleum Association), the calculation of the force of sea current, that is, the force F_c of the current force on the unit length of the grouting clamp, is calculated by the simple calculation of the force of the sea current:

$$F_c = \frac{1}{2} \rho C_D D u_c |u_c| \quad (13)$$

If waves and currents exist simultaneously, waves and currents should be chosen to act in the same direction as conduits and grouting clamps. The motion characteristics of water quality points should consider the combined action of wave and flow, so wave and flow should be simulated in the same load condition. The combined effect of ocean currents and waves greatly increases the drag force of seawater on marine engineering structures, F_{HD} . At this time, the pulling force of the unit length of the grouting clamp is combined as follows:

$$F_{HD} = \frac{1}{2} C_D \rho D (\mathbf{V} + \mathbf{V}_c) |\mathbf{V} + \mathbf{V}_c| \quad (14)$$

In the Eq (14):

\mathbf{V} -- the velocity vector of the wave, m/s;

\mathbf{V}_c -- the velocity vector of the ocean current, m/s.

Due to the steady flow of the current, the velocity and direction of the flow do not change with time. Therefore, the acceleration caused by the motion acceleration of the water point has no effect on the inertia force of the grout hoop, and the inertia force is still used in the wave load analysis. Therefore, the integral force of the grouting clamp can be applied to the total wave force on the grouting clamp.

$$F_H = \frac{1}{2} C_D \rho D (\mathbf{V} + \mathbf{V}_c) |\mathbf{V} + \mathbf{V}_c| + C_M \rho \frac{\pi D^2}{4} \dot{V} \quad (15)$$

The velocity direction of ocean current is the same as the horizontal movement direction of wave water quality point:

$$v = v_x + v_c = \frac{\pi H}{T} \frac{\text{ch}[k(z+d)]}{\text{sh}(kd)} \cos \theta + v_c \quad (16)$$

The drag force F_{HD} on the length of the pipe and the grout clamp is the following:

$$F_{HD} = \frac{1}{2} C_D \rho D \left| V_c + \frac{\pi H \cosh(k(d+z)) \cos \theta}{T \sinh(kd)} \right| \cdot \left(V_c + \frac{\pi H \cosh(k(d+z)) \cos \theta}{T \sinh(kd)} \right) \quad (17)$$

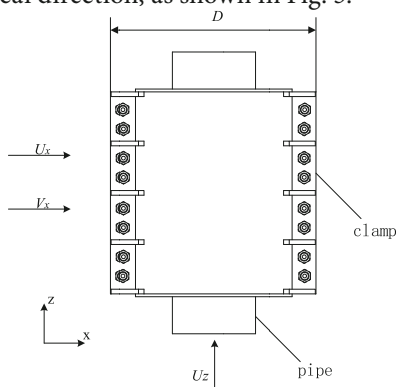
In this paper, the current velocity of the sea V_c is 0.6m/s, and the environmental depth of the pipe and grouting clamp is d 100m, the wave period T is 10s, the wave height H is 1.5m, the wavelength is 150m.

HYDRODYNAMIC LOAD CALCULATION OF CLAMPS

1) Vertical clamps subjected to wave combined forces

The impact of the duct on the vertical conduit is shown in Fig. 4. Under the action of wave, the water quality points both in the horizontal direction and in the vertical direction, and the wave water points in different directions both have speed and acceleration at the same time, so the wave force of the hoop on the vertical guide pipe is mainly composed of the following four forces: horizontal

direction drag force, horizontal direction inertia force, vertical direction drag. The force and the vertical force in the vertical direction, as shown in Fig. 5.



Note: U_x is the horizontal velocity of wave water quality, U_z is the vertical velocity of wave water quality point, and V_x is the horizontal velocity of ocean current.

Fig. 4. Diagram of wave flow in vertical direction clamp

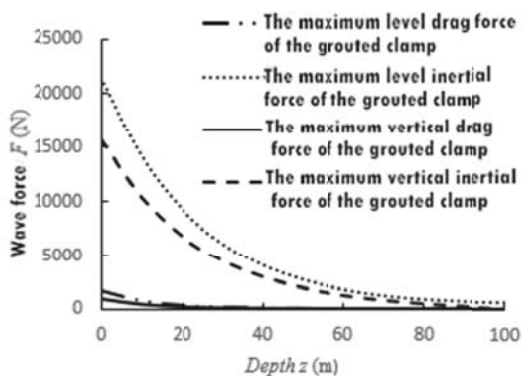


Fig. 5. Variation of wave force component of vertical hoop with depth of water

Besides the wave force, the vertical clamp is also affected by the current force. In this paper, the force of the uniform current on the hoop is mainly studied, so the horizontal drag force of the current only needs to be considered. The Morison formula can be obtained:

$$F_1 = \frac{1}{2} C_d \rho D V_x^2 h = 2899.72 \text{ N} \quad (18)$$

Combined wave force and ocean current force, the maximum horizontal force can be obtained under the combined action of wave and current, as shown in Fig. 6.

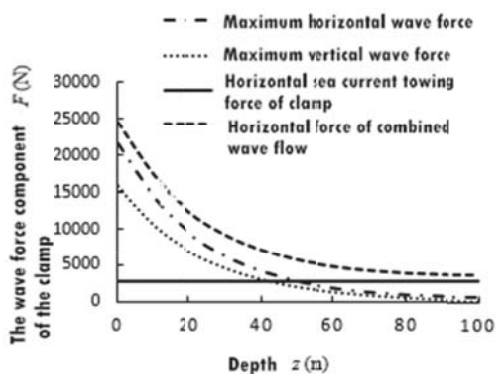


Fig. 6. The joint force of the wave flow in the hoop

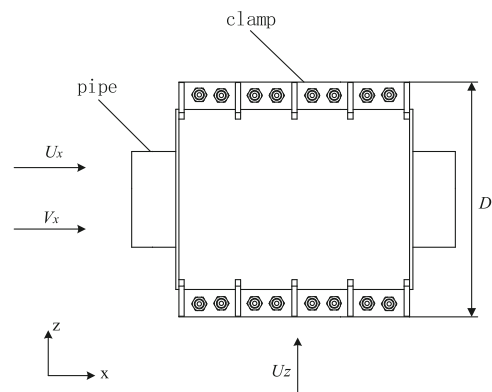
The vertical force of the vertical hoop at 0 m and 100 m can be obtained as follows Tab.1.

Tab. 1. Vertical clamps subjected to wave combined forces

Depth of water	0 m	100 m
Axial force	15677 N	0 N
Radial force	24450 N	3553 N

2) Horizontal clamps subjected to wave combined forces
When the pipe is in a horizontal state, it is necessary to consider the force of the current and wave from the axial and radial to the clamp, as the position of the clamp is different, as shown in Fig. 7 and 8.

(1) Axial flow



Note: U_x is the horizontal velocity of wave water quality, U_z is the vertical velocity of its ocean current.

Fig. 7. Diagram of wave flow in horizontal direction clamps

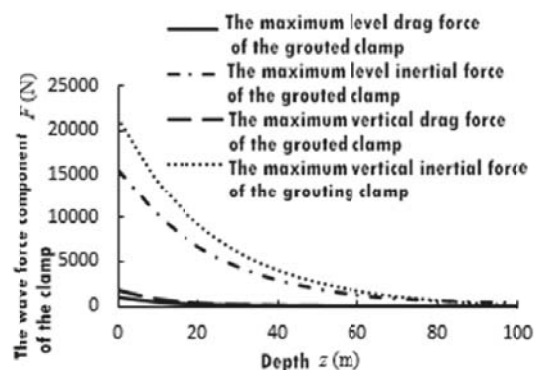


Fig. 8. Wave forces in different directions of clamps under different depths of water

Besides the wave force, the axial flow clamp is also affected by the ocean current force. In this section, we mainly study the effect of uniform current on horizontal hoop, so we only need to consider the horizontal drag force of current. The Morison formula can be obtained:

$$F_1 = \frac{1}{2} C_d \rho A V_x^2 = 1504 \text{ N} \quad (19)$$

Combined wave force and ocean current force, the maximum horizontal force can be obtained under the combined action of wave and current, as shown in Fig. 9.

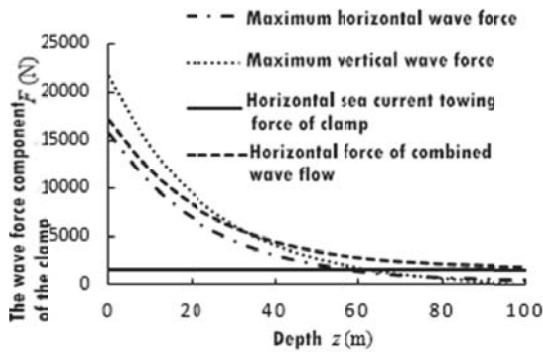


Fig. 9. The joint force of the wave flow in the hoop

The horizontal force of the horizontal hoop at 0 m and 100 m can be obtained as Tab.2.

Tab. 2. Horizontal clamps subjected to wave combined forces

Depth of water	0 m	100 m
Axial force	17188 N	1979 N
Radial force	21540 N	0 N

(2) Radial flow

Besides the wave force, the hoop is also affected by the current force, as shown in Fig. 10.

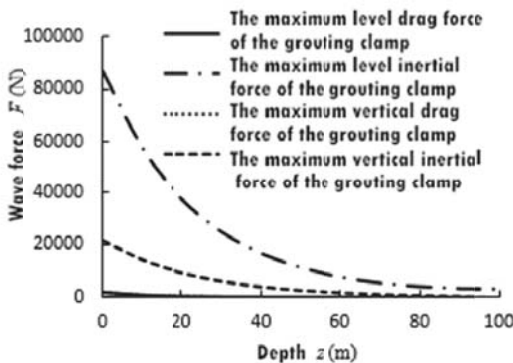


Fig. 10. Wave forces in different directions of clamps under different depths of water

Besides the wave force, the hoop is also affected by the current force. In this paper, the force of the uniform current on the hoop is mainly studied, so the horizontal drag force of the current only needs to be considered. The Morison formula can be obtained:

$$F_1 = \frac{1}{2} C_d \rho D V_x^2 h = 2899.72 \text{ N} \quad (20)$$

The horizontal force amplitude can be obtained under the combined action of wave and current under different wave depths, as shown in Fig. 11.

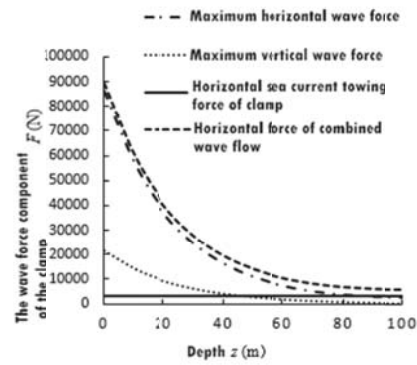


Fig. 11. The joint force of the wave flow in the hoop

The combined force of the horizontal hoop at 0 m and 100 m can be obtained as Tab.3:

Tab. 3. Horizontal clamps subjected to wave combined forces

Depth of water	0 m	100 m
Axial force	0 N	0 N
Radial force	89102	5512

Considering the influence of the hoop gravity and buoyancy, the gravity buoyancy of the hoop and the combined force vector of the wave current are added to the resultant force of the hoop in the sea water. Because the loosening of the hoop is due to the axial force of the hoop, all the axial forces of the clamp are superimposed on the axial force, and the axial force of the clamp is calculated, and the data of the analysis of the slipping and the determination of the pretension are provided [22]. As the analysis of the slipping of the clamp requires the maximum resultant force under different conditions, Tab. 4 is the resultant force of the clamp in the three working conditions.

Tab. 4. Axial joint force of clamps under three operating conditions

Hoop condition	Vertical clamp		Horizontal clamp Axial flow		Horizontal clamp Radial flow	
	100m	0m	100m	0m	100m	0m
Axial force	535476 N	551153 N	1979N	17188N	0N	0N

In this section, the force of the grout clamps under different wave conditions is determined. The analysis of the combined force of the wave flow can provide the design data for the

subsequent analysis of the loosening of the hoop and the pre-tightening force of the bolt.

THE PARAMETERIZED DESIGN OF THE MAIN STRUCTURE OF THE GROUT HOOP

DETERMINATION OF THE AXIAL DESIGN LENGTH OF THE GROUT HOOP

The parametric design method is designed according to the strength of the local defect of the jacket and the size of the defect. The force of the offshore jacket in the depth of 100 to 500 meters is analyzed. The actual size of the vertical guide jacket is $\Phi 1828 \times 25 \text{ mm}$, for example, the radial stress of the jacket is 1 MPa and the stress under the combined action of the wave flow when the water depth is 100 meters deep, and the stress of the combined action of the wave flow under the 100 meter water depth is 158 Pa for the size of the jacket under the 100 meter depth of water [23]. The combined force of the current is very small and negligible. The axial force of the jacket is the gravity of the offshore platform, and the weight of the platform is shared on the four jacket. The force value on each jacket is multiplied by a safety factor, that is, the axial force, which is 150 MPa. The material of the jacket is DH36, the yield limit is 355 MPa, and the safety factor is $n_s=1.5$. The maximum should be as follows:

$$[\sigma] = \frac{355}{1.5} = 237 \text{ MPa} \quad (21)$$

The diameter of the defect is 300 mm to 1200 mm, and a value of 100 mm is taken from each other. As shown in Fig. 12, the simulation result of the defect of 1200 mm diameter in ANSYS is shown in Fig. 12.

In the ANASY, the stress size of different color regions is set. The red area in the diagram is that the stress is greater than the allowable stress, which is the dangerous area near the tube defect, and the axial distance of the danger zone is measured [24]. The following is a simulation diagram of the different sizes of defects in the jacket at the depth of 100 meters. It can be seen that the range of stress exceeding allowable stress is gradually expanding, as shown in Fig. 13.

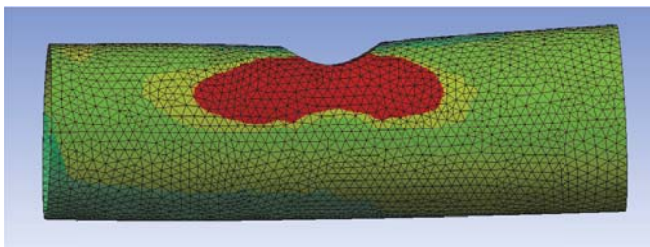


Fig. 12. Diameter 1200mm defect simulation cloud map

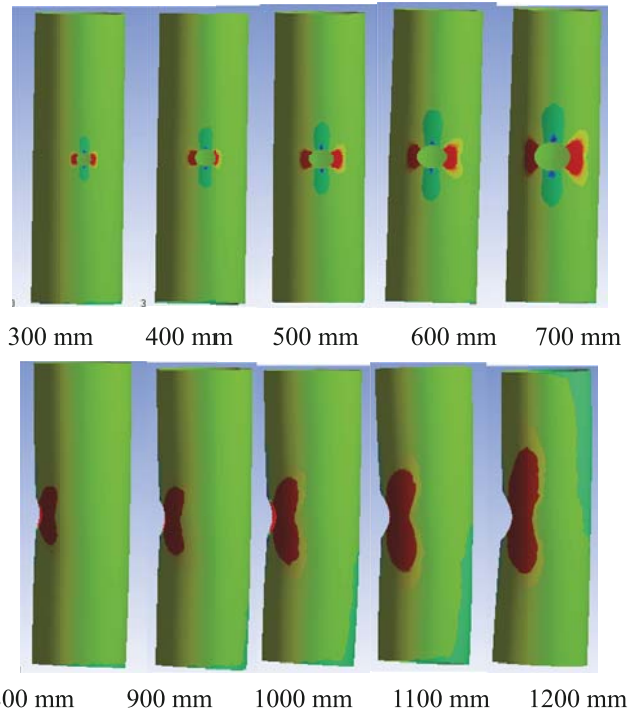


Fig. 13. Simulation diagram of 100 meter water depth defect tube frame

The range of the dangerous area is butterfly type, the axial stress near the defect is smaller, and the circumferential stress is the largest. When the size of the clamp is designed, the axial length of the clamp is larger than the axial length of the danger zone, and the stress concentration part is covered while the defect is covered [25]. A safety factor of 1.5 is obtained for the axial distance of the dangerous area, and the axial length of the clamp design is obtained. Therefore, the axial size of the hoop should be calculated according to the size of the dangerous area corresponding to the different water depths and different defect sizes.

In order to get the change law of the design size of the jacket with the defect diameter under different water depth, the data are synthesized to obtain the change law of the design size of the clamp with the defect diameter, as shown in Fig. 14.

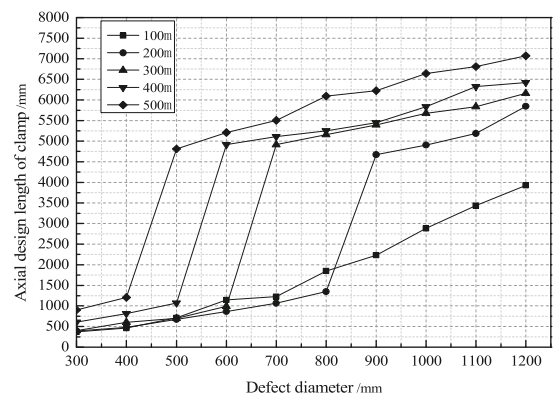


Fig. 14. Design length of clamp for different defects in different depths

In order to form a parameterized form for hoop design and improve the efficiency of the hoop design, the data of each point in the graph are synthesized, as shown in Fig. 15.

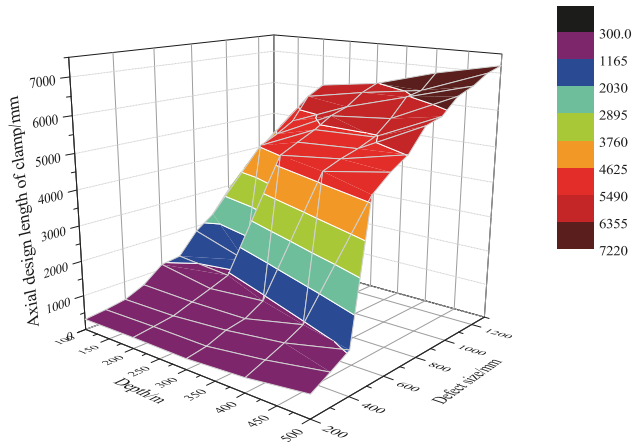


Fig. 15 the relationship between the axial length of the hoop and the size of the water depth and defect

1) The corresponding relationship between the design dimension of the clamp axis and the defect diameter is 100 m depth.

$$P(x) = 703.4 - 3.33x + 7.79 \times 10^{-3} x^2 - 2.33 \times 10^{-6} x^3 \quad (22)$$

2) The corresponding relationship between the design dimension of the clamp axis and the defect diameter is 200 m depth.

$$P(x) = \begin{cases} 316.21 - 0.56x + 2.8 \times 10^{-3} x^2 - 6.24 \times 10^{-7} x^3 & (x \leq 800) \\ 53232.8 - 137.6x + 0.127x^2 - 3.75 \times 10^{-5} x^3 & (x > 800) \end{cases} \quad (23)$$

3) The corresponding relationship between the design dimension of the clamp axis and the defect diameter is 300 m depth.

$$P(x) = \begin{cases} -176.25 + 3.46x - 7.06 \times 10^{-3} x^2 + 7.54 \times 10^{-6} x^3 & (x \leq 600) \\ 3603.89 + 1.14x + 1.4 \times 10^{-3} x^2 - 4.99 \times 10^{-7} x^3 & (x > 600) \end{cases} \quad (24)$$

4) The corresponding relationship between the design dimension of the clamp axis and the defect diameter is 400 m depth.

$$P(x) = \begin{cases} -201 + 4.245x - 7.75 \times 10^{-3} x^2 + 8.7 \times 10^{-6} x^3 & (x \leq 500) \\ 7919.21 - 12.02x + 0.0145x^2 - 4.54 \times 10^{-6} x^3 & (x > 500) \end{cases} \quad (25)$$

5) The corresponding relationship between the design dimension of the clamp axis and the defect diameter is 500 m depth.

ANALYSIS OF SLIPPING OF GROUT HOOP

According to the slippage of the hoop, the bolt is pre-tightened. The compression of the hoop in the expansion process of the cement slurry will offset the load of a part of the bolt and reduce the pre-stress on the outer wall of the

inner tube, which should be taken into account in the design process [26].

1) Taking the saddle plate as the research object, according to the pressure balance between the cement slurry ring, the bolt and the saddle plate, the interface pressure of the inner surface of the cement slurry ring and the clamp is P_0 [20]:

$$P_0 = \frac{NF}{2R_0L} \quad (27)$$

2) According to the transfer of pressure between the inner cavity of the hoop and the outer surface of the cement slurry ring, the strain equivalent relation Eq. (4-9) of the cement slurry ring and the inner tube is obtained by combining the strain boundary condition and the strain equilibrium relationship. The interface pressure of the cement slurry ring and the damaged inner tube can be solved by the data of P .

$$\varepsilon_{steel}(P, R) = \varepsilon_{grout}(P_0, R) + \varepsilon_{grout}(P, R) \quad (28)$$

In the Eq. (28): R is the inner ring radius of the grouting ring

$$\varepsilon_{steel}(P, R) = -\frac{P \cdot R}{E_s} \left[\frac{(R^2 + R_1^2)}{(R^2 - R_1^2)} - \mu_s \right] \quad (29)$$

$$\varepsilon_{grout}(P_0, R) = -\frac{P_0}{E_g} \cdot \frac{2 \cdot R_0 \cdot R}{R_0 - R^2} \quad (30)$$

$$\varepsilon_{grout}(P, R) = \frac{P \cdot R}{E_g} \left[\frac{(R_0^2 + R^2)}{(R_0^2 - R^2)} + \mu_g \right] \quad (31)$$

In the Eq. (29-31):

- R_1 -- Inner wall radius of inner tube, mm;
 - E_s -- The modulus of elasticity of the steel, G'Pa;
 - μ_s -- Poisson ratio of steel;
 - E_g -- Cement modulus of elasticity, GPa;
 - μ_g -- Poisson's ratio of cement.
- The relationship between P_0 and P is as follows:

$$P = \lambda P_0 \quad (32)$$

In the formula: λ is the pressure transfer coefficient.

3) From the interfacial pressure between the cement slurry and the damaged inner tube, the sliding stress of the hoop on the jacket can be obtained according to the empirical formula of the self-stress and the sliding stress of the clamp [21]. The design formula is as follows:

$$f_{sa} = \left(\frac{0.95c_s}{SF_b} + \frac{0.35c_{s1}P}{SF_f} \right) \left[1 - 0.13 \left[\frac{S}{D} \right] \right] \left[1 + 12 \left[\frac{T}{D} \right] \right] \quad (33)$$

In the Eq. (33):

- f_{sa} -- The allowable sliding stress of the clamp, Mpa;
- C_s, C_{s1} -- The surface coefficients of cement paste and friction part were $C_s=0.6$ and $C_{s1}=1$, respectively.
- SF_b -- Bond safety factor, take 4.5;
- SF_f -- Friction safety factor, take 1.7;

S -- The contact length of the inner pipe with the cement slurry, mm;

D -- Inner diameter of cement slurry ring, mm;

T -- Inner tube wall thickness, mm.

4) The allowable sliding stress of the clamp is obtained by introducing the interface pressure P between the damaged inner pipe and the mud ring into the Eq. (33). The slipping stress of the hoop under external loads is f_s , and the formula is as follows:

$$f_s = \frac{F_x}{\pi DS} \quad (34)$$

In the Eq(34):

F_x -- Axial load of grout hoop, N.

The axial force of the vertical jacket is the joint force of the wave flow, the vector of gravity and the buoyancy, and the horizontal jacket is acted by the axial force at the position of the axial flow, and the axial force is the joint force of the wave flow.

When $f_s < f_{sa}$, the hoop will not slip, thus reducing the pre-tightening force of the single bolt when the hoop is not slippage. The results are as follows:

Vertical jacket: deep in 0 meters of water, $F > 19688.4815$ N;

Deep in 100 meters of water, $F > 19128.46$ N;

Horizontal jacket: deep in 0 meters of water, $F > 6211.143$ N;

Deep in 100 meters of water, $F > 715.235$ N.

In order to select the type and preload of the bolt, the design process of the hoop is finished by referring to the minimum pretightening force of the bolt. The main steps of parameterized design is shown in Fig. 16.

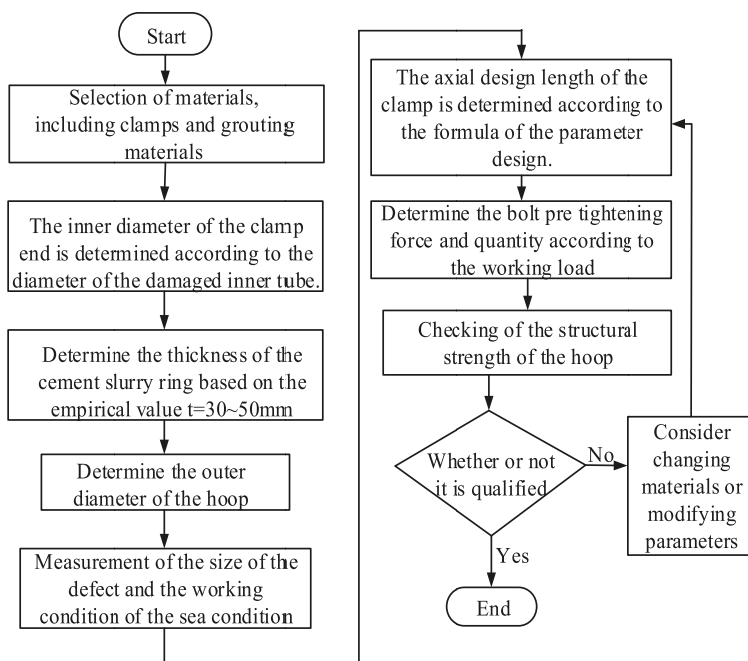


Fig. 16. Main steps of parameterized design

EXPERIMENT OF STRAIGHT TUBE LONG BOLT HOOP SLIPPING

The slipping test of the hoop is carried out by WDW3100 micro controlled electronic universal testing machine. The maximum loading pressure is 10 t. In order to make the side of the bolt plane, the bolt is designed into the form of the long square, and the strain gauge of the bolt is used to measure the strain of the bolt [27]. The gluing form of the strain gauge on the bolt side is shown in Fig. 17.



Fig. 17. Long bolt form grouting clamp and strain gauge on the side of bolt

The slipping force of the hoop is tested with a circular end cover so that the hoop is detached from the inner tube, and the force exerted on the clamp from the inner tube is determined as the slipping force of the clamp. Three computers were used to measure the pressure and displacement of the press respectively, the strain of the bolt and the strain of the inner tube, as shown in Fig. 18.

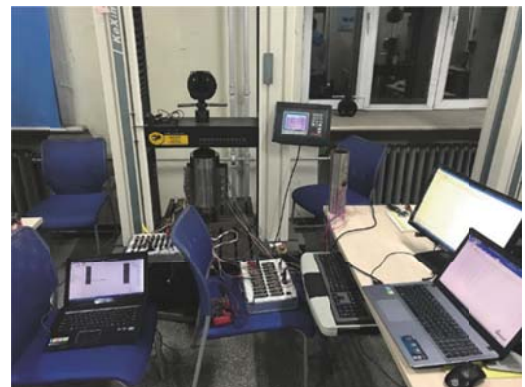


Fig. 18. Hoop slippage axial compression test

A certain pre-tightening force is applied to the bolt. The strain value of each bolt can be obtained by the computer connected with the strain gauge of the bolt. The pre tightening force of the bolt is adjusted, until the strain value of the eight bolts is almost stable and the difference of the value of each bolt strain is small, and the first group pre-tightening force of the bolt is obtained, as shown in Tab. 5.

Tab. 5. First pre-tightened strain stress values of each bolt

Number of bolts	1	2	3	4	5	6	7	8
strain	216	79	227	251	203	217	203	120
Stress/MPa	44.49	16.27	46.76	51.70	41.81	44.48	41.81	24.6

The bolt is M8 coarse tooth bolt, and the stress of the eight sets of bolts is 311.959 MPa, and the bolt preload is:

$$F = \sum \sigma_0 \times A_s$$

The A_s is the nominal stress cross section of the bolt, and the A_s for the coarse tooth bolt of M8 is 36.6 mm². The pre-tightening force of the first pre-tightening bolt is calculated to be 11417.7 N.

When the axial pressure is applied, a mark is made on the inner tube at the edge of the hoop. As shown in Fig. 19 and Fig. 20, the axial pressure is applied to the clamp. The slipping and moving of the clamp can be judged according to the position of the clamp on the edge of the clamp and the pressure and displacement curve of the press on the computer.



Fig. 19. Before the first pre-tensioning slipping



Fig.20. After the first pre-tensioning slipping

Compared with Fig. 19 and Fig. 20, it can be seen that the clamp edge coincides with the drawn line after the first preload slipping. When the clamp is relatively slipping, the force of the press reaches 5.85 KN, and the pressure value changes abruptly.

Tighten the bolt again, observe the strain value of each bolt, adjust the pre-tightening force on each bolt until the value of each strain is close, and Tab. 6 is the stress and strain value of the second pre tightened bolts.

Tab. 6. Second pre tightened strain stress values of each bolt

Number of bolts	1	2	3	4	5	6	7	8
strain	430	305	453	504	406	434	406	240
Stress/MPa	88.6	62.8	93.3	103	83.6	89.4	83.6	49.4

The pre-tightening force of the second bolt is 23960.85 N. The line drawn on the second preload slipping is completely blocked by the edge of the clamp. The pressure exerted on the press reaches 10.22 KN.

Tighten the bolt again, observe the strain value of each bolt, adjust the pre-tightening force on each bolt until the value of each strain is close, and Tab. 7 is the third pre tightening strain stress value of each bolt pre-tightening.

Tab. 7. Third pre tightened strain stress values of each bolt

Number of bolts	1	2	3	4	5	6	7	8
strain	441	313	465	516	415.5	436.9	420	240.4
Stress/MPa	90.84	64.48	95.79	106.2	85.59	90	86.52	49.52

The pre-tightening force calculated for third times is 24487.047 N. Axial pressure is applied to the clamp to observe the slipping of the clamp again and record the pressure exerted by the press when sliding.

Before the third slippage experiment is re marked, it can be seen from Tab.7 that the clamp is sliding downward towards the marking line. When the hoop slips, the pressure exerted on the press changes abruptly. When the clamp is slipping, the pressure value is 12.34 KN.

The pretension of the long bolt on the three slip test clamp is 11417.7 N, 23960.85 N and 24487.047 N respectively. The corresponding slipping force is 5850 N, 10220 N and 12340 N respectively. The equivalent friction coefficient can be calculated to be 0.512, 0.427, 0.504, respectively, as shown in Fig. 21. The pre tightening force of the bolt and the slip force of the clamp are linear, and the equivalent friction coefficient is 0.481.

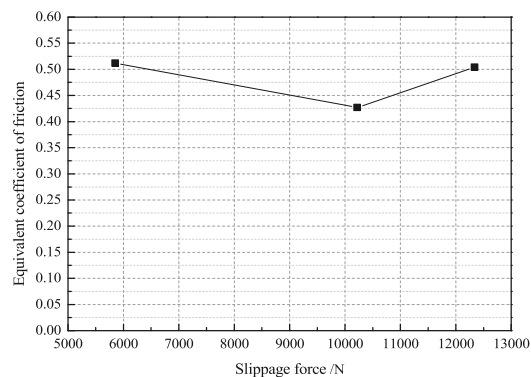


Fig. 21. The equivalent friction coefficient of different slip forces

According to the relationship between the slipping force of the clamp and the bolt preload, the reliability of the experimental results can be proved. Therefore, when the clamp is designed, the minimum pre tightening force required by the bolt can be calculated according to the axial force of the clamp under a specific working environment, so the bolt selection can be made.

CONCLUSIONS

In this paper, the combined force of wave and current under different working conditions is calculated to analyze the loosening of hoop and the pre-tightening force of bolts. The axial distance of the dangerous zone near the defect is determined by simulation analysis, and the axial design length of the clamp is determined, and the parameterized design mode is formed, and the parameterized design process of the whole structure of the hoop is summarized. The relationship between slipping force and bolt pre-tightening force is obtained through experimental analysis of hoop slippage.

ACKNOWLEDGEMENTS

This paper is funded by NSFC (Contract name: Research of Analysis and Experiments of Gripping and Bearing Mechanism for Large-scale Holding and Lifting Tools on Ocean Foundation Piles), (Contract number:51479043).The views expressed here are the authors alone.

BIBLIOGRAPHY

1. Rathnayaka, K.F., Amayotte P.: Accident modeling and risk assessment framework for safety critical decision-making: application to deepwater drilling operation. *Proceedings of the Institution of Mechanical Engineers, Part O: Journal of risk and reliability*, 2013, 227(1), Pp. 86-105.
2. Dong, W., Moan, T., Gao, Z.: Fatigue reliability analysis of the jacket support structure for offshore wind turbine considering the effect of corrosion and inspection. *Reliability Engineering & System Safety*, 2012, 106, pp. 11-27.
3. Jiang, Y., Chi J., Liu, J.Y.: Damage assessment on structural concave of jacket pipe. *Ship structure*, 2016, 27(06), Pp. 35-40.
4. Zhan, X.H.: Model tests on long-term capacity properties of expansive stressed grouted clamp. *Ocean University of China, Qing Dao*, 2012, Pp. 1-3.
5. Barltrop, N.D.P., Adams, A.J.: Dynamics of fixed marine structures. *Butterworth-Heinemann*, 2013, Pp. 86-105.
6. Li, F., Xu, C.H., Liu, C.S.: Vibration-based Damage Detection Research on Offshore Platform. *Coal technology*, 2011, 30(8), Pp. 207-209.
7. Yin, X.Z., Ta, N.: Vibration-based Damage Diagnosis Research on Offshore Platform. *Journal of Zhejiang Water Conservancy and Hydropower College*, 2009, 21(2), Pp. 96-99.
8. Shuttleworth, F.P., Billington, C.J.: A New Approach to Designing Repair Clamps for Offshore Structures. 21st Annual otc, no. 05, pp. 317-330, 1989.
9. <http://www.foundocean.com/en/what-we-do/inspection-repair-maintenance/grouted-repair-clamps/>, 2017.12.15.
10. Jeff, S.: Update on development of subsea grouted tee - subsea hot tap. *Pipeline & Gas Journal*, 2008, 10, Pp. 70-71.
11. Djukic, L.P., Sum, W.S., Leong, K.H.: Development of a fibre reinforced polymer composite clamp for metallic pipeline repairs. *Materials & Design*, 2015, 70, Pp.68-80.
12. Li, C.: The capacity properties and design method of short-bolts expansive stressed grouted clamp. *Ocean University of China, Qing Dao*, 2014, Pp.57-62.
13. Sum, W.S., Leong, K.H., Djukic, L.P.: Design, testing and field deployment of a composite clamp for pipeline repairs. *Plastics, Rubber and Composites*, 2016, 45(2), Pp. 81-94, 2016.
14. Chen, B., Zhang, R.G., Zang, Y.: Design of grouting clamps and grouting material selection and tests on jacket maintenance in hectometer water depth. *China Offshore Oil and Gas*, 2016, 06, Pp.128-132.
15. Shi, X., Ma, Y., Zhang, H.H.: Tests on capacity properties of the real-size expansive stressed grouted clamp. *The Ocean Engineering*, 2018, 36(1), Pp.122-127.
16. Jensen, J., Juncher, S.: procedures for extreme wave load predictions – Wave bending moment in ships. *Marine Structures*, 2008, 22(2), Pp. 245-249.
17. Hänninen, S., Mikkola, T., Matusiak, J.: On the numerical accuracy of the wave load distribution on a ship advancing in short and steep waves. *Journal of Marine Science and Technology*, 2012, 17(2), Pp.73-77.
18. Zhang, H.B., Ren, H.L., Dai, Y.S.: Wave load computation in direct strength analysis of semi-submersible platform structures. *Journal of Marine Science and Application*, 2004, 3(1), Pp.7-13.
19. Roeder, C.W., Cameron, B., Brown, C.B.: Composite action in concrete filled tubes. *Journal of structural engineering*, 1999, 125(5), Pp. 477-484.
20. Jiao, G.Y., Zhou, L., Shi, X.: Capacity performance of large-scale model of expansive stressed grouted clamp. *Periodical of Ocean University of China*, 2017, 47(1), Pp. 111-118.
21. Shi, X., Zhang, H.H., Li, C.: Tests on slip capacity for the short-bolt-type expansive stressed grouted clamp. *The Ocean Engineering*, 2015, 33(5), Pp.113-117.

22. Ibrahim, M.S., Kasim, S., Hassan, R., Mahdin, H., Ramli, A.A., Md Fudzee, M.F., Salamat, M.A.: Information Technology Club Management System. *Acta Electronica Malaysia*, 2018, 2(2), Pp. 01-05.
23. He, Z.G., Gu, X.N., Sun, X.Y., Liu, J., Wang, B.S.: An efficient pseudo-potential multiphase lattice Boltzmann simulation model for three-dimensional multiphase flows. *Acta Mechanica Malaysia*, 2017, 1(1), Pp. 08-10.
24. Ememu, A.J., Nwankwoala, H.O.: Application of Water Quality Index (Wqi) For Agricultural and Irrigational Use Around Okpoko, Southeastern Nigeria. *Engineering Heritage Journal*, 2018, 2(1), Pp. 14-18.
25. Sen, S.C., Kasim, S., Md Fudzee, M.F., Abdullah, R., Atan, R.: Random Walk from Different Perspective. *Acta Electronica Malaysia*, 2017, 1(2), Pp. 26-27.
26. Sathishkumar, S., Kannan, M.: Design and Fatigue Analysis of Multi Cylinder Engine And Its Structural Components. *Acta Mechanica Malaysia*, 2018, 2(2), Pp. 10-14.
27. Abdul Sukor, N.S., Mohd Sadullah, A.F.: Addressing the road safety results impasse through an outcome-based approach in the state of Penang, Malaysia. *Engineering Heritage Journal*, 2017, 1(1), Pp. 21-24.

CONTACT WITH THE AUTHORS

Zhuo Wang, Ph.D.

e-mail: wangzhuo_heu@hrbeu.edu.cn

College of Mechanical and Electrical Engineering
Harbin Engineering University
Harbin
Hei Longjiang 150001
CHINA